CALIBRATION AND DATA PROCESSING TECHNIQUES FOR GROUND PENETRATING RADAR SYSTEMS WITH APPLICATIONS IN DISPERSIVE GROUND

by

Charles P. Oden

A thesis submitted to the Faculty and Board of Trustees of the Colorado School of Mines in partial fulfillment of the requirements for the degree of Doctor of Philosophy (Geophysical Engineering).

Golden, Colorado

Date:_____

Signed:_____
Charles P. Oden

Approved:_____
Dr. Gary R. Olhoeft
Thesis Advisor

Golden, Colorado

Date:_____

_____
Dr. Terence K. Young
Professor and Head
Department of Geophysics

ABSTRACT

The ground penetrating radar (GPR) method has the highest resolution of any standard geophysical technique. One of the biggest difficulties with this method is that the depth of penetration can be limited, especially in dispersive ground. Further, images obtained from dispersive ground usually have less spatial resolution due to dispersion (attenuation and dilation) of the waveforms traveling in the subsurface. This dissertation describes steps that can be taken to predict subsurface waveforms and improve the subsurface images in lossy ground. The work here has been tailored for use with the U. S. Geological Survey RTDGPR (a real-time digitizing GPR specifically designed for use in conductive ground), but the methodology can be applied to properly characterize and process data from essentially any impulse GPR system.

To help estimate the shape of the subsurface waves, the response of the RTDGPR electronics were calibrated using laboratory measurements. The antennas were calibrated using numerical simulations because laboratory tests of antennas require prohibitively expensive apparatus. Because the RTDGPR antennas are ground-coupled, their response changes as a function of the ground properties directly beneath the antennas. Therefore, many numerical simulations were made to determine the antenna response for a wide range of ground conditions. The accuracy of the GPR system calibration was tested by comparison with actual data recorded in air and over water.

With a calibrated GPR system and knowledge of the ground properties near the antennas, the subsurface waveforms may be calculated. A non-linear inversion algorithm was constructed to estimate the material properties near the antennas using the early arrivals in the GPR trace. The limitations to the use of the inversion algorithm that arise from horizontal and vertical heterogeneity are discussed.

The remainder of the dissertation addresses methods to illustrate the usefulness of information about the subsurface waveforms. Since most GPR surveys are interpreted in

the field with no subsequent processing, a method to quickly calculate the subsurface fields is presented. Knowledge of the subsurface wave fields is used with real survey data to estimate the material properties of a subsurface reflector. A migration algorithm is presented to enhance resolution and reduce image blurriness caused by dispersive soils.

TABLE OF CONTENTS

LIST OF FIGURES

LIST OF TABLES

LIST OF SYMBOLS

a_{1r}	effective norm. wave amplitude incident on port 1 of the receiver electronics module
$a_{1r,dBm}$	effective norm. wave amplitude incident on port 1 of the receiver electronics module in decibels above 1 mW.
a_i	normalized amplitude of incident wave
a_t	normalized amplitude of wave at transmitting antenna feed port
a_{1a}	normalized wave amplitude incident on port 1 of device *a* (pickoff tee)
A_a	attenuation of the receiver module attenuator in dB
$\mathbf{A}$	forward operator returning waveform parameters as a function of model parameters
b_{2a}	normalized wave amplitude scattered from port 2 of device *a* (pickoff tee)
b_{2b}	normalized wave amplitude scattered from port 2 of device *b* (balun)
b_r	normalized amplitude of wave at receiving antenna feed port
b_{2DUT}	normalized wave amplitude scattered from port 2 of device *DUT* (DUT)
$b_{ij,tk}$	norm. wave amplitude scattered from port *i* of device *j* at time index *k*
$b_{\mathrm{VNA},dBm}$	normalized vector network analyzer average output level in dB
b_i	normalized amplitude scattered wave
c	speed of light *in vacuo* ($3 \cdot 10^8$ m/s)
d	standoff (antenna height above ground)
D	normalized RMS difference between measured and predicted waveform parameters
D_s	dynamic range needed to image a scatter with cross section σ_s
E	electric field (arbitrary component)
E_x	component of electric field vector in *x* direction
E_y	component of electric field vector in *y* direction
E_z	component of electric field vector in *z* direction
E_{0x}	component of $\mathbf{E_0}$ in *x* direction
$E_{0x,t}$	
$E_{\rho 0}$	component of $\mathbf{E_0}$ in ρ direction
$E_{\phi 0}$	component of $\mathbf{E_0}$ in ϕ direction
$\mathbf{E}$	electric field vector
$\mathbf{E_0}$	constant electric field vector, value of $\mathbf{E}$ on reference plane
$\mathbf{E_{0,t}}$	
G_{tx}	gain of transmitting antenna in direction of scatterer
G_{rx}	gain of receiving antenna in direction of scatterer
G_r	gain of receiving electronics
$h(t)$, $h(\omega)$	impulse response and transfer function
H_x	component of magnetic field vector in *x* direction

H_y	component of magnetic field vector in y direction
H_z	component of magnetic field vector in z direction
$H_{t,tx,rx}$	response of transmitting electronics and antennas over a reflector
$H_{t,tx,rx,r}$	response of transmitting electronics, antennas, and receiving electronics over a reflector
H_l	weighted system excitation
i	imaginary number
i (subscript)	enumeration index
J	number of waveform parameters
$\mathbf{J}$	the Jacobian matrix, contains the derivatives of the waveform parameters with respect to the model parameters
k	wave number
k_x	wave number in direction of propagation projected into x axis
k_y	wave number in direction of propagation projected into y axis
k_z	wave number in direction of propagation projected into z axis
$\mathbf{k}$	wave number in direction of propagation
l,m,n	indices of grid cell corners
p	iteration index
$p_{e,j}$	j^{th} waveform parameter from experimental data
$p_{s,j}$	j^{th} waveform parameter from simulated data
P_t	power incident on the transmitting antenna
P_{rx}	power received by receiving antenna
QD	quartile deviation
r	the residual, a measure of the distance between the predicted and actual waveform parameters
r	radial position (spherical coordinates)
$\mathbf{r}$	position vector $\mathbf{r} = \hat{\mathbf{x}}\,x + \hat{\mathbf{y}}\,y + \hat{\mathbf{z}}\,z$
$\mathbf{R_0}$	plane wave spectrum of waves produced by receiving antenna on reference plane due to a unit impulse at feed port
s_{ij}	scattering parameter relating incident wave i to scattered wave j
s_{ijDUT}	scattering parameter for *DUT* (device under test)
s_{21r}	transfer function of receiver electronics
$s_{21r,dB}$	transfer function of receiver electronics in decibels
$s_{21r,dB,fit}$	polynomial fit to transfer function of receiver electronics in decibels
$s_{+21PROBE}$	forward scattering parameter for positive scope probe
$s_{-21PROBE}$	forward scattering parameter for negative scope probe
$\tan \delta_e$	electric loss tangent
t	time
$\mathbf{T_0}$	plane wave spectrum of waves produced by transmitting antenna on reference plane due to a unit impulse at feed port
V_i^+	amplitude of the wave incident on port i

V_i^-	amplitude of the wave leaving port i
V_+	signal measured by the positive scope probe
V-	signal measured by the negative scope probe
$\mathbf{V}$	model space basis vectors from SVD
x	component of position in x direction
x_i	the ith model parameter (ε_r, σ, or d)
$x(t)$, $x(\omega)$	network signal, Fourier transform pairs
$x_{i,l,m,n}$	the ith model parameter (ε_r, σ, or d) at grid cell corner i,l,m
$\widetilde{x}$	median value
$\hat{\mathbf{x}}$	unit vector in x direction
$\mathbf{X}$	vector containing all model parameters
$\mathbf{X}_{pq}$	model parameters vector at p^{th} iteration of q^{th} initial model
$\mathbf{X}_\Sigma$	an acceptable solution to the inverse problem
$\overline{\mathbf{X}}$	mean value of set of acceptable solutions
$\mathbf{X}_{\Sigma q}$	an acceptable solution to the inverse problem found from the q^{th} initial model
y	component of position in y direction
y_i	the ith waveform parameter
$y(t)$, $y(\omega)$	network signal, Fourier transform pairs
Y	admittivity
$\hat{\mathbf{y}}$	unit vector in y direction
$\mathbf{Y}$	vector containing all waveform parameters
z	component of position in z direction
z_0	z position of reference plane
$\hat{\mathbf{z}}$	unit vector in z direction
Z	impedivity
Z_i	characteristic impedance of port
Z_0	characteristic impedance of port or wave-guide at antenna feed port
α	scale factor for simulated waveform parameters
α	distribution coefficient
α	attenuation constant
β	phase constant
γ	low pass filter or smoothing parameter
Γ	reflection coefficient
$\ddot{\mathbf{\Gamma}}$	dyadic reflection coefficient
ε	dielectric permittivity
ε_r	relative dielectric permittivity
$\varepsilon_{r,dc}$	relative zero frequency permittivity
$\varepsilon_{r,\infty}$	relative permittivity at infinite frequency
ε_1	relative dielectric permittivity in medium 1

ε_2	relative dielectric permittivity in medium 2
ε'	real component of dielectric permittivity
ε''	imaginary component of dielectric permittivity
ε_{dc}	zero frequency permittivity
ε_∞	permittivity at infinite frequency
$\mathbf{\Sigma}$	uncertainty vector, components uncertainties due to are various mechanisms
$\|\mathbf{\Sigma}\|/\|\mathbf{Y}\|$	normalized uncertainty
λ	pre-whitening or peak reduction parameter (Chapter 2)
λ	wavelength (Chapter 4)
θ	volumetric moisture content
$\varnothing$	azimuthal position (cylindrical coordinates)
$\hat{\boldsymbol{\rho}}$	unit vector in ρ direction
ρ	radial position (cylindrical coordinates)
$\boldsymbol{\sigma}_x$	standard deviation of set of acceptable solutions
σ_s	radar cross section of scatterer
σ	electrical conductivity at d.c. (zero frequency)
τ	time, dummy variable
τ	relaxation time
μ	magnetic permeability
μ_r	relative magnetic permeability
ω	radian frequency
∂_t	derivative with respect to t (time)
∂_t^2	second derivative with respect to t (time)
∇^2	laplacian operator
∇_z^2	laplacian operator with respect to z

LIST OF ACRONYMS AND ABREVIATIONS

AUT	antenna under test
BPF	band pass filter
cm	centimeters
CPU	central processing unit
dB	decibels
dBm	decibel with respect to one milliwatt
DC	direct current or zero frequency
DUT	device under test
FDTD	finite difference time-domain
FFT	fast Fourier transform
FIR	finite impulse response
GHz	gigahertz
GPR	ground penetrating radar
GPU	graphics processing unit
IMSP	inverse model for soil properties
kHz	kilohertz
m	meters
mm	millimeters
MHz	megahertz
mS/m	millisiemens per meter
mV	millivolts
ns	nanoseconds
ps	picoseconds
RDP	relative dielectric permittivity
RF	radio frequency
RMS	root mean squared
RTDGPR	real time digitizing ground penetrating radar
SMA	atype of miniature coaxial cable connector
SVD	singular value decomposition
TE	transverse electric
TDR	time-domain reflection
TDT	time-domain transmission
TM	transverse magnetic
USGS	United States Geological Survey
VNA	vector network analyzer

ACKNOWLEDGEMENTS

This work is the result of contributions and suggestions from many people. Without their help, this would not have been possible. I would like to express my sincere appreciation to the principle investigators who put this project together. They are Dr. David Wright, Dr. Michael Powers, and Dr. Gary Olhoeft. Through this project, they provided financial and logistic support for this thesis. I would also like to thank my advisor and thesis committee members: Dr. Gary Olhoeft, Dr. John Scales, Dr. Tom Boyd, Dr. Eileen Poeter, Dr. Frank Kowalski, and Dr. Michael Powers. They offered many suggestions and kept my best interests in mind even though they suffered through lengthy papers and meetings. The staff at the U.S. Geological Survey was an enormous help; notably Craig Moulton, Ray Hutton, Jeff Lucius, and Dave Kibler. They were always ready to lend a hand, and idea, or some moral support. They contributed greatly to this thesis. A number of students at Colorado School of Mines spent a lot of time building test apparatus and collecting field data. They are Bill Woodruff, Justin Rittgers, Trevor Irons, and Alison Meininger. These students rolled up their sleeves and tackled many difficult tasks with good spirits. Dr. Antonis Giannopoulos generously provided the source code to his *GPRMax* FDTD program, and offered detailed assistance through many email letters.

I would like to thank the following organizations for providing financial assistance. This research was supported through the USGS by the Office of Science (BER), U.S. Department of Energy, Project No. DE-AI07-05ER63513. I received an annual scholarship from the Society of Exploration Geophysicists. The Geophysics department provided assistance for travel to scientific meetings.

Finally, I would like to thank my family, Amy, Ian, and Leah. Amy took on the many responsibilities I shirked while pursuing the degree even while carrying and caring for two new children. I am forever indebted – as I was before going back to school.

CHAPTER 1

INTRODUCTION

1.1 Introduction

Ground penetrating radar (GPR) is a mature technology that has found use in many different industries (Daniels, 1996; Olhoeft, 1996). GPR is used in geotechnical and environmental work, hydrogeology, structural assessment of infrastructure, archeology, forensics, mining and geology, utility location, and agriculture. GPR provides higher resolution images than other standard geophysical techniques. The biggest drawback to GPR surveys is that the depth of investigation is often limited. Conductive or dispersive ground is often the biggest reason for limited penetration of the radar waves (scattering and clutter are other common causes). The goals of this work are to improve GPR imaging in dispersive ground and to provide better estimates of material properties of the subsurface reflectors. This is facilitated by calibrating the GPR system, and estimating the subsurface waveforms generated in GPR surveys.

This thesis contains four main chapters and a summary, and Figure 1.1 contains an overview of the topics covered. Chapter 2 documents a collection of tools and experiments for modeling, characterizing, and calibrating the response of an impulse GPR. The procedures have been applied to an actual GPR system that has been designed for conductive ground. The procedures include building a catalog of numerical simulations for the antenna response, and a means to verify the accuracy of these simulations through physical experiment. Using the results of this characterization, clearer images of the subsurface can be made using the procedures outlined in Chapters 3 and 4.

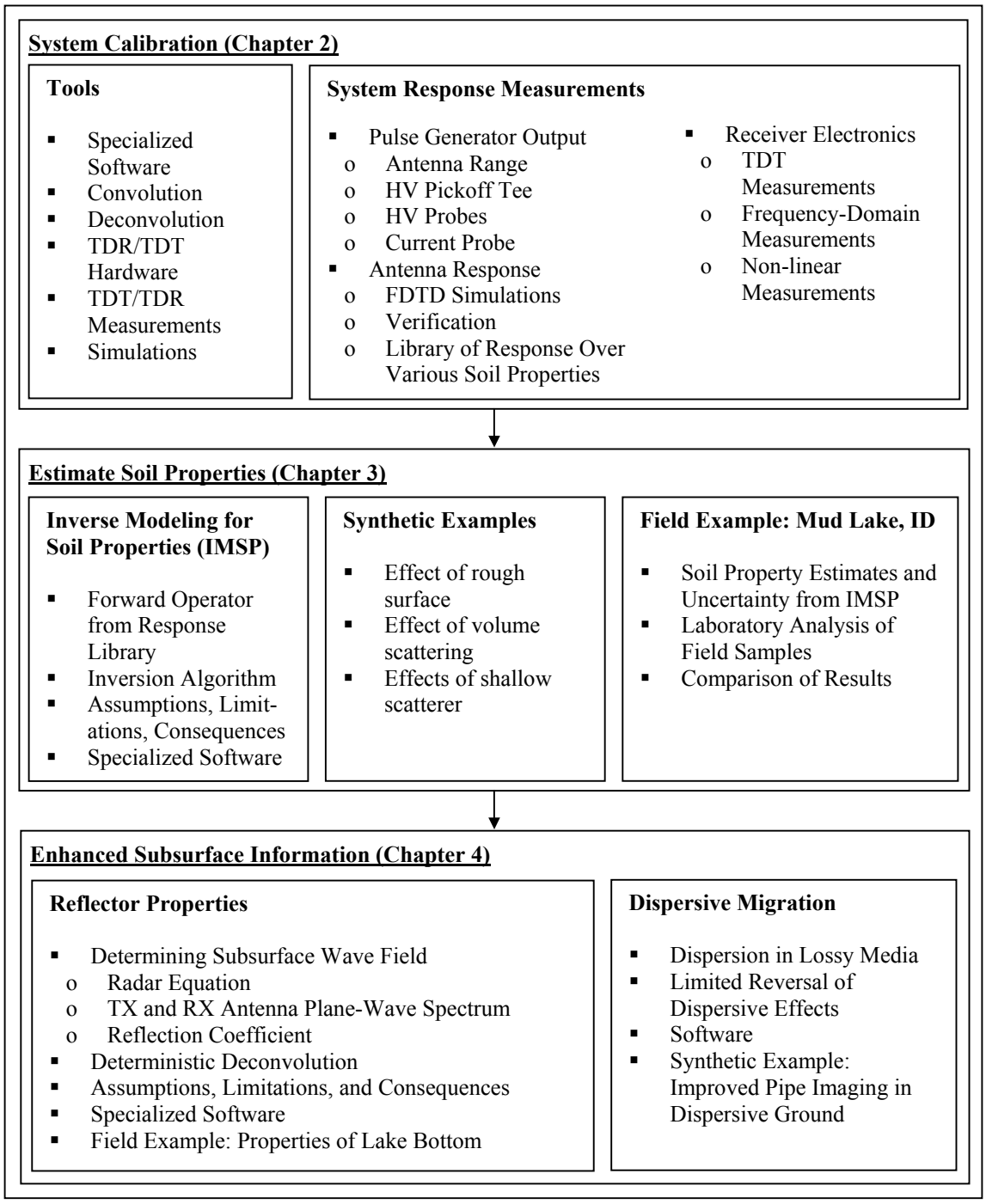

Figure 1.1. Overview of topics covered in this dissertation. Tasks on the top must be completed before tasks below can begin. Arrows indicate workflow. See Appendix B for more information about specialized software.

Chapter 3 describes a procedure to estimate the ground properties directly beneath the antennas from the early arrivals at the receiving antenna. These properties must be known in order to predict the waveforms transmitted into the subsurface because the response of the antennas changes depending on the properties of the ground directly beneath the antennas. The early portions of simulated received waveforms for the bi-static antenna array show considerable change due to changing ground properties, but this change is not a function of a simple waveform attribute such as arrival time or amplitude. A non-linear inversion method based on the early arrivals is developed to estimate material properties near the antennas.

Once the antenna response is known through modeling, and the properties of the ground directly beneath the antenna have been estimated, the next goal is to estimate the wave fields transmitted into the subsurface. This is discussed in Chapter 4. Existing methods for calculating these fields exist, but they are time consuming. A faster method of calculating these fields is needed so that information about the subsurface can be obtained when the survey is conducted. Using estimates of the subsurface waveforms, the material properties at selected locations in a survey site can be estimated using deconvolution. Once the frequency dependent subsurface material properties have been estimated, then the section can be migrated in a manner that increases image resolution by reversing the effects of dispersive wave propagation due to lossy ground.

This dissertation does not provide a theoretical overview of GPR operation. Many good references exist on this topic (Annan, 1973; Daniels, 1996; Olhoeft, 1996; Balanis, 1997; Annan, 2001). Rather, this dissertation is focused on the challenges of conducting GPR surveys in lossy ground. Knowledge of the subsurface waveforms is key to producing better images and better subsurface information in dispersive environments. There has been much research into predicting subsurface GPR wave fields, and some specific research is described in the chapters that follow. Some researchers do not consider a realistic GPR antenna with a back shield (i.e. Radzevicius, 2001; Arcone, 1995; Engheta and Papas, 1982). Others do not account for the changing

antenna response due to changing soil properties beneath the antennas (Lambot et al., 2004a; Lambot et al., 2004b;Klysz, 2004; Valle, 2001; Roberts and Daniels, 1997). This dissertation addresses both of these problems.

1.2 GPR Hardware

There are two basic types of commercially available GPR systems, those operating in the frequency-domain and those operating in the time-domain. Time-domain systems use the 'pulse-echo' method of locating objects. They emit a brief impulse and then passively wait for reflected energy to arrive at the antenna array. Frequency-domain systems emit and receive a continuous sinusoidal signal. During the survey, the frequency is varied (continuously or through a series of discrete frequencies) until a wide band is covered (usually two or more decades in frequency). The frequency-domain data are then transformed into the time-domain so the data can be interpreted in the same manner as the 'pulse-echo' systems. Time-domain systems are less expensive than frequency-domain systems to manufacture, but are more susceptible to noise – especially in urban environments. Frequency-domain systems (Langman, 2002) are able to filter out much of the noise that is outside the current operating frequency. But they require more expensive high resolution signal processing because the source signal is emitted continuously and the reflected signals must be resolvable in the presence of this large source. Further, the generation of a variable frequency source requires hardware that is more expensive. For these reasons, most commercial GPR systems are time-domain impulse radars. As cultural noise becomes more problematic, frequency-domain systems may be necessary, but currently they are not commercially viable in the competitive GPR market. Note that when radio frequency (RF) interference becomes large enough, the sources of interference can be used as the signal for GPR surveys (Wu et al., 2002). Since the vast majority of existing GPR systems are time-domain systems, this dissertation will only be concerned with time-domain systems.

Time-domain GPR systems commonly use equivalent time sampling to digitize the received signals. Equivalent time sampling is necessary due to the relatively high frequency content of received radar signals compared with the speed of available digitizing equipment. Equivalent time sampling is accomplished by repeatedly firing the radar system in rapid succession, receiving a waveform after each firing, and digitizing a single (or a few) sample(s) from each received waveform. The position of the sampled point in time increments with subsequent waveforms until a sample has been digitized for each sample point on the waveform. When using equivalent time sampling, it is assumed that firing the GPR many times in rapid succession results in very little difference between successive waveforms. Recently however, the availability of faster digitizers has made real time digitizing possible for some lower frequency systems such as the RTDGPR (discussed below). With real time digitizing, the radar fires once, and the entire waveform is digitized. Real time digitizing may allow faster surveys and/or the collection of more spatially dense data because the radar only needs to fire once per recorded waveform. Real time digitizing can also result in increased dynamic range by stacking digitized waveforms.

There are two basic types of GPR antennas – ground-coupled and air-launched. Ground-coupled antennas are placed close to or directly on the ground, while air-launched antennas are raised above the ground. The ground-coupled antennas generally transmit more energy into the ground than the air-launched antennas, therefore ground-coupled antennas are often used when conductive or lossy ground conditions exist to maximize the depth of penetration. Ground-coupled antennas induce electromagnetic fields in the subsurface that evolve into propagating waves. Conversely, air-launched antennas send waves towards the ground, and much of the energy in these waves is reflected at the air-ground interface. One difficulty with ground-coupled antennas is that the shape of the waveform transmitted into the ground depends on the material properties near the antenna. This usually results in changing transmitted waveforms as the survey is conducted due to changing ground properties near the antennas. This is not a problem

with air-launched antennas because the material close to the antenna (air) does not change. Since ground-coupled antennas are preferred in lossy environments, and since the transmitted waveforms change during the survey, a large part of this dissertation is concerned with determining the shape of the transmitted waveforms from ground-coupled antennas throughout the course of the survey.

A portion of this dissertation is involved with the calibration of a GPR system so that the amplitude and spectral character of the subsurface reflections can be utilized in signal processing. Currently, most commercial manufacturers do not offer calibrated instruments, since this is an additional cost that most users view as unnecessary. One of the goals of this dissertation is to demonstrate the value of calibrated radar systems through their ability to provide higher quality subsurface images.

The methodology developed in this dissertation is applicable to nearly any impulse GPR. The actual GPR that was used in this work is a real time digitizing GPR (RTDGPR) tailored for use in conductive ground, which was built by the USGS and the Colorado School of Mines (see Figure 1.2; Wright et al., 2005). The RTDGPR has a large dynamic range achieved through a real time digitizer (as opposed to equivalent time sampling) and a high output transmitter. The center frequency of the transmitted signals is about 50 MHz. This frequency was selected as a mutual compromise between increased penetration depth with lower frequencies, excitation of propagating waves, and size limitations of the antennas. Because the RTDGPR was a necessary vehicle for the work contained in this dissertation, a large engineering effort went into building, modifying, and debugging the prototype. These details are not included in this dissertation.

Figure 1.2. The USGS RTDGPR system designed for operation over conductive ground. Photograph courtesy of the USGS.

A simplified block diagram of the RTDGPR is shown in Figure 1.3. The components in the bottom row are in the instrument rack on the tractor. The remaining components are located in the transmitter and receiver modules, which are located inside their respective antennas. When possible, optical cables are used in lieu of metallic cable between the tractor and the antenna cart so that reflections or interference from currents induced on metal cables near the antennas is avoided. To acquire a radar trace, the system sends a synchronization signal to the pulse generator and to the analog to digital converter. The pulse generator then sends a signal that is transmitted into the subsurface. Reflected signals from the subsurface that arrive at the receiving antenna are routed through the receiving electronics. The programmable attenuator in the receiver module can be used to reduce the signal amplitude to levels within the linear range of the logarithmic amplifier. For low amplitude signals, the logarithmic amplifier has about 40 dB of gain, and the gain is gradually reduced to a limiting value of 0 dB for large signals.

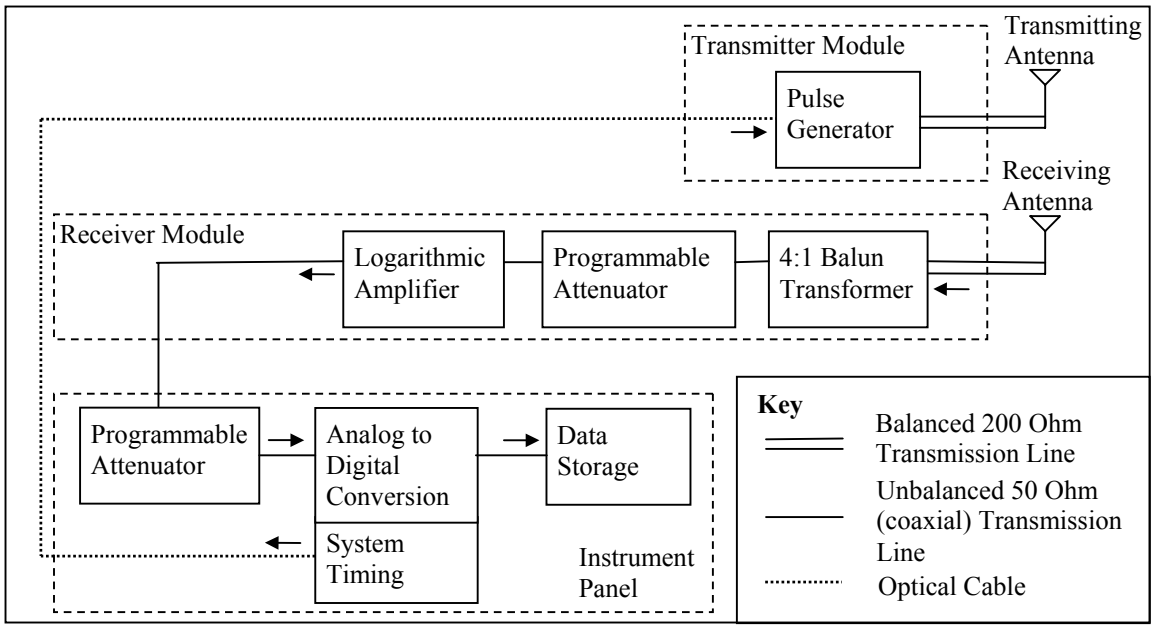

Figure 1.3. Simplified block diagram of the RTDGPR. Arrows indicate direction of signal propagation.

The role of the logarithmic amplifier is to increase the dynamic range of the recording system. The instrument panel attenuator may further reduce the signal so that is in the digitizer's range, but the gain of this attenuator is nearly always set to 0 dB for normal operation. The RTDGPR employs a real time digitizer with stacking capability for noise reduction and increased dynamic range. The real time digitizer records eight bit samples at a rate of 2 GHz. Up to 4096 stacks can be used to increase the digitizer dynamic range by a factor of 64. Consult Wright et al. (2005) for more details on the RTDGPR.

The block diagrams for most impulse GPR systems are similar to Figure 1.3. In other systems, optical links may replace transmission lines and visa versa. Linear amplifiers may replace logarithmic amplifiers, and attenuators may be absent. Finally, the location of various components may differ. The impedance of the transmission lines may change from system to system. Even with this variability, the methods presented in this dissertation are applicable to most impulse GPR systems.

1.3 Electromagnetic Wave Propagation

Geophysical methods based on wave phenomenon (such as GPR, remote sensing, and seismic surveys) generally provide more realistic images and have better resolution than other methods such as those based on diffusion or potential fields. One reason for this is that the distance to reflectors can be easily measured using the two-way travel time of the waves. Another reason is that wavelets propagating through a lossless non-dispersive medium are stationary, and the spatial resolution in the direction of wave propagation does not decrease with distance from the reflector. This contrasts with all potential fields methods (such as gravity, magnetic, and DC resistivity surveys) and many diffusion based measurements (such as small induction number electromagnetic conductivity surveys). With these methods, it can be more difficult to determine the range to the anomalous body, and the spatial image resolution decreases with distance to the anomalous body. Wave based methods are not without limitations however. The spatial resolution of wave based methods is limited, and the size of detectable anomalies is a function of the wavelength of the investigating waves. The resolution of the GPR method is generally higher than that of the seismic method because the waves used in GPR surveys have shorter wavelengths than those used in seismic surveys.

When a GPR is operated in a conductive or lossy environment, the preceding comments are less accurate. In general, the fields close to the antennas are better described by diffusive energy transport rather than wave propagation. Thus, the spatial resolution of images produced very near the antennas is less than that of the images further away. For the case of conductive or dispersive ground, fully propagating fields never develop at any distance from the antennas because the energy transport is a combination of diffusion and propagation. In this case, the entire survey space is filled with either energy being transported diffusively or with waves that have a diffusive component. Even so, the standard propagating wave analysis techniques can be used for dispersive ground if modified appropriately (see Chapter 4). The point is that high

resolution GPR imaging in lossy ground poses unique challenges that require better techniques than the current state of the art due to the presence of diffusive energy transport. Therefore, one of the goals of this dissertation is to present means for improved imaging and signal processing in conductive or lossy ground conditions. The primary tool for these improvements is a means to estimate the shape of the subsurface waveforms.

The propagation of waves in a homogenous medium can be described with knowledge of the electrical properties of the medium. The propagation and attenuation versus distance of a monochromatic wave (or a spectral component of a wave field) is specified in a given medium by the wave number k

$$k = \sqrt{-YZ} = \beta - i\alpha\,, \tag{1.1}$$

where Y is the admittivity and Z is the impedivity of the medium, β is the phase constant, α is the attenuation constant, and i is the square root of negative one (Ward and Hohmann, 1987). Fourier decomposition can be used to express any wave field in terms of its spectral components. The admittivity and impedivity are in turn properties of the electrical properties of the material according to

$$Y = \sigma + i\omega\varepsilon \tag{1.2}$$

$$Z = i\omega\mu \tag{1.3}$$

where σ is conductivity, ε is dielectric permittivity, μ is magnetic permeability, and ω is radian frequency. The dielectric permittivity and the magnetic permeability are functions of frequency and are in general complex numbers. Throughout this dissertation however, the magnetic permeability is assumed to be that of free space, and all materials are assumed to be linear and isotropic. The propagation constant is composed of a real and an imaginary part. The real part describes the change in phase of the wave versus distance, and the imaginary part describes the attenuation versus distance. The ratio of the imaginary and real parts is called the loss tangent, and is proportional to the ratio of the energy lost per cycle (dissipation only) to the amount of energy stored (or

propagated). With the permeability being that of free space, the electric loss tangent is given by

$$\tan \delta_e = \frac{\sigma + \omega \varepsilon''}{\omega \varepsilon'} \tag{1.4}$$

where tan δ_e is the electric loss tangent, ε' and ε'' are the real and imaginary dielectric permittivity respectively. An analogous magnetic loss tangent can be written, however in this dissertation it is assumed that no magnetic losses occur. Olhoeft (1984) estimated the depth of penetration (in meters) for most commercial GPR systems to be about 0.5 divided by the loss tangent. Equipment improvements in the last 20 years push this depth to about 0.75 divided by the loss tangent. Generally, conductivity values greater than about 30 mS/m cause too much loss for effective GPR surveys.

When waves travel through a medium, the amplitude of the wave is attenuated by dissipative losses and scattering losses. Generally, dissipative loss and scattering are functions of wave polarization for anisotropic media. In this dissertation however, the attenuation properties of all media are assumed isotropic and independent of polarization. Dissipative losses occur in mediums with non-zero conductivities and with dielectric losses. In addition to zero frequency conductivity, several dominant processes contribute to the lossy dielectric effects observed in low frequency (10 to 500 MHz) GPR surveys (there are other loss mechanisms which produce smaller effects). They are bound water polarization, the Maxwell-Wagner effect, colloidal polarization, and double layer polarization (Ishida et al., 2000). These dielectric loss mechanisms can be modeled using a simple relaxation model. This model describes the frequency dependent changes in dielectric properties using relaxation oscillators where charge is displaced. Relaxation oscillators have a characteristic recovery time, which affects the frequency response. A good discussion of these phenomena is given by Olhoeft (1985), Wtorek (2003), and Sihvola (1999).

Scattering losses occur at all frequencies due to scatterers of all sizes, and are frequency dependent. Rayleigh scattering occurs when the scatterers are smaller than

about a tenth of a wavelength, Mie scattering occurs for larger scatterers, and optical scattering occurs when the scatterer is larger than a few wavelengths. Ulaby et al. (1982), Balanis (1989), and Mishchenko et al. (2002) discuss the scattering of electromagnetic waves in detail. Although multiple scatterers located within the same Fresnel zone may cause amplitude loss, they cannot be independently resolved by far-field observations due to the diffraction limit. Under some circumstances, it may be possible to resolve small heterogeneities beyond the diffraction limit in the near-field region if short wavelength evanescent waves can be measured (Kelso et al., 2001; Durig et al., 1986). Scatterers too small to be imaged may cause loss, and the composite lossy effect of the small scatterers can be accounted for in the frequency dependent material properties. However, the effects of scattering are often treated separately so that the material properties reflect only conductivity and dielectric relaxation effects. The frequency dependence of scattering losses varies widely, but often follows a power law (ω^n where n varies from -1 to 4, see Balanis, 1989).

1.4 Electrical Properties of Soil

The material properties of the soils and rocks encountered in GPR surveys can vary over a wide range. In some cases, this range can be reduced by only considering a limited frequency band. GPR surveys over lossy ground are generally made at frequencies between 10 MHz and 500 MHz to achieve reasonable penetration. This frequency band will be referred to as the low frequency GPR band, and the discussion below applies to this frequency band. Water wet or dry course grained sediments will rarely have a relative dielectric permittivity (RDP) significantly greater than 25 because interfacial polarization effects are minimal due to the relatively small surface area (Kaya and Fang, 1997). For example, the RDP of dry sand is about four, and water saturated sand is about 25 (Duke, 1990). With sand and water mixtures, any dissipative loss is

mostly due to the conductivity of the water. Soils with fined grained sediments often exhibit losses due to dielectric relaxation because interfacial polarization effects are often large. Hence, the permittivity of fined grained sediments can vary widely. Ishida et al. (2000) discuss the observed relaxation phenomenon for moist clay-water systems. The dielectric spectroscopy of clay-water systems is quite complex, but some generalizations can be made. The relaxation frequencies and distributions are a strong function of the cations in solution, the amount of water in the system, which clay minerals are present, soil density, and soil texture. Laboratory measurements of the (real) RDP of wet clay minerals as high as 200 at 10 MHz were reported by Olhoeft (1987), and as high as 40 at 50 MHz were reported by Rowe et al. (2001). The expected permittivity values for actual soils and rock is somewhat lower, because most soils contain significant amounts silt and/or sand.

Despite the complexity of the dielectric spectroscopy of clay minerals and soils, the results of many laboratory tests to determine electrical properties of these materials are found in the literature. Robinson (2004) reports that the RDP values of dry kaolinite, illite, and montmorillonite are generally less than 18 when tested using broad band (0.001 to 1.75 GHz) time-domain reflectometery. Fam and Dusseault (1998) report that the RDP of wet Queenston Shale, Mancos Shale, and Pierre Shale samples did not exceed 14 in the low frequency GPR band. Rowe at al. (2001) examine the changes in permittivity in the Halton Till (soil with about 23% illite) after permeating the samples with different $CaCl_2$ solutions. They found significant change in the permittivity values using different permeating solutions. The values were generally less than 25 over the frequency range of 100 MHz to 700 MHz, but increased significantly to about 40 near 50 MHz. They concluded that dielectric spectroscopy is a good tool for monitoring contaminated fluids. Olhoeft (1987) presents laboratory results showing the frequency dependent RDP of various sand-clay-water mixtures. The RDP is less than 25 over the low frequency GPR band for all mixtures where the clay concentration is less than five percent clay. For

higher clay concentrations, higher permittivity values are observed, however the conductivity values also increase to a level too high to warrant GPR surveys.

According to Olhoeft (1985), conductivity values of rock and soil can vary by 24 orders of magnitude. Zero frequency conductivity values are mostly controlled by the fluid present in the rock or soil (Wtorek, 2003; Sihvola, 1999). The presence of saline water or ground water contaminants is a common scenario where the conductivity of the ground is usually too high for GPR surveys (> 30 mS/m). Clay minerals generally increase the conductivity of soils, especially when combined with water. In addition to the mineralogy and fluid content of rocks and soils, the structure of the constituents plays a large role. For instance, the large surface area of clay minerals provides a large number of conductive paths and hence higher conductivities. Electrochemical interaction between different soil constituents often occurs, which usually enhances conductivity. Many electrochemical effects cause frequency dependent electrical properties (Olhoeft, 1985), but these are not usually important at radar frequencies. Non-linear electrical properties of rocks are generally due to electrochemical effects, but non-linear effects are not generally seen at frequencies above 10 MHz. Non-linear electrical properties are therefore ignored in this work. Note also that the effects of real permittivity and the imaginary conductivity are equivalent, as are the effects of imaginary permittivity and real conductivity. The convention used here is that conductivity is a real quantity measured at DC (zero frequency), and frequency dependent properties are reflected in the real and imaginary permittivity components. Various mixing laws have been proposed to predict bulk electrical properties of soils and rocks from the properties of their constituents. Sihvola (1999), Wtorek (2003), and Olhoeft (1985) provide a useful overview of these mixing laws.

When the magnetic properties of the ground are other than that of free space, wave velocity is affected, but attenuation may be the largest effect. Usually, magnetic materials exhibit relaxation effects that are analogous to dielectric relaxation, although the magnetic phenomenon is generally more nonlinear than dielectric polarization.

Properties of lossy magnetic soil are presented in Olhoeft and Capron (1994). A knowledge of the mineralogy of a given type of soil or rock can aid in identifying magnetic soil. Rocks and soils that do not contain ferrous minerals are generally non-magnetic. Moreover, most ferrous minerals are only weakly magnetic (e.g. diamagnetic or paramagnetic; van Dam et al., 2004). Strongly magnetic (ferromagnetic) ferrous minerals include magnetite and maghemite, and pyrhotite to a lesser extent. In some instances, iron oxides and ferrous clay minerals can be magnetic. According to van Dam et al. (2004), ferrous minerals in arid climates are generally more magnetic than in wet climates. Volcanic rocks are often magnetic. Because most GPR systems are based on electric field antennas, they are unable to distinguish between magnetic and dielectric effects. Therefore, if magnetic soil is suspected, additional tests should be conducted to determine or estimate magnetic properties. Dragging a magnet through the soil is a crude method to identify magnetic soil. Ideally however, laboratory and field measurements of soils and/or samples can be conducted to determine magnetic properties. It is important to note that many instruments measure the magnetic susceptibility at different frequencies (often below 10 kHz), and a particular measurement may not reflect the magnetic properties at GPR frequencies.

1.5 Data Processing Software

Two data processing programs were written for this dissertation. *GPR Workbench* is a general purpose GPR field data processing package. It provides the standard gridding, filtering, and imaging capabilities of a commercial GPR processing package. Further, it has a forward modeler (Powers, 1995), and a dispersive migration algorithm. It can produce section views or plan views. *GPR Wave Utilities* provides the data processing algorithms discussed in this dissertation. This program primarily operates on single traces of data rather than complete data sets. *GPR Wave Utilities*

includes routines for convolution, deconvolution, Hilbert transforms, prediction of soil properties beneath antennas through the IMSP algorithm (see Chapter 3), and forward propagating GPR wave fields (see Chapter 4).

These programs and their source code are included with this dissertation to provide tools for calibrating GPR equipment, and as vehicle for testing new data processing algorithms for GPR data. They were written using Microsoft Visual C++ 6.0 for the Windows operating system. Testing new algorithms is difficult when using commercial packages. Some Matlab (The MathWorks, Inc., Natick, MA) programs for processing GPR data are publicly available, but they do not provide the processing speed and features needed for processing a large amount of data. More details can be found in Appendices B and C, and on the DVD-ROM accompanying this dissertation.

Numerical simulations of antenna response were made using two programs. Both are based on the finite-difference time-domain (FDTD) method (Yee, 1966). The first program, *GPRMax*, is available in the Internet (GPRMax, 2004). A version of this program can be found on the DVD-ROM accompanying this dissertation (see Appendix C). The second, *XFDTD*, is commercially available (Remcom, Inc., State College, PA).

CHAPTER 2

CHARACTERIZING THE RESPONSE OF A GPR

2.1 Background and Previous Work

This chapter describes the methodology that has been used to determine the response of an impulse GPR. The characterization includes a response function for the receiving electronics, simulations of the antenna response, and measurement of the signal produced by the transmitter electronics (i.e. the pulse generator). Several different tools are needed to determine the system response. The response of the receiver electronics and the input signal to the transmitting antenna are measured using various laboratory techniques such as time-domain reflectometry (TDR). Finite-difference time-domain (FDTD) simulations are used to investigate the antenna response. Some of the methods outlined here produced good results for the RTDGPR, and some did not. The methods that did not produce good results are included in this dissertation because they have strong potential to produce good results for other radar systems. As a whole, the collection of methods outlined in this chapter has sufficient functionality and flexibility to be able to determine the response for essentially any impulse GPR. This Chapter describes the results of these methods when applied to the USGS RTDGPR. The raw and processed data are available on the accompanying DVD-ROM. Each data directory on the DVD-ROM contains a processing history file that lists each operation made to data in the directory (see Appendix C).

Calibrating the response of a GPR system is essential for making measurements of subsurface material properties. Duke (1990) calibrated the overall response of a GPR system by making measurements of the system response in air. This dissertation adds to Duke's work by characterizing individual components of the system and modeling the

antenna response. This is crucial for several reasons. First, the response of each component can be properly determined, and weak links in the system can be isolated and evaluated. Second, the response of ground-coupled antennas depends on the material around them. Measurements of antenna response in air are not an accurate representation of the antenna response over ground. Finally, since it is impractical to conduct physical experiments encompassing the wide variety of situations encountered in actual surveys, numerical simulations of antenna response are required to predict antenna response when experimental data are not available. Lambot et al. (2004) calibrated a frequency-domain GPR system with air coupled antennas, and accounted for changing soil properties in the antenna response. To date however, no full calibration accounting for changing ground properties has been realized for an impulse GPR using ground-coupled antennas. This dissertation involves the characterization and modeling of the response of a field worthy GPR (i.e. not a laboratory system) to a level that has not yet been published. A fully calibrated system has many benefits such as facilitating a method to estimating soil properties (see Chapter 3), and a method to sharpen images of the subsurface (see Chapter 4). A calibrated system is needed in order to estimate subsurface wave fields and their spectra, which can then be used to improve subsurface imaging (see Chapter 4). For example, some of the seismic data processing methods outlined in Yilmaz (1987) require estimates of the source spectrum, and can be applied to GPR data.

A computer program called *GPR Wave Utilities* has been written to perform the numerical operations discussed in the following sections. This program, together with the methods presented in this Chapter, provide the tools for calibrating essentially any time-domain GPR. Appendix B contains an overview of the features of this program. The source code and MS Windows executable can be found on the DVD-ROM accompanying this dissertation.

2.2 Signal Processing Tools

There are many techniques for making high frequency electrical measurements in electrical networks and antenna systems, and there are also many methods for manipulating the data from these measurements. This Chapter does not provide a comprehensive review. Rather, the following Sections describe the numerical procedures and experimental methods used to characterize the RTDGPR system, which can be applied to other impulse GPR systems.

Unless otherwise noted, the methodology presented in this Chapter requires that the radar equipment, the antennas, and the earth materials around the antennas behave as linear systems. The response of a linear system can be described by linear differential equations with constant coefficients multiplying each term of the equation (McGillem and Cooper, 1984). Examples of linear systems include wave propagation through homogeneous media and transmission lines; passive electronic circuits composed of resistors, capacitors, and inductors; and some active electronic circuits where the response can be described by a linear equation. If a system is made up of linear components, then the response of the entire system is also linear. The properties of linear materials do not change as a function of applied (electric or magnetic) field strength. The magnetic properties of most magnetic materials change as a function of applied field strength and these materials are therefore nonlinear. They can be approximated as linear materials if the field strength varies over a small range. Most systems are only approximately linear over a given range in field strength (usually specified), and become nonlinear when this range is exceeded. An important feature of linear systems is that the superposition principle applies. For instance, if the response of an antenna is known for incident fields A and B, then the antenna response due to the simultaneous incidence of fields A and B is the sum of the individual responses.

2.2.1 Convolution and Deconvolution Methods

Convolution is a mathematical operation that can be used to describe how a linear network element modifies a signal as the signal passes through it in the time-domain. McGillem and Cooper (1984) define the convolution of a transient time-domain signal $x(t)$ with the response of a network element $h(t)$ as

$$y(t) = x(t) * h(t) = \int_{-\infty}^{\infty} x(\tau)h(t-\tau)d\tau\,, \tag{2.1}$$

where $y(t)$ is the output of the network element, t is time, τ is a variable of integration, and $*$ is the convolution operator. Each of these time-domain signals $x(t)$, $h(t)$, and $y(t)$ has a frequency-domain representation $x(\omega)$, $h(\omega)$, and $y(\omega)$. The following Fourier transform pair can be used to change from a representation in one domain to the other,

$$x(\omega) = \int_{-\infty}^{\infty} x(t)e^{-i\omega t}dt\,, \tag{2.2}$$

$$x(t) = \frac{1}{2\pi}\int_{-\infty}^{\infty} x(\omega)e^{i\omega t}d\omega\,, \tag{2.3}$$

where ω is the radian (temporal) frequency, and i is the square root of -1. These transforms require bounded integrable functions with a finite number of discontinuities. With these transforms, the time-domain convolution operator becomes a multiplication in the frequency-domain,

$$y(\omega) = x(\omega)h(\omega)\,. \tag{2.4}$$

If the impulse response $h(t)$ or transfer function $h(\omega)$ of a two-port network element is known, the convolution operation can be used to determine the signal at the output port of the network element for a given signal on the input port of the network element.

Deconvolution is a process whereby the input signal $x(t)$ is found from knowledge of the output signal and the transfer function of a two port network. Alternatively, deconvolution can be used to determine the transfer function of a two port network from

the input signal and the output signal. One might simply try to perform time-domain deconvolution by dividing the two corresponding frequency-domain signals,

$$h(\omega) = \frac{y(\omega)}{x(\omega)}. \tag{2.5}$$

Unfortunately, there are many problems associated with this approach. If the input signal $x(\omega)$ has no energy at certain frequencies, then Equation 2.5 will be undefined at these frequencies due to division by zero. The fact that real signals and the measurements of these signals have noise further complicates the problem. If $x(\omega)$ is small at certain frequencies and has noise at these frequencies, then the quotient (Equation 2.5) will vary wildly depending on the noise. These problems can be minimized by using an adaptive filter in the deconvolution process. In this dissertation, frequency-domain deconvolution is used. Time-domain deconvolution is also possible, but it is computationally more demanding and has many of the same problems as frequency-domain deconvolution (Riad, 1986).

Dhaene et al. (1994) describe an adaptive filter to reduce many of the problems associated with frequency-domain deconvolution. The realization of their filter used in this work is given by

$$F(\omega, \gamma, \lambda) = \frac{|\, x(\omega)\,|^2}{|\, x(\omega)\,|^2 + \gamma\omega^2 + \lambda}, \tag{2.6}$$

where λ is a pre-whitening or peak reduction parameter, and γ is a low pass filter or smoothing parameter. In the resulting deconvolution,

$$h(\omega) = F(\omega, \gamma, \lambda)\frac{y(\omega)}{x(\omega)}, \tag{2.7}$$

the peak reduction parameter reduces the effect of noise at frequencies where $x(\omega)$ is small, and the smoothing parameter reduces the effect at high frequencies where most of the power in $x(\omega)$ is noise. In this work, the parameters λ and γ are selected to maximize the power in the resulting deconvolution at frequencies below 200 MHz, and minimize the power above 400 MHz. The assumption is that the most power in $x(\omega)$ and $y(\omega)$ is

distributed over the lower frequencies, and that the power at higher frequencies is mostly noise. This assumption is based on the fact that the RTDGPR produces a negligible amount of energy above 250 MHz. Noise at high frequencies can be due to radio frequency interference and system noise (thermal noise, shot noise, etc.).

In practice, the fast Fourier transform (FFT) is used to convert discrete sampled time-domain signals to discrete sampled frequency-domain signals and visa-versa because of the computational efficiency of the FFT (Stanley et al., 1984). The conventional butterfly FFT requires that the sampled data contain 2^n samples; and samples are usually added to the data to obtain the proper number of samples (a.k.a. padding). In some cases, the additional samples can nearly double the total number of samples. A more efficient alternative is the prime factor FFT, which usually requires the addition of only a few samples to achieve the proper length (Cohen and Stockwell, 2003). The prime factor FFT is used in *GPR Wave Utilities* and all processing described in this dissertation.

There are some additional problems that arise when convolving and deconvolving signals represented by discrete sampled time series. Since the FFT produces a discrete frequency spectrum, if the spectral content of the time-domain signal does not correspond exactly to one of the discrete frequency-domain frequencies, then the spectral content will be distributed across a wide range of discrete frequencies (i.e. spectral leakage). Also, when using the FFT the signal is assumed to be periodic at the fundamental frequency (i.e. the frequency with a period equal to the length of the sampled time series). This means that the first and last samples are effectively adjacent as the fundamental period is repeated. For some signals such as the step-like signal at the transmitting antenna feed port, the last sample will be at a much higher level than the first sample (e.g. see Figure 2.1). When the FFT is used, the signal is interpreted as having a negative step at the end of the sampled signal. The resulting discrete frequency-domain representation will be contaminated with the broad band power in the negative going step. One solution to this problem is to differentiate the waveform, but this approach enhances noise. The

solution used in this dissertation is to use a Nicolson ramp (Nicolson, 1973). A linearly decaying ramp is subtracted from the signal so that the first and last samples have the same amplitude. Although subtracting the ramp changes the original signal, the spectral content of the new signals differs from the original signal only at frequencies other than those used in the discrete spectral representation. Subtracting the ramp also alters the DC (i.e. zero frequency) amplitude. The result is that the spectral content associated with the step at the end of the sampled signal is removed, but the original spectral content in the signal is preserved (at the discrete FFT frequencies). This is illustrated in Figure 2.1. Note the effect of the discontinuity at the end of the time sequence in the frequency-domain. The convolution and deconvolution operations described here can be performed with *GPR Wave Utilities*.

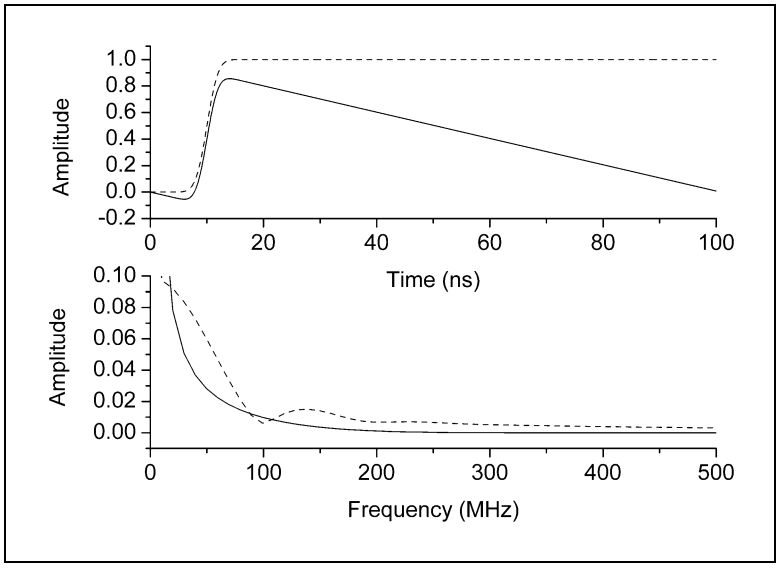

Figure 2.1. The top panel contains an integrated Gaussian step like time-domain waveform (dashed), and the same waveform with a ramp subtracted (solid). The bottom panel shows the frequency-domain representation of the waveforms as calculated using the FFT. Both graphs represent discrete data.

2.2.2 Scattering Parameters

Scattering parameters (S parameters) are often used to discuss the scattering of guided waves traveling in electrical networks (Smith, 1995). S parameters are also used to describe volumetric scattering of waves from inhomogeneities (Mishchenko et al., 2002) and antennas (Kerns, 1981). A two port network is shown in Figure 2.2. Each side of the network represents a port. The parameter a_i represents the normalized amplitude of a monochromatic wave incident on port i, and b_i represents the normalized amplitude of a monochromatic wave leaving port i due to transmission or reflection. The waves are assumed to exist in all time. Each port of a network couples a wave of a specific mode onto a wave guide, a transmission line, or into space. The incident, transmitted, and reflected waveforms are normalized according to

$$a_i = \frac{V_i^+}{\sqrt{Z_i}} \qquad \text{and} \qquad b_i = \frac{V_i^-}{\sqrt{Z_i}}, \tag{2.8}$$

where V_i^+ is the amplitude of the wave incident on port i, and V_i^- is the amplitude of the wave leaving port i, and Z_i is the characteristic impedance of the transmission line or wave guide connected to port i. For waves in space, Z_i is the intrinsic wave impedance of the wave incident on or leaving port i. All voltages in this dissertation are peak voltages unless otherwise specified. The characteristic impedance of a port is usually the ratio of the wave amplitudes of the electric and magnetic fields propagating into or out of the ports, although other definitions are sometimes used. The characteristic impedance of network ports, wave-guides, and transmission lines is determined by design and by natural physical laws for guided waves. The details are beyond the scope of this dissertation; consult Kerns (1981) for a more detailed discussion. Using the normalization in Equation 2.8, the power of the incident, transmitted, and reflected waves are one half of the square of the appropriate normalized amplitude. The scattering matrix of a two-port network is defined as

$$\begin{bmatrix} b_1 \\ b_2 \end{bmatrix} = \begin{bmatrix} s_{11} & s_{12} \\ s_{21} & s_{22} \end{bmatrix} \begin{bmatrix} a_1 \\ a_2 \end{bmatrix}, \tag{2.9}$$

where s_{ij} are the scattering parameters. These parameters describe how the amplitude or power of incident waves are reflected from and transmitted through the two port network, and are generally complex numbers. The wave amplitudes and scattering parameters pertain to monochromatic waves, or are functions of frequency and describe the frequency-domain wave amplitudes. In some cases, there is no incident wave on port two and the reflected wave at port one is of no interest; therefore all scattering parameters other than s_{21} can be ignored. In this case, when a wave is incident on port one, part of the wave energy travels through the network to port two and only s_{21} is required to describe the forward network response. The result is called the transfer function of the network as is usually denoted as $h(\omega)$ in the frequency-domain.

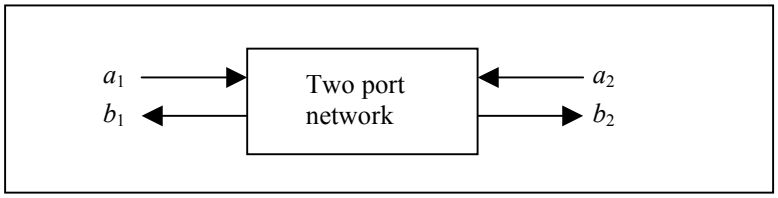

Figure 2.2. A two port network. Port 1 is on the left and port 2 is on the right.

The two port network can be generalized as an N port network. In this case the scattering matrix becomes an N by N matrix. The N port network formalism can be used to describe the response of an antenna. In this case, one port is the antenna feed and all other ports make up the wave number spectrum of waves traveling towards or away from the antenna. A spectrum of waves is a set of waves traveling in different directions, or a set of wave modes describing the wave field around the network. The fields reflected by

a scatterer in space can also be described by an N port network. In this case, the ports are the wave number spectrum of waves traveling towards or away from the scatterer.

Throughout this dissertation, comparisons between data recorded on an oscilloscope, data recorded with the RTDGPR system, and numerically simulated data are made. Most of the operations on individual waveforms require all waveforms to have the same number of samples, and be sampled at the same frequency. All waveforms are standardized using the steps outlined in Figure 2.3. A pertinent feature of the waveform is identified for temporal alignment such as the sample time of a waveform peak or inflection point. Standardization involves aligning the pertinent feature to a common starting point (20 ns is used to provide early time padding), extracting the relevant portion of the recorded waveform, truncating or padding the data to obtain a 100 ns time series, and re-sampling using a 20 ps interval. Then a ramp is subtracted to remove the amplitude difference between the first and last samples, and the average value is subtracted. The data are then normalized according to Equation 2.8. Finally, the data are padded as needed to obtain the proper number of samples for using prime factor fast Fourier transforms (FFT). With 100 ns record lengths, the FFT provides spectral amplitudes at 10 MHz intervals. More details on individual operations and the reasons

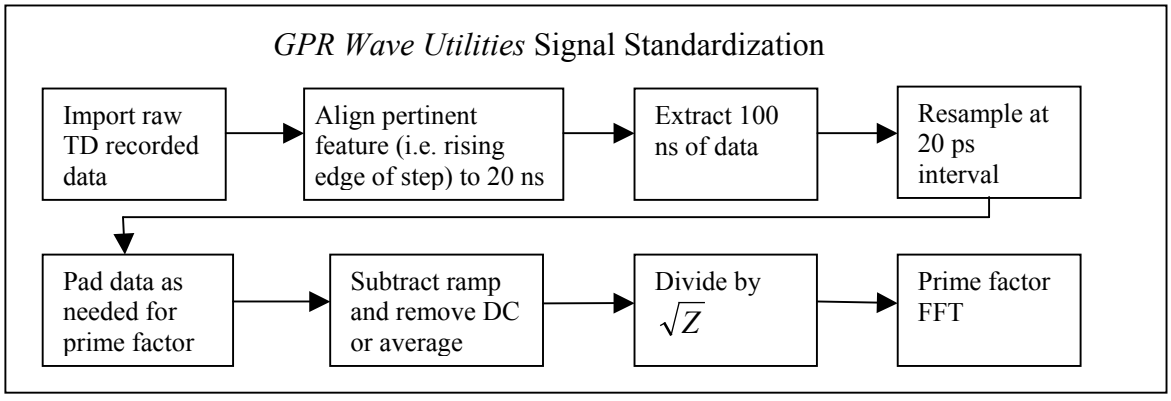

Figure 2.3. Signal standardization flow chart.

for making the operations are explained in the following Sections. *GPR Wave Utilities* is used to perform these operations.

2.2.3 Time-Domain Reflection and Transmission Measurements

There are many ways to measure the response of two port networks. The response of the two port networks can be determined using frequency-domain or time-domain measurements. Frequency-domain measurements require that each physical component in the signal flow path be tested separately (or added to the system one at a time) so that any energy reflected back and forth between components can be separated from the response of each component. With time-domain measurements, individual reflected or transmitted signals from individual components can be separated in time. When testing antennas (N port networks), multiple reflections can be a severe problem due to reflected waves from objects near the antenna (i.e. the ground, walls, etc.), and reflected in the equipment (i.e. from discontinuities in cables and connectors). Regardless of the measurement method used, the response of individual components and the entire system are often described in the frequency-domain using frequency dependent S parameters. Time-domain measurements require additional processing to determine the frequency dependent S parameters. To avoid the problems associated with multiple reflections between system components, the time-domain method was used in this work.

Time-domain reflection (TDR) and time-domain transmission (TDT) measurements require a known signal to be coupled onto a port of the device under test (DUT). The arrangements used in this work are shown in Figure 2.4. In addition to the nomenclature introduced in Equations 2.8 and 2.9, the last part of the subscript indicates the device. For instance *a* represents the pickoff tee, *b* represents the 1:4 balun, and *c* represents the 4:1 balun. TDR tests to measure s_{11DUT} or s_{22DUT} are made with signals recorded at the pickoff tee. TDT tests measure s_{12DUT} or s_{21DUT} with signals at the pickoff

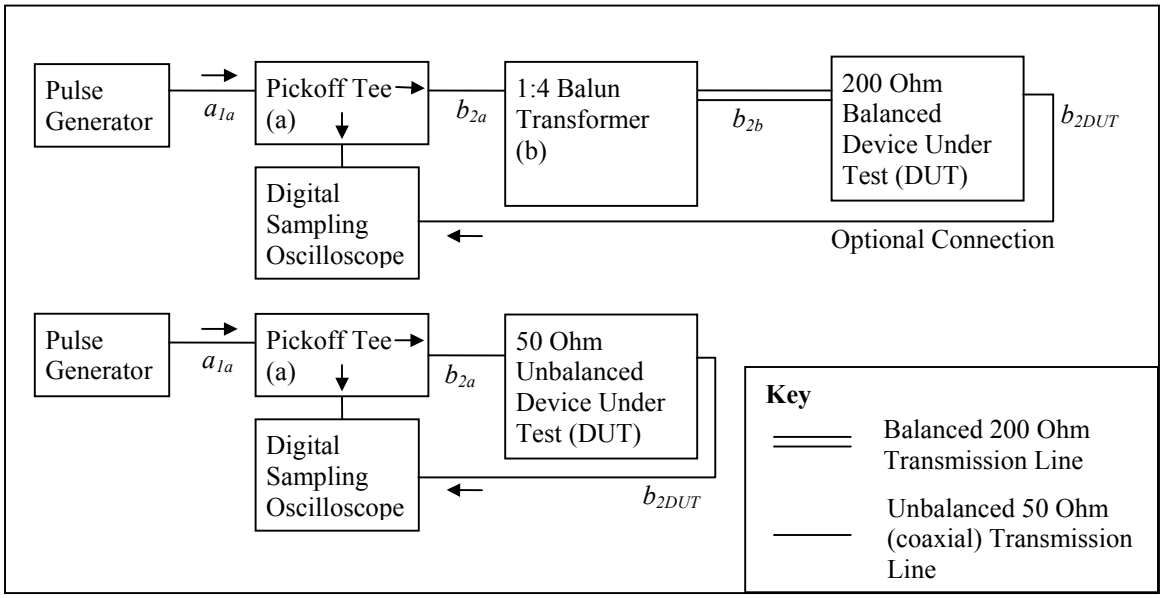

Figure 2.4. TDR/TDT lines for coupling a known signal to a device under test. Arrows indicate direction of signal propagation.

tee and also at the output port of the network. In this dissertation, the DUT port connected to the TDR line is referred to as port one, and the other port is referred to as port two. The pulse generator (Picosecond Pulse Labs model 2500) produces a voltage step with a 1 ns rise time into a 50 ohm coaxial (unbalanced) transmission line. The pickoff tee (Picosecond Pulse Labs model 5370) is a three port network that sends a signal to a digital oscilloscope that represents the voltage of the traveling wave moving through the tee. The tee couples a signal to the oscilloscope that is 14 dB below the signal passing through the tee. The impedance of the through line of the tee is carefully controlled at 50 ohms so as not to reflect any of the traveling waves incident on the tee. All of the unbalanced transmission lines are high quality 4.597 mm (0.181 inch) diameter 100% shielded coax with SMA connectors. The length of each section of transmission line is selected such that the entire test signal can be observed at the pick off tee before any reflected waves. Thus, all of the lines used in this work were at least 1.5 m long

(which is more than adequate). A balun transformer (Minicircuits model ADT4-1WT) is used to couple signals from a 50 ohm unbalanced line to a 200 ohm balanced line. The balanced line was constructed from a 1.524 m (5 feet) long 25.4 cm (10 inches) diameter PVC pipe. The interior of the pipe was shielded with 0.1 mm (0.00405 inches) thick copper foil. Two 6.35 mm (0.25 inches) diameter brass rods offset by 19.05 mm (0.75 inches) center to center were used as the center conductors (see Figure 2.5). This arrangement results in a balanced transmission line with a characteristic impedance of 201 ohms (Smith and Nordgard, 1980). This arrangement can be used to couple signals onto a DUT port with a characteristic impedance of 200 ohms such as the antenna feed ports of many GPR antennas or the circuits that connect to the antennas (i.e. banana jacks separated by 19.05 mm (0.75 inches) center to center). If a particular GPR uses antennas with a different feed port impedance, an appropriate balun transformer and balance transmission line can be used.

The TDR lines must be calibrated before any measurements of a DUT can be made. Figure 2.6 shows the configurations used to measure a_{1a} (bottom), b_{2a} and b_{3a} (middle), and b_{2c} (top). The scattering parameters for the pickoff tee and the 1:4 balun are determined by standardizing the data recorded by the oscilloscope (see Figure 2.3) and then using the following equations

$$s_{21a} = s_{12a} = \frac{b_{2a}}{a_{1a}}, \tag{2.10}$$

$$s_{31a} = s_{13a} = s_{32a} = s_{23a} = \frac{b_{3a}}{a_{1a}}, \text{ and} \tag{2.11}$$

$$s_{21b} = s_{12b} = s_{21c} = s_{12c} = \sqrt{\frac{b_{2c}}{b_{2a}}}. \tag{2.12}$$

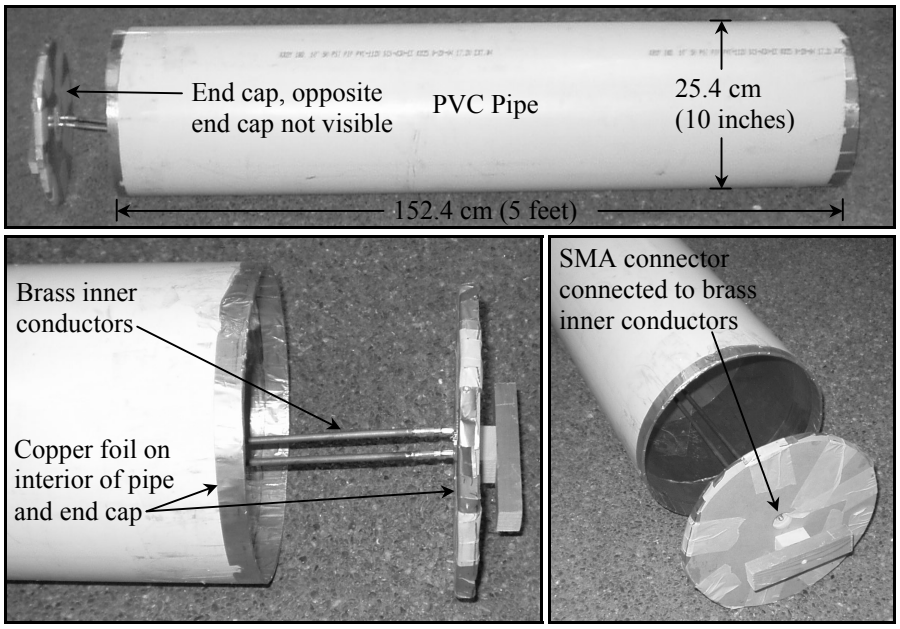

Figure 2.5. Photographs of the disassembled balanced transmission line. Interior of PVC pipe is covered with copper foil. The end cap has been removed to show the interior conductors (brass rods). A balun transformer is located in one end cap to couple a 50 ohm unbalanced SMA connection to the balanced line. The end cap that is not visible has banana jacks to connect to the conductors inside the shield. Both end caps are shielded with copper foil.

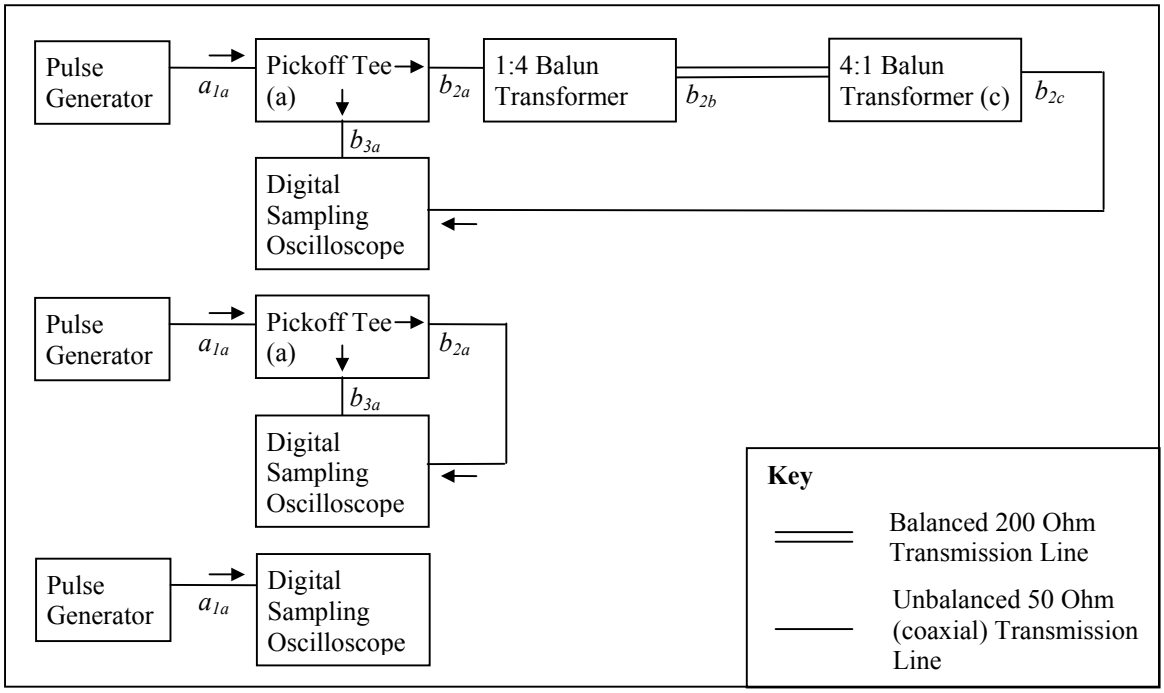

Figure 2.6. Equipment setup to calibrate the pickoff tee and the balun transformer. Arrows indicate direction of signal propagation.

Here a_{1a} is the signal from the generator, b_{2a} is the signal transmitted through the pickoff tee, b_{3a} is the signal sampled by the pickoff tee, and b_{2c} is the signal transmitted through the 4:1 balun. Note that the sampling port shown on the bottom of the pickoff tee is port three (see Figures 2.4 and 2.6). Some of the scattering parameters for the pickoff tee are equal because it is a reciprocal device (Liao, 1985) and because it is symmetrical about port three. The balun transformers are also reciprocal devices, which stipulates that s_{12} equals s_{21} for these devices. The same type of transformer component was used to make both the 1:4 and the 4:1 baluns. If it is assumed that the transformers are identical, then s_{12a} and s_{12b} are equal. Note that Equations 2.10-2.12 contain frequency-domain parameters, and multiplications represent convolution operations in the time-domain and division represents deconvolution operations. A quality control check on the calibration

of the TDR lines can be made since all of the devices used are nearly lossless. For lossless devices, the incident and reflected energy must balance. For the pickoff tee,

$$|s_{11}|^2 + |s_{21}|^2 + |s_{31}|^2 = 1. \tag{2.13}$$

Assuming that $|s_{11}|$ is zero, the calculated values of $|s_{21}|$ and $|s_{31}|$ from Equations 2.10, 2.11 can be verified against 2.13.

To make TDT measurements, the signal incident on the DUT must be known. If port one on the DUT has a 50 ohm impedance, then the incident signal b_{2a} is known from the calibration measurements. If the port has a 200 ohm impedance, the incident signal is simply

$$a_{1DUT} = b_{2a}s_{21b} = \sqrt{b_{2a}b_{2c}}\ . \tag{2.14}$$

For the TDT tests on most GPR equipment, port two will often be a 50 ohm port so the output signal b_{2DUT} can be measured using a standard oscilloscope with a 50 ohm port. In another common scenario, the output signal b_{2DUT} will be recorded directly by the radar system. This is the case when testing the RTDGPR's receiver electronics. The forward scattering parameter s_{21DUT} is simply

$$s_{21DUT} = \frac{b_{2DUT}}{a_{1DUT}}. \tag{2.15}$$

Since the pick off tee samples waves moving in both directions on the TDR line, TDR measurements can be made from the signals measured at the pickoff tee. TDR measurements are slightly more complicated than TDT measurements however, and the signal nomenclature will be modified slightly. Figure 2.7 (top) shows the signal recorded on the oscilloscope, which was sampled at the pickoff tee when conducting a TDR experiment on a DUT with 200 ohm input port. The pulse generator signal arrives at 25

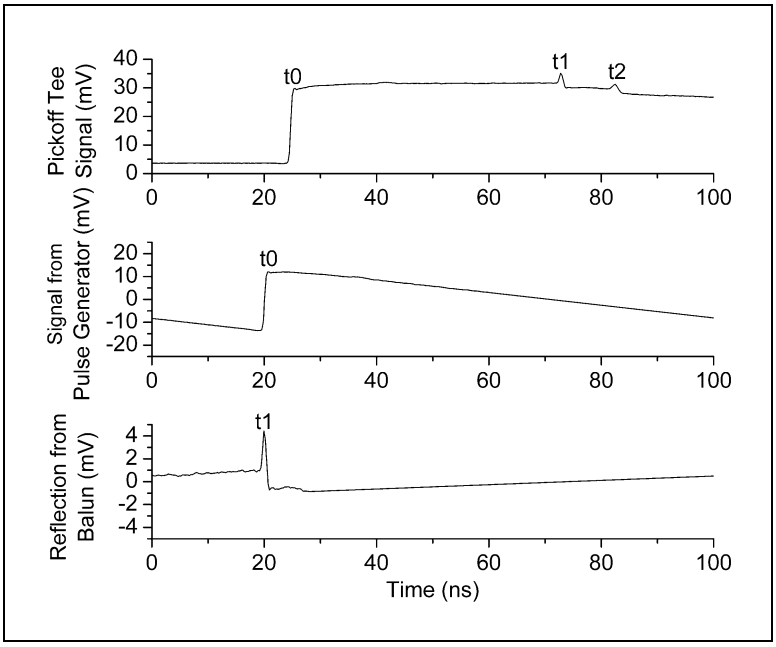

Figure 2.7. The top panel shows the recorded TDR waveform sampled at the pickoff tee, the center panel shows standardized pulse generator signal sampled at the pickoff tee, and the bottom panel shows the standardized reflection from the balun.

ns, the reflected signal from the 1:4 balun transformer arrives at 72 ns, and the reflection from the DUT arrives at 82 ns. These events will be referenced sequentially as event t0, t1, and t2. The event reference will be added to the signal variable subscripts to indicate the relevant portion of the waveform recorded at the pickoff tee. The event index for the first three events is shown in Figure 2.7 (top). Figure 2.7 (middle and bottom) shows the standardized waveforms extracted from the recorded waveform. For determining the reverse scattering parameters, the incident waveforms are determined as in the TDT tests above. If port one on the DUT has a 50 ohm impedance, then the reflected signal b_{1DUT} is

$$b_{1DUT} = \frac{b_{3a,t1}}{s_{32a}} = \frac{b_{3a,t1} a_{1a,t0}}{b_{3a,t0}}, \tag{2.16}$$

and the s_{11DUT} scattering parameter is calculated by

$$s_{11DUT} = \frac{b_{1DUT}}{a_{1DUT}} = \frac{b_{3a,t1}}{b_{2a,t0}s_{32a}} = \frac{b_{3a,t1}a_{1a,t0}}{b_{2a,t0}b_{3a,t0}}. \tag{2.17}$$

If port one on the DUT has a 200 ohm impedance, then the incident signal b_{2b} is determined with Equation 2.14. The reflected signal b_{1DUT} is given by

$$b_{1DUT} = \frac{b_{3a,t2}}{s_{12b}s_{32a}} = \frac{b_{3a,t2}}{\sqrt{\frac{b_{2c,t0}}{b_{2a,t0}}}\frac{b_{3a,t0}}{a_{1a,t0}}}, \tag{2.18}$$

and the s_{11DUT} scattering parameter is calculated by

$$s_{11DUT} = \frac{b_{1DUT}}{a_{1DUT}} = \frac{b_{3a,t2}}{b_{2a,t0}s_{21b}s_{12b}s_{32a}} = \frac{b_{3a,t2}a_{1a,t0}}{b_{2c,t0}b_{3a,t0}}. \tag{2.19}$$

The operations, equipment setup, and equations needed for conducting TDT and TDR tests on most GPR equipment are summarized in Table 2.1. Finally, it should be noted that since deconvolution is a filtering operation that affects signal fidelity, the product of all terms in the denominator should generally be calculated first so that multiple deconvolution operations are not needed.

Table 2.1. Summary of operations for make TDT and TDR tests.

Operation	DUT Input Port Impedance	Equipment Setup	Relevant Equations
Calibration	50	Fig. 2.6 bottom and middle	2.10, 2.11
TDT	50	Fig. 2.4 bottom	2.15
TDR	50	Fig. 2.4 bottom	2.16, 2.17
Calibration	200	Fig. 2.6 all	2.10-2.12.
TDT	200	Fig. 2.4 top	2.14, 2.15
TDR	200	Fig. 2.4 top	2.14, 2.18, 2.19

2.3 The Response of the RTDGPR Receiving Electronics

The signal flow path in most GPR receiver electronics follows a series of two port networks. Usually, the receiver electronics as a whole can be considered a single two port network, with the receiving antenna connected to one port, and the data recording device connected to the other. TDT measurements can be used to characterize the receiver electronics of impulse radar systems as long as the response is linear. This is true for most commercial GPR systems, although the response will likely be different at different gain settings. Investigators should be wary of problems that may arise with some systems due to inherent non-linearity or system drift with time or temperature. If the system response is nonlinear, or changes with time or temperature, then large errors between the actual response and the measured response can result when using measurement techniques designed for linear systems. Often, a nonlinear element can be isolated, and characterized separately using methods designed specifically to address the nonlinear nature of the element. The techniques described in this Chapter can be used to characterize the linear parts of the system.

Frequency-domain measurements of a network response can be quite accurate. Unfortunately, frequency-domain measurements may not be possible with some impulse GPRs because the steady state frequency-domain system response may not reflect the actual transient time-domain response. For example, multiple transmission line reflections due to impedance mismatches cause the response from a transient excitation to be different than the response from a steady state excitation. The transient response of some active circuits (i.e. amplifiers with feedback) can be different than the steady state response. Additionally, measuring the response of the digitization unit may be difficult in the frequency-domain because digitizers can usually only operate for short bursts of time, and frequency-domain characterization normally requires steady state measurements. If equivalent time sampling is used, then it may be difficult to synchronize the frequency-domain source with the digitizer. Finally, many impulse

GPRs use a time varying range gain, which precludes steady state frequency-domain measurements. For these reasons, it is best to measure the response of the radar in the time-domain. Ideally, the excitation would be synthesized with an arbitrary waveform generator that could be synchronized with the radar's digitizer. Unfortunately, an arbitrary waveform generator that operated at GPR frequencies was not available for this work. Rather, two synchronous sources were used – an impulse generator and a ramp generator. For this work, some frequency-domain measurements were also made and the results are compared with the time-domain measurements.

The components of the RTDGPR receiver electronics are essentially linear elements with the exception of the logarithmic amplifier. The logarithmic amplifier has a nominal gain of 40 dB, and responds linearly for input signals smaller than about -40 dBm. For input signals larger than -40 dBm, the amplifier's gain is reduced. The minimum gain of 0 dB occurs for input signals greater than 0 dBm. When the input signal level is between -40 dBm and 0 dBm, the amplifiers gain decreases as the input signal level increases, which results in a non-linear response. It is possible to characterize the system response using TDT experiments as long as the input to the logarithmic amplifier remains less than -40 dBm (or greater than 0 dBm). This is the situation when most of the GPR trace is being recorded. Because the RTDGPR can change the attenuator setting in the receiving electronics record during the survey, it is always possible to record data in the linear response region of the receiving electronics (as long as the input signal is less than 20 dBm). The response of the RTDGPR was characterized for the linear region of operation. An attempt was made to characterize the non-linear region of operation, but the results were unsatisfactory for reasons explained below.

An inexpensive synchronous ramp generator was constructed to aid in calibrating the RTDGPR receiving electronics. The goal was to calibrate the non-linear response of the RTDGPR. The ramp generator produces a repeatable triangular waveform when triggered, and can be used with GPR systems with stacking capabilities and/or equivalent

time sampling. The generator connects to the 200 ohm port balanced input port of the receiving electronics that normally connects to the receiving antenna feed port, and provides a reference signal on a 50 ohm port (see Figure 2.8). A test waveform is sent into the receiving electronics when triggered by the optical synchronization signal from the GPR. The generator produces a linearly decreasing ramp followed by a linearly increasing ramp (see Figure 2.9), and the slopes of the ramps can be varied. *GPR Wave Utilities* can build a non-linear mapping function relating the standardized signal recorded by the radar system to the standardized reference signal recorded by an oscilloscope. The mapping function can then be used to convert data from a non-linear system to a linear response. For the RTDGPR, the main difficulty with this approach is that a triangular waveform contains a broad spectrum of frequencies, and frequencies

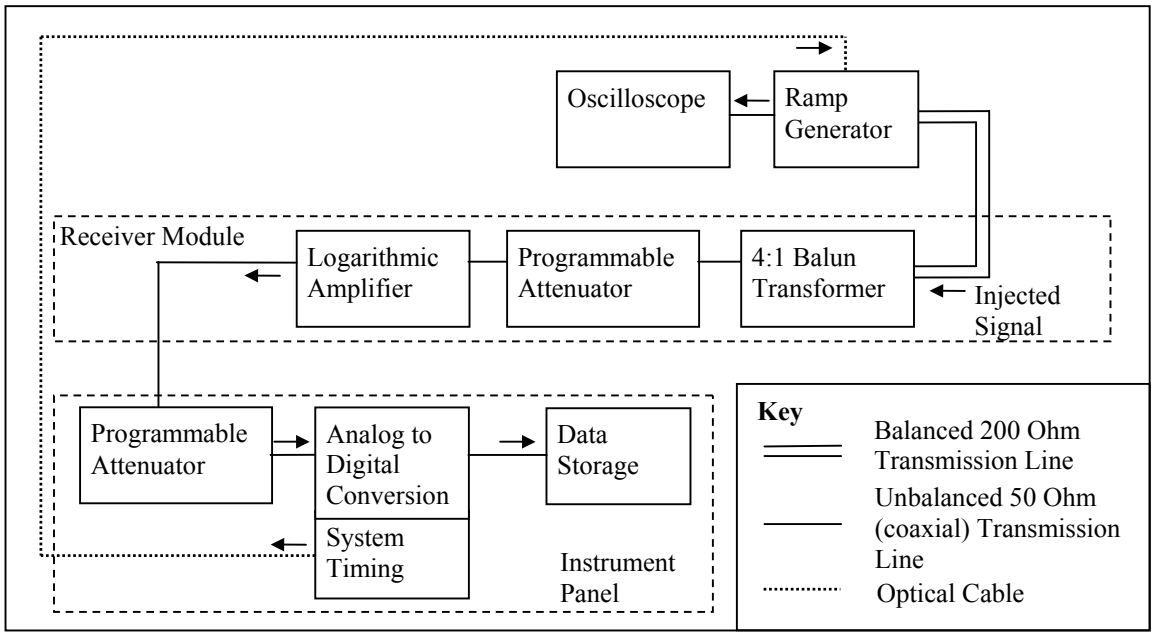

Figure 2.8. Connection of the ramp generator to the RTDGPR. Arrows indicate direction of signal propagation.

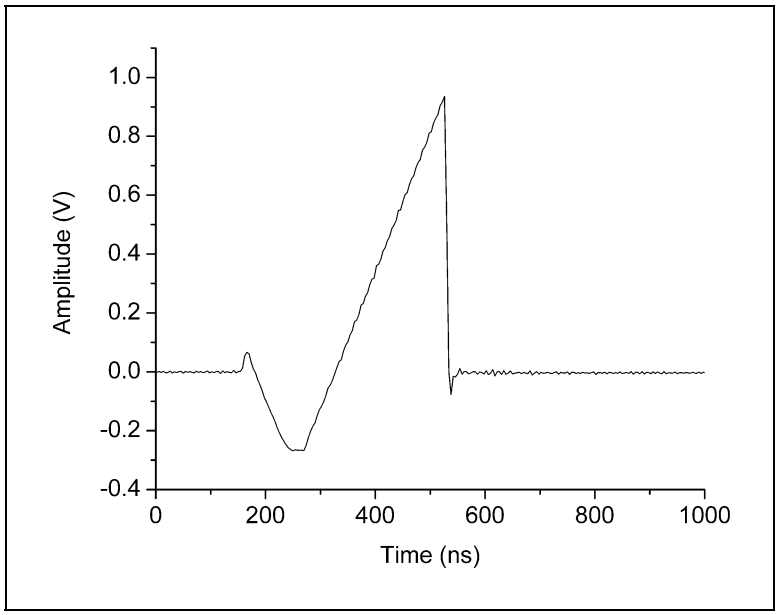

Figure 2.9. Signal produced by the inexpensive ramp generator.

outside the pass-band of the receiving electronics were attenuated or not present in the output waveform. Since the signal recorded by the RTDGPR had spectral distortions, a time-domain mapping of the amplitude response was not possible. This calibration method would provide good results for GPRs with a non-linear amplitude response, and a flat frequency response. A schematic diagram and parts list of the generator is included in Appendix A. For general use, the generator could be easily modified for triggering with an electrical synchronization signal.

TDT experiments were conducted to calibrate the linear response of the receiving electronics. Figure 2.10 shows how the TDT equipment was connected. The step generator, pickoff tee, and balun transformer are of the types discussed in Section 2.2.3. The input signal level at the injection point was calculated as follows. The signal incident in the 1:4 balun transformer a_{1b} was measured using the setup shown in the

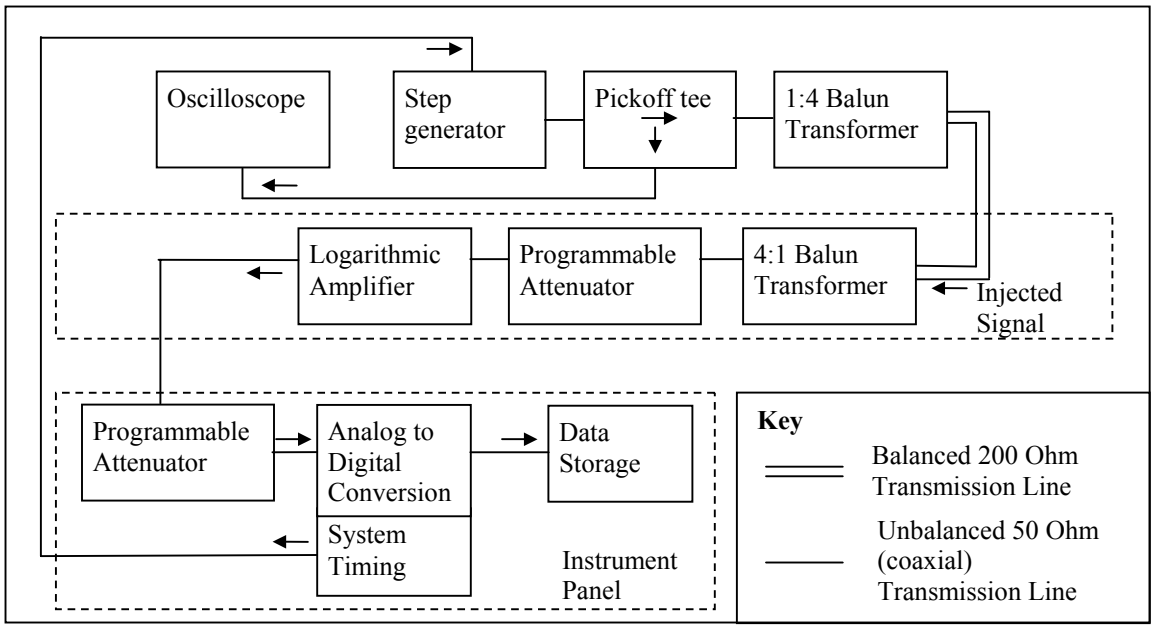

Figure 2.10. Connection of the step generator to the RTDGPR. Arrows indicate direction of signal propagation.

middle of Figure 2.6, and the signal exiting the 4:1 balun transformer b_{2c} was measured using the setup shown in the upper part of Figure 2.6. In this measurement, the 4:1 balun is assumed to have the same response as the one used in the RTDGPR receiving electronics since it is the same transformer model. The only change in the response of the RTDGPR in the linear operating region (input signal less than -40dBm) should be due to the attenuator setting. Since attenuators are passive devices with attenuation that is usually flat over the operational frequency band, the effective receiver module input level is equal to the actual input level (in dBm) minus the attenuation of the receiver module attenuator. The effective input level a_{1r} and $\left| a_{1r,dBm} \right|$ in dBm are given by

$$a_{1r} = b_{2c} \cdot \sqrt{\frac{a_{1b}}{b_{2c}}} \cdot 10^{-A_a/20}, \tag{2.20}$$

$$\left|a_{1r,dBm}\right| = 20 \cdot \log\left(\frac{\left|b_{2c}\right|/\sqrt{2}}{0.03162}\right) + 10 \cdot \log\left(\left|\frac{a_{1b}}{b_{2c}}\right|\right) - A_a, \tag{2.21}$$

where the first term is the output level from the 4:1 balun transformer, the second term is the gain of the 4:1 balun transformer, and A_a is the attenuation of the attenuator in dB. The response of the receiving electronics $\left| s_{21r,dB} \right|$ is given by

$$s_{21r} = \sqrt{\frac{b_{2r}^2}{b_{2c}a_{1b}}} \cdot 10^{A_a/20}, \tag{2.22}$$

$$\left|s_{21r,dB}\right| = 10 \cdot \log\left(\left|\frac{b_{2r}^2}{b_{2c}a_{1b}}\right|\right) + A_a, \tag{2.23}$$

where b_{2r} is the signal recorded by the RTDGPR. The system response was determined at several effective input levels, and the results discussed in the following paragraphs. The attenuator in the instrument panel is nearly always operated in the 0 dB setting, so all calibration data are for this setting. Note that coefficients in Equations 2.20-2.23 are frequency-domain parameters, and the division operation of amplitude variables are deconvolution operations as described in Section 2.2.1. The principal value is used in the square root operation.

A frequency-domain vector network analyzer (VNA; Agilent model 4395A) was used to test the response of the receiving electronics. The receiving circuitry was connected as shown in Figure 2.11. Note that the response of the input balun transformer and the digitizer were not measured in this test. To incorporate the balun transformers in the frequency-domain measurement, a complete scattering matrix is needed for each transformer. Determining the transformer scattering matrices is straightforward, but was not done in this work. Incorporating the digitizer response would be difficult unless the VNA signal could be synchronized with the RTDGPR system. This could be accomplished for some GPR systems by using a high frequency arbitrary waveform generator. The frequency-domain response for various effective input levels is shown in Figure 2.12. The input levels are calculated using

$$\left|a_{1r,dBm}\right| = \left|b_{VNA,dBm}\right| - 1 - A_a \,, \tag{2.24}$$

where $\left| b_{\mathrm{VNA},dBm} \right|$ is the VNA average output level in dB, and A_a is the receiver module attenuator setting in dB. One dB is subtracted to account for losses in the VNA coupling hardware. Note that the response changes at effective input levels greater than about -40 dBm due to the changing gain of the logarithmic amplifier.

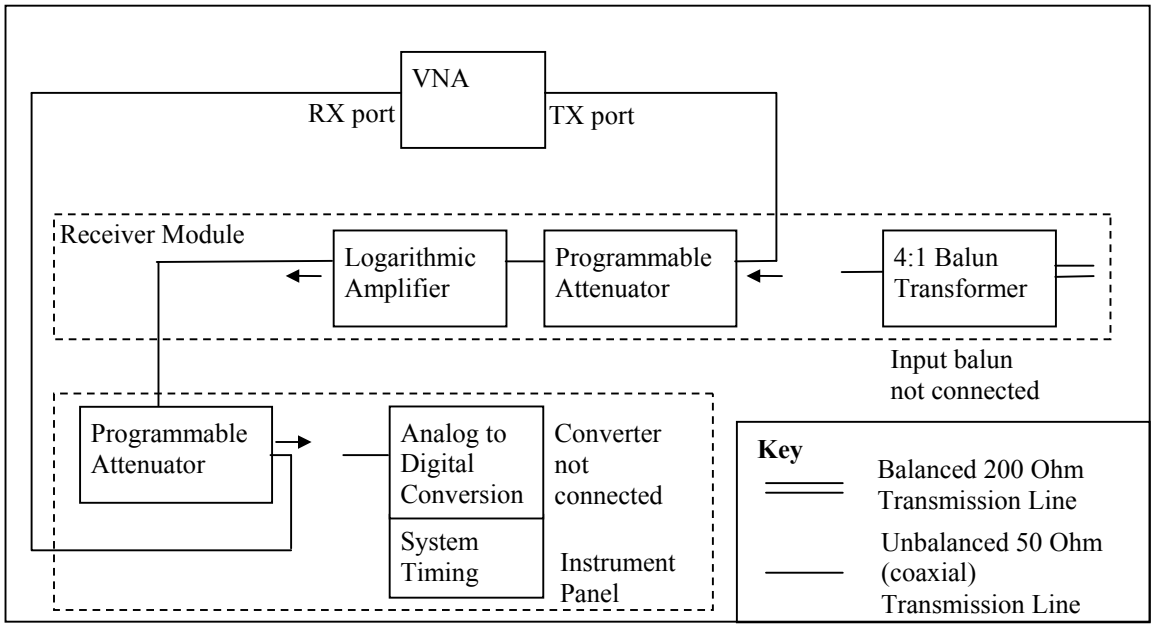

Figure 2.11. Connection of the vector network analyzer (VNA) to the RTDGPR. Arrows indicate direction of signal propagation.

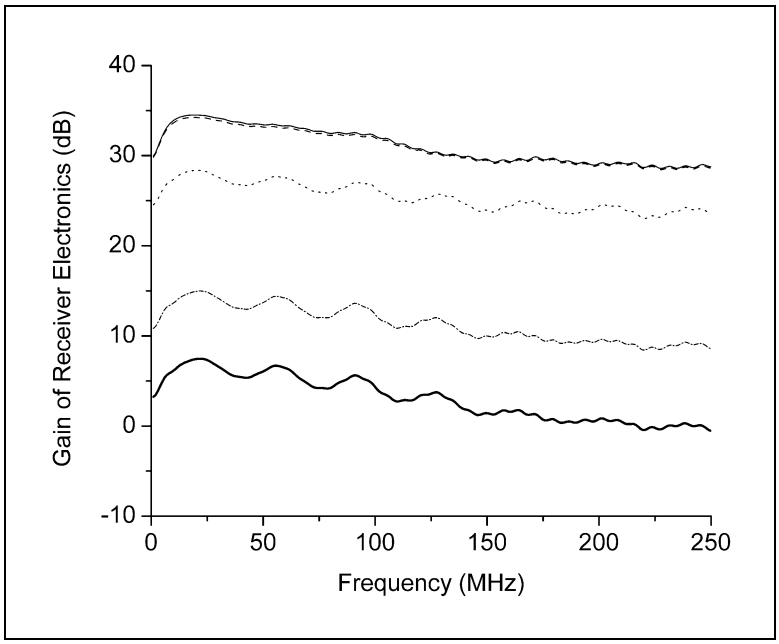

Figure 2.12. Frequency-domain response of receiver electronics determined using a VNA. Input level is -71 dBm (thin solid), -51 dBm (dashed), -31 dBm (dotted), -21 dBm (dash-dot), and -11 dBm (thick solid).

Figure 2.13 shows the gain of the receiver electronics as a function of frequency and effective input level as determined by the TDT and frequency-domain experiments. The input levels were calculated using Equations 2.21 and 2.24. The corresponding input (at 200 ohm port) and output (recorded) waveforms are shown in Figure 2.14. For TDT measurements, the response was calculated at 10 MHz intervals. No TDT results were available for input levels of -19.5 dBm and higher because the digitizer saturated during these tests. The frequency-domain response is slightly higher because it does not include the loss of the 4:1 input balun transformer, and any loss by the digitizer. Note that the gain changes by about 6 dB over the operating frequency band, and that the response is no longer linear for input levels of -39.5 dBm and greater. A fifth order polynomial was fit to the receiver electronics response determined by the TDT measurements for the

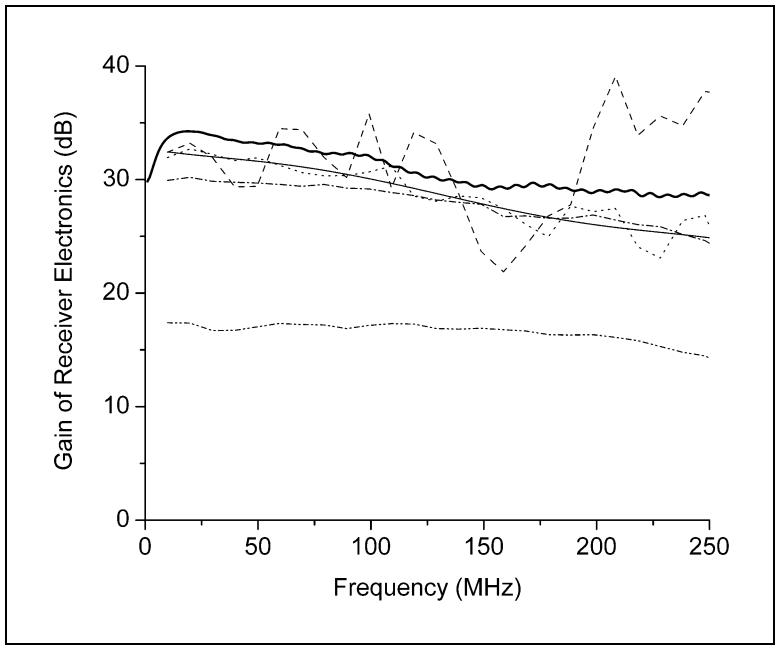

Figure 2.13. TDT response of receiver electronics. Dotted line is for -59.5 dBm input level, dashed line is for -79.5 dBm, dash-dot line is for -39.5 dBm, and the dash-dot-dot line is for the -19.5dBm input level. Solid line is polynomial fit to -59.5 dBm line. Thick line is frequency-domain measurement at -51 dBm input.

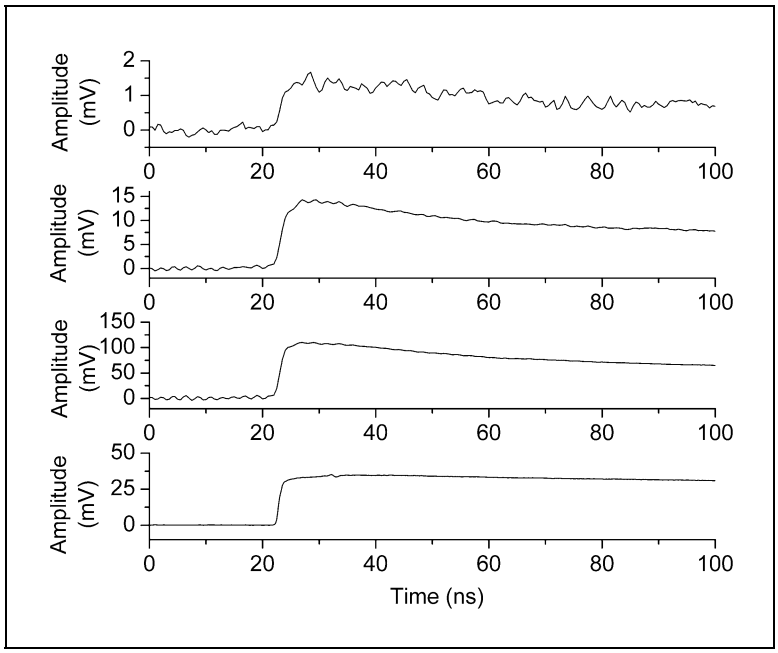

Figure 2.14. Recorded signal for various receiver attenuator settings. From bottom panel to top: signal output from pickoff tee, recorded output with receiver module attenuator settings of 20, 40, and 60 dB respectively.

-59.5 dBm input power level. The response polynomial is given by

$$\left|S_{21r,dB,fit}\right| = 32.73478 - 3.432\cdot10^{-2} f + 5.3426\cdot10^{-4} f^2 - 7.6413\cdot10^{-6} f^3 + 3.5844\cdot10^{-8} f^4 - 5.4579\cdot10^{-11} f^5 \quad (2.25)$$

where f is frequency in MHz. This polynomial relates the recorded signal level to the effective input level. Note that the frequency-domain results plotted in Figure 2.12 have less noise than some of the TDR results. Nevertheless, frequency measurements are not generally recommended for calibrating impulse radars for the reasons mentioned at the beginning of this section. If multiple reflections occur in the receiver electronics, the frequency-domain response may not represent the time-domain response. In this case, the frequency-domain results compare well with the time-domain results for the RTDGPR because multiples have been kept to a minimum. In general however, since the

signals measured by impulse radars in normal operation are transient time-domain signals, TDT measurements are recommended for calibrating these instruments. Finally, the TDT measurements give a good indication of the signal to noise ratios for transient time-domain signals. Note that the noise in the receiver transfer function increases with frequency. This is because the power in the TDT step excitation decreases as frequency increases. A detailed error analysis was not made, however some experiments were repeated on different dates. The difference in amplitude response between the original and repeated experiments was always less than 5%.

The phase response of the system over the operating frequency band is essentially flat. Figure 2.15 shows the phase response and impulse response determined from the TDT at the -59.5 dBm input level. In all subsequent calculations, the phase response is estimated as being independent of frequency. This is reasonable for several reasons. First, the amplifiers and attenuators used in the RTDGPR were designed to have a flat phase response, and the recorded step response closely resembles the excitation. Generally, changes in the frequency response of most broad band signal processing systems occur over a broad frequency range unless the system is specifically designed to have sharp changes (i.e. a notch filter or a very selective band pass filter). Second, since the amplitude response is nearly constant over the operating frequency range, the Kramers-Kronig relations (Jackson, 1999) stipulate that the phase response will also be nearly constant. Finally, the impulse response appears as a nearly zero phase wavelet (i.e. symmetrical wavelet).

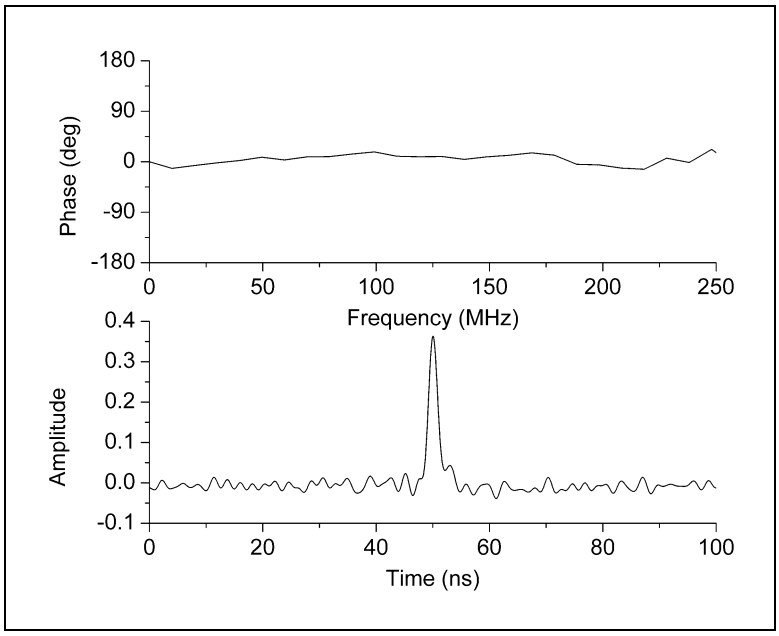

Figure 2.15. Phase response and impulse response of receiver electronics.

The receiver module was modified after conducting the experiments in which the antenna response was measured in air and over water (these experiments are described later in the Chapter). The modifications flattened the frequency response of the system over the operating frequency range. Figure 2.16 shows the frequency-domain response, and a polynomial fit to this response is given by

$$\left|s_{21r,dB,fit}\right| = 41.00861 - 1.7321\cdot 10^{-2} f + 5.6885\cdot 10^{-4} f^2 - 1.0762\cdot 10^{-5} f^3 + 5.8585\cdot 10^{-8} f^4 - 1.0096\cdot 10^{-10} f^5 \quad (2.26)$$

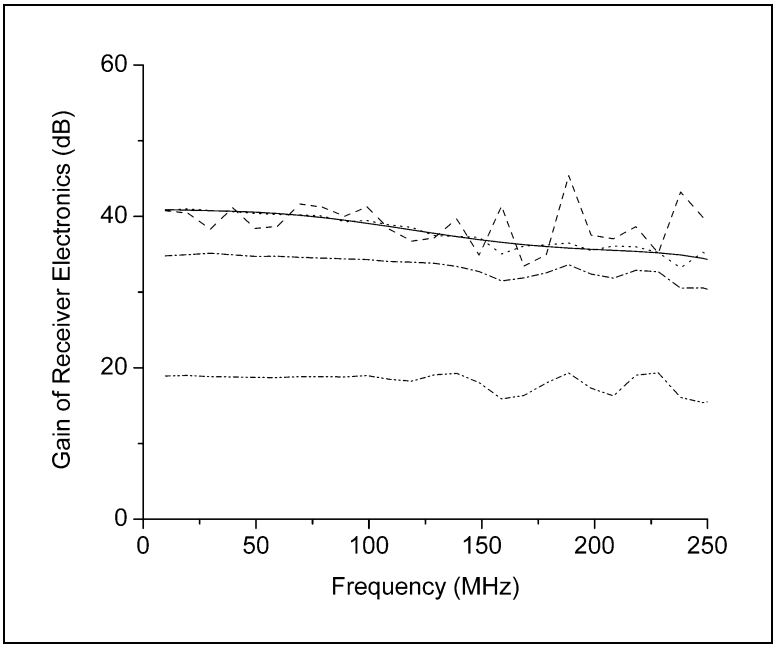

Figure 2.16. TDT response of the modified receiver electronics. Dotted line is for -59.5 dBm input level, dashed line is for -79.5 dBm, dash-dot line is for -39.5 dBm, and the dash-dot-dot line is for the -19.5dBm input level. Solid line is polynomial fit to -59.5 dBm line.

A few comments are in order to end this Section that pertain to the calibration of GPR systems in general. It is difficult to make the proper measurements and write a suitable calibration algorithm for systems whose response depends on time, amplitude, frequency, and state of the system. If all but one of these factors can be removed for a particular class of signals (i.e. linear response over a certain frequency range), then calibration is straightforward. If more than one factor is active, then it is possible in principal to calibrate. But in practice, significant errors may result when a small error in accounting for changes in one parameter causes a large error in accounting for changes in another parameter. Furthermore, more sophisticated test apparatus may be required. Therefore, it is suggested that only GPR systems whose response depends on a single

variable are considered to reduce the probability of poor results. The measured response at various recording times, amplitudes, and frequencies which span the operating range of the instrument must be studied to insure that this is the case.

2.4 The Pulse Generator Response

In order to simulate the response of a GPR system, the excitation must be known. Several techniques are presented for measuring the waveforms incident on the transmitting antenna feed port. For the RTDGPR antenna, the generator is located at the antenna feed port so that there is no transmission line between the generator and the antenna, however some GPR systems may use a transmission line between the generator and the antenna. In either case, the transmitting antenna feed port has incident waves from the generator and also from the antenna. This is because in general, the antennas are not perfect traveling wave antennas, and some of the waves traveling along the dipole (that originated at the feed port) may be reflected back towards the feed port. Further, the generator and the antenna are not perfectly matched at all frequencies, and not all of the energy incident on the port will be transmitted through the port (regardless which direction the waves are traveling). The point is that the coupling between the source, the transmission line, and the antenna feed must be adequately characterized and specified for accurate simulations. Since the output impedance of the RTDGPR pulse generator is only a few ohms (simulated as zero ohms), and the transmission line is absent, specification of the source for simulations was trivial. The FDTD simulations of the antenna response (discussed in Section 2.5) use a 'hard source' model with no internal resistance, but other simulation packages may use a different convention.

The feed port voltage should be measured while in circuit so that any effects of source loading and incident waves from the antenna are properly accounted for. This is a difficult and crucial task. Generally, the addition of a measuring device changes the load

on the pulse generator and likely the effective output. Several experiments were made to estimate the pulse generator output, and are discussed in the following paragraphs. Unfortunately, some produced inadequate results. Some of the difficulties are related to the large amount of energy produced by the RTDGPR. Only the current probe method and the high-voltage probes method produced reasonable results (see below).

In an effort to estimate the pulse generator output using deconvolution, the response of the antenna system was measured with a known excitation and then compared to the response when driven with the RTDGPR pulse generator. The antennas were held in a fixed reference position and orientation when making these experiments. The antennas were arranged such that the bottom of the antennas faced each other in a co-polarized manner (see Figure 2.17), and the distance between the base of the antennas was 125 cm. The experiment was performed outdoors in an open area to insure no unwanted reflections would be received. No metallic parts were located between the antennas, and the use of metallic parts near the antennas was avoided as much as possible. The foam absorber was absent from the antennas during these experiments because it had not yet been procured (see antenna description in Section 2.5.2). The transmitting antenna was fed using the balanced TDR line shown in Figure 2.4. The signal at the receiving antenna was recorded, and the transfer function for the antennas held in this reference position was determined by deconvolution. Then the TDR line was removed, the RTDGPR pulse generator was connected to the transmitting antenna feed port, and the resulting signal was recorded at the receiving antenna. Because the fixed antenna array can be viewed as a linear two port system, deconvolving the received waveform with the transfer function of the antennas results in an estimate of the pulse generator output. Unfortunately, the transfer function of the RTDGPR antennas in the reference position had essentially no response below about 75 MHz, which results in an estimated pulse generator output with essentially no frequencies below about 75 MHz. The RTDGPR pulse generator produces a step output (or facsimile thereof), and the low frequency components are a very important part of the generator excitation, therefore a

Figure 2.17. Face to face antenna reference arrangement used to estimate the impulse generator waveform. The frame is made from fiberglass.

better means of determining the generator output was sought. Even with these shortcomings, the estimated rise time of the pulse generator was 2.5-3 ns.

A logical method for making high frequency measurements is to use transmission lines and TDR/TDT measurements. Rather than using the laboratory pulse generator discussed in section 2.2.3, the radar's impulse generator is used. For the RTDGPR, this requires a 200 ohm balanced pickoff tee that capable of withstanding the high voltage generated by the impulse generator. A balanced pickoff tee was constructed that could be placed between the generator and the feed port. The tee was designed to be electrically very short (a small fraction of a wavelength long), and be as physically small as possible to minimize any distortion of the fields near the feed port. If the fields near the feed port are distorted by changing the material properties in the vicinity of the port, then the input impedance of the port will change. A photograph of the pickoff tee is shown in Figure

2.18. A schematic of the tee is shown in Figure 2.19. Note that a coil of coaxial cable is used as a choke balun to prohibit coupling any of the sampled signal to the exterior of the coaxial cable. The entire unit is shielded to minimize stray currents induced on the signal paths from the high strength fields near the feed port. When this tee was used with the RTDGPR high voltage pulse generator, corona and arcing occurred resulting in damage to the generator; despite the fact that the tee components were conformal coated with an anti-corona agent. This was caused by physically locating the components too close together. Building a pickoff tee with more separation between the components may have made the unit large enough that the input impedance of the feed port would have been affected. This approach was abandoned so as not to risk damaging the impulse generator again. The technique is presented here because it is a viable technique for traditional radar systems with lower pulse generator output levels. This method should work well for systems with a transmission line between the pulse generator and the antenna feed port.

A method that provided reasonable results was simply to use a pair of identical high voltage high input impedance oscilloscope probes (Tektronics P5100). The first step was to determine the impulse response of the oscilloscope probes using the setup shown in Figure 2.20 where one probe is designated as positive, and the other negative. The forward scattering parameters ($s_{+21PROBE}$ and $s_{-21PROBE}$) and the impulse response of each probe was determined using deconvolution (see Figure 2.21). Here, the oscilloscope probe was the DUT, and the incident signal was calculated using Equation 2.14. Next, the pulse generator was connected to the antenna feed port as usual, and the voltage at the port was monitored by connecting the two high-voltage probes at the antenna port terminals. The probe cables were oriented so that traverses were perpendicular to the radiating dipole. Ferrite beads (Panasonic KRCBC130714B) were also installed every 10 cm on the probe cables to attenuate any current induced on the exterior of the cables. The pulse generator output was calculated from the measured waveforms by deconvolving the

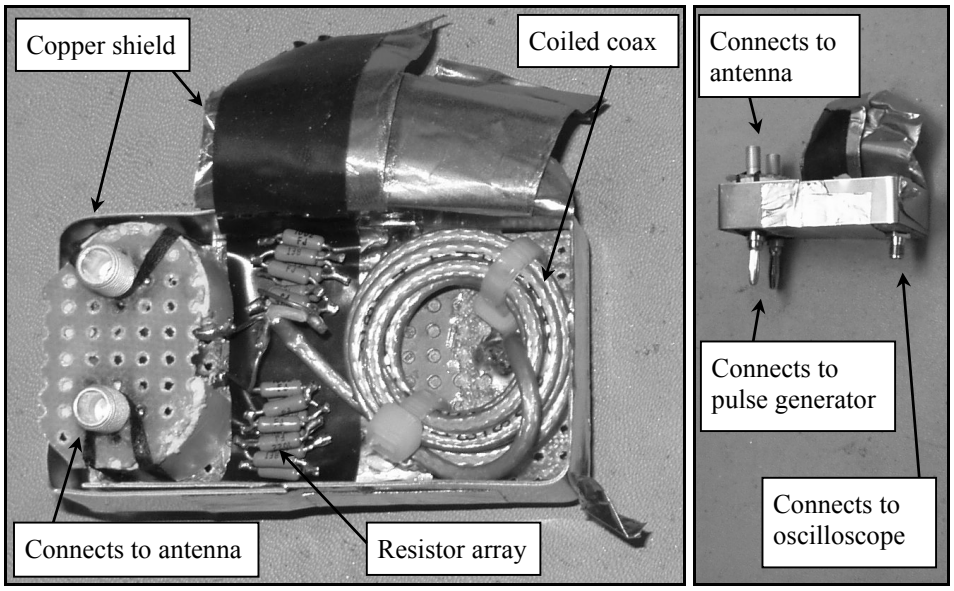

Figure 2.18. Photographs of pickoff tee with copper shield pulled open. Banana jacks are spaced 1.905 cm (0.75 inches) apart.

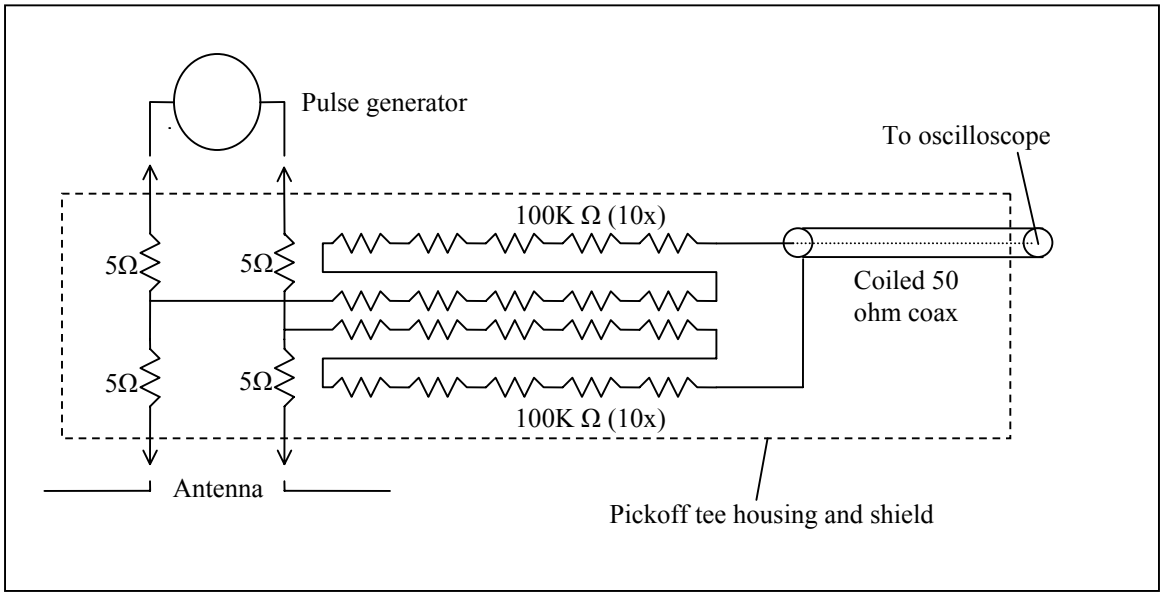

Figure 2.19. Schematic diagram of the balanced pickoff tee.

impulse response of the probes (see Figure 2.22). The frequency-domain generator output is given by

$$V_{gen} = \frac{V_+}{s_{+21PROBE}} - \frac{V_-}{s_{-21PROBE}} \tag{2.27}$$

where V_+ is the signal measured by the positive probe, and V_- is the signal measured by the negative probe. The deconvolved waveform has some late time ringing that is probably not in the actual generator output since this ringing is not present in the waveforms at the probe input. This is likely due to unintended energy coupling paths between the pulse generator and the probe cable and oscilloscope. These paths exist due to stray inductance and capacitance, and wave guiding on the exterior of the probe cable. Since the position of the cables changed between measuring the impulse response of the probes and measuring the pulse generator output, the unintended coupling paths also changed. The only practical methods to completely avoid unintended coupling are to use shielded wave guides and pickoff tees, or to use non-metallic cables such as optical fiber.

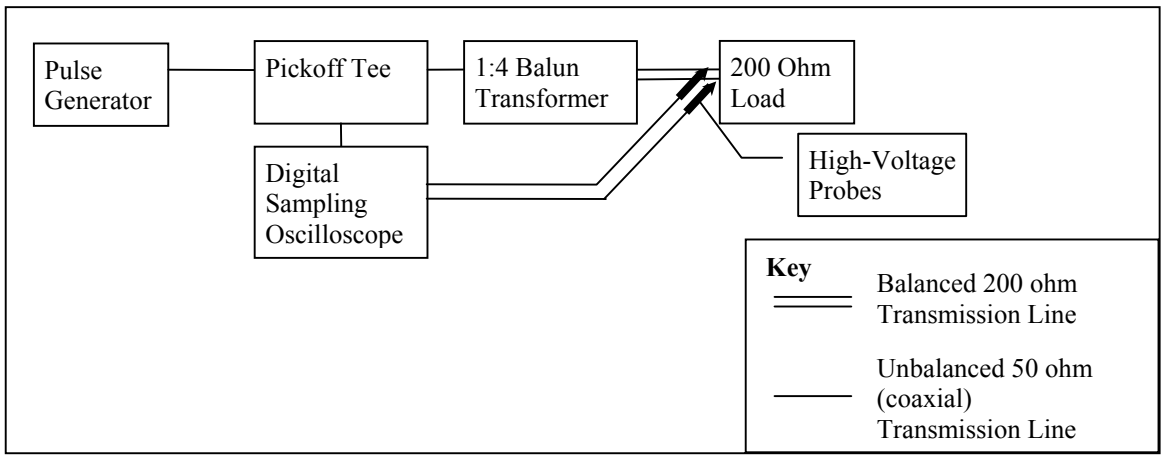

Figure 2.20. Setup to calibrate high-voltage oscilloscope probes.

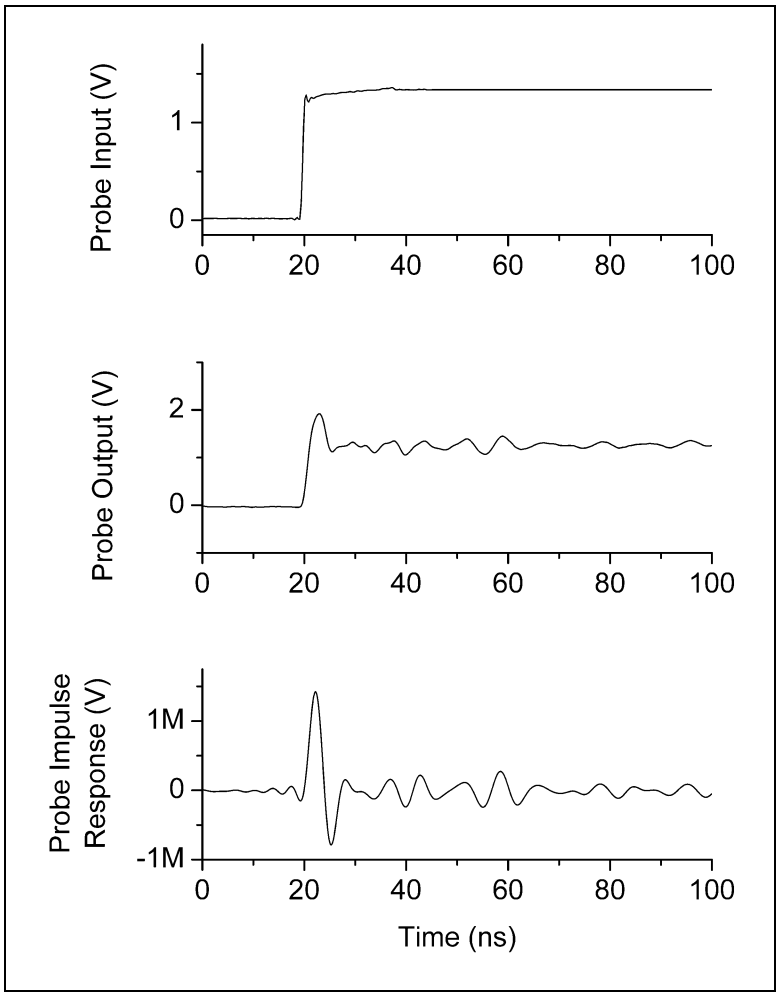

Figure 2.21. High-voltage oscilloscope probe response.

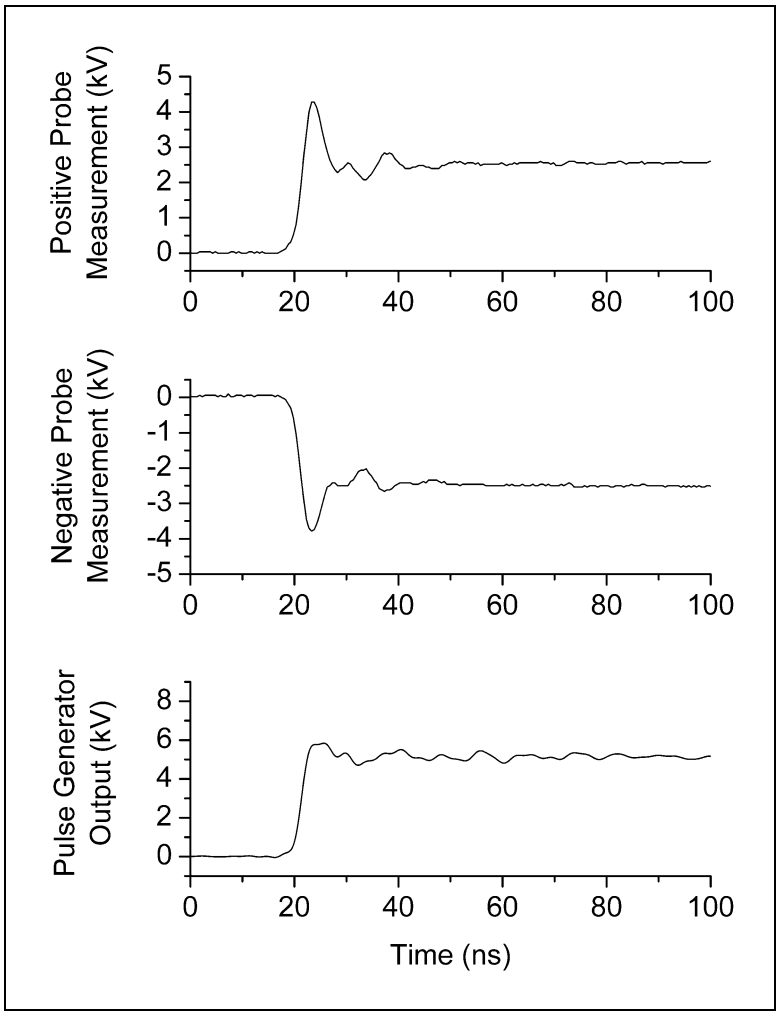

Figure 2.22. RTDGPR impulse generator output.

The output of the pulse generator was determined with a current probe. The measurements setup is shown in Figure 2.23 (tests conducted by C. Moulton, CICT, USGS, Denver, CO). A small inductive feed-through current sensor (Tektronics CT1) was used, which has a bandwidth of 1 GHz. The physical layout of the resistors and the current probe was kept as small as possible to avoid the effects of stray capacitance and inductance. The 300 ohm resistive load is similar to the load presented by the RTDGPR antenna. The voltage output from the pulse generator is the product of the measured current and the load impedance (300 ohms). This type of measurement should be made with caution to avoid damage to the pulse generator. Some generators cannot tolerate a purely resistive load, and require a series capacitance in the load to preclude damage. Figure 2.24 shows the RTDGPR antenna input impedance as calculated from FDTD simulation results (see Section 2.5.2), and also shows the waveform produced by the pulse generator as determined using the current probe and the oscilloscope probes. In both cases, the measured rise time is about 2.5 ns. These generator waveforms were used as a guide in specifying the integrated Gaussian waveform (rise time of 2.5 ns) that was used as the excitation for the FDTD simulations as described in section 2.5.2.

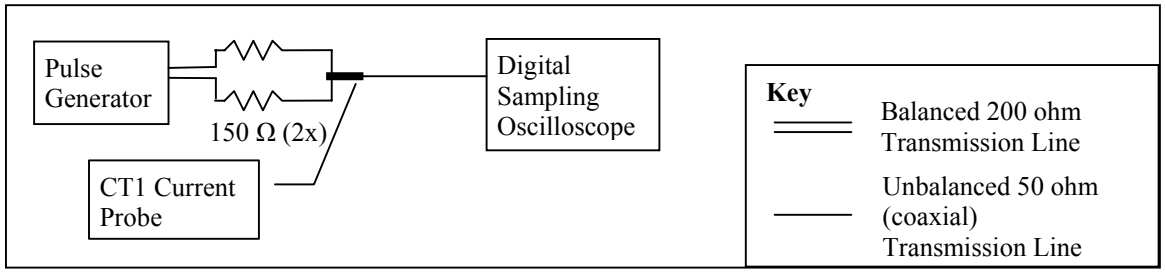

Figure 2.23. Setup to measure pulse generator output using a current probe.

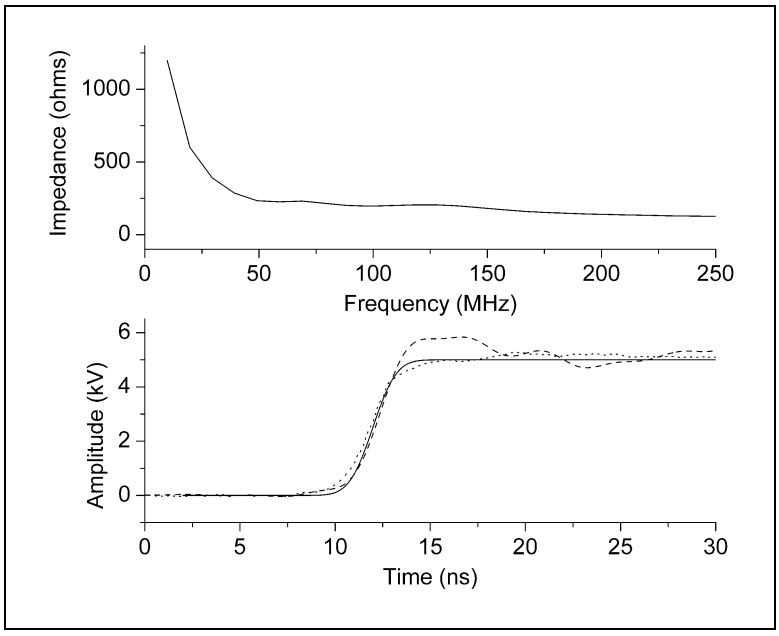

Figure 2.24. RTDGPR antenna input impedance and impulse generator output from current probe (dotted), high-voltage probes (dashed), and an integrated Gaussian with a 2.5 ns rise time (solid).

2.5 Determining the Antenna Response

There are many ways to determine the response of GPR antennas. A common method used in communications applications is to make field measurements around the antenna using an antenna range and an electric or magnetic field probe. Another method is to conduct computer simulations of the antenna response. Physical measurements are generally more accurate, but there are often logistical problems in conducting physical measurements with GPR antennas. Both methods are discussed in this section because both can be used to calibrate GPR antennas. The RTDGPR antennas were characterized using numerical simulations because their size and frequency of operation make physical measurements difficult. The numerical simulations were then verified by experiment.

2.5.1 Direct Measurement Methods

It is common practice to make measurements of antenna response in an antenna range. The measurements are often performed in the frequency-domain (Kerns, 1981; Hansen, 1999). The fields generated by the antenna under test (AUT) can be measured using B dot or D dot antennas (de Jongh, 2000). These antennas usually have a linear response over a wide range of frequencies with little distortion, and their response is easy to calculate. To conduct the measurements, an antenna range is required where no unwanted reflections (i.e. from the ground, walls, etc.) can influence the measurement. Therefore antenna ranges are usually quite large so that reflectors are far from the AUT, or reflectors are covered with an absorbing material to minimize reflections. The RTDGPR antennas are relatively large (60 cm high and 108 cm in diameter), and operate at a center frequency of about 50 MHz. At these frequencies, absorbing material is very bulky and expensive. If absorbing materials are not used, then the antenna range must be large enough so that signals generated by the antenna can be measured before any unwanted reflections arrive, which requires a very large range (~20 m) at these frequencies.

Another problem with antenna ranges is that they generally measure the response of antennas in air. Since the response of ground-coupled GPR antennas changes as a function of the material properties of the ground under the antennas, it is difficult to build an antenna range that adequately simulates changing ground conditions. Commonly, air, sand boxes, or water bodies are used to represent different ground conditions. These proxies are a very poor sampling of the range of material properties that can be encountered in GPR surveys. It is possible to simulate widely varying ground properties using various mixtures of water, salt, and acetic acid in a large tank. Acetic acid has a RDP of about six at 100 MHz and is miscible. Kaatze et al. (1991) describe the frequency dependent dielectric properties of mixtures of acetic acid and water. Unfortunately, very large tanks would be required for experiments with the RTDGPR

making this method impractical. This method is a viable option for higher frequency GPR systems and should be considered for these systems because physical measurements are usually more accurate then computer simulations.

Another method that has promise is based on the plane wave scattering matrix of an antenna (Kerns, 1981). Kerns discusses the interaction of two antennas and a scatterer with known properties. The response of this system can be completely determined if the response of each antenna has been completely determined in air. Determining antenna response in air is routine in the communications industry and is commonly referred to as near-field scanning. According to Hansen and Yaghjian, (1999), Kern's theory accounts for but does not provide quantitative information about the multiple interactions. Meincke and Hansen (2004) present a method to determine the system response of two GPR antennas over a half space based on this method. Although there may be difficulties with this approach due to the limited spectral response of the antenna in air (similar to the problem in determining the pulse generator response from the antenna response on page 42), it warrants further investigation.

It may be efficient to model the response of GPR antennas with rectangular or cylindrical shaped back shields using an iterative mode matching method. With this method, the natural modes in each region of the antenna are matched at the boundaries between each region. One region would contain the radiator, another the back shield, and another the space between the antenna and the ground. The biggest drawback to this approach is that there are few degrees of freedom to account for subtleties or non-ideal aspects of the physical antenna. The calculations could be made quickly, but they may not accurately represent the antenna response unless the antenna was very carefully constructed to conform to modeled geometry.

2.5.2 FDTD Simulations

Finite difference time-domain (FDTD) simulations are a popular method of simulating transient fields in regions close to antennas (Yee, 1966; Kunz and Leubers, 1993; Giannopoulos, 1997; Taflove and Hagness, 2000). This method was selected for the antenna simulations for several reasons. It is accurate and rather simple compared to other numerical techniques. A large body of published research exists discussing the method, and source codes are available so that specific modifications can be made if necessary. The accuracy of the FDTD method has been demonstrated by many published comparisons between FDTD results, analytical solutions, and physical experiments. For instance, Teixeira et al. (1998) presented a method to account for dispersive wave propagation using FDTD and compared the numerical results with the Sommerfeld solution. Several researchers report accurate results when using FDTD for the GPR problem. Bourgeois and Smith (1996) made FDTD simulations of a bi-static GPR antenna array over lossy ground and compared the results to the response of physical scale models. Lampe et al. (2003) compared FDTD simulations with experimental results for the input impedances of GPR bowtie antennas as a function of frequency. Lestari et al. (2001) compared the FDTD and method of moments numerical simulations of GPR bowtie antennas with theoretical results.

Even though accurate results have been published, the FDTD method has limitations and can give inaccurate results if certain guidelines are not followed. Several authors have discussed these errors. Buechler et al. (1995) investigated the sources of error in FDTD modeling when the simulated fields are close to a source and when the source is close to a material boundary. Bergmann et al. (1998) studied numerical dispersion that can result with FDTD simulations. Orthogonal grids are often used in FDTD codes because they are easy to implement. However, errors arise when objects with curved surfaces that do not conform to orthogonal grid boundaries are modeled. Finally, unwanted reflections from the edge of the FDTD modeled region can be

problematic if not treated properly. Taflove and Hagness (2000) discuss solutions to these difficulties.

2.5.3 RTDGPR Antenna Simulations

To determine the RTDGPR antenna response, the FDTD simulations were made for the antennas and the region near the antennas using the *GPRMax* program (GPRMax, 2004). The source code to *GPRMax* was obtained through a private agreement with the author. A small modification to *GPRMax* was made to record current density as well as the electric and magnetic fields at user specified locations. The entire suite of final simulations required about 10 weeks of run time on a 3 GHz Pentium Pro PC with 2 GB of RAM. Before the final suite of simulations was run, many pilot simulations were run with small changes to the model before reasonable accuracy in the simulations was obtained. For the simulations, a 1 cm grid interval was used, and the time step interval was 19. 25808 ps (according to the Courant criterion; see Taflove and Hagness, 2000). The grid interval was selected to be a tenth of a wave length, based on a maximum frequency of 300 MHz and a maximum RDP of 10 (Giannopoulos, 1997). The antenna geometry illustrated in Figure 2.25 was specified as accurately as possible using an orthogonal grid with a 1 cm grid interval. Details of the FDTD simulations and all of the model specification and result files can be found on the accompanying DVD ROMs (see Appendix C).

The RTDGPR antennas consist of resistively-loaded dipole radiators (Wu and King, 1965) with metallic back shields. Figure 2.25 illustrates the RTDGPR antenna geometry. The antenna frame is made of low density polypropylene. The interior of the electronics enclosure and the interior of the outer shell are shielded with 0.1 mm (0.00405 inches) thick copper foil except on the bottom of the antenna. The interior of the outer shell is filled with a radar absorbing material (graphite loaded foam) to attenuate

reverberations inside the shell. The dipole radiator is embedded in polypropylene. An RTDGPR antenna with the top removed is pictured in Figure 2.26. For the simulations, a transmitting antenna and a receiving antenna were offset laterally by either 113 or 173 cm (center to center); and both antennas were polarized perpendicular to the survey line (see Figure 2.27). These antennas and the (idealized) soil beneath them make up the three dimensional model space used in the FDTD simulations. The magnetic permeability was assumed to be unity in the simulations (and through this dissertation). It is also assumed that all materials used in the simulation, both in the antenna and the ground, are linear and isotropic.

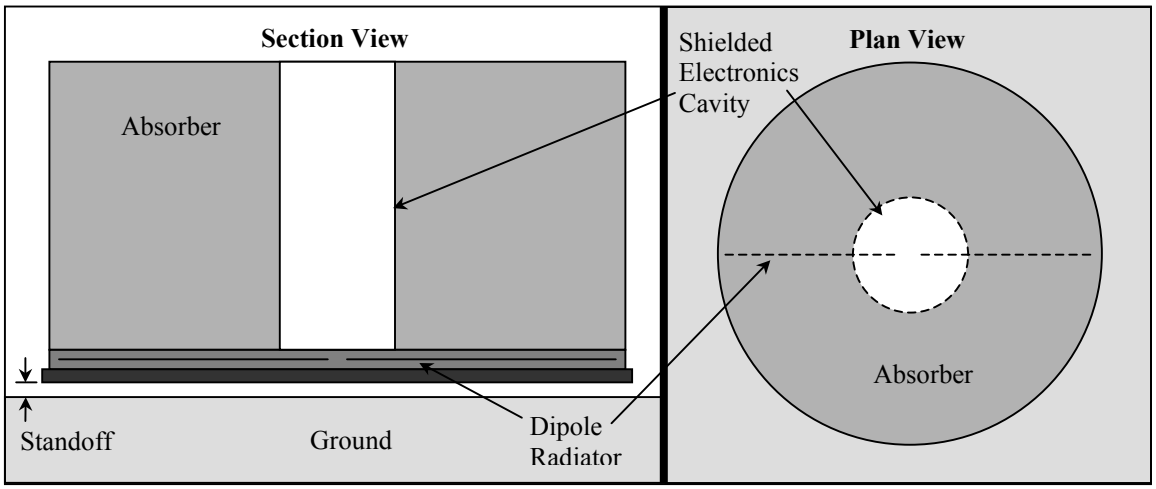

Figure 2.25. RTDGPR antenna construction. Left is section view and right is plan view (not to scale). The frame of the antenna is a polypropylene cylinder with a diameter of 110 cm and a height of 60 cm. The electronics cavity is a cylinder with a diameter of 25.4 cm and a height of 60 cm.

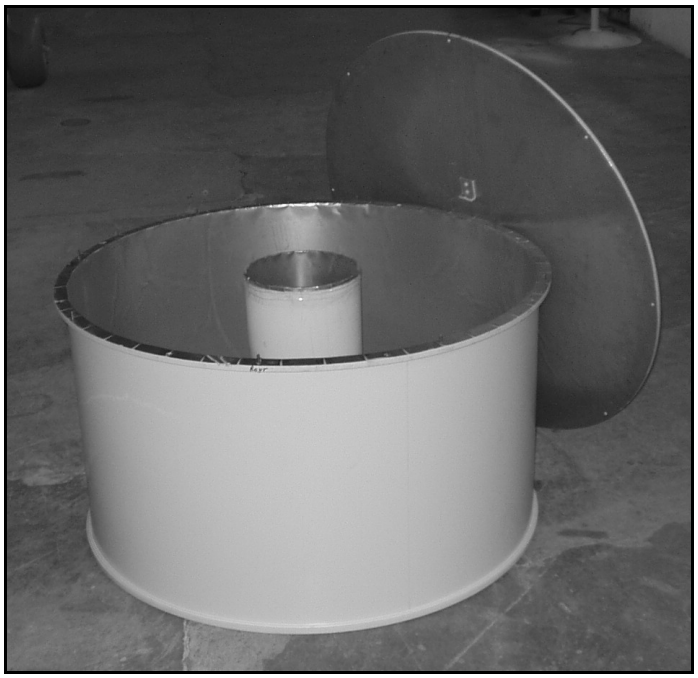

Figure 2.26. Picture of an RTDGPR antenna with top and absorber removed.

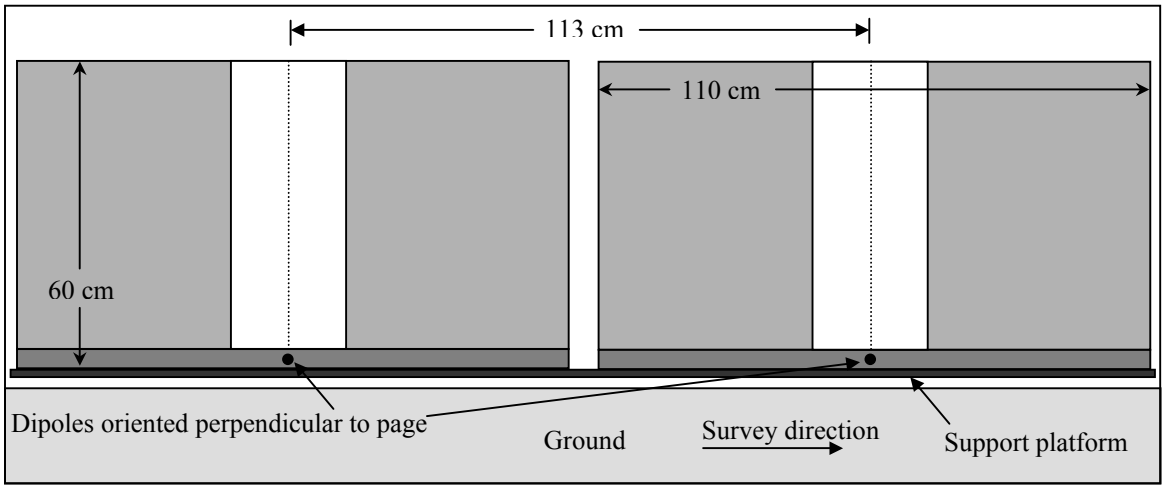

Figure 2.27. Section view of transmitting and receiving antenna orientation on survey cart. The antennas are identical (not to scale).

The RTDGPR antennas employ an approximation to a Wu-King (Wu and King, 1965) traveling wave dipole. The current distribution on a Wu-King traveling wave dipole linearly decreases to zero at the ends of the radiators. The Wu-King dipole is based on a continuously changing resistance so that no reflections from sharp impedance contrasts occur. The RTDGPR antenna approximates this resistance distribution using discrete resistors, therefore reflected waves from the dipole are possible at the feed port. Numerical simulations show that the current distribution along the radiator is nearly linear and the input impedance at the antenna feed port is essentially constant when the ground properties below the antenna change. Figure 2.28 shows the peak simulated current along one half of the RTDGPR dipole for an antenna height of 7 cm over a ground with a RDP of 25 and a conductivity of 10 mS/m. Figure 2.29 shows the simulated feed port current for the transmitting antenna with a 7 cm standoff above water ($\varepsilon_r = 81$, $\sigma = 0.049$ mS/m), and the transmitting antenna in air ($\varepsilon_r = 1$, $\sigma = 0$). Note that the current changes very little (a few percent) due to changing ground properties.

The simulated waveform at the feed port of the transmitting antenna was an integrated Gaussian step with a rise time of 2.5 ns (10% to 90% of peak value; see Figure 2.24). The integrated Gaussian was used rather than the pulse generator measurements to avoid adding noise to the simulated data. This waveform has a smoothly varying, broadly distributed frequency-domain representation (see Figure 2.1). The integrated Gaussian excitation readily lends itself to deconvolution without producing artifacts (in the frequency range of interest). Since the antennas are linear systems, the simulated fields at a subsurface point generated by the transmitting antenna can be calculated for any antenna excitation by deconvolving the original excitation from simulated results, and then convolving with the arbitrary excitation. Applying this procedure using *GPR Wave Utilities* produces excellent comparisons with simulated waveforms using different excitations; and the convolution method requires a few seconds rather than hours of calculation. The only requirement is that the spectral content of the deconvolved and convolved signals should be similar.

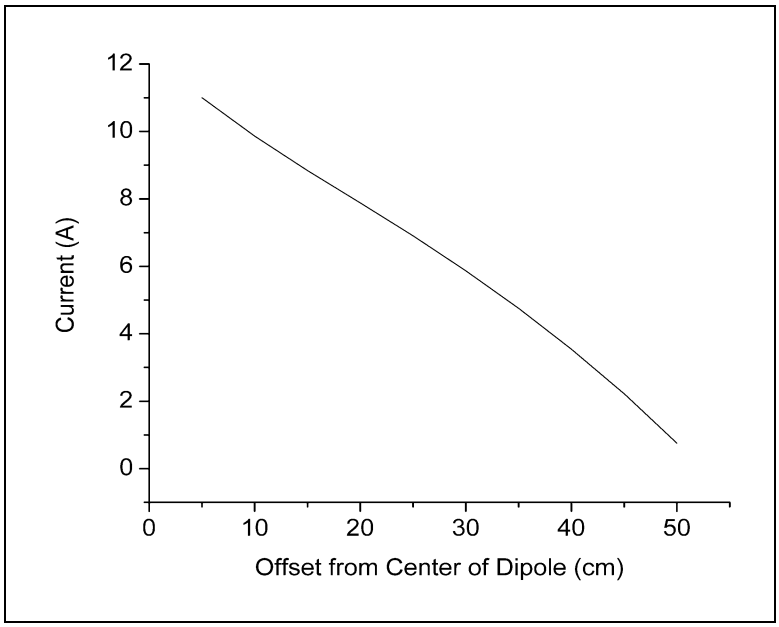

Figure 2.28. Peak current distribution along one half of the dipole radiator.

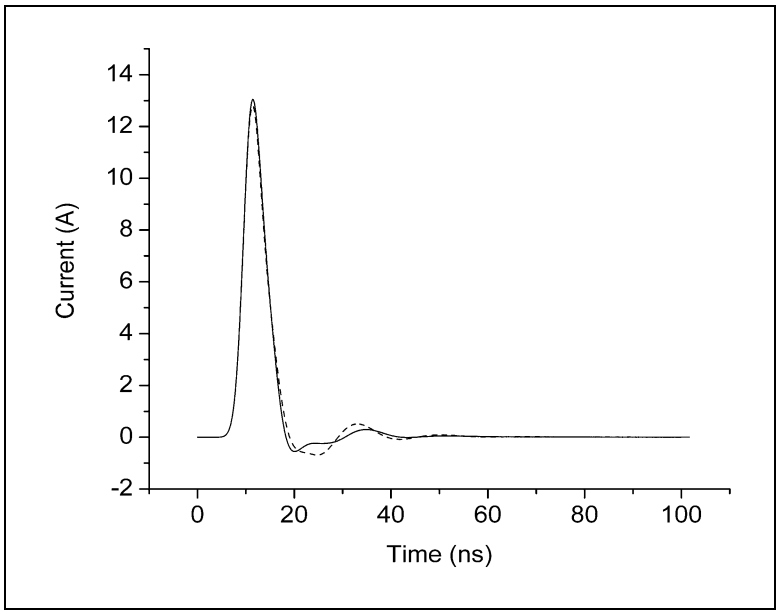

Figure 2.29. Feed port current for transmitting antenna over water (solid) and in air (dashed).

2.5.4 Experimental Validation of Simulations

Physical experiments were conducted to verify the results of the FDTD simulations. In all experiments, the antennas were co-polarized such that their H field planes were co-linear. The orientation of the E and H planes are depicted in Figure 2.30. The response of the antennas with and without the absorber was measured in each experiment. Photographs of the experimental setups are shown in Figure 2.31, and Table 2.2 lists the conditions used to collect measurements. For the first set of experiments, the antenna response was measured over water. A floating frame was constructed to support the antenna base plates and antennas. The frame was adjusted so that the antenna base plates were 7 cm above the water, which is the standard operating standoff for the antennas on land (see Figure 1.2). The floats were separated by about 2 meters, and the antenna polarization was orthogonal to the floats. The floating antennas were launched on a lake at the end of a dock in about 4 meters of water. The lake water conductivity was 49 mS/m (as tested with a galvanic conductivity probe). The surface panel and computer were operated from the dock, while the floating antennas were tethered about 10-15 meters away from the dock. There were no objects within a 10-15 meter horizontal radius from the antenna (both above and below the water). The second set of experiments measured the antenna response in air. The antennas and their base plates were placed on the ground so that their radiating apertures faced up into the air. The tests were conducted in a parking lot where the nearest vehicle was at least 25 meters from the antennas. The surface panel and computer were operated at a distance of about 15 meters from the antennas. The air and water 'half spaces' provided convenient homogenous media that bracket the range of conductivities and permittivities that would be encountered in GPR surveys.

Some processing steps are necessary before comparisons between simulated and experimental data can be made. The data directories on the accompanying DVD-ROM contain a detailed processing history file that describes each operation made, and an

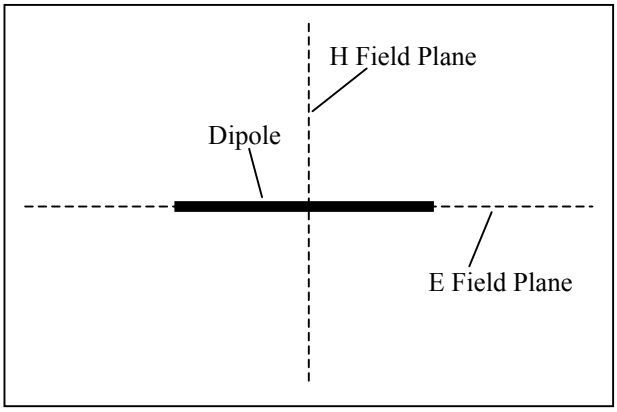

Figure 2.30. Plan view of E field plane and H field plane of a dipole.

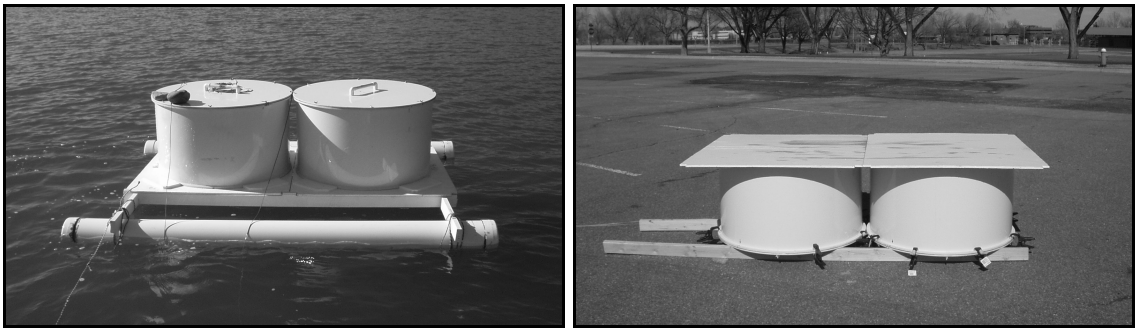

Figure 2.31. RTDGPR antenna tests with antennas radiating down into water (left), and radiating up into air (right).

Table 2.2. Conditions used in measuring the response of the RTDGPR.

Half Space Material	Antenna Offset	Antenna Absorber Used
Air	113 cm	Yes
Air	113 cm	No
Air	173 cm	Yes
Air	173 cm	No
Lake Water	113 cm	Yes
Lake Water	113 cm	No

overview is given here. Since the simulations only account for the antenna response, the simulated response must be convolved with the response of RTDGPR receiving circuitry described in Section 2.3 using *GPR Wave Utilities*. One of the primary goals is to be able to predict the waveforms of early arriving energy at the receiving antenna because these early waveforms will be used to predict the soil properties under the antennas (see Chapter 3). Therefore, the comparisons between simulated and experimental data will target the first 40 ns of the waveforms. To make the comparisons, *GPR Wave Utilities* processes the data as follows. First, the waveforms are aligned temporally at the largest peak in the early part waveforms. The waveform peak times can be picked using *GPR Wave Utilities* or by inspecting ASCII data files. A cosine squared taper centered at 40 ns is then used to eliminate late time energy. Next, attributes of the waveforms are extracted using one of two methods. The first method extracts the FFT spectral amplitudes at 10 MHz intervals to create a *Spectral* attribute set. The second method calculates the Hilbert envelope of the waveform (i.e. the modulus of the waveform and its Hilbert transform) and samples the envelope at 2 ns intervals to create a *Hilbert* attribute set. The use of other waveform attributes was investigated, but these results are not presented because these attributes are not used in the method to estimate ground properties (discussed in Chapter 3). Last, the simulated waveform attributes are scaled (see α below) such the RMS difference between simulated and measured waveform attributes is minimized. The normalized difference is calculated by

$$D = \frac{\sqrt{\frac{1}{J}\sum_{j}(p_{e,j} - \alpha p_{s,j})^2}}{\sqrt{\frac{1}{J}\sum_{j} p_{e,j}{}^2}} \tag{2.28}$$

where D is the difference, α is the scale factor, and $p_{e,j}$ and $p_{s,j}$ are the j^{th} of J attributes from the experimental and simulated waveforms respectively. The accuracy of a simulation is measured by examining the magnitude of the scale factor and also the RMS difference between attributes of the simulated waveforms and the experimental data. The

goal is to minimize the difference between waveform attributes and obtain scale factors near unity.

Specifying the antenna model for the FDTD simulations was straight-forward because most of the operating parameters and material properties were well known for the parts used in the RTDGPR antennas and electronics. However, there was some uncertainty as to the precise rise time of the pulse generator, the properties of the antenna base plates, and of the absorbing foam used in the antennas. These parameters were systematically varied until the simulated results most closely matched the experimental results. To eliminate the properties of the absorbing foam as a variable, the simulation results for changing pulse generator rise time and the base plate properties were compared with experimental data collected without absorbing foam in the antennas. The electrical properties of wood have a natural variability that is related to the amount of drying that occurred during processing. During the experiments, the plywood base plates absorbed water (even though they were painted), and therefore a rather high relative permittivity is plausible. Simulations were run for base plate RDP values of 4, 10, and 25, and for pulse generator rise times of 2, 2.5, 3, 4, and 5 ns. The optimal values are 25 for the base plate, and 2.5 ns for the rise time. The experimental and best match simulated waveforms are shown in Figure 2.32. The RMS difference between the experimental and simulated waveform attributes, and the relevant scale factors are listed in Table 2.3. Scale factors between 0.5 and 2.0 are reasonable since this corresponds to a few dB in error in the system response. The experimental waveforms from the antennas in air have late time arrivals at about 40 ns that are not present in the simulated waveforms. There were no above ground objects that could have caused these reflections, so they must be caused by some aspect of the antennas that was not modeled.

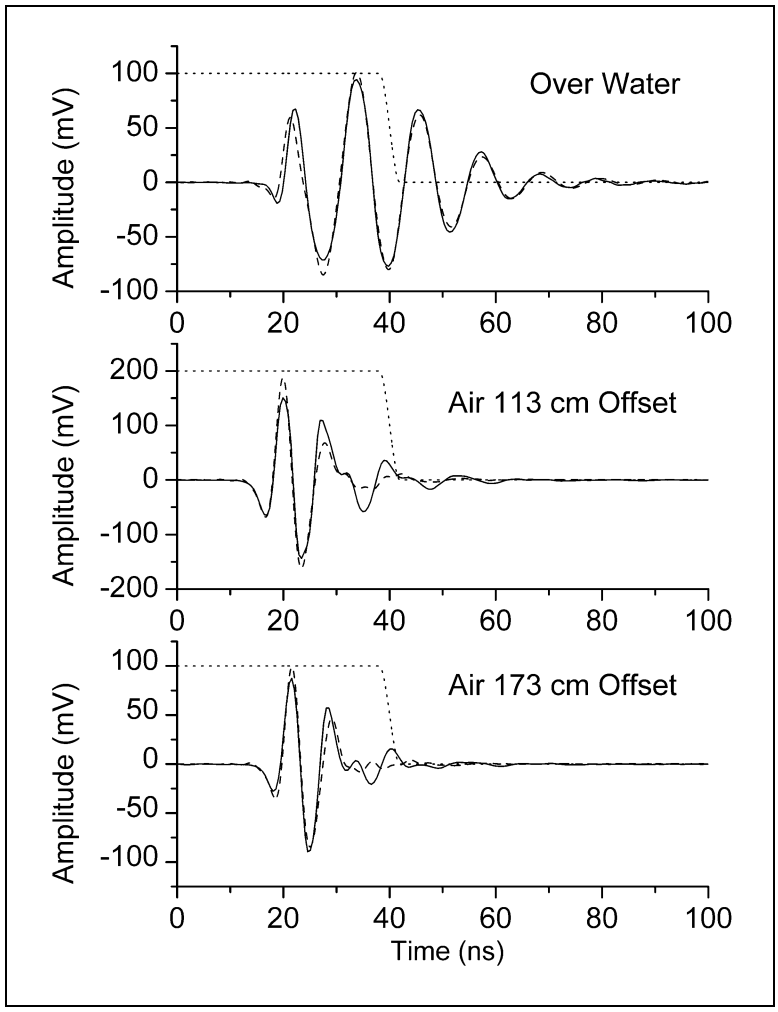

Figure 2.32. Comparisons between simulated response (dashed) and experimental response (solid) for antennas without absorbing foam. Amplitude of cosine taper is scaled for plot (dotted).

Table 2.3. Comparison of simulation and experimental results for antennas without absorbing foam. Comparisons were made using the *Hilbert* and *Spectral* waveform attributes.

Material/Offset (cm)	Waveform Attributes Compared	Amplitude Scaling (α)	RMS Difference (%)
Water/113	*Hilbert*	0.797	9.10
Water/113	*Spectral*	0.797	14.3
Air/113	*Hilbert*	0.423	27.6
Air/113	*Spectral*	0.423	18.5
Air/173	*Hilbert*	0.545	15.6
Air/173	*Spectral*	0.545	17.5

Transmission line tests (Kutrubes, 1986; Canan, 1999) were made using 14 mm by 10 cm GR-900 sample holders to determine the frequency dependent electrical properties of the absorbing foam. The electrical properties were modeled using a Debye single relaxation model

$$\varepsilon(\omega) = \varepsilon_{\infty} + \frac{\varepsilon_{dc} - \varepsilon_{\infty}}{1 + i\omega\tau} \tag{2.29}$$

were ε_{dc} is the zero frequency permittivity, ε_{∞} is the permittivity at infinite frequency, and τ is the relaxation time. Unfortunately, simulations using the Debye representation (Olhoeft, 1985) of the foam properties determined from the transmission line tests were a poor match to experimental data (see Table 2.4 and Figure 2.33). Since the antenna response without the absorbing foam matched experimental results much better, it was concluded that the results of the transmission line tests were not indicative of the actual absorber properties. This is likely due to the small sample size tested using the GR-900 sample holders. The sample holder annulus is about 4 mm, which is about the same size as the pores in the foam. Further, the foam manufacturing process does not accurately control the amount of graphite (the part of foam providing the loss) used in each foam sheet, therefore the spatial variation in electrical properties could vary significantly. The *GPRMax* FDTD code only provides for a Debye relaxation when specifying material

Table 2.4. Material properties of absorbing foam measured in the laboratory and used for simulations.

Condition	$\varepsilon_{dc}/\varepsilon_0$	$\varepsilon_\infty/\varepsilon_0$	τ (ns)	σ (mS/m)
Lab Test	5.5	2.5	3	3.6
Simulation	12	6	2.5	7
Simulation	10	4	4	4
Simulation	11.5	5.5	2.5	8
Simulation	13	7	4	9

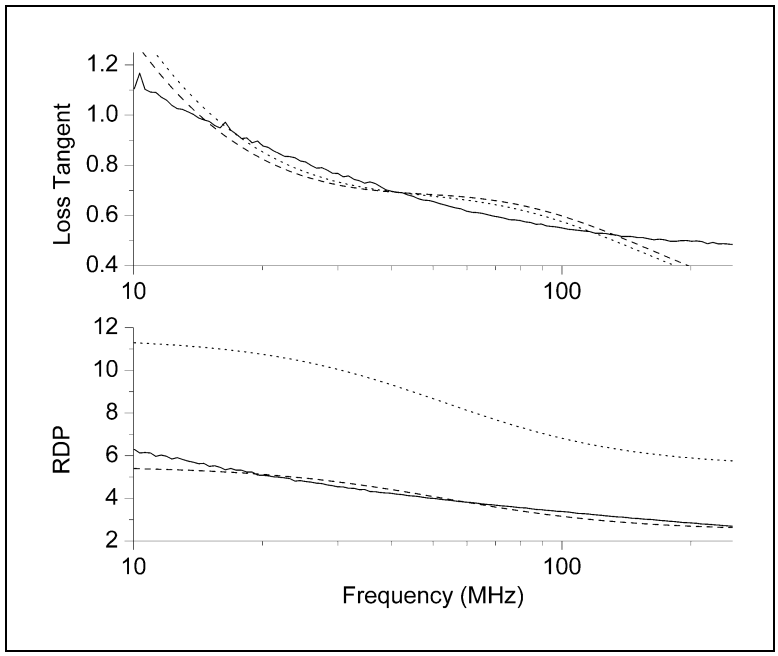

Figure 2.33. RDP and electric loss tangent for laboratory test (solid) of absorbing foam properties, and Debye model used in simulations. Dashed line is the Debye model corresponding to laboratory test, and dotted line is the Debye model used in the simulations.

properties, and the Debye model does not fit the actual material properties as well as the Cole-Cole model (Olhoeft, 1985). However, this is not the main reason for the inaccurate simulations. It is likely that measured absorber permittivity is too low because the frequency content of the simulated waveforms is too high. Therefore, the absorber permittivity was increased such that the loss tangent remained similar to the values obtained in the transmission line test. Simulations using several Debye permittivity distributions for the foam were made (see Table 2.4). The Debye model with $\varepsilon_{dc} = 11.5$ resulted in the best match in the first 40 ns of data. The waveforms plotted in Figure 2.34 show the difference between simulated and experimental response after adjusting the absorber permittivity to achieve a better match. The RMS difference between the experimental and simulated waveform attributes, and the relevant scale factors are listed in Table 2.5. There is late time discrepancy between the experimental and simulated results. The dispersion in the experimental waveforms is not properly reflected in the simulations. This is likely due an inadequate specification and/or determination of the absorber properties. The Debye relaxation model does not effectively represent the absorber properties. Despite this shortcoming, the comparison is reasonable in the time window of interest (i.e. the first 40 ns).

Table 2.5. Comparison of simulation and experimental results for antennas with absorbing foam. Comparisons were made using the *Hilbert* and *Spectral* waveform attributes.

Material/Offset (cm)	Waveform Attributes Compared	Amplitude Scaling (α)	RMS Difference (%)
Water/113	*Hilbert*	0.370	18.8
Water/113	*Spectral*	0.369	6.80
Air/113	*Hilbert*	0.319	20.7
Air/113	*Spectral*	0.319	16.4
Air/173	*Hilbert*	0.351	6.98
Air/173	*Spectral*	0.351	8.98

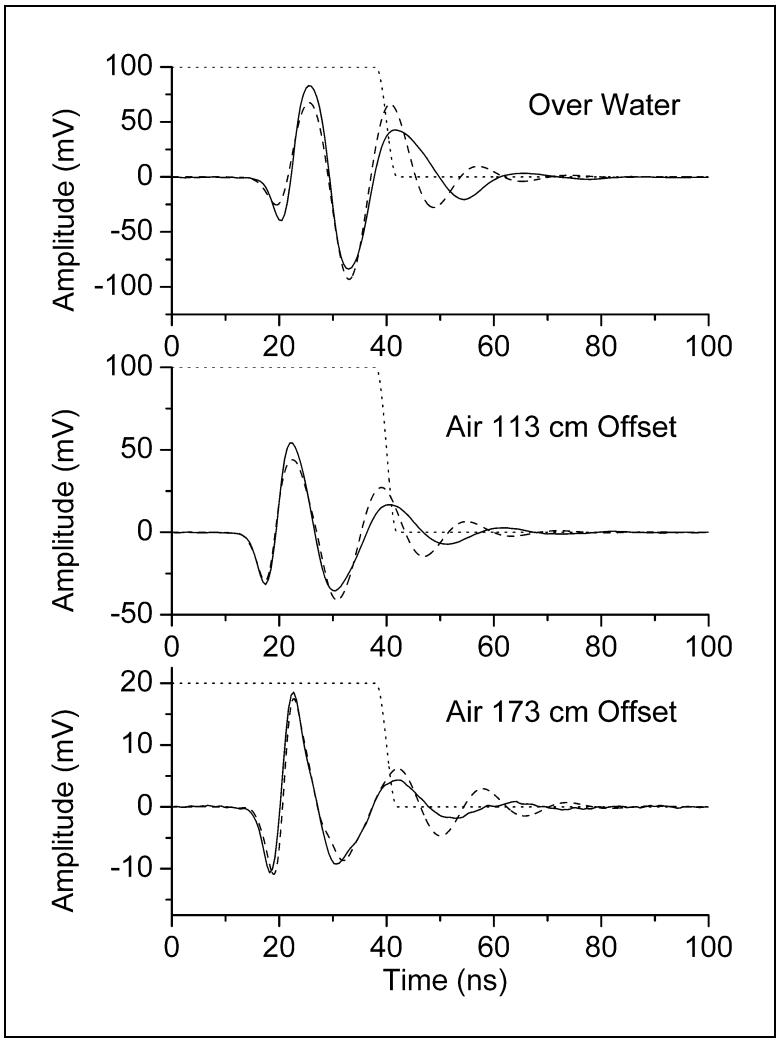

Figure 2.34. Comparisons between simulated response (dashed) and experimental response (solid) for antennas with absorbing foam.

There are many reasons for the differences between the experimental data and the simulated response. The RTDGPR is not a simple system like a dipole in air as treated by many researchers who report accurate FDTD results (see Section 2.5.2). Lee et al. (2004) made FDTD simulations for geometrically complex GPR antennas. They measured the response of co-located cross-polarized GPR antennas over sand, and report differences as large as 10 dB (a factor of more than 3) between experimental measurements and FDTD simulations. Every reasonable effort was made to make the simulated antenna identical to the physical antenna, but this simply cannot be achieved in practice. The dimensions of the antennas are not in whole centimeter increments as were specified in the simulations. Further, there is small scale structure in the antennas that could not be modeled due to the size of the FDTD grid cells such as gaps and seams between parts. The feed port could not be accurately modeled using a one centimeter grid. Conducting rods, wires, and resistors were simulated as being infinitely thin. A slot was cut in the polypropylene to accommodate the wire dipole, which was filled with a material with properties similar to but not the same as the polypropylene. The degree to which the system response changes as a function of environmental variables such as temperature and humidity is unknown. The water surface during the experiments had small waves and was not planar. The absorbing foam properties are not well known. The curved surfaces in the antenna were not accurately modeled with the Cartesian grid used in *GPRMax*. There are inaccuracies in the pulse generator waveform estimate, with the receiving electronics transfer function, and the actual FDTD antenna simulations. The cumulative effects of these differences between the actual antennas and the simulated models may be significant. In considering the above reasons for differences, it is concluded that the amplitude scale factors listed in Tables 2.3 and 2.5 are as near to unity as reasonably achievable.

A number of consistency checks have been made to insure that the simulations are providing results that are principally correct. GPR antenna simulations over a half space using *GPRMax* were compared to equivalent simulation results using a commercial

FDTD program called *XFDTD* (Remcom, Inc., State College, PA). XFDTD is a mature product with a large user base. There is very little difference (less than 1%) between the results. *GPRMax* simulations of simple current filament sources and dipoles have been compared favorably with their analytic solutions (Giannopoulos, 1997). Simulation results from *GPRMax* executables compiled for Linux and Windows give the same results. The simulated results have a reasonable propagation delay between the transmitting antenna and the receiving antenna. And finally, the simulations show significant changing character of the simulated waveforms due to changing soil conditions as is expected.

A detailed sensitivity analysis of the system response to model parameters has not been made. It would be a huge undertaking to calculate the change in each waveform parameter due to the change of each model parameter because the number of components is large. The investigations do show that the RMS change in the calculated waveform versus rise time of the pulse generator is about 5% per nanosecond change in rise time as calculated using Equation 2.28. Figure 2.35 shows the response for integrated Gaussian waveforms with rise times varying between 2 and 5 ns. Although the waveforms have different amplitudes, they are all quite similar in character. The change in the simulated waveforms due to different antenna base plate properties is about 5% when changing the base plate RDP from 10 to 25. A more exhaustive investigation into the material properties of the unknown antenna components could be made. However, the specification of model parameters can become subjective, and a significant reduction in the differences between the simulated and experimental results would require a large effort. A computer model based on known physical properties and dimensions can be more confidently extrapolated to scenarios beyond the verified configurations than a model adjusted with no physical basis to affect a better fit to the verification configurations.

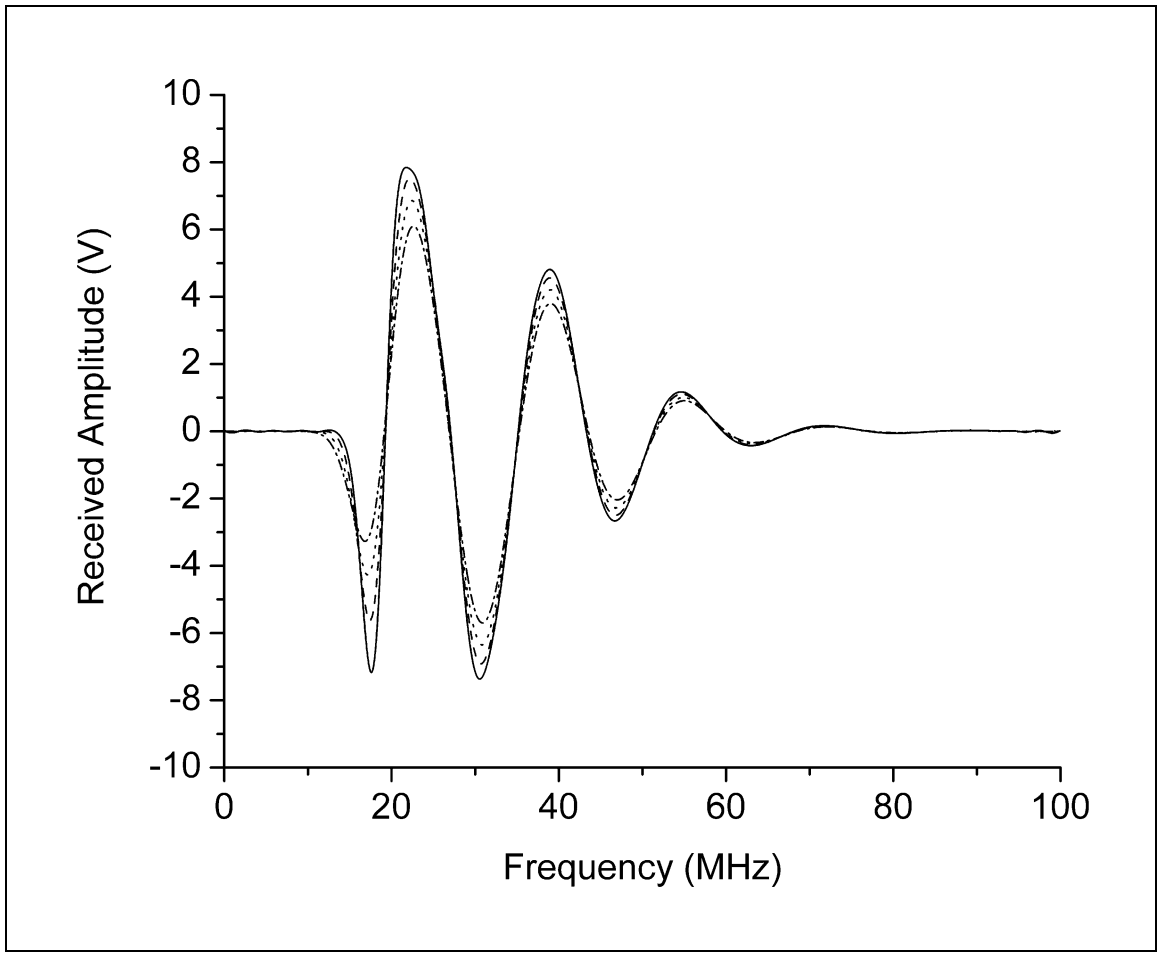

Figure 2.35. Effect of changing pulse generator rise time for antennas in air. Rise times are 2 ns (solid), 3 ns (dotted), 4 ns (dashed), and 5 ns (dash-dot).

2.6 Simulated System Response

Two sets of numerical simulations were made over a range of different ground properties to determine the system response under different conditions. The center-center antenna offset was 113 cm for the first set, and 173 for the second set. Since RDP values higher than about 25 are not common for soil types with conductivities low enough for GPR surveys (wet coal is an exception, see Chapter 1), ground permittivity values greater then 25 were not simulated. Different vertical standoffs (i.e. distance between the bottom of the antenna and the ground) were also simulated. The goal was to sample the range of permittivity, conductivity, and standoff values commonly expected in survey work. All combinations of the permittivity, conductivity, and standoff listed in Table 2.6 were simulated, with RDP ranging from 4 to 25, and conductivity ranging from 0-50 mS/m. Appendix D contains plots of the waveforms at the receiving antenna port for each of these combinations. The accompanying DVD-ROM contains all of the *GPRMax* configuration files required to make the FDTD simulations as well as the results (see Appendix C).

Table 2.6. Parameter values used in the FDTD simulations. All combinations of these values were simulated.

Relative Permittivity	Conductivity (mS/m)	Standoff (cm)
4 (dry sand)	0 (173 cm offset only)	2
9 (moist sand)	10	7
16 (wet sand)	20	12
25 (saturated sand)	30	
	50	

2.7 Effects of Ground Properties on Zero Time

One of the biggest problems in characterizing the response of GPR systems is the temporal drift between the pulse generator fire time and the digitizer time base. Temporal drift causes the time between the start of the recorded trace and the time the transmitter fires to change – often during a survey. This causes problems when trying to process and interpret the data. A sensing circuit has been implemented with the RTDGPR to sense the time the transmitted pulse arrives at the transmitting antenna feed port. This circuit is needed because the propagation delay of timing signals in the electronics and cables changes due to variations in operating and environmental conditions such as temperature, humidity, battery voltage, etc. These variable delays are not accounted for in many commercial instruments. Many practitioners of GPR use the first-break time (or a constant offset from this time) of the first arriving waves to determine time zero for data processing. The FDTD simulations conducted for this study (see plots in Appendix D) show that for a constant antenna offset, the time between the pulse arrival at the transmitting antenna feed port and the first arrival time at the receiving antenna varies as a function of antenna standoff and ground properties. These variations are likely due to the changing velocity of the traveling waves on the antenna radiators and changing coupling between the antennas due to changing ground properties. These variations must be accounted for when using equipment that is not synchronized with the transmitted pulse arrival time at the transmitting antenna feed port, or with another event such as the pulse arrival time at the ground surface. FDTD simulations can be used as a basis for accounting for these variations.

It is often erroneously assumed that the first break time (or a constant offset from this time) reflects the time when the transmitted waves enter the ground. Precision surveys for target depth should consider a more proper reference for time zero. A logical reference time is when the transmitted waves leave the near-field region of the antenna. This reference time can then be corrected for the ray path propagation time through the

near-field region, and the ray path propagation time between the antennas and the ground surface. The RTDGPR FDTD simulations indicate that the time offset between pulses arriving at the transmitting antenna feed port, a subsurface location, and the receiving antenna feed port varies beyond the above ray path propagation times as a function of ground properties and antenna standoff. This point is illustrated in Figure 2.36, which shows pulses arriving at the receiving antenna feed port and a subsurface point one meter below the transmitting antenna for different ground properties and antenna standoff. The time scales on these plots are synchronous with the pulse arrival time at the transmitting antenna feed port (the inflection point of this pulse is at 10 ns). The subsurface field times have been adjusted for the velocity difference between the two media and the standoff difference. Note that the first arrival times of the received waveforms are not a constant offset from the leading edge of the subsurface electric fields. Additionally, there is an offset between the first break of the subsurface fields. Proper characterization of the antennas, and knowledge of the soil properties and antenna standoff will allow these changing time offsets to be accounted for.

There are several reasons for these time offsets. First, by varying the soil properties and the height of the antennas above the ground, the phase velocity of the currents on the dipole change due to loading of the antennas. This causes a soil dependent time offset between the time a pulse arrives at the transmitting antenna feed port and the time the pulse is radiated from the phase center of each element of the dipole. A reciprocal phenomenon occurs at the receiving antenna. Second, the travel time of early arriving waves at the receiving antenna (assuming a bi-static array) that have been reflected and refracted by the ground surface depend on antenna height and soil properties. Finally, distortion and extensional dilation of the transmitted wave packet by dispersive media can also cause similar effects.

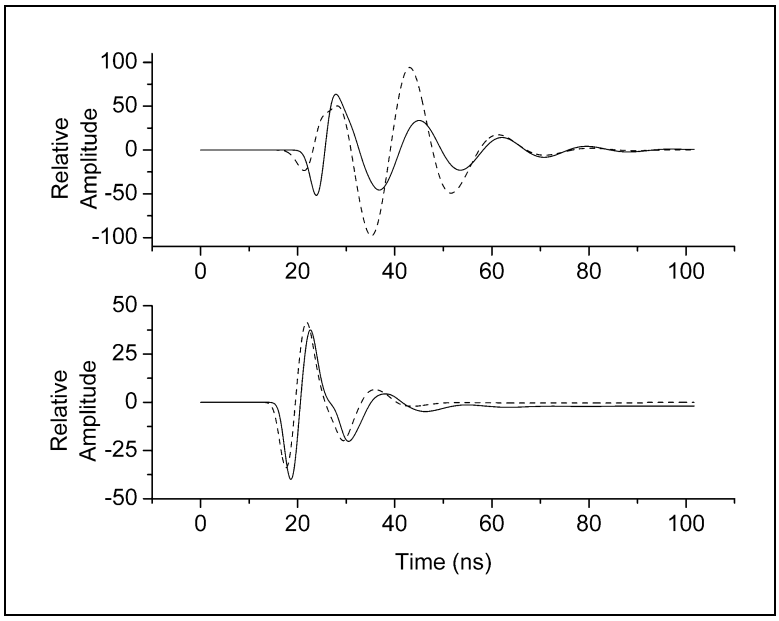

Figure 2.36. Illustration of changing first arrival times with changing ground properties and standoff. Top graph shows first arrivals at the receiving antenna feed port for $\varepsilon_r = 4$, $\sigma = 0$, $d = 2$ cm (solid), and $\varepsilon_r = 25$, $\sigma = 0$, $d = 12$ cm (dashed). Bottom plot shows the corresponding electric fields one meter below the ground surface after corrections for propagation time differences. The antenna offset was 173 cm.

CHAPTER 3

ESTIMATING THE SOIL PROPERTIES

3.1 Background and Previous Work

This chapter describes a methodology to estimate the properties of the ground directly beneath a bi-static antenna pair. Because the shallow ground properties strongly influence the response of ground-coupled antennas, a fundamental part of predicting the antenna response includes estimating these properties. The inverse model for soil properties (IMSP) algorithm estimates these ground properties using the early-time waveforms of energy received before reflections from subsurface objects arrive. For each antenna location in the survey, the algorithm provides estimates of the soil's RDP (ε_r), conductivity (σ), and the standoff (height) of the antennas (d) above the ground. The algorithm is based on the FDTD simulations described in Chapter 2 and Appendix D, which describe the antenna system response for the range of soil properties expected in most surveys. The IMSP algorithm requires a forward operator that predicts attributes of the received waveforms as a function of the model parameters (ε_r, σ, d). For this dissertation, forward operators were constructed for both the 113 and 173 cm offset co-polarized antenna arrangements for the RTDGPR, where the antenna polarization is transverse to the survey line. It is quite feasible to construct forward operators for other arrangements and other radar systems as well.

This IMSP method provides reasonable estimates of the ground properties in many situations, however it is unable to provide satisfactory results in all situations. Rough surface scattering, volume scattering, heterogeneities, magnetic soil, changing antenna attitude over an undulating surface, and anisotropic soils are deviations from ideal circumstances. For example, consider a survey using the RTDGPR. Because the

RTDGPR antennas are towed on a three-wheeled cart (see Figure 1.2), when the cart is driven over an undulating surface, the standoff value under the antenna will not be constant. Curved and rough surfaces negatively affect the results. The effects of adverse survey conditions are discussed in more detail in Section 3.4.

Previous efforts (Fisher et al., 1992; Arcone et al., 2003) to estimate the ground properties under GPR antennas are based on measurements made with multiple antenna offsets (i.e. horizontal distance between antennas). When using a large offset (i.e. greater than a wavelength), attributes of the surface-wave arrivals such as arrival time and amplitude can be used to estimate the permittivity and conductivity of the ground. In some cases, large offsets allow the surface waves to be distinguished from the many other early arriving waves at the receiving antenna. Oftentimes however, data at several offsets are needed to be able to clearly extract the refracted wave. Unfortunately, large offset measurements are undesirable in lossy media because larger offsets reduce penetration depth by increasing the distance waves must travel between antennas. Alternatively, multiple offset data can be used for amplitude versus offset (AVO) processing of reflected waves. AVO processing can estimate the material properties of some reflectors (Zeng at al., 2000; Jordan and Baker, 2002). Generally, multiple offset methods are unattractive because acquiring these data sets is quite time consuming or requires expensive multi-channel equipment. Soil properties determined with large and multiple offset methods may not represent the properties that affect antenna response because of large scale measurements and averaging effects of these methods. The IMSP method presented below has a smaller scale of measurement that is more sensitive to the actual region affecting the antenna response.

Calibrated air-launched antennas have also been used to estimate soil properties through the analysis of the signal reflected from the ground (Olhoeft and Smith, 2000; Lambot et al., 2004a; and Lambot et al., 2004b). Accurate calibrations can be achieved because air-launched antennas are not affected by changing ground properties. However, air-launched antennas are not optimal because they do not transmit as much energy into

the subsurface as ground-coupled antennas, and maximizing the energy transmitted into the ground is very important in dispersive environments.

Ground properties can also be estimated using ground-coupled standing wave dipoles. Wakita and Yamaguchi (1996) showed how the input impedance of a standing wave dipole over a lossy half space varies as a function of changing ground properties, but they did not consider a variable antenna standoff (height). Standing wave dipoles are not effective impulse antennas, and consequently impulse radars commonly use traveling wave antennas. Since the input impedance of traveling wave antennas changes much less due to changing ground properties, the standing wave dipole method is not applicable to impulse radars. In considering the above options, it is concluded that a method to estimate the soil properties that affect antenna response should be based on the small-offset bi-static ground-coupled antenna array – especially when lossy soils are present.

The early arrivals at the receiving antenna for a small-offset bi-static ground-coupled antenna array are complicated due to the interference of many waves arriving at similar times from different paths (see Figure 3.1). These waves include direct waves, reflected waves, multiples, lateral and/or evanescent surface waves, reactively coupled energy, and reverberations within the shields. The FDTD simulation results described in Chapter 2 and Appendix D indicate that early arrivals show good sensitivity to changes in ground properties, but the relationships between ground properties and the wave shape are not straightforward. Waveform attributes such as arrival time and amplitude do not change in a simple monotonic manner over the range of permittivity and conductivity values expected for most soils. However, Oden et al. (2005) showed that the amplitude of certain spectral components of the received waveforms have a reasonable sensitivity with the ground properties. The work presented in this Chapter builds upon this early work.

The early arriving energy at the receiving antenna is a combination of several energy transfer mechanisms or components, and a conceptual understanding of these mechanisms is useful when considering the results in the following Sections. The

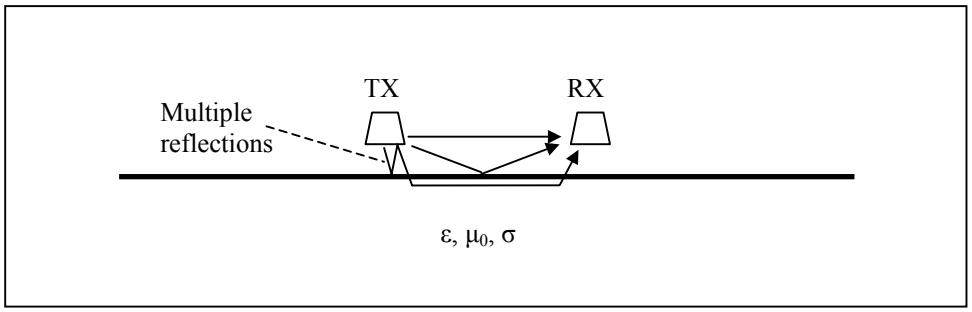

Figure 3.1. Diagram showing direct, reflected, and surface waves between transmitting and receiving antennas. Multiple reflections can be significant between the antennas and the soil surface.

response of each component changes differently due to changing standoff and ground properties and is discussed here according to first principles. The frequency response of a traveling wave dipole depends on the admittance and impedance per unit length along the dipole. Furthermore, closely spaced antennas have a mutual impedance (inductance) and admittance (capacitance). For a given antenna standoff, the admittance and impedance of the dipole, and the mutual impedance and admittance between the antennas will vary monotonically with changing ground properties. As a crude approximation, the effect of the ground on these coupling mechanisms decreases with increasing standoff as $1/d$ where d if the distance from the ground. This crude approximation is based on a loose analogy between antennas with conductive radiators (i.e. dipole elements) and simple charge distributions above a planar conductor. The resistive loading on the dipoles reduces the sensitivity of the mutual impedance to changing standoff and ground properties. According to these principles, the amplitude of the reactively coupled early arrivals should change monotonically with changing soil properties and standoff.

Another component of the early arrivals is reflected waves from the ground surface. These waves likely have one of the biggest effects on the received waveform. A crudely analogous problem is the reflection of waves at an interface over two horizontal layers. For this analysis, the incident and reflected wave fields are decomposed into

transverse electric (TE) and transverse magnetic (TM) wave components (see Figure 3.2). This is relevant because all waves propagating in a given plane of incidence can be decomposed into TE and TM components (Balanis, 1989). Figures 3.3 and 3.4 show the TE and TM reflection coefficient for this three layer problem, where the upper medium (i.e. the antennas) properties were $\varepsilon_r = 9$, $\mu_r = 1$, and $\sigma = 10$ mS/m (similar to the absorbing foam properties), the middle layer is air, and the lower layer is soil with various properties as indicated in the Figures. The air layer is 7 cm thick, and the outer layers are infinitely thick. In this analogy, the transmitting and receiving antennas are part of the absorber layer shown in Figure 3.2. This crude analogy does not consider inhomogeneous waves incident on the interface, which certainly occurs due to the proximity of the source (i.e. the dipole). This analogy does show that the reflection coefficients change markedly due to changing ground properties and angle of incidence. The waves incident on the receiving antenna will have reflected from a broad range of angles, with more emphasis on larger angles. For a given incidence angle, the changes in amplitude of the reflection coefficients are generally monotonic over ranges of soil

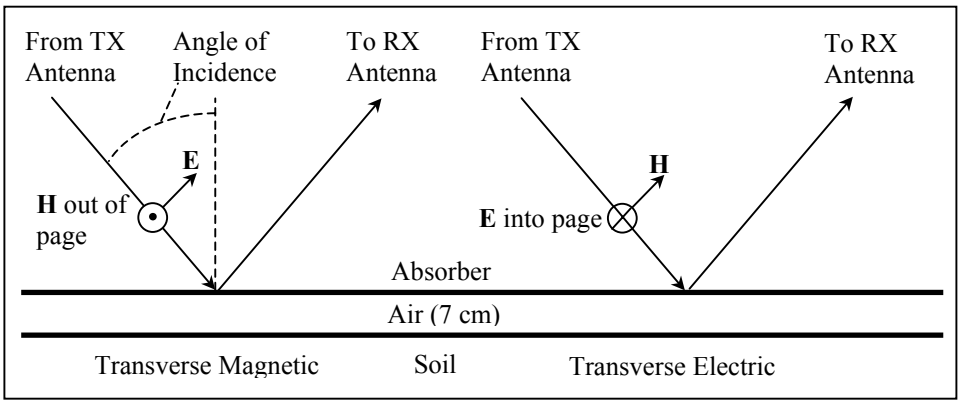

Figure 3.2. Transverse magnetic (TM) and transverse electric (TE) polarizations in the plane of incidence.

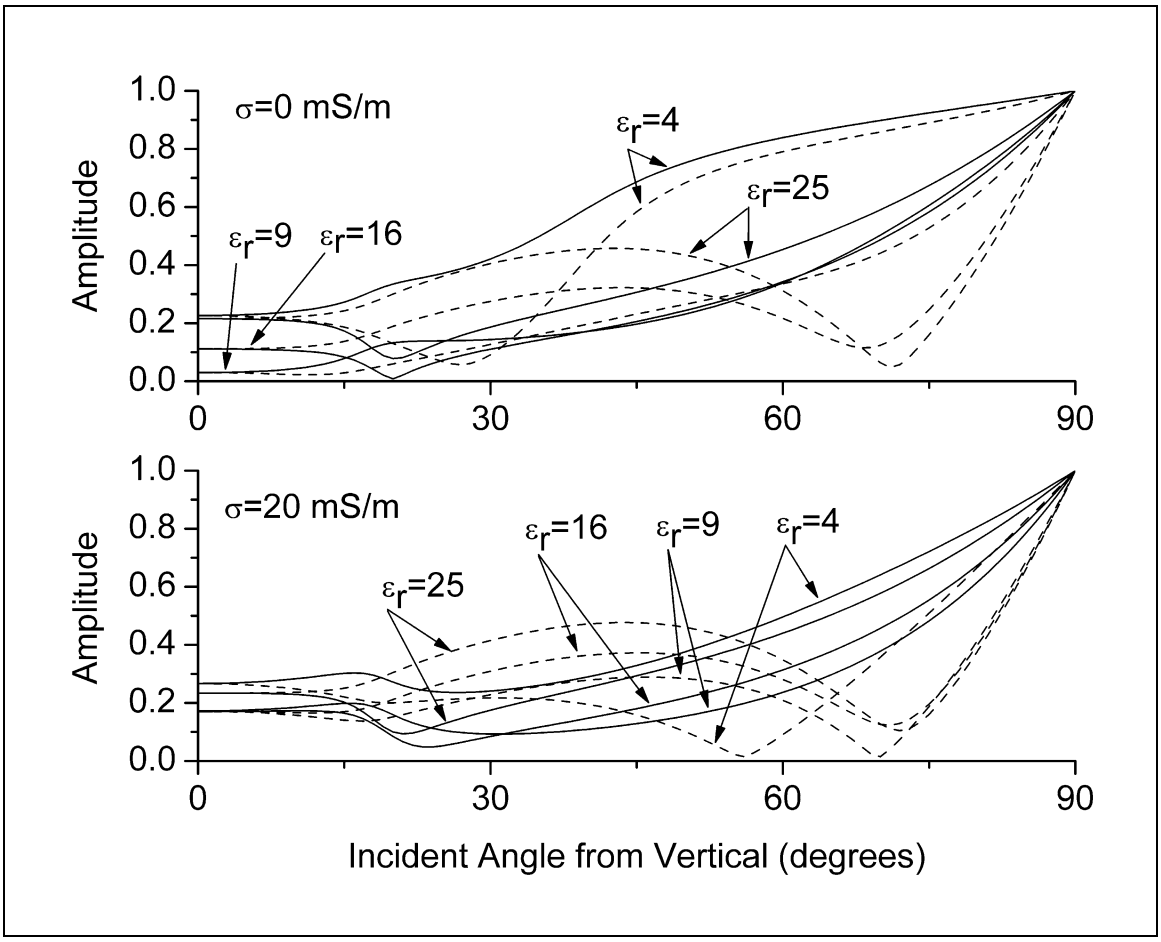

Figure 3.3. Reflection coefficients between antenna and soil with various RDP values. Both the TE component (solid) and the TM (dashed) components are shown. For a given incidence angle, the changes in amplitude of the reflection coefficients are generally monotonic over ranges of soil properties that do not include the absorber properties (ε_r = ~10 and σ = ~10 mS/m).

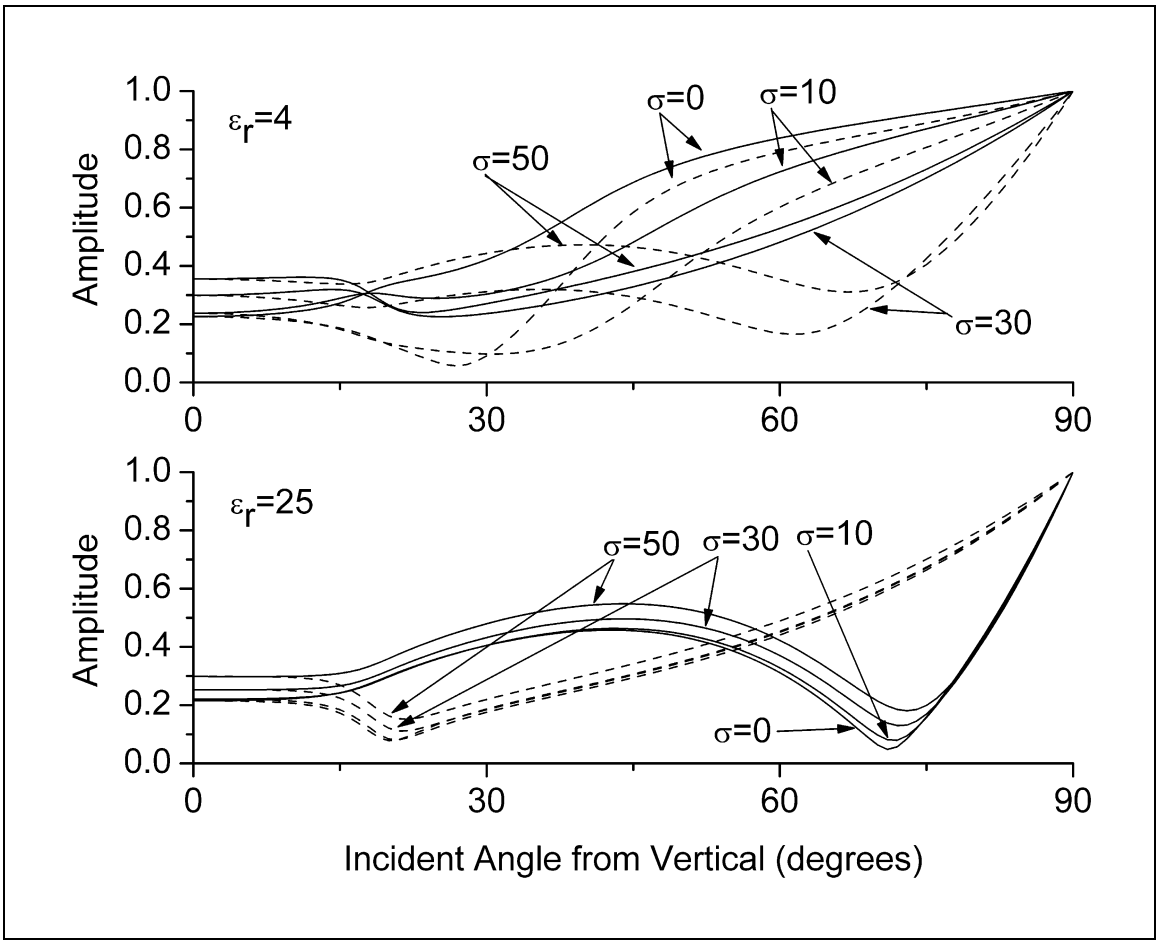

Figure 3.4. Reflection coefficient between antenna and soil with various conductivity values. Both the TE component (solid) and the TM (dashed) components are shown. For a given incidence angle, the changes in amplitude of the reflection coefficients are generally monotonic over ranges of soil properties that do not include the absorber properties (ε_r = ~10 and σ = ~10 mS/m).

properties that do not include the absorber properties. Further analysis (not shown) indicates that the changes in amplitude of the reflection coefficients versus standoff are monotonic and approximately linear over the 2-12 cm standoff range. Multiple reflections (see Figure 3.1) between the antennas and the ground may result in a significant contribution to the received waveforms, especially when the mismatch between the antennas and the ground and the standoff are large.

The only energy path between transmitting and receiving antennas over a homogeneous half space that can be sensitive to the subsurface must incorporate surface waves. This path must pass through the air-soil interface twice before reaching the receiving antenna. Since $1+\Gamma=T$ (where Γ and T are the reflection and transmission coefficients respectively), the contribution from the surface wave path will behave in a similar manner as the reflected waves. The phase along the surface wave path will change in a monotonic fashion with changing ground permittivity, and the amplitude of the received waves will vary in a manner similar to that of the reflection coefficients.

3.2 Constructing the Forward Operator

The IMSP routine uses attributes of the waveforms recorded by the GPR in order to reduce the dimensionality of the problem. Rather than directly using hundreds of sampled points from the relevant portion of the recorded waveform, a description of the waveform of approximately 20 attributes is used. Reducing the dimensionality makes a real-time inversion algorithm possible. The forward operator used in the IMSP routine provides a set of waveform attributes as a function of the RDP, conductivity, and antenna standoff above the ground (i.e. the model parameters). The recorded and simulated waveforms must be standardized before extracting waveform attributes for processing with the IMSP algorithm. This process is outlined in Figure 3.5. The first step is to temporally align the waveforms with respect to the excitation pulse. For all FDTD

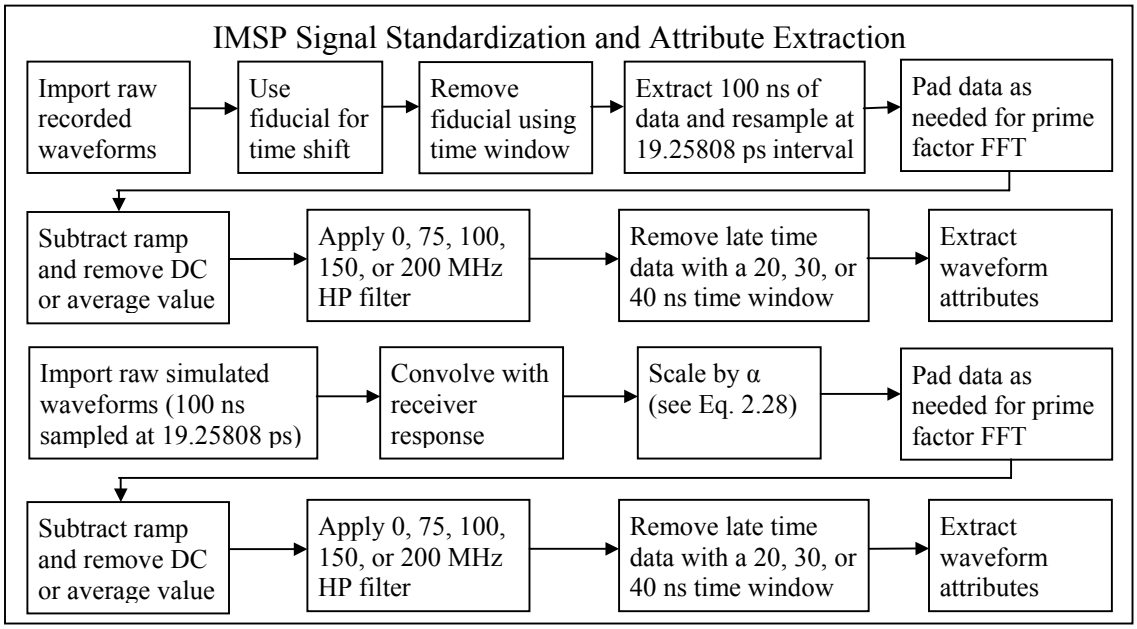

Figure 3.5. Signal standardization and parameterization for recorded and simulated data.

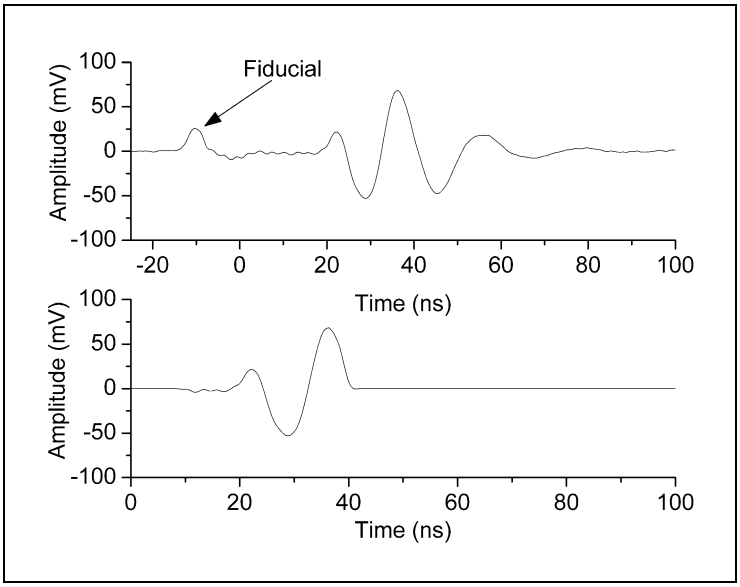

Figure 3.6. Upper panel shows raw recorded data after time shift based on fiducial. Lower panel shows the waveform after standardization and application of a 10-40 ns time window.

simulations discussed in this dissertation, the inflection point of the integrated Gaussian excitation occurs at 10 ns. The RTDGPR places a fiducial on the recorded waveform indicating the time when the pulse generator fires. To standardize RTDGPR data, the recorded data are aligned with the simulations using the fiducial. The data are then re-sampled using the time interval used in the simulations (19.25808 ps). Last, an early time cutoff filter (125 MHz cosine squared taper) removes the very early part of the waveform containing the fiducial (see Figure 3.6). To standardize the simulated waveforms, they are convolved with the receiver response function and multiplied by the scaling parameter α (see Equation 2.28). After the waveforms (simulated or recorded) have been standardized, their attributes are determined by high pass (HP) filtering, removing late time data (125 MHz cosine squared taper), and extracting a set of waveform attributes using one of the methods described below. The complete specification of an attribute set includes the HP filter frequency, the late cutoff time, and the attribute set type (discussed next).

Various attribute sets were tested to determine their suitability for use in the inversion (see Table 3.1). The *Spectral* attribute set is comprised of FFT spectral amplitudes to represent the simulated waveform. The phase information provided by the FFT was not used due to the phase unwrapping problem. The *BPF-time* attribute set provides some temporal information about the waveforms. To construct this set, the waveforms are passed through a bank of band-pass filters (BPF), and the arrival time of the energy peak from each filter output is used. The filter bank is made up of finite-impulse response (FIR) filters with a bandwidth of 10 MHz, a roll off of 180 dB per octave, and center frequencies corresponding to frequency components returned by the FFT routine (approximately 10 MHz intervals). The *Hilbert* attribute set contains time-domain samples at 1.5 ns intervals of the Hilbert envelope. The Hilbert envelope is the modulus of the waveform and its Hilbert transform (or quadrature component, Feldman, 1994). The remaining attribute sets in Table 3.1 are self-explanatory. Using the *Spectral* and *Hilbert* attribute sets in the IMSP algorithm resulted in the least amount of

Table 3.1. Methods of extracting waveform attribute sets.

Attribute Set	Description	Results
Spectral	FFT spectral amplitudes at approximately 10 MHz intervals from 10-200 MHz.	Good
Hilbert	20 samples of the Hilbert waveform envelope evenly spaced throughout time window.	Good
BPF-peak	Peak amplitudes of waveform after applying a BPF bank. The filter bandwidths were 10 MHz and centered at frequencies between 10-200 MHz at approximately 10 MHz intervals.	Marginal
BPF-time	Time of energy peak of waveform after applying a BPF bank. The filter bandwidths were 10 MHz and centered at frequencies between 10-200 MHz at approximately 10 MHz intervals.	Poor
BPF-peak-time	All parameters from methods B and C.	Poor
Time-amp	Time and amplitude of first four peaks.	Poor
RMS-time-amp	RMS amplitude and time of energy peak of waveform.	Poor
Wave	20 samples evenly spaced throughout the time window.	Poor

uncertainty in the estimated soil properties (more details in Section 3.3).

Forward operators can be constructed from the FDTD simulations using a tri-linear interpolation. These forward operators return a set of waveform attributes as a function of soil properties and antenna standoff. The catalog of simulation results described in Table 2.6 and by Figures D.2-D.21 (see Appendix D) is used to construct the forward operator and the Jacobian matrix needed for the inversion. The forward operator and Jacobian matrix are defined over model space, which is gridded as shown in Figure 3.7. For the model parameters (permittivity, conductivity, and standoff) at each grid cell corner in Figure 3.7, the FDTD simulations produced a waveform, from which attributes are extracted for the IMSP routine. Within a grid cell, the tri-linear interpolation for each attribute is given by

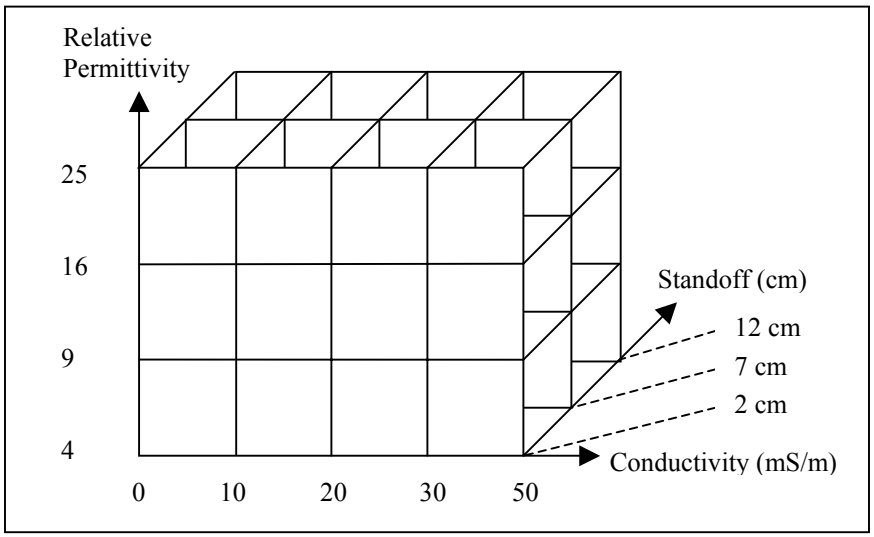

Figure 3.7. The model space grid. The simulated response is known at the corners of each grid cell.

$$y_j = A_j(\mathbf{X}) = \begin{bmatrix} (1-\Delta x_1)(1-\Delta x_2)(1-\Delta x_3)y_{j,l,m,n} + \\ (1-\Delta x_1)(1-\Delta x_2)(\Delta x_3)y_{j,l,m,n+1} + \\ (1-\Delta x_1)(\Delta x_2)(1-\Delta x_3)y_{j,l,m+1,n} + \\ (1-\Delta x_1)(\Delta x_2)(\Delta x_3)y_{j,l,m+1,n+1} + \\ (\Delta x_1)(1-\Delta x_2)(1-\Delta x_3)y_{j,l+1,m,n} + \\ (\Delta x_1)(1-\Delta x_2)(\Delta x_3)y_{j,l+1,m,n+1} + \\ (\Delta x_1)(\Delta x_2)(1-\Delta x_3)y_{j,l+1,m+1,n} + \\ (\Delta x_1)(\Delta x_2)(\Delta x_3)y_{j,l+1,m+1,n+1} \end{bmatrix}, \tag{3.1a}$$

$$\Delta x_1 = \frac{(x_1 - x_{1,l,m,n})}{(x_{1,l+1,m,n} - x_{1,l,m,n})}, \tag{3.1b}$$

$$\Delta x_2 = \frac{(x_2 - x_{2,l,m,n})}{(x_{2,l,m+1,n} - x_{2,l,m,n})}, \tag{3.1c}$$

$$\Delta x_3 = \frac{(x_3 - x_{3,l,m,n})}{(x_{3,l,m,n+1} - x_{3,l,m,n})}, \tag{3.1d}$$

and

$$\mathbf{X} = \begin{bmatrix} x_1 \\ x_2 \\ x_3 \end{bmatrix} = \begin{bmatrix} \varepsilon_r \\ \sigma \\ d \end{bmatrix}, \tag{3.1e}$$

$$\mathbf{Y} = \begin{bmatrix} y_1 \\ y_2 \\ \vdots \\ y_j \end{bmatrix}, \tag{3.1f}$$

where **X** is the model vector, **Y** contains the waveform attributes, and **A** is the forward operator. The vector element x_i refers to the ith model parameter (ε_r, σ, or d), and the element $x_{i,l,m,n}$ refers to the ith model parameter at grid location l,m,n (see Figure 3.8). The element y_j and $y_{j,l,m,n}$ are the analogous waveform attributes. The Jacobian at point **X** is given by the following formula

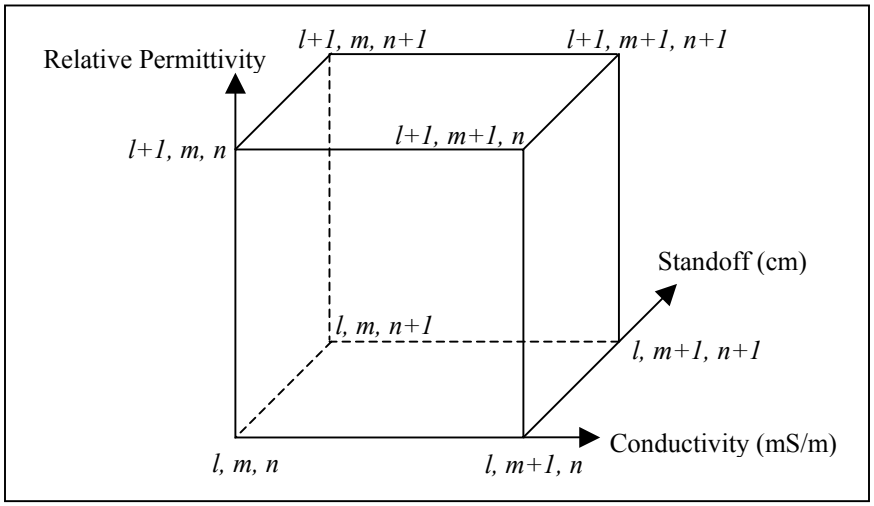

Figure 3.8: Numbering of grid cube indices.

$$\frac{\partial y_j}{\partial x_1} = \begin{bmatrix} (-\delta x_1)(1-\Delta x_2)(1-\Delta x_3) y_{j,l,m,n} + \\ (-\delta x_1)(1-\Delta x_2)(\Delta x_3) y_{j,l,m,n+1} + \\ (-\delta x_1)(\Delta x_2)(1-\Delta x_3) y_{j,l,m+1,n} + \\ (-\delta x_1)(\Delta x_2)(\Delta x_3) y_{j,l,m+1,n+1} + \\ (\delta x_1)(1-\Delta x_2)(1-\Delta x_3) y_{j,l+1,m,n} + \\ (\delta x_1)(1-\Delta x_2)(\Delta x_3) y_{j,l+1,m,n+1} + \\ (\delta x_1)(\Delta x_2)(1-\Delta x_3) y_{j,l+1,m+1,n} + \\ (\delta x_1)(\Delta x_2)(\Delta x_3) y_{j,l+1,m+1,n+1} \end{bmatrix}, \tag{3.2a}$$

$$\frac{\partial y_j}{\partial x_2} = \begin{bmatrix} (1-\Delta x_1)(-\delta x_2)(1-\Delta x_3) y_{j,l,m,n} + \\ (1-\Delta x_1)(-\delta x_2)(\Delta x_3) y_{j,l,m,n+1} + \\ (1-\Delta x_1)(\delta x_2)(1-\Delta x_3) y_{j,l,m+1,n} + \\ (1-\Delta x_1)(\delta x_2)(\Delta x_3) y_{j,l,m+1,n+1} + \\ (\Delta x_1)(-\delta x_2)(1-\Delta x_3) y_{j,l+1,m,n} + \\ (\Delta x_1)(-\delta x_2)(\Delta x_3) y_{j,l+1,m,n+1} + \\ (\Delta x_1)(\delta x_2)(1-\Delta x_3) y_{j,l+1,m+1,n} + \\ (\Delta x_1)(\delta x_2)(\Delta x_3) y_{j,l+1,m+1,n+1} \end{bmatrix}, \tag{3.2b}$$

$$\frac{\partial y_j}{\partial x_3} = \begin{bmatrix} (1-\Delta x_1)(1-\Delta x_2)(-\delta x_3) y_{j,l,m,n} + \\ (1-\Delta x_1)(1-\Delta x_2)(\delta x_3) y_{j,l,m,n+1} + \\ (1-\Delta x_1)(\Delta x_2)(-\delta x_3) y_{j,l,m+1,n} + \\ (1-\Delta x_1)(\Delta x_2)(\delta x_3) y_{j,l,m+1,n+1} + \\ (\Delta x_1)(1-\Delta x_2)(-\delta x_3) y_{j,l+1,m,n} + \\ (\Delta x_1)(1-\Delta x_2)(\delta x_3) y_{j,l+1,m,n+1} + \\ (\Delta x_1)(\Delta x_2)(-\delta x_3) y_{j,l+1,m+1,n} + \\ (\Delta x_1)(\Delta x_2)(\delta x_3) y_{j,l+1,m+1,n+1} \end{bmatrix}, \tag{3.2c}$$

$$\delta x_1 = \frac{1}{(x_{1,l+1,m,n} - x_{1,l,m,n})}, \tag{3.2d}$$

$$\delta x_2 = \frac{1}{(x_{2,l,m+1,n} - x_{2,l,m,n})}, \tag{3.2e}$$

$$\delta x_3 = \frac{1}{(x_{3,l,m,n+1} - x_{3,l,m,n})} \ . \tag{3.2f}$$

Note that the forward operator is continuous at grid cell boundaries, but the Jacobian is not. The condition number of the Jacobian is rarely greater than 200 for interpolated forward operators based on the *Spectral* and *Hilbert* attribute sets. Finally, note that the range of the forward operator is limited to the model grid shown in Figure 3.7.

Interpolated forward operators were constructed for two antenna offsets, 113 and 173 cm. Plots of the interpolated forward response for the 113 cm and 173 cm offsets using the *Spectral* and *Hilbert* attribute sets are shown in Figures D.22-D.33 (see Appendix D). Although abbreviated, these plots convey the nature of the interpolated forward response. Sharp changes in direction of the contour lines at one of the points on the model space grid (see Figure 3.7) or significant curvature of the contours may indicate under sampling of the operator. The ramifications of operator under sampling are discussed in Section 3.3.

3.3 The Inversion Algorithm

To estimate the model parameters (ε_r, σ, d), the inversion algorithm uses the forward operator and the Jacobian matrix with the Gauss-Newton method (Gill et al., 1996; Zhdanov, 2002; Press et al., 1992; Tarantola , 2005) to iteratively move from an initial model to improved estimates of a solution. The goal is to find an estimated solution where the predicted data and the actual data agree to within the level of uncertainty between them. A measure of how well the predicted data agree with the actual data is determined using

$$r = \left\| \mathbf{A}(\mathbf{X}) - \mathbf{Y} \right\|, \tag{3.3}$$

where r is the residual. The residual function is non-linear, but can be treated in a piece-wise linear fashion by using a local value of the Jacobian **J** to find the direction in which

the residual can be reduced. The pseudo-inverse of **J** is used to find a value of **X** that further reduces the residual, and iterating. Specifically,

$$\mathbf{Y}_{p,q} = \mathbf{A}(\mathbf{X}_{p,q}), \tag{3.4a}$$

$$\Delta\mathbf{Y}_{p,q} = \mathbf{Y} - \mathbf{Y}_{p,q}, \tag{3.4b}$$

$$\Delta\mathbf{X}_{p,q} = a\mathbf{J}^{\dagger}_{p,q}\Delta\mathbf{Y}_{p,q}, \tag{3.4c}$$

$$\mathbf{X}_{p+1,q} = \mathbf{X}_{p,q} + \Delta\mathbf{X}_{p,q}, \tag{3.4d}$$

where $\mathbf{J}^{\dagger}$ is the pseudo-inverse of **J**, p is the iteration index, q is the initial model index (see below), and a is a constant. In practice, $a = 0.25$ is used so that the solution does not significantly overshoot the point where the stopping criterion is met (discussed below), and to reduce possible pathological effects due to discontinuities in the Jacobian at cell boundaries. The pseudo-inverse of **J** is calculated using singular value decomposition (SVD). Initial models are specified using five initial values for each model parameter to uniformly span the parameter's allowed range (see Figure 3.7), making 125 initial models. The algorithm starts with each initial model $\mathbf{X}_{0q}$ ($p = 0$, q of 125), and proceeds by iteratively reducing the residual of every initial model using Equations 3.4. The goal is not to find the minimum residual value because there is no point in further minimization of the residual beyond the uncertainty between the predicted and actual waveform attributes. Rather, the iterative process is truncated when the following relationship (the stopping criterion) is satisfied

$$\left\|\mathbf{A}(\mathbf{X}) - \mathbf{Y}\right\|^2 \le \left\|\mathbf{\Sigma}\right\|^2, \tag{3.5}$$

where $\mathbf{\Sigma}$ is the uncertainty between the predicted and measured waveform attributes (Scales et al., 1990). An acceptable solution to the inverse problem $\mathbf{X}_{\Sigma q}$ is obtained when the stopping criterion is satisfied. The residual of each initial model q (q of 125) is iteratively reduced until Equation 3.5 is satisfied, and an $\mathbf{X}_{\Sigma q}$ value is tabulated as a valid solution if the stopping criterion is met. The $\mathbf{X}_{\Sigma q}$ values form the solution set to the inverse problem. The pseudo-code for this algorithm is shown in Figure 3.9.

```
remove data beyond 20,30,or 40us with cosine squared taper
extract waveform attributes Y
for each initial model of 125
{
    X=initial model
    Yp=A(X)
    while ((Yp-Y, Yp-Y) > (Sigma, Sigma))
    {
         calculate Yp=A(X) and J(X)
         calculate pseudo-inverse of J
         if ((Yp-Y, Yp-Y) <= (Sigma, Sigma))
            add X to Xtally
         X += 0.25*InvJ*(Yp-Y)
         limit X to valid range of model parameters
    }
}
calculate statistics of tallied solutions: Xmean and Xsig
```

Figure 3.9. Pseudo-code for IMSP algorithm.

Deterministic prior information was incorporated into the algorithm by limiting the allowable range of model parameters. The permittivity range is bounded using permittivity values for dry sand and water-saturated sand. The presence of clay minerals in soil can increase relative permittivity values to more than 25 (see Chapter 1). However, the conductivity values in this situation will usually be in excess of 50 mS/m and the GPR method will not produce usable results due to poor penetration. The standoff values bracket the antenna height settings commonly used with the RTDGPR. During each iteration, the model parameters are constrained from leaving the region of valid model parameters listed in Table 3.2.

Table 3.2. Allowable range of model parameters.

Parameter	Range
RDP	4-25
Conductivity	0-50 mS/m
Standoff	2-12 cm

To illustrate the progress made by each iteration of the algorithm, the problem has been made two-dimensional by assuming that the standoff is known. In this case, the algorithm constrains the standoff from changing, and this known parameter value is used for all initial models. This reduces the number of initial models from 125 to 25. Figures 3.10 and 3.11 depict the evolution of the solution set for this 2-dimensional problem. To generate these Figures, the IMSP routine was applied to an FDTD simulated waveform for soil properties of $\varepsilon_r = 9$, $\sigma = 20$ mS/m, and an antenna standoff of 7 cm. The relative uncertainty $\|\mathbf{\Sigma}\|/\|\mathbf{Y}\|$ (discussed below) was 10% in Figure 3.10, and 1% for Figure 3.11. As the process evolves, each initial model moves toward a local minimum until either the stopping criterion (Equation 3.5) is satisfied, a minimum is reached without meeting the stopping criterion, or the algorithm fails to reach a minimum after a large number of iterations (250). The size of the bubbles corresponds to the size of the residual. The initial models are plotted with a triangle, and the models where the stopping criterion is met are plotted with a square. The models plotted with a square make up the solution set. Initial models with an RDP of 15 or less are located in a basin of attraction where the basin minimum meets the stopping criterion (i.e. Equation 3.5; Deng, 1997). These initial models evolve into the solution set. Initial models with an RDP greater than 15 are in another basin of attraction whose minimum does not meet the stopping criterion. These initial models move towards the minimum of the basin, but never meet the stopping criterion and are not part of the solution set. If the uncertainty becomes large enough, models in the second basin may become part of the solution set.

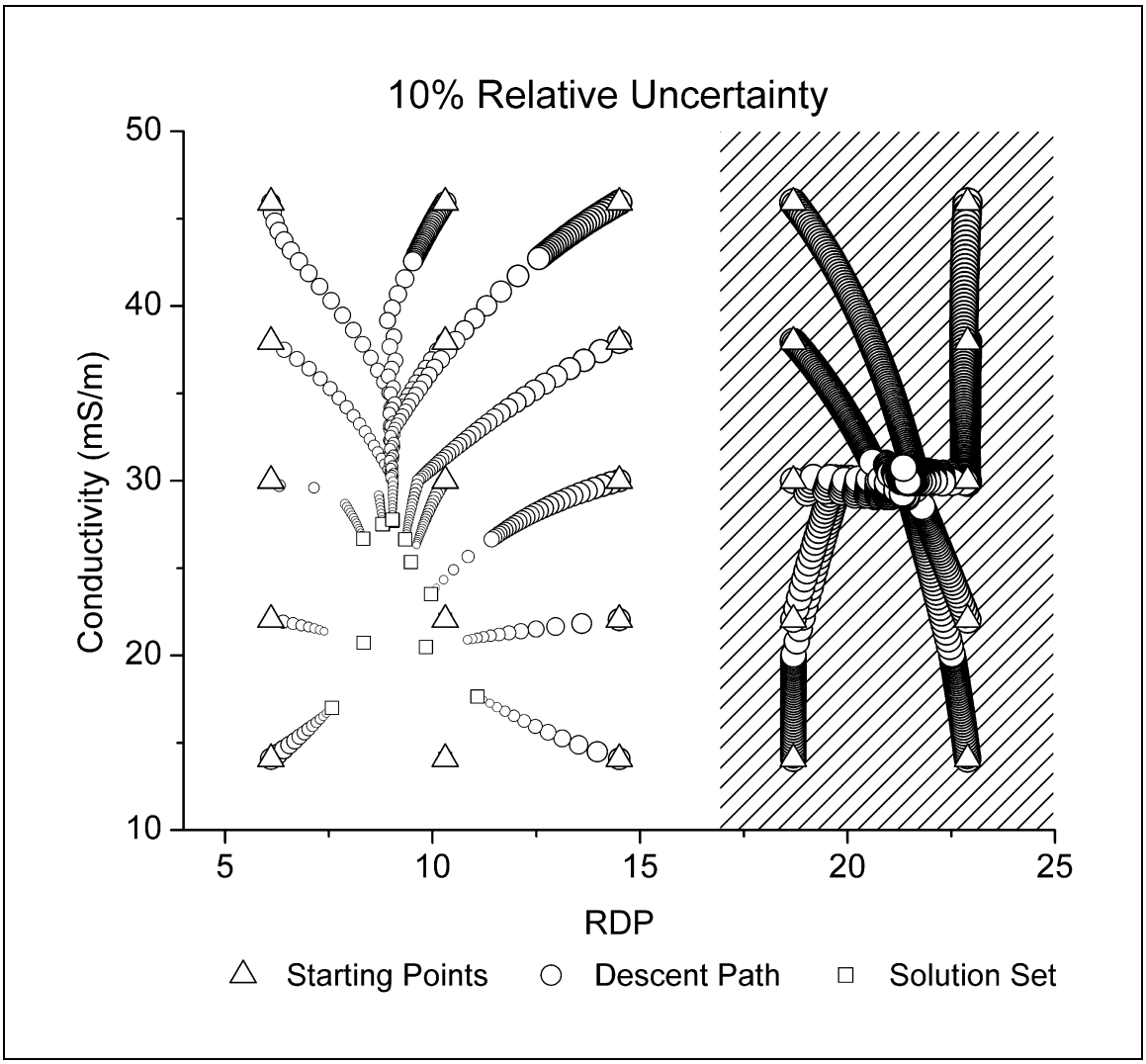

Figure 3.10. IMSP inversion history for known standoff and a relative uncertainty of 10%. Starting models in the shaded region descend to a local minimum that does not meet the stopping criterion. Members of the solution set are shown as squares.

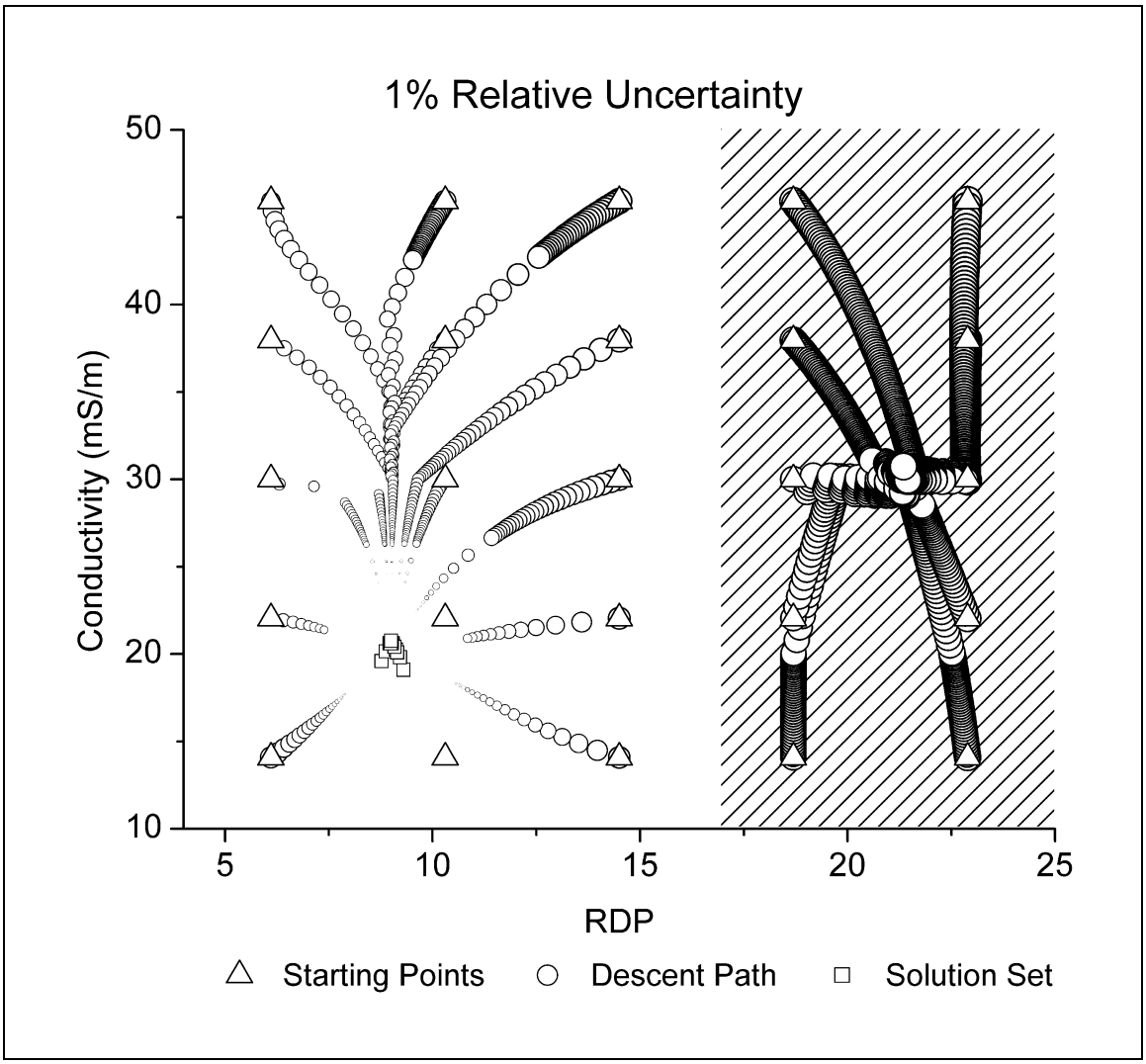

Figure 3.11. IMSP inversion history for known standoff and a relative uncertainty of 1%. Starting models in the shaded region descend to a local minimum that does not meet the stopping criterion. Members of the solution set are shown as squares.

3.3.1 Assessing Uncertainty

Three components of the uncertainty $\boldsymbol{\Sigma}$ between the predicted and measured waveform attributes are considered here. The first component Σ_1 is a systematic error, and is the RMS difference between the attributes of the simulated waveforms and those determined experimentally. An estimate of Σ_1 is taken from the comparisons between the simulated and experimental waveform attributes (see Chapter 2, Table 2.5). For instance, when using a 173 cm antenna offset and the *Hilbert* attribute set, this relative uncertainty component $\Sigma_1 / \|\mathbf{Y}\|$ is about 7% as determined by equation 2.28. The second component of uncertainty Σ_2 is due to the noise in the recorded data. Since the RTDGPR records at least 50 ns of data before the fiducial arrives, this component is estimated by determining the RMS amplitude of the recorded data before the fiducial pulse (see Figure 3.8). The final component of uncertainty Σ_3 is also a systematic error, and is due to the sparse sampling used to construct the interpolated forward operator. Quantifying this component is more difficult and requires further discussion. It is assumed that each component of $\boldsymbol{\Sigma}$ is independent, uncorrelated, and normally distributed. This may not be true in practice since the bias of Σ_1 and Σ_3 may be significant and correlated.

To assess the uncertainty Σ_3 associated with approximating the actual forward problem by interpolation of a relatively sparsely sampled forward problem, a more detailed look into how the early arrivals change with model parameters is needed. In plots of the interpolated forward response (see Figures D.22-D.33, Appendix D), the change in attributes with model parameters is monotonic and approximately linear except when the soil properties are similar to the absorber properties (i.e. at low RDP and conductivity values). Thus, a linear interpolation is reasonably accurate in portions of model space where the RDP and conductivities are high. Conversely, for low conductivities and RDP, the linear interpolation over a sparse grid introduces more error. Even with these generalizations, it is unclear exactly how uncertainty is introduced by interpolating.

To estimate the errors of the interpolated forward operator, several FDTD simulations were made with model parameter values located inside the grid cells rather than at the corners. The relative RMS errors between the simulated and predicted waveform attributes are shown in Table 3.3. Note that the errors are insignificant in regions of the model parameter space where conductivity and RDP values are large. Conversely, the errors are quite significant when the conductivity and RDP values are small. The interpolation errors listed in Table 3.3 reasonably estimate of the range of Σ_3 because tests were made in portions of the model space where the interpolation errors are expected to be near maximum and also near minimum. The assertion that the estimates of Σ_3 in Table 3.3 are reasonable is also supported by the fact that the received waveforms are not expected to change very quickly with changing model parameters in a pathological manner. Phenomena such as resonance are not expected due to the attenuating properties of the foam absorber, and because the dominant wavelengths are much longer than standoffs considered. Resonance can occur due to a metal conductor such as a wire or a pipe near the antenna, but the presence of a surface or subsurface

Table 3.3. The relative RMS interpolation error between interpolated and simulated waveform attributes. The time window was 10-40 ns and the frequency range was 0-250 MHz for all cases.

Soil Properties	Standoff	Attribute Set	Relative RMS Interpolation Error $\Sigma_3 / \|\mathbf{Y}\|$
$\varepsilon_r = 6.5$, $\sigma = 0.005$ mS/m	7 cm	*Spectral*	3.11 %
$\varepsilon_r = 6.5$, $\sigma = 0.005$ mS/m	7 cm	*Hilbert*	11.6 %
$\varepsilon_r = 20.5$, $\sigma = 0.04$ mS/m	7 cm	*Spectral*	0.0172 %
$\varepsilon_r = 20.5$, $\sigma = 0.04$ mS/m	7 cm	*Hilbert*	0.0176 %
$\varepsilon_r = 6.5$, $\sigma = 0.005$ mS/m	5 cm	*Spectral*	9.41 %
$\varepsilon_r = 6.5$, $\sigma = 0.005$ mS/m	5 cm	*Hilbert*	15.4 %
$\varepsilon_r = 20.5$, $\sigma = 0.04$ mS/m	5 cm	*Spectral*	1.07 %
$\varepsilon_r = 20.5$, $\sigma = 0.04$ mS/m	5 cm	*Hilbert*	1.09 %

scatterer near the antennas precludes the use IMSP algorithm (see Section 3.4 for a discussion on limitations and assumptions). The uncertainty component Σ_3 can be minimized with a more dense set of FDTD simulations, and/or perhaps with the use of higher order spline functions. The IMSP routines in *GPR Wave Utilities* can make use of essentially any number of FDTD simulations as long as they can be placed on a Cartesian grid. Therefore, the Σ_3 uncertainty component can be made insignificant over all model space with sufficiently dense collection FDTD simulations.

Only three components of the uncertainty between the predicted and actual waveform attributes are considered. Certainly, there are many other sources of uncertainty. For instance, changes in the radar calibration due to changing temperature, humidity, and connector coupling have not been considered. Many assumptions are made for the valid application of the IMSP algorithm, and ideal survey conditions are assumed. Deviation from these ideal conditions causes uncertainty. Real world survey conditions will almost certainly deviate from the ideal conditions. The ideal survey conditions, assumptions, and limitations for application of the IMSP algorithm, as well as the effects of non-ideal conditions are discussed in Section 3.4.

The solution set is an estimator of the solution space, and a statistical description of the solution set is used to describe the extent of the solution space and the uncertainty in the inversion results. It is possible however, that a solution set may not represent the actual extent of the solution space of a non-linear inverse problem. This is unlikely with the IMSP algorithm for the following reasons. The population of solution sets at a given location in model space is a function of the relative uncertainty. In tests made at various locations in model space, the population of the solution sets is approximately 100 (out of a possible 125) for a relative uncertainty of 1%, and slowly increases with uncertainty. According to Deng (1997), each local (or global) minimum in model space is surrounded by a basin of attraction. Since the initial models uniformly span the model space, the large solution set population indicates that the basin of attraction containing the IMSP solution space is quite broad. In general, the solution space is approached from many

directions and the solution set reasonably estimates the bounds of the solution space. For the tested locations, small increases in population occur with increasing uncertainty, but these inaccuracies are not abrupt for relative uncertainties less than about 15%. This indicates that small shallow satellite basins exist in the larger basin containing the global minimum. These small shallow basins are minor topographic features in the global basin of attraction, and have a small effect on the statistical distribution of the solution set. Finally, the possibility that an unsampled portion of the solution space extends appreciably from the solution set is unlikely because of smooth monotonic response of the forward operator over most of model space. For these reasons, the statistical distribution of the solution set is a practical estimate of the extent of the solution space and the uncertainty of the inverse solution.

Assessing the uncertainty of the solution to a non-linear inverse problem involves several issues. If the uncertainties between the predicted data and the actual data are normally distributed, then the uncertainty in the solution to a linear inverse problem can be described by normal statistics (Scales et al., 1997). For a non-linear problem such as the IMSP algorithm, it is possible to have a multi-modal statistical distribution of the solution set that cannot be described by normal statistics. However, since the increase in the solution set population changes little with an increase in relative uncertainty (for $\|\mathbf{\Sigma}\|/\|\mathbf{Y}\|$ less than about 15%), the solution set is essentially contained in a single basin of attraction and the statistical distribution of the solution set is essentially uni-modal. Furthermore, a uni-modal response is expected for a monotonically changing forward operator. The interpolated forward response plots in Figures D.22-D.33 (see Appendix D), show a monotonic response across most of model space, with some exceptions. A non-monotonic response occurs in the region of model space where the soil properties are similar to the absorber properties. Even in these regions, population changes in the solution set due to increasing relative uncertainty indicate uni-modal solution sets. Since the IMSP solution sets have a uni-modal distribution, it is assumed that the inverse

problem is approximately linear in the vicinity of the solution space, and normal statistics are used to describe the solution set. Therefore, all IMSP solution sets ($\mathbf{X}_{\Sigma q}$ values) are described by their mean $\overline{\mathbf{X}}$ and standard deviation $\boldsymbol{\sigma}_x$.

3.3.2 Uncertainty of Parameter Estimates

The statistical dispersion of an IMSP solution set (i.e. the breadth of the solution set distribution) depends on which attribute set is used, the relative uncertainty $\|\boldsymbol{\Sigma}\|/\|\mathbf{Y}\|$ between the measured and predicted data, and location of the solution set in model space. Figure 3.12 shows conceptually how the statistical dispersion of the solution set varies with position in model space. The actual statistical dispersion is described in Tables 3.4 and 3.5 for various attribute sets, relative uncertainty $\|\boldsymbol{\Sigma}\|/\|\mathbf{Y}\|$ values, and the 113 cm and 173 cm antenna offsets. For each row in these Tables, a collection of solutions sets was assembled by inverting each simulated waveform that was used to construct the forward operator. Since the statistical dispersion (i.e. $\boldsymbol{\sigma}_x$) of the solution sets is not normally distributed, the variability of solution set standard deviations in the collection is described by the median ($\tilde{\sigma}$) and the quartile deviation (*QD*). The quartile deviation conveys the variability of statistical dispersion of the solution sets at different locations in model space. Entries in Tables 3.4 and 3.5 with a 10% relative uncertainty are significant because this is the approximate relative uncertainty for the forward operators for the RTDGPR system. The relative uncertainty can be reduced by finer sampling of the forward operator, and possibly by directly measuring the antenna response (as discussed in Section 2.5.1). If the uncertainty becomes too small however, then the IMSP algorithm may be less able to tolerate deviations from ideal survey conditions such as a non-specular soil surface or a heterogeneous half-space (see Section 3.4). The *Spectral* and *Hilbert* attribute sets

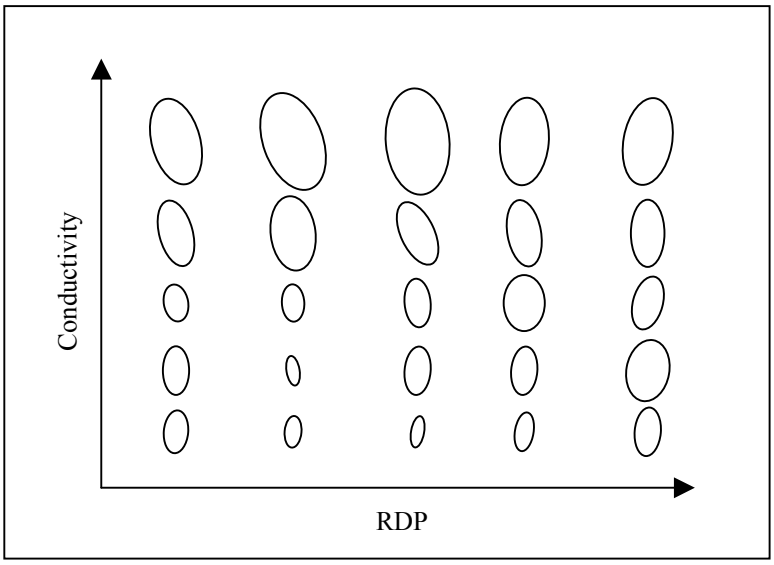

Figure 3.12. Cartoon illustrating the variation in statistical dispersion of the solution sets for different locations in model space. Cartoon is for illustrative purposes only and does not reflect actual breadth of the solution sets. Illustration is two-dimensional for simplicity. Actual solution sets are distributed over three-dimensions. Larger ovals indicate a large statistical dispersion. Tables 3.4 and 3.5 list actual statistical dispersion values.

Table 3.4. Statistics of acceptable solution sets for true models uniformly distributed across model space using the 113 cm antenna offset. The median $\tilde{\sigma}$ standard deviation and quartile deviation (*QD*) of each parameter are listed.

Attribute set, time window (ns), freq. range (MHz)	Normalized RMS uncertainty $\|\mathbf{\Sigma}\|/\|\mathbf{Y}\|$	Median standard deviation of RDP ($\tilde{\sigma} \pm QD$)	Median standard deviation of conductivity (mS/m) ($\tilde{\sigma} \pm QD$)	Median standard deviation of standoff (cm) ($\tilde{\sigma} \pm QD$)
Spectral, 10-40, 0-250	1%	0.141 ± 0.107	0.431 ± 0.277	0.093 ± 0.059
Spectral, 10-40, 0-250	10%	4.31 ± 2.02	6.18 ± 2.40	0.949 ± 0.515
Spectral, 10-30, 0-250	1%	0.155 ± 0.196	0.405 ± 0.505	0.095 ± 0.095
Spectral, 10-30, 0-250	10%	4.63 ± 1.72	6.62 ± 3.02	0.812 ± 0.435
Spectral, 10-20, 0-250	1%	1.51 ± 1.10	4.20 ± 3.08	0.189 ± 0.178
Spectral, 10-20, 0-250	10%	3.94 ± 1.60	9.64 ± 2.50	0.629 ± 0.336
Hilbert, 10-40, 0-250	1%	0.127 ± 0.140	0.459 ± 0.414	0.100 ± 0.066
Hilbert, 10-40, 0-250	10%	4.84 ± 2.40	6.90 ± 2.79	0.940 ± 0.607
Hilbert, 10-30, 0-250	1%	0.381 ± 0.364	0.684 ± 0.642	0.095 ± 0.075
Hilbert, 10-30, 0-250	10%	4.60 ± 1.07	8.09 ± 2.38	0.884 ± 0.490
Hilbert, 10-20, 0-250	1%	0.472 ± 0.803	2.92 ± 2.45	0.121 ± 0.119
Hilbert, 10-20, 0-250	10%	3.91 ± 1.53	9.02 ± 2.09	0.637 ± 0.396

Table 3.5. Statistics of acceptable solution sets for true models uniformly distributed across model space using the 173 cm antenna offset. The median $\tilde{\sigma}$ standard deviation and quartile deviation (*QD*) of each parameter are listed.

Attribute set, time window (ns), freq. range (MHz)	Normalized RMS uncertainty $\|\mathbf{\Sigma}\|/\|\mathbf{Y}\|$	Median standard deviation of RDP ($\tilde{\sigma} \pm QD$)	Median standard deviation of conductivity (mS/m) ($\tilde{\sigma} \pm QD$)	Median standard deviation of standoff (cm) ($\tilde{\sigma} \pm QD$)
Spectral, 10-40, 0-250	1%	0.140 ± 0.175	0.512 ± 0.493	0.075 ± 0.065
Spectral, 10-40, 0-250	10%	2.25 ± 1.74	7.39 ± 4.25	0.885 ± 0.538
Spectral, 10-30, 0-250	1%	0.258 ± 0.304	1.04 ± 0.699	0.093 ± 0.114
Spectral, 10-30, 0-250	10%	2.98 ± 1.59	8.52 ± 4.31	1.04 ± 0.562
Spectral, 10-20, 0-250	1%	1.54 ± 1.54	2.89 ± 1.87	0.381 ± 0.372
Spectral, 10-20, 0-250	10%	3.40 ± 1.91	8.59 ± 3.92	0.790 ± 0.606
Hilbert, 10-40, 0-250	1%	0.196 ± 0.207	0.528 ± 0.665	0.080 ± 0.116
Hilbert, 10-40, 0-250	10%	2.56 ± 1.74	9.25 ± 4.15	1.05 ± 0.659
Hilbert, 10-30, 0-250	1%	0.171 ± 0.151	0.762 ± 0.740	0.077 ± 0.071
Hilbert, 10-30, 0-250	10%	3.01 ± 1.78	8.76 ± 2.68	0.810 ± 0.595
Hilbert, 10-20, 0-250	1%	0.695 ± 0.569	2.20 ± 1.32	0.218 ± 0.162
Hilbert, 10-20, 0-250	10%	3.26 ± 1.25	8.46 ± 2.48	0.797 ± 0.512

both produced similar results. Surprisingly, both antenna offsets also produced similar results.

The discussion of some traditional measures of the performance of inversion algorithms is in order. The sensitivity of the waveform attributes to changes in the model parameters is greatest for frequencies below 100 MHz for the *Spectral* attribute set, and greatest for times greater than 20 ns for the *Hilbert* attribute set. The resolution of the model parameters by the Jacobian matrix is essentially perfect. The resolution matrix ($\mathbf{V}\mathbf{V}^T$) formed from the SVD model space Eigen vectors is the identity matrix plus some small off-diagonal numbers ($\sim 10^{-16}$) associated with numerical inaccuracies. Therefore, this approach should be quite accurate if the uncertainties can be made smaller and ideal survey conditions are present. The principal components of the solution set covariance matrix show cross correlation between the parameter estimates. This cross correlation is most pronounced between the standoff and conductivity estimates. The principal components indicate that the resolution of the standoff is best and that of the conductivity is worst. Note however that the allowable range of the conductivity is largest and the standoff range is the smallest. The effects of non-ideal survey conditions such as a rough ground surface are discussed in the following Section.

The current implementation of the algorithm in *GPR Wave Utilities* requires about 2.5 seconds to invert one waveform on a 2.6 GHz Pentium PC. No attention was given to optimizing for speed when writing the algorithm, and it is likely that it could be made to run in real time (i.e. process 5-10 waveforms per second). Since the model vector only has three components, the number of waveform attributes can likely be reduced from 20. In fact, it is possible that only three waveform attributes are necessary in a given local region. By studying the forward operator, it is likely that null space waveform attributes (i.e. data null space components) and redundant waveform attributes can be removed, which would accelerate the inversion. The Gauss-Newton method is one of the most primitive in the arsenal of inverse methods. It is an acceptable method in this application because the condition number rarely exceeds 200. Still, a more advanced approach such

as Newton's method may improve the speed of the algorithm. Also, when one model parameter is known, the IMSP algorithm runs about an order of magnitude faster because initial models are selected from two rather than three dimensions of model space. To achieve this, the standoff could be carefully controlled during the survey or measured using an additional sensor such as an acoustic ranging device. An independent measurement of standoff also reduces the uncertainty of the conductivity estimates due to the cross correlation between these parameter estimates. An additional sensor such as an electromagnetic induction sensor could measure the conductivity, however the volume of investigation would almost certainly be different than with the GPR antennas. For these reasons, and since the forward operator is quite sensitive to standoff, it is the recommended that standoff should be measured if any of the model parameters are independently measured.

The IMSP algorithm has been written with the assumption that the recorded waveforms can be aligned with the time the transmitted pulse arrives at the transmitting antenna feed port. A sensing circuit has been implemented with the RTDGPR to sense the pulse at the transmitting antenna feed port. This circuit is needed because the propagation delay of timing signals in the electronics and cables changes due to variations in operating and environmental conditions such as temperature, humidity, battery voltage, etc. Some commercial radar systems account for system timing drift, and others do not. If it is not possible to determine when the transmitted pulse arrived at the feed port of the transmitting antenna with a given system, then the IMSP forward operator must be re-defined to use waveforms referenced to the first arrival time at the receiver. The results of changing the time reference of the simulated waveforms has not been investigated, but reasonable results are expected. See Section 2.7 for more details.

3.4 Investigation of Limitations and Assumptions

The ideal survey conditions for the IMSP algorithm are described in this Section. Results from non-ideal survey conditions should be considered invalid except for the allowable conditions described in this Section. The IMSP algorithm is sensitive to soil within the 'sensitive region' under the antennas. This region is the 3.5 by 1.5 meter area centered beneath the RTDGPR antenna array, and extends to a depth of 50-200 cm (discussed in more detail later in the Section). The electrical properties of the soil in the sensitive region are assumed homogeneous, linear, isotropic, and frequency independent. It is assumed that the soil is non-magnetic with a magnetic permeability equal to that of free space. The modeled soil surface was a flat specular reflector in the FDTD simulations used to build the forward operator. The antennas remain perfectly co-polarized during the survey, and the bottoms of the antennas remain parallel to the ground. Finally, visible reflections from subsurface scatterers are not allowed in the first 30 ns of data recorded after the transmitter fires. The signal to noise ratio should be greater than 10. Because the antenna offset is small, early arriving waveforms often have a large amplitude, and a typical signal to noise ratio for the early arrivals is greater than 100:1.

In order to determine the range of applicability of the IMSP algorithm, it is useful to examine the natural variations in soil heterogeneity. Soil heterogeneity is studied in several disciplines. In precision agriculture, the spatial variability of soils and moisture content is studied. In land mine remediation, the distribution of soil properties that affect the contrast of mines with natural features is studied in order to achieve better detection and discrimination. The horizontal variability of soil properties is discussed in Olhoeft (1994), Rea and Knight (1998), Hendrickx et al. (2001), van Dam et al. (2004), and Gish et al. (2002). These researchers calculated semi-variograms and autocorrelations for soil properties at a number of sites, and found spatial correlation lengths ranging from 50 cm to over 10 meters. In fact, variations in earth material properties vary over many

different length scales, and are often of a fractal nature (Turcotte, 1997; Tindall and Kunkel, 1999; Hunt and Gee, 2002). Because of the wide variety of length scales that occur when correlating soil properties, it is difficult to arrive at typical vertical and horizontal length scales. In general however, the scale of heterogeneity is smaller in the vertical direction than in the horizontal direction. Fortunately at a given survey site, the GPR survey data are a good indicator of the length scales involved, and correlation lengths can often be calculated from the GPR data (i.e. see Olhoeft, Rea and Knight, and Gish et al. above). For instance, Rea and Knight found average semi-variogram ranges in 100 MHz GPR images of 2.0 meters horizontally and 0.8 meters vertically for unlithified sand and gravel. These studies suggest that in many cases, the natural lateral variations in permittivity and conductivity are slow enough to allow application of the IMSP algorithm. When lateral variations occur over small length scales, they usually produce visible indications in the GPR section. Anthropogenic activities such as paving and trenching commonly cause rapid lateral changes in material properties that are very often visible in GPR surveys. Vertical variations are discussed in more detail below.

Mixing models (Sihvola, 1999; Wtorek, 2003) indicate that the permittivity and conductivity of soil are very sensitive to moisture content, which is primarily responsible for vertical heterogeneity in electrical soil properties. The moisture content of unsaturated soils (i.e. field water) is a function of precipitation, evapotranspiration, root zone depth, field capacity, and the gravity and matric potentials (Fetter, 2001; Tindall and Kunkel, 1999). Field capacity and matric potentials are in turn dependent on the moisture content and salinity of the fluid, and the packing geometry, size, shape, and mineralogy of the grains making up the soil. Field capacity can be hysteretic depending on whether the moisture content is increasing or decreasing. During a precipitation event, infiltration causes an increase in the volumetric moisture content (θ) of the vadose zone. During infiltration, the moisture content is approximately constant above the wetting front (see Figure 3.13), although small depressions will collect more precipitation than the surrounding areas (i.e. ponded infiltration). Redistribution of field water after infiltration

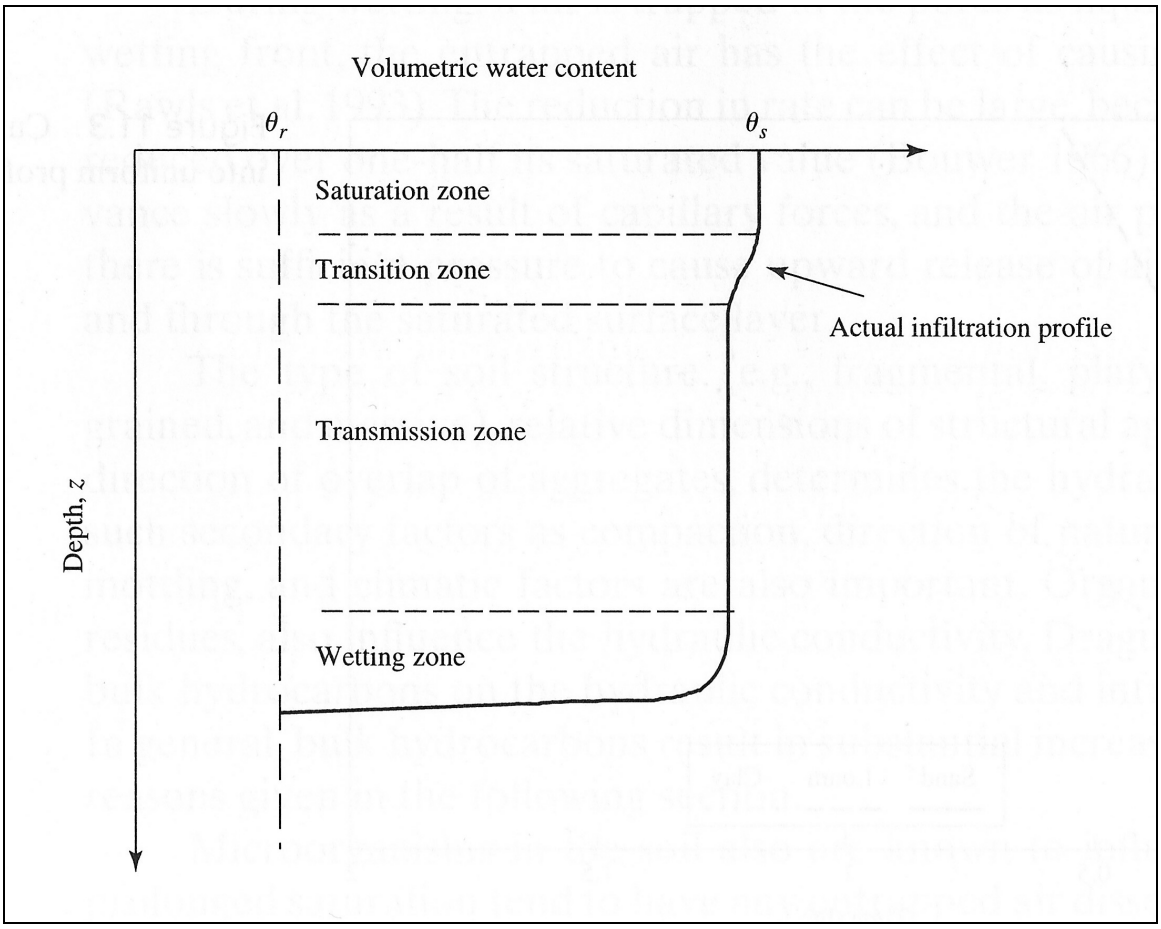

Figure 3.13. Typical vadose zone moisture content during infiltration. θ_r and θ_s are the residual and saturated volumetric moisture content respectively. Adapted from Tindall and Kunkel (1999).

can cause moisture to move up and/or down. Figure 3.14 (Wang et al., 2004) shows some typical redistribution profiles. Evapotranspiration will tend to draw moisture up, while gravity drainage tends to draw moisture down. Moisture profiles after redistribution can vary widely depending on previous saturation history, mechanical and chemical soil properties, and environmental factors such as weather. For example, Suleiman and Ritchie (2003) measured shallow moisture profiles over time for a variety of soil types. Figure 3.15 shows results from two soil types. They found that most of the variability in the profile occurs in the first 10 cm, and is due to evaporation. Dahan et al. (2003) found that moisture content in a hot desert environment was nearly constant in the first 3.5 meters when there had been no precipitation for 5 months, although no measurements shallower than one meter were made. Olhoeft (1991) showed that migrating wetting fronts can be mapped using GPR when they are in the far-field region. Generally, moisture profiles that are most optimal for the IMSP algorithm occur either

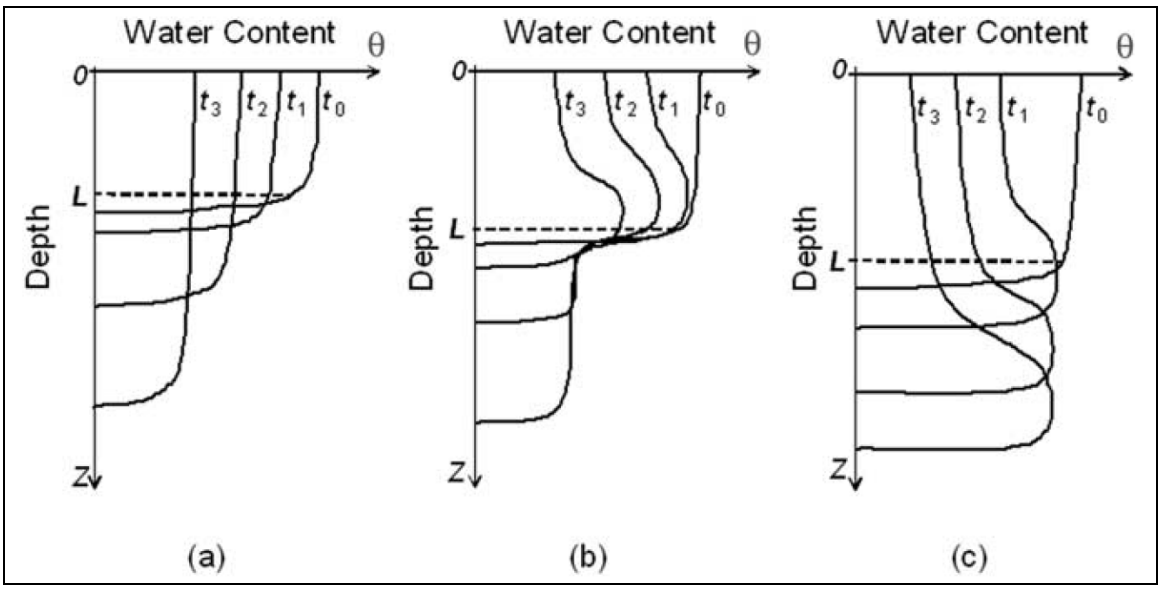

Figure 3.14. Different types of moisture profiles during vadose zone redistribution. Increasing subscripts on *t* indicate increasing time. Adapted from Wang et al. (2004).

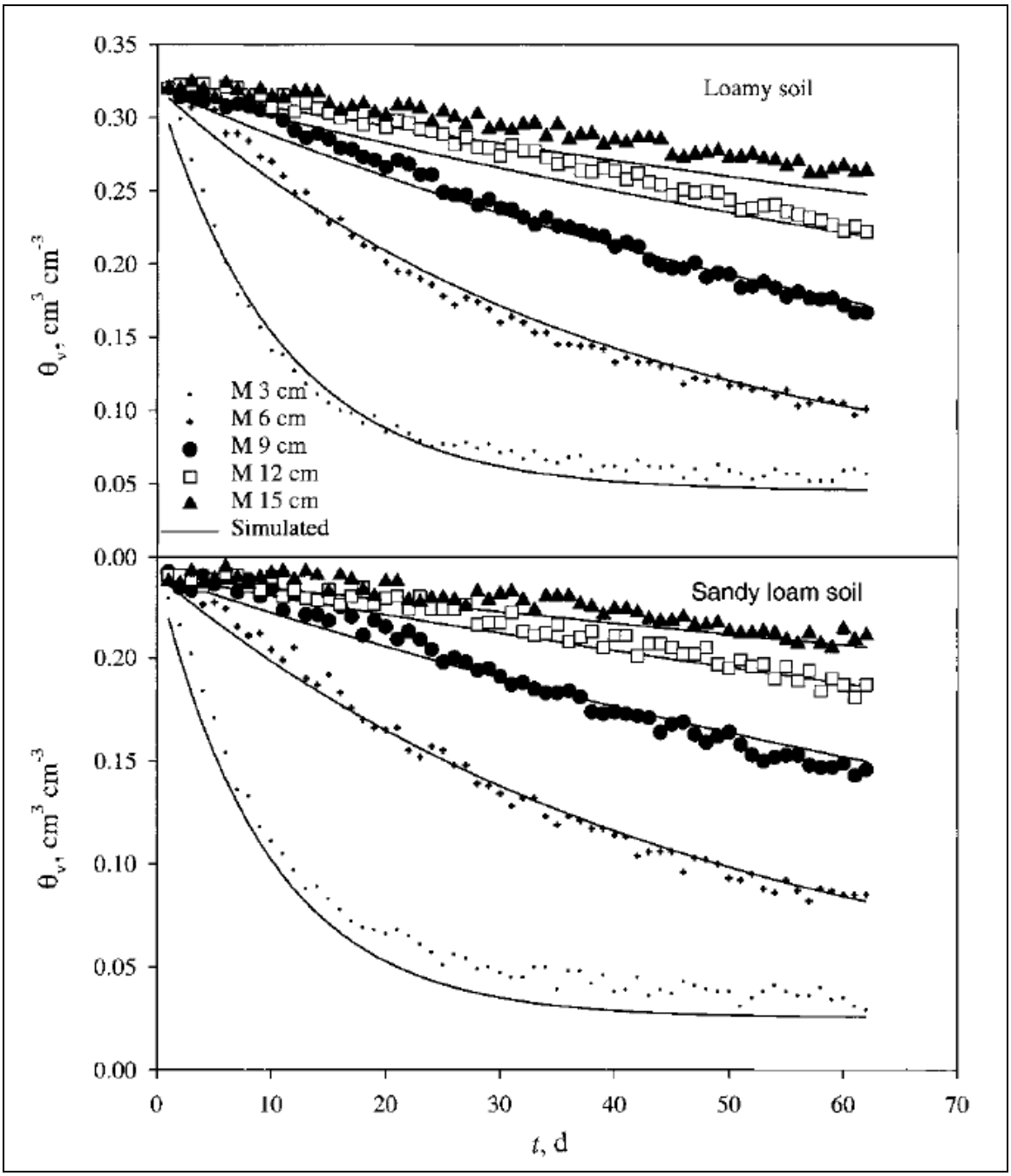

Figure 3.15. Symbols show measured volumetric moisture content θ at several depths versus time for two soil types (solid lines are from simulations). Adapted from Suleiman and Ritchie (2003).

immediately after a lengthy precipitation event where moisture content is approximately uniform throughout the sensitive region, or after a long hiatus in precipitation where redistribution has created an approximately uniform moisture profile in the sensitive region. Many common scenarios such as frequent precipitation will not allow development of an approximately uniform shallow moisture profile. Note that higher frequency antennas will have a shallower sensitive region, which may allow the IMSP algorithm to be applied in more scenarios. The response of the IMSP algorithm to vertical heterogeneity is discussed in more detail below.

The IMSP algorithm requires an effectively flat and smooth ground surface, and it is assumed that only specular reflection occurs at the surface. Specular scattering and diffuse surface scattering are illustrated in Figure 3.16. A specularly reflected plane wave is reflected into a single angle. A diffusely scattered plane wave is reflected into many different angles. Because of this, diffuse scattering will change the angular spectrum of waves reflected by the ground surface. To see this, consider Figure 3.17, which shows the horizontal wave number spectrum of waves reflected by a horizontal planar reflector. The incident wave field was generated by a uniformly-illuminated finite-aperture source, which produces the familiar sinc function pattern in the frequency-domain. The transmitting antenna can be crudely approximated as such a source (see Smith, 1997, for a relevant discussion on diffraction). The wave number spectrum is unchanged after reflection from a specular plane. The Figure also shows the resultant spectra after reflection off of increasingly rough surfaces, where a Gaussian beam has been used to approximate the diffuse reflected waves due to incident plane waves. Rougher surfaces scatter into broader beam widths. The Figure shows that scattering into a beam width of up to 10 degrees has little effect and will not adversely affect the IMSP algorithm. The reflected beam width is closely related to the average slope of the rough surface, which is discussed below.

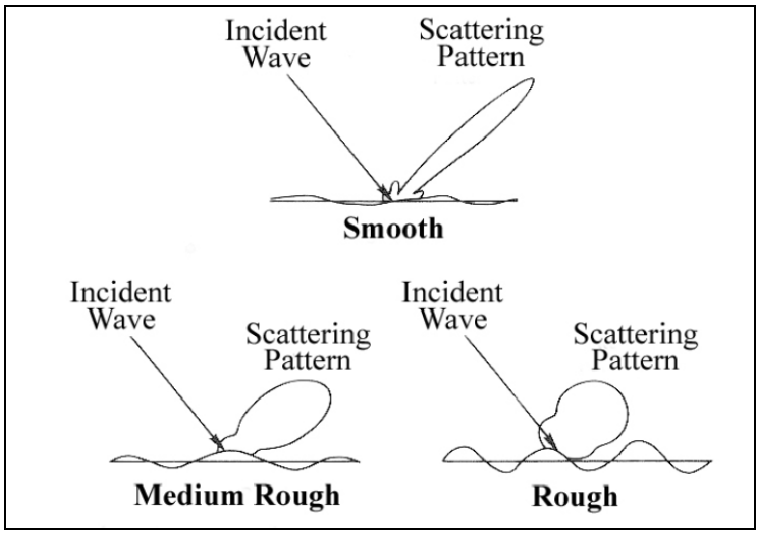

Figure 3.16. Illustration contrasting the nearly specular scattering from a relatively smooth surface with diffuse scattering from a rough surface (adapted from Ulaby et al., 1982).

Ulaby et al. (1982) provide several guidelines and methods of analysis to determine if a surface can be approximated as a specular reflector. There are two factors that primarily determine the extent of diffusive scattering – the vertical roughness and the average slope. The phase difference of received waves that have back scattered off peaks and troughs is a measure of the vertical roughness. The range of angles that the reflected waves are scattered into is analogous to the average slope. A rough surface can be described by the height of the protrusions and their horizontal correlation length. The average surface slope is found by dividing the average height of the protrusions h by the correlation length l. The correlation length of a specular reflector is infinitely long, while the correlation length of a surface with a mostly high spatial frequency content is small. Ulaby et al. offer their Fraunhofer criterion to determine if surface roughness is a significant factor. This criterion states that if the phase difference between waves coming

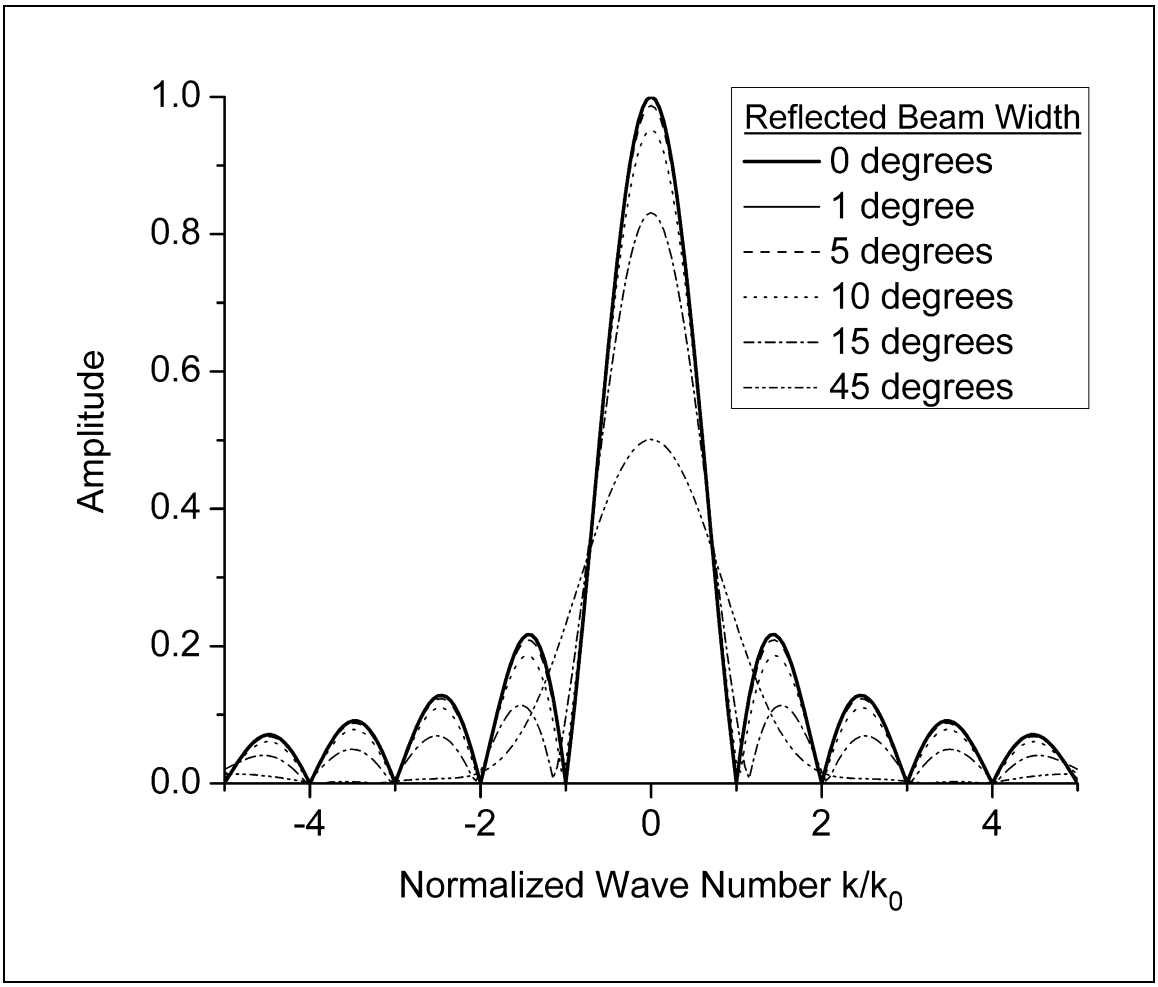

Figure 3.17. Figure shows the amplitude spectrum of waves reflected off of a perfect specular plane (thick line). The incident waves were generated by a finite aperture antenna producing the familiar sync function pattern. Also shown are the distorted spectra due to diffuse scattering off of rough surfaces. A Gaussian beam is used to represent diffuse scattering. A beam width of zero degrees is specular reflection. The wave number is normalized by the intrinsic wave number of the medium. The spectrum reflected into a beam width of one degree is cannot be distinguished from the specularly reflected spectrum on this plot.

from a surface peak and a surface trough is less than $\pi/8$ radians ($kh < \pi/8$, where k is the wave number), then the surface can be considered smooth regardless of the correlation length (or scale of heterogeneity).

Ulaby et al. have analyzed several classes of surface scattering, and these analyses give more insight into the phenomenon. For mildly rough surfaces, scattering can be calculated using a scalar approximation of physical optics. This approach requires that the average slope is less than 0.25, and that the correlation length is larger than a wavelength. Using this scalar approximation, the scattered waves are described by is a power series in $k_z h$, where k_z is the vertical component of the incident wave's wave number. The first order term in the series corresponds to specular reflection, and the higher order terms correspond to diffusive scattering. Thus, if $k_z h$ is much greater than $(k_z h)^2$, then specular reflection dominates. When the horizontal correlation length is not larger than a wavelength, then a small perturbation model may be an alternate method for estimating the amount of rough surface scattering. The small perturbation model can be used when $kh < 0.3$ and $h/l < 0.212$. With this model, the scattering amplitude increases as $k^4 h^2$, and the directivity is specified by the Fourier transform of the surface autocorrelation coefficient. A compact surface autocorrelation coefficient results in more diffuse reflection. In summary, surface scattering is a complicated phenomenon but some generalizations can be made. For average slopes less than 10%, the reflected wave can be approximated using a beam width of about 10 degrees. When the reflected beam width is less than 10 degrees and the product kh is less than $\pi/8$, then the IMSP algorithm can be applied.

Most of the preceding guidelines for rough surface scattering were established for the far-field region (i.e. more than a few wavelengths from the source). In order to test the applicability of the above guidelines to the near-field region, several FDTD simulations were made, and the simulated waveforms are shown in Figure 3.18. Rough surfaces with 2, 3 and 6 cm vertical asperities and a correlation length of 20 cm were simulated using convex and concave spherical sections where the spherical radius was

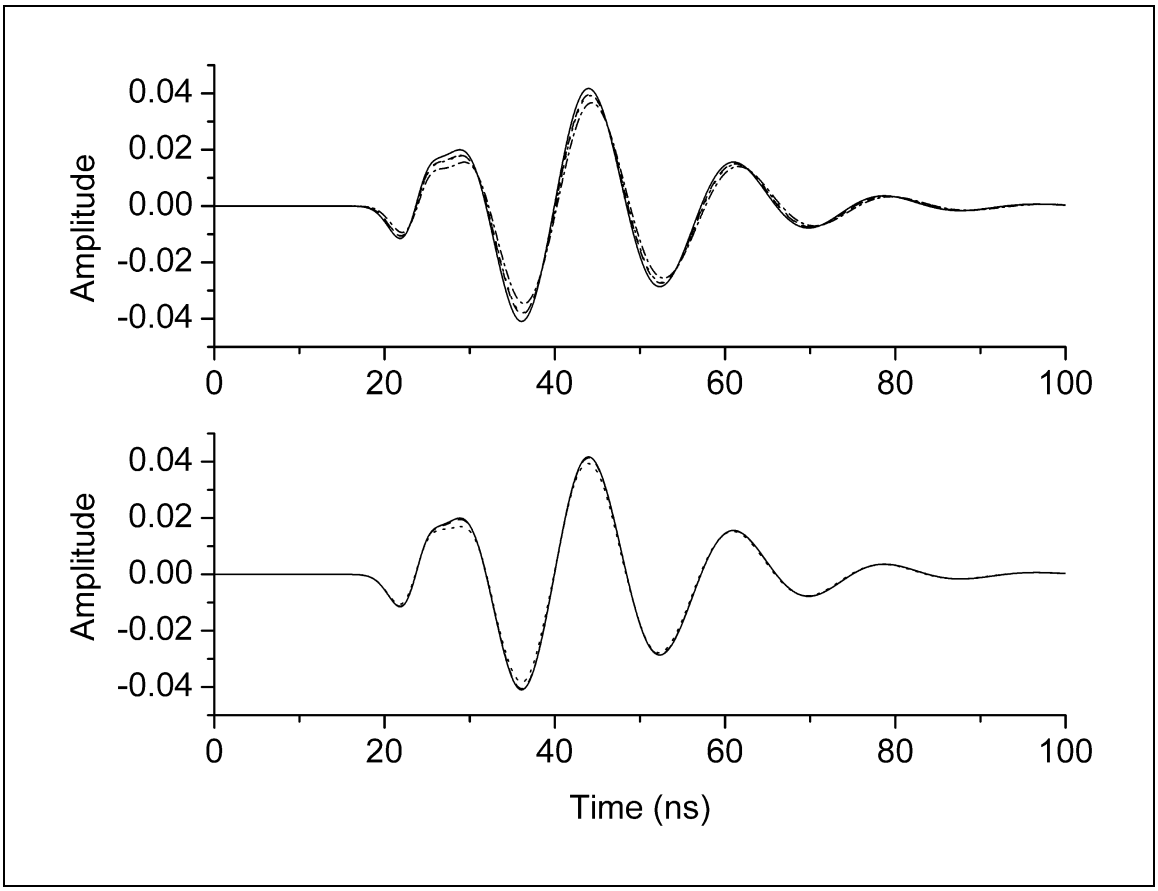

Figure 3.18. Upper graph shows the effect of rough surface scattering. Simulated results for a smooth (solid) surface, 2 cm (dashed), 3 cm (dotted), and 6 cm (dash-dot) asperity heights are shown. Lower graph shows the effect of volume scattering. Simulated results for a homogeneous (solid) half-space, 6 cm diameter inclusions (dashed, barely visible beneath the solid line), and 12 cm (dotted) diameter inclusions are shown. The wavelength in the soil is 1.87 m.

chosen in each case to minimize spatial frequency. The soil properties were $\varepsilon_r = 9$, $\sigma = 20$ mS/m, and the standoff was 7 cm. The mean difference in IMSP parameter estimates (using the *Hilbert* attribute set) between the flat and rough surfaces was less than 4% for 2 and 3 cm asperity heights, but rose to 12% for the 6 cm asperities. These results indicate that the above guidelines for surface scattering are valid for the near-field region of the RTDGPR antennas.

A further assumption of the IMSP algorithm is that no volume scattering occurs within the sensitive region. Volume scattering caused by objects or groups of objects larger than ~$\lambda/3$ in the direction transverse to the propagation direction of incident waves are generally visible in the pseudo-section (Rossiter, 1977), and scatterers smaller than ~$\lambda/10$ may not be visible. Studies of volume scattering of radar signals in temperate glaciers show that melted water bubbles smaller than ~$\lambda/10$ have a negligible effect on wave propagation and loss (Watts and England, 1976). Reflectors measuring less than ~$\lambda/8$ are generally not resolvable, and the amplitude of the reflected wave depends on the reflector's contrast and thickness (Widess, 1973). Nonetheless, all of these types of scatterers cause losses by redirecting the incident energy out of the original propagation direction. Losses due to invisible scatterers usually increase with frequency, and their effects can often be described with a power law (ω^n where *n* varies from -1 to 4, Balanis, 1989). For instance, Rayleigh scattering increases as ω^4.

Volume scattering of aerosols is routinely studied by the remote sensing community, however only a few studies have been made for low frequency electromagnetic scattering in earth materials. Watts and England (1976), Smith and Evans (1972), and Bogorodsky et al. (1985) discuss volume scattering in temperate glaciers at frequencies down to 10 MHz. These authors discuss and provide analysis for volume scattering of variously distributed scatterer sizes. Smith and Evans concluded that air or water bubbles in ice smaller than 1 mm were insignificant at 1 GHz. Thus, low contrast objects as large as 20 cm are insignificant at 50 MHz where the host medium has an RDP of four. Lampe and Holliger (2003) found that, for a 400 MHz unshielded

bowtie antenna, the effects of randomly distributed subsurface properties were minimal when the standard deviation of the material properties was less than 2.5%, or when the correlation length was greater than five meters. Scattering effects were most pronounced when the correlation length l is near $1/k$.

Volume scattering due to particles smaller than ~$\lambda/10$ have a negligible effect on the IMSP algorithm. Conversely, the RTDGPR algorithm cannot be applied when shallow scatterers are visible in the pseudo-section. Since particles larger than ~$\lambda/3$ are generally visible, there is a small range (~$\lambda/10$ to ~$\lambda/3$) of invisible particle sizes that can possibly affect the IMSP algorithm. Since the refracted wave is the only subsurface energy transport mode contributing to early arrivals, the effect of subsurface volume scattering by these invisible scatterers is not expected to be large. To investigate this hypothesis, FDTD simulations were made to investigate the effects of volume scattering. In the simulation, 6 cm and 12 cm diameter spheres were placed on a 20 cm grid throughout the subsurface, with the antennas placed 7 cm above the ground. The balls had $\varepsilon_r = 4$ and $\sigma = 0$, and the matrix had $\sigma = 20$ mS/m and ε_r was adjusted so the volume average RDP was 9. The results are shown in Figure 3.18. The simulated waveforms for the 6 cm spherical volume inclusions are very similar to the waveform for the case of a homogeneous half-space. The mean difference in IMSP parameter estimates (using the *Hilbert* attribute set) between the homogeneous and heterogeneous subsurface was less than 5% for the 6 cm spheres. Since subsurface objects that are invisible due to their small size have little effect on the IMSP algorithm in comparison to rough surface scattering (see Figure 3.18), no restrictions are made for invisible subsurface objects. Invisible graded or layered subsurface properties are an exception, and may affect the IMSP algorithm (see below).

Both surface and volume scattering cause depolarization of the transmitted waves Beckmann, 1968). For example, the diffuse scattering depicted in Figure 3.16 can cause depolarization. The amount of amplitude reduction of an incident plane wave due to depolarization is accounted for in the rough surface scattering analysis made by Ulaby et

al. Mild rough surface scattering causes reflected waves to be scattered out of a given polarization, and it also causes waves to be scattered into a given polarization. Within the realm of minimal diffuse scattering allowed by the IMSP algorithm, depolarization effects can be ignored.

The depth of the sensitive region varies depending on material properties. In general, no visible subsurface reflections are permitted in the IMSP time window. In the case of a lossless medium and the longest time IMSP window (10-40 ns), the subsurface must be homogeneous to a depth of $\sim 4/\sqrt{\varepsilon_r}$ meters. However, when conductive or lossy ground is present, this depth can be shallower. To investigate this phenomenon, FDTD simulations were made where a shallow 15, 30, 50, or 72 cm thick layer ($\varepsilon_r = 9$, $\sigma = 20$ mS/m) overlies an infinitely thick layer ($\varepsilon_r = 25$, $\sigma = 0$ mS/m). The simulated response is shown in Figure 3.19. Note that the response when the top layer is 50 cm thick is essentially identical to the homogeneous case for time less than 40 ns, and the IMSP algorithm returns very similar soil property estimates when the thickness is greater than or equal to 50 cm. Some moisture profiles discussed above have changing dielectric properties near the surface. FDTD simulations were made where the soil properties graded linearly from $\varepsilon_r = 5$, $\sigma = 0$ to $\varepsilon_r = 15$, $\sigma = 10$ mS/m, and from $\varepsilon_r = 5$, $\sigma = 10$ to $\varepsilon_r = 15$, $\sigma = 20$ mS/m over the first 10 cm of the subsurface. For these cases, the IMSP soil property estimates reflected the properties of the lower layer, and the conductivity estimates were 30-40% too high. To avoid inaccurate results, varying soil properties in the sensitive region should be avoided when possible. When material properties in the sensitive region change slowly in the vertical direction or are laterally continuous, the inhomogeneity may not be visible in the pseudo-section. The following paragraphs discuss various indicators of invalid environmental conditions for applying the IMSP algorithm such as shallow inhomogeneity. These indicators should be used when invisible inhomogeneity is suspected.

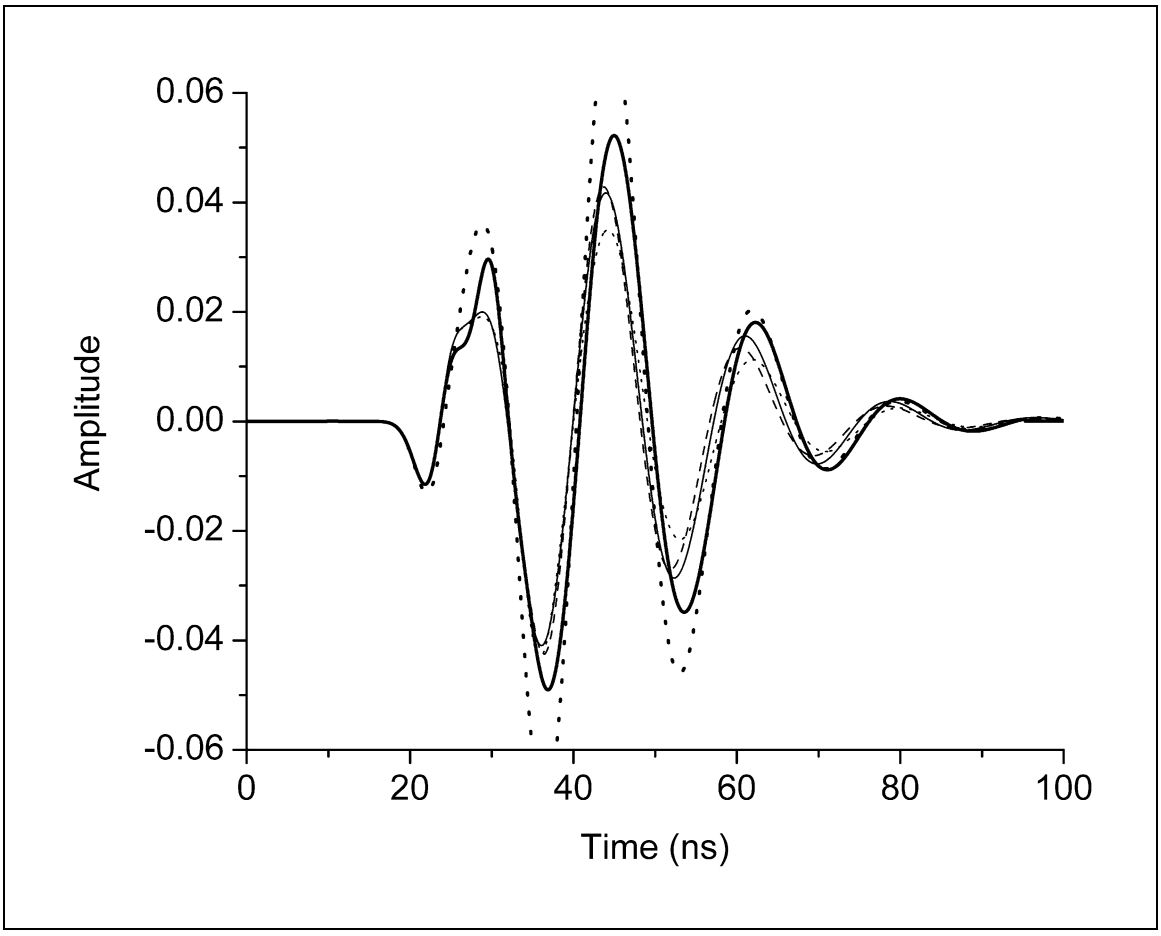

Figure 3.19. Effects of thin surface layer. Simulated results for a homogeneous (thin-solid) sub-surface, a 72 cm layer (thin-dashed), 50 cm layer (thin-dotted), 30 cm layer (thick-solid), and 15 cm layer (thick-dot) are shown. The wavelength in the soil is 1.87 m.

The IMSP algorithm assumes that the soil properties are not frequency dependent, however most soils do have frequency dependent dielectric properties. Fortunately, the bandwidth of most impulse GPR systems is limited to a few octaves, and the dielectric properties do not usually vary significantly over this small bandwidth. To test the performance of the IMSP algorithm with a frequency dependent dielectric, an FDTD simulation was made for soil with a conductivity of 10 mS/m, and a Debye dielectric with $\varepsilon_{r,dc} = 9$, $\varepsilon_{r,\infty} = 4$, and $\tau = 3 \cdot 10^{-9}$. The antenna standoff was 7 cm. Figure 3.20 shows the real and imaginary RDP for this dielectric where the DC conductivity is reflected in the imaginary RDP. The IMSP estimates of the soil properties using a 10% relative uncertainty and the *Spectral* attribute set are $\varepsilon_r = 11.5 \pm 3.7$, $\sigma = 23.5 \pm 10.0$ mS/m, $d = 5.4 \pm 1.2$ cm, and $\varepsilon_r = 12.1 \pm 4.5$, $\sigma = 30.2 \pm 10.2$ mS/m, $d = 5.1 \pm 1.2$ cm for the *Hilbert* attribute set. If the standoff is constrained to be 7 cm during the inversion, then the

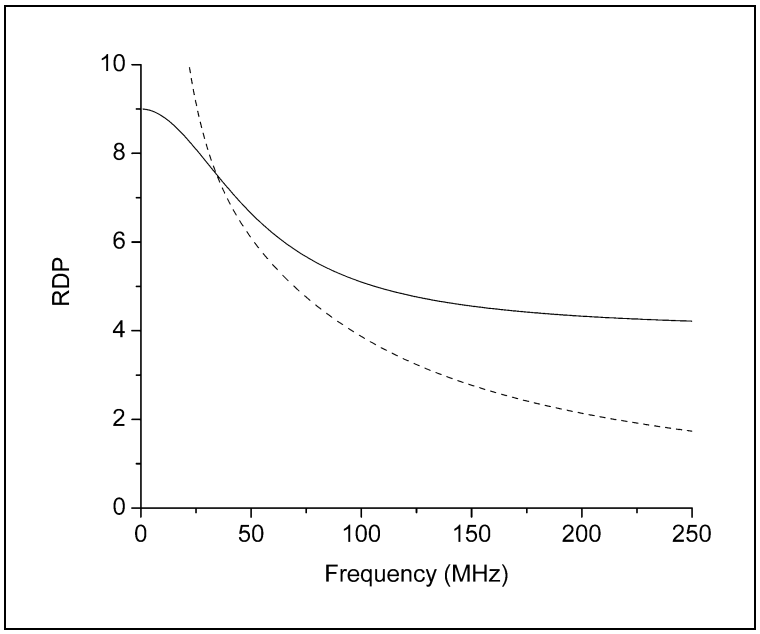

Figure 3.20. Frequency response of a Debye dielectric with $\varepsilon_{r,dc} = 9$, $\varepsilon_{r,\infty} = 4$, and $\tau = 3 \cdot 10^{-9}$. A DC conductivity of 10 mS/m is reflected in the imaginary RDP (dashed).

IMSP estimates are $\varepsilon_r = 5.2 \pm 0.8$, $\sigma = 18.1 \pm 6.2$ mS/m for the *Spectral* attribute set, and $\varepsilon_r = 5.8 \pm 2.4$, $\sigma = 17.4 \pm 6.9$ mS/m for the *Hilbert* attribute set. Several conclusions can be drawn from these numbers. First, the frequency dependent response is different enough from the frequency independent case to cause the IMSP algorithm to select incorrect soil property estimates. However, by properly constraining the standoff, reasonable estimates are returned. An independent measure of the standoff becomes more beneficial as survey conditions deviate from ideal. Also, since the IMSP algorithm only considers real RDP values, the dielectric loss contributes to the conductivity estimate. In this case, an effective conductivity of 17 mS/m accounts for both DC conductivity and dielectric losses at 50 MHz. Note that this test case is a worst-case scenario. Fortunately, most earth materials exhibit a broader relaxation than that of the Debye model. As stated previously, frequency dependent attenuation due to volume scattering is ignored because only the surface waves sample the subsurface and the resulting effect is small.

Several indicators can be used to determine if the assumptions and limitations of the IMSP algorithm have been violated. The assumption of horizontal homogeneity can be tested by looking at changes in the early arrivals along the survey line. A horizontal variogram has been implemented in *GPR Workbench* and can be used for this task. Detecting vertical homogeneity can be more difficult when there is no lateral indication of variation. Vertical inhomogeneity can be indicated by considering successively smaller time windows. To illustrate this idea, the simulated response due to thin shallow layers ($\varepsilon_r = 9$, $\sigma = 20$ mS/m) of various thicknesses over an infinitely thick layer ($\varepsilon_r = 25$, $\sigma = 0$ mS/m) are shown in Figure 3.19. Figure 3.21 shows the IMSP soil property estimates for different layer thicknesses using different window lengths when extracting waveform attributes (the *Spectral* attribute set was used here). Figure 3.22 shows the results when the standoff is constrained to 7 cm during the inversion. These results indicate that vertical heterogeneity may be indicated when the IMSP soil property estimates change significantly using different window lengths, and that this indicator is

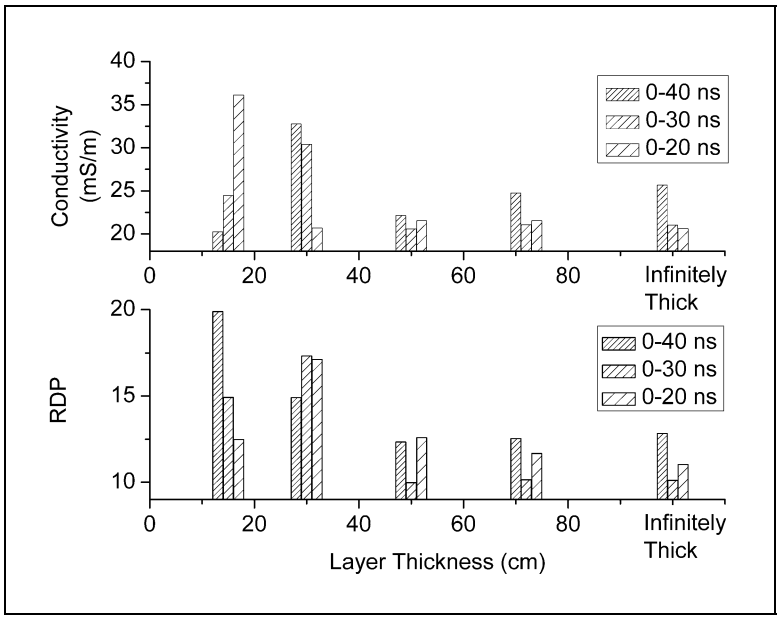

Figure 3.21. The results of different windows lengths used in the IMSP waveform parameterization can indicate vertical heterogeneity. Bars are for layer thicknesses of 15, 30, 50, 72 cm, and infinitely thick.

better when the standoff is independently determined. When using this method one must consider that IMSP estimates using shorter time windows produce solution sets with more statistical dispersion.

A small solution set population (e.g. less than about 25 out of a possible 125) indicates that the inversion algorithm has not satifactorily fit early arrivals. The likely causes of this case are that the material properties are beyond the range of cataloged of FDTD simulations, a near zone scatterer is present, graded or layered soil properties exist in the sensitive region, or significant surface scattering is occurring. Comparing survey results collected a few days apart may indicate active vadose zone moisture redistribution. Independent knowledge often exists to help determine if conditions are in the bounds of the limitations and assumptions. For instance, the paving on a road surface may be thin enough to cause a subsurface reflection in the early time window, but the

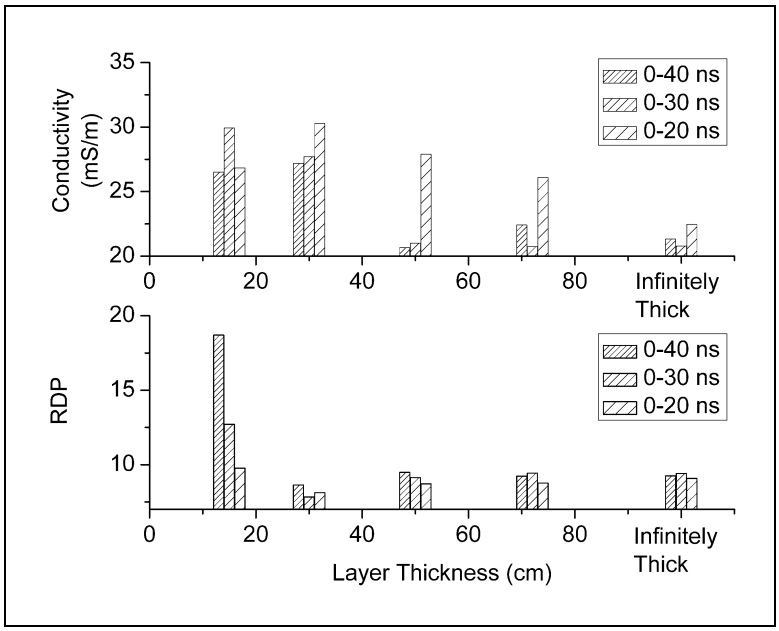

Figure 3.22. The results of different windows lengths as in Figure 3.21, except standoff was constrained to 7 cm during inversion. Bars are for layer thicknesses of 15, 30, 50, 72 cm, and infinitely thick.

pseudo-section may not contain laterally changing waveforms indicating a reflector moving into the early time window. Other knowledge includes recorded precipitation, depth of the water table, and estimated vertical extent of the capillary fringe based on soil type (i.e. typically ~10 cm for sand and ~1 meter for clay), etcetera. Always compare results to independent information such as TDR probe measurements, neutron probe measurements, cone penetrometer resistivity measurements, and core samples when they are available. Finally, an estimate of the height of surface asperities and the distance between them at the survey site should be made to determine if surface scattering is excessive. Schneeberger et al. (2004) discuss an automated method to generate a digital surface map of a survey area from digital photographs taken with a hand-held camera and

a global positioning unit. Measures of surface roughness can be calculated from digital surface maps.

Some comments regarding the possibility of extending the IMSP method to markedly heterogeneous surface properties are in order. As an example, consider the case of one antenna on a sidewalk and the other over soil. The frequency response of each antenna will be different because ground due to loading by different materials beneath them. Since the mutual reactance is frequency dependent, it will be affected by the differing response frequencies. The surface reflection coefficient is highly dependent on material properties and is nonlinear over the range of expected soil properties. Since some waves will reflect off of the soil and some will reflect off of the sidewalk, the effect on the net response is difficult to generalize. The refracted wave will have a different travel time and will have reduced amplitude due to the reflection of some of the refracted energy at the soil-sidewalk boundary. Changing the air-soil reflection coefficient changes the energy backscattered into the antenna and changes the character of the shield reverberations. From these generalizations, it must be concluded that it would be difficult to make a hybridized response or mixing formula using the response of both antennas over the sidewalk together with the response of both antennas over the soil. This conclusion is also supported by the non-linearity of the IMSP forward operator versus RDP and conductivity. Characterizing vertical heterogeneity may be a different matter. Lambot et al. (2004c) has successfully produced moisture profile information using air-launched antennas. A similar approach may be viable with ground-coupled antennas. Finally, note that higher frequency antennas may be more useful in heterogeneous regions because the size of sensitive region will be reduced when using higher frequency antennas. At a given locale, the sensitive region for a 50 MHz antenna pair may be heterogeneous, and the sensitive region for a 500 MHz antenna pair may be approximately homogeneous. For example, GPR data collected by Olhoeft et al. (1994) illustrates that a shallow object can be in the near field region of the antennas and in the

IMSP sensitive region at low frequencies, and beyond the near field and sensitive regions at high frequencies.

3.5 Field Example: Soil Properties and Standoff

A data set collected with the RTDGPR at the Mud Lake test site at the Idaho National Laboratories is ideal for testing the performance of the IMSP algorithm. The Laboratory buried a number of objects (plastic and steel drums) at known depths at the test site. Unfortunately, the soil was too lossy to permit GPR imaging of the buried objects. Even so, the IMSP algorithm was applied to estimate the shallow soil properties and the results are presented below. The soil at the survey site is composed of silt and clay derived primarily from Tertiary rhyolitic volcanic ash (Ralston and Chapman, 1969). The soil was dry to the touch (the site is in a high desert), and the water table is at least 50 meters deep. The soil is essentially homogeneous in terms of grain size, texture, and color for the shallow depths investigated by the IMSP algorithm (< 1 meter). Soil samples were collected from a single boring at depths of approximately 15, 30, 45, and 60 cm. The electrical properties of the collected soil samples were measured in the laboratory, and the results support the homogeneous assertion (see results below). The transmission line method was used to make the laboratory measurements (Kutrubes, 1986; Canan, 1999). The field site is shown in Figure 3.23. The ground surface at the site had broad hummocks, which caused the antenna standoff to vary as the cart rolled along. The survey consists of 11 parallel lines 25 meters long spaced one meter apart.

A number of survey configurations (different antenna polarizations, antenna offsets, attenuator settings, etc.) were planned, however equipment failure prevented data collection in all configurations. The RTDGPR receiver module attenuator is usually set to either record quality late time arrivals and clip the early time arrivals, or to provide high fidelity early arrivals. Several surveys were made with the attenuator set for optimal

Figure 3.23. The RTDGPR antennas and cart (left), and the actual survey site (right) where the brush has been removed.

late time arrivals, and only one survey was made using the early time attenuator setting (i.e. large attenuation so that the logarithmic amplifier response was linear). The intention was to collect high-fidelity early-time data at several antenna offsets, but the transmitting pulse generator completely failed moments after collecting only one early time data set. In fact, the generator output was most likely reduced during all of the surveys. Several facts support this conclusion. First, the amplitude of the early time arrivals is about 50% of the expected value based on the laboratory tests of the soil samples and the IMSP forward operator. Second, after the manufacturer of the pulse generator repaired the unit, they reported that a component failure caused one of the two high voltage power supplies to fail. These high voltage power supplies are switched to the generator output to produce the output voltage step. Failure of one of the power supplies would reduce the output amplitude by 50%. Third, the manufacturer reported that this failure mode has occurred previously with other pulse generators. In analyzing the data, it is assumed that the pulse generator output was 50% of the normal level, and the recorded data were compensated by multiplying by two before normal processing by the IMSP algorithm.

Before the IMSP algorithm can be applied to the survey data, each component of uncertainty between the predicted and actual data must be evaluated. The uncertainty component Σ_1 due to the difference between the simulated and experimental waveforms is taken from Table 2.5 (8.98% and 6.98% for the *Spectral* and *Hilbert* attribute sets respectively). Uncertainty component Σ_2 is estimated using the signal to noise ratio for early time arrivals, which is about 150:1 for the RTDGPR. The early arrivals of other GPR systems should have similarly high signal to noise ratios due to the proximity of the transmitting and receiving antennas. Finally, the uncertainty component due to discrete sampling of the IMSP forward operator is estimated by interpolating between the values listed in Table 3.3 using laboratory measured values of the soil properties. The estimated discretization errors are 4.5% and 9.3% for the *Spectral* and *Hilbert* attribute sets respectively. Using these values, the calculated relative uncertainty for the *Spectral* and *Hilbert* attribute sets are 10.1% and 13.7% respectively.

Figure 3.24 shows the results from the IMSP algorithm using the *Hilbert* attribute set for the survey line that traversed the sample borehole. The laboratory results for the soil properties (triangles) are shown along with the IMSP estimated soil properties and antenna standoff. The standoff estimates agree well with the expected value. The antenna heights were adjusted to 7 cm when the antenna cart was fabricated, but later damage to the steering yoke caused a small (undetermined) reduction in height. The assumption of a flat specular surface is invalid near the center of the line (11-17 meters) where large hump is evident. The estimates of conductivity and permittivity agree well with the laboratory values. There is some negative correlation between the standoff estimates and the conductivity. This correlation is likely due to the fact that the principal components of the solution set covariance are not generally well aligned with the model parameter axes. The IMSP algorithm could not find an acceptable solution near the hump in the middle of the line, and also in the 20-22 meter interval where some vertical banding is visible in the pseudo-section. This banding may be due to problems with the

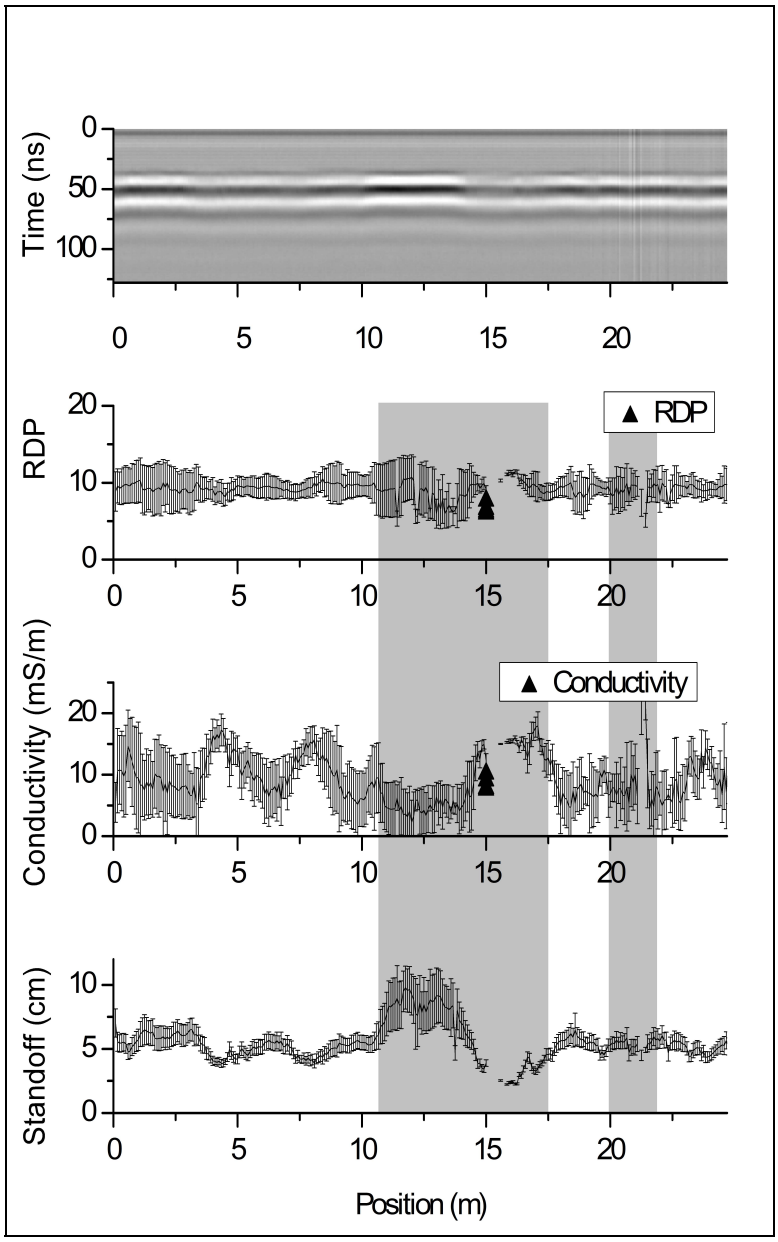

Figure 3.24. The top panel is a pseudo-section of the early arriving radar data. Lower panels show estimates of soil properties from IMSP algorithm from Mud Lake site. The *Hilbert* attribute set was used. Estimates are the mean value of the solution set, and the bars indicate the standard deviation of the set. Triangles indicate laboratory results. The results are invalid in the shaded regions (see text).

pulse generator. These regions are shaded in Figure 3.24, and the results are considered invalid in these regions.

When using the *Spectral* attribute set and a relative uncertainty of 10.1%, no solutions could be found. Figure 3.25 shows the results for a relative uncertainty of 20%. Note the large error bars due to the increased uncertainty. The standoff and RDP values compare well with the *Hilbert* attribute set results. However, the conductivity estimate is much different from the laboratory results and the *Hilbert* attribute set results. One plausible explanation is that the sparse sampling of the forward operator did not capture the character of the changing waveform attributes in this region of model space. This region of model space is coincidentally where the gradients of the waveform parameters are highest (see Section 3.3.1). There is also less confidence in the accuracy of the FDTD simulations in this region of model space because the antenna response is sensitive to the properties of the absorber used in the antennas, which are not precisely known. Note also that the resolution of the conductivity is less than the other model parameters according to the covariance of the solution set.

The *GPR Wave Utilities* program facilitates building IMSP forward operators using various waveform attribute sets, and inverting for soil properties and antenna standoff. The program can process a single trace, or all of the traces in an RTDGPR data file. More information about *GPR Wave Utilities* can be found in Appendices B and C, and the accompanying DVD-ROM. The processing records for building the forward operators and processing the Mud Lake data can also be found on the DVD-ROM, along with the raw Mud Lake RTDGPR data.

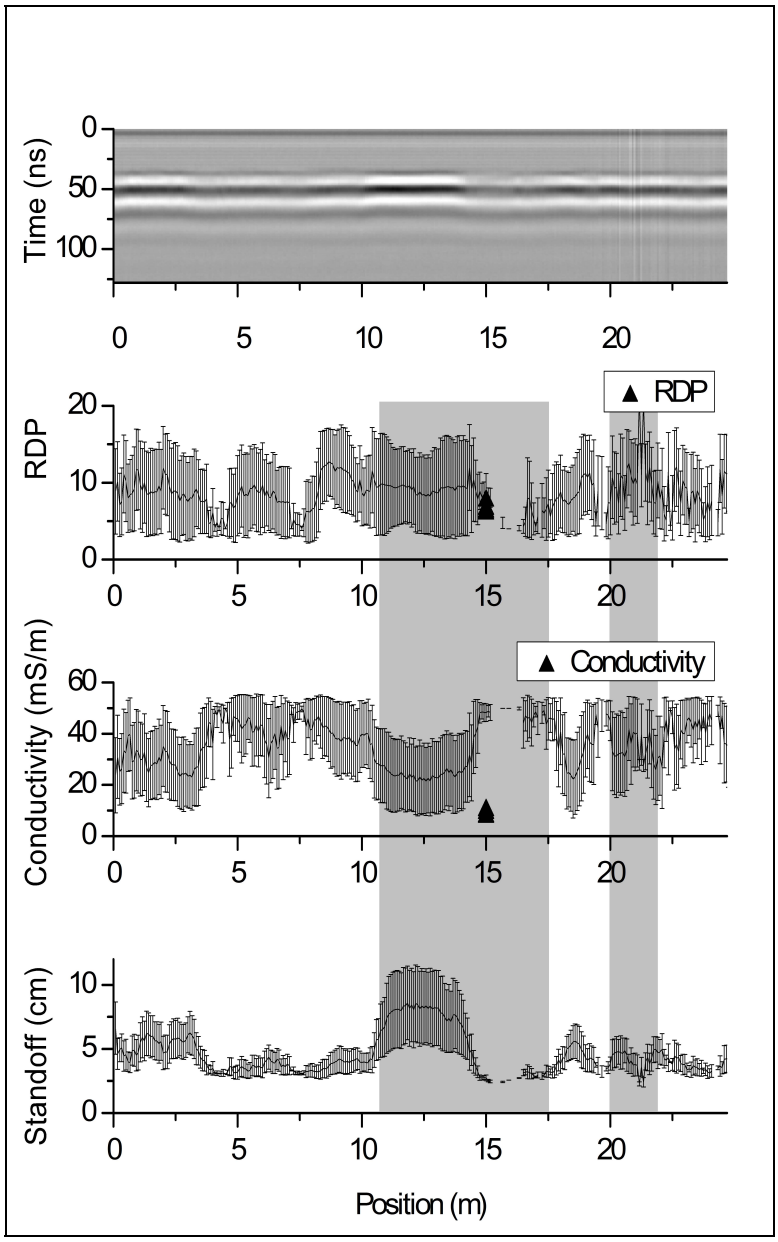

Figure 3.25. The top panel is a pseudo-section of the early arriving radar data. Lower panels show estimates of soil properties from IMSP algorithm from Mud Lake site. The *Spectral* attribute set was used. Estimates are the mean value of the solution set, and the bars indicate the standard deviation of the set. Triangles indicate laboratory results. The results are invalid in the shaded regions (see text).

CHAPTER 4

PROCESSING ALGORITHMS TO CLARIFY IMAGES

4.1 Introduction

This chapter serves as an illustration of the utility of a calibrated radar system. Knowledge of the shallow ground properties and the antenna response are cornerstones to clarifying subsurface images. This is especially true when conductive or lossy ground is present. In this Chapter, the utility of a full characterization of the antenna response including the shallow ground properties is demonstrated through two algorithms. The first algorithm estimates the material properties of a planar reflector using deterministic deconvolution, and the second algorithm produces higher resolution migrated images in conductive and/or dispersive ground. These algorithms require information about the system response, which can be estimated using the methods in Chapters 2 and 3, and Section 4.3.1. These examples are a small sample of the many ways to improve imaging and subsurface information when the system response is known.

The method to estimate the properties of a scatterer involves several steps. Once the response of the GPR electronics and antennas are known, and an estimate of the ground properties in the vicinity of the antennas is available, then it is a straight-forward matter to calculate the fields incident on any subsurface scatterer under the assumption that the ground is homogeneous and isotropic between the antennas and the scatterer. Using the energy reflected from the scatterer, it's electrical properties can be estimated, as in the example presented in this Chapter. In general, this procedure is much more difficult when the shape of the scatterer is irregular and when reflections from multiple scatterers arrive at the receiving antenna simultaneously.

The method to improve image resolution partially reverses the effects of dispersion. Wave propagation through dispersive media causes a filtering effect that causes distortion of the subsurface waves. Usually this filter removes the high frequency portions of the transmitted spectrum and changes the phase of the transmitted wavelet, which often results in poor image quality. The resolution of GPR images in lossy media can be improved by reversing dispersion and by migration. Migrating GPR images improves resolution by collapsing diffraction patterns onto their scatterers. Oftentimes however, migrating GPR images of dispersive soils does not improve resolution and may even degrade image quality. This problem may be partially alleviated by reversing dispersion during migration. The dispersive migration routine presented in this Chapter improves resolution by treating both diffraction and dispersion.

Application of the methods described in this Chapter requires making a number of assumptions. Irregular scatterers, multiply scattered fields, multi-pathing, guided waves, caustics, and targets in magnetic, anisotropic, or heterogeneous media are beyond the scope of this dissertation. When calculating the subsurface fields, it is further assumed that the ground surface is a specular reflector, that the bottoms of the antennas are parallel to the ground, and that the antennas are perfectly co-polarized. The data processing algorithms presented in this Chapter can tolerate poor signal to noise and signal to clutter ratios, although these ratios should be significantly greater than unity to achieve practical results. Generally, the more noise and clutter, the more uncertainty in the results. Further assumptions for specific procedures are stated in the discussion of the procedures below.

4.2 Calculating the Subsurface Fields

There are many ways to calculate subsurface fields generated by antennas, and Chew (1995) presents a thorough introduction to many methods. The task of calculating

subsurface fields generated by antennas located above the surface can be generalized as a diffraction problem. The first part of a diffraction problem involves calculating the fields generated by the sources and scatterers (i.e. antenna parts and the ground surface). The second part of the problem is to propagate these fields away from their generators. The first task is usually the most difficult. Common methods for calculating the fields due to their generators include analytic methods based on integral equations, and numerical methods such as finite difference, finite element, and the boundary element method. These methods generally require significant computing time. A goal for many of the methods presented in this dissertation is that they can be adapted to run in real-time. The ability to quickly estimate the subsurface wave fields enables other algorithms such as image processing to help provide better information to the GPR user in a field situation. Therefore, the fields due to generators at the surface are calculated *a priori* using FDTD simulations for the RTDGPR, and the fields further from the sources can be quickly calculated with a propagator when needed.

There are many schemes for propagating fields away from their sources, and many propagators are based on the Kirchhoff integral (Chew, 1995; Jackson, 1999; Tai, 1971). The Kirchhoff integral states that the fields anywhere in a linear, homogeneous, isotropic volume containing no sources can be determined from the known fields on a closed surface around the volume. In the case of a GPR, it is assumed that the fields produced by the antennas are known on a disk of infinite radius just beneath the ground surface (see Figure 4.1). A half-hemisphere of infinite radius intersects the disk. The fields on the surface of the hemisphere are zero according to the Sommerfeld radiation condition. An asymptotic evaluation of the Kirchhoff integral can be made to quickly approximate the far-field waves when the source distribution has compact support on the disk. Unfortunately, this approximation is invalid in regions close to the sources and is therefore not applicable to the GPR problem. The wave fields and the Kirchhoff operator can be written in terms of a set of basis fields such as plane-waves. Using FFTs, the entire plane-wave spectrum of the fields near their sources can be efficiently propagated

to any distance or time. The decomposition of electromagnetic fields produced by antennas into plane-wave spectra for propagation and scattering is frequently discussed in the literature (i.e. Kerns, 1981; Hansen and Yaghjian, 1999; Chew, 1995). For these reasons, and because calculations based on FFTs are cost-effective, the plane-wave approach will be used here. The method presented in this Chapter is equivalent to the Kirchhoff approach, and calculates the fields in a user specified vertical plane.

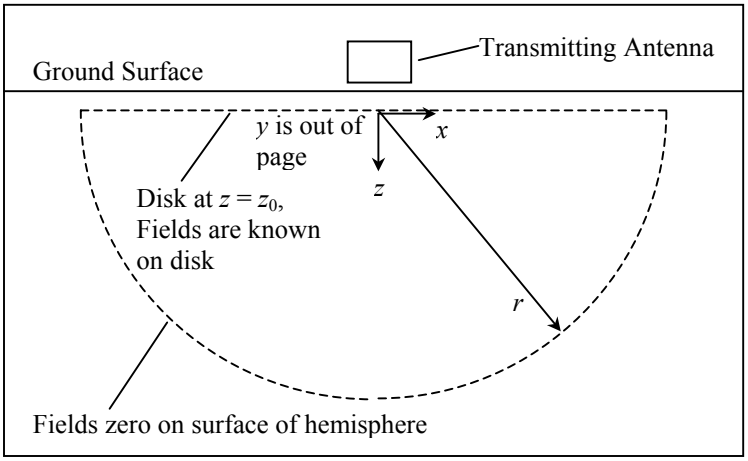

Figure 4.1. Section view of disk and half-hemisphere.

The subsurface fields can be quickly calculated using a catalog of FDTD simulations (see Chapter 2), the IMSP algorithm (see Chapter 3), a field propagator, and an optional interpolation scheme. In this Section a field propagator is introduced, and then the details of taking the simulated fields and propagating them to the desired subsurface depth are presented. To apply this method of calculating subsurface fields, a variety of assumptions must be made. In order to use the IMSP algorithm to estimate the soil properties, the soil surface beneath the antennas must be a specular reflector, and the shallow soil must be non-magnetic, linear, homogeneous, isotropic, and have a frequency

independent permittivity as discussed in Section 3.4. When using the propagator, the assumptions listed in Section 4.1 must be made.

In this work, a frequency-domain propagator advances the known fields on the disk in Figure 4.1. Although only two field components are required on the disk to arrive at a complete solution of electromagnetic waves below the disk (Hansen and Yaghjian, 1999), it is assumed that all six components (i.e. E_x, E_y, E_z, H_x, H_y, and H_z) are available since FDTD simulations compute all six. In a homogeneous and isotropic medium with no sources, the dynamic electric (and magnetic) fields obey the homogeneous telegraph equation

$$\nabla^2 \mathbf{E}(x,y,z,t) - \mu\sigma\,\partial_t \mathbf{E}(x,y,z,t) - \mu\varepsilon\,\partial_t^2 \mathbf{E}(x,y,z,t) = \mathbf{0} \tag{4.1}$$

where x, y, and z are the Cartesian coordinates (see Figure 4.1), t is time, σ is conductivity, and μ and ε are magnetic permittivity and dielectric permittivity respectively. A plane-wave solution to the telegraph equation has the form

$$\mathbf{E}(\mathbf{r},t) = \mathbf{E_0} e^{i(\omega t - \mathbf{k}\cdot\mathbf{r})} \tag{4.2}$$

where $\mathbf{k}$ is the complex wave number in the direction of propagation, $\mathbf{k} = k_x\hat{\mathbf{x}} + k_y\hat{\mathbf{y}} + k_z\hat{\mathbf{z}}$, $\mathbf{r} = \hat{\mathbf{x}}\,x + \hat{\mathbf{y}}\,y + \hat{\mathbf{z}}\,z$ is the position vector, ω is the radian frequency, and $\mathbf{E_0}$ is a constant. Taking the temporal Fourier transform of Equation 4.1 yields the Helmholtz equation

$$\nabla^2 \mathbf{E}(x,y,z,\omega) + k^2 \mathbf{E}(x,y,z,\omega) = \mathbf{0} \tag{4.3}$$

where k is the wave number for the homogeneous medium described by Equation 1.1, and $k^2 = \mathbf{k}\cdot\mathbf{k}$. Taking Fourier transform over the x and y variables yields

$$\nabla_z^2 \mathbf{E}(k_x,k_y,z,\omega) + k_z^2 \mathbf{E}(k_x,k_y,z,\omega) = \mathbf{0} \tag{4.4}$$

where k_z is defined by the dispersion relation

$$k_z = \pm\sqrt{k^2 - k_x^2 - k_y^2}\,, \tag{4.5}$$

and the positive sign is used for downward propagating (or attenuating) waves. Note the spatial Fourier transforms use the opposite sign convention as the temporal transforms defined in Equations 2.11 and 2.12. A solution to equation 4.4 is

$$\mathbf{E}(k_x, k_y, z, \omega) = \mathbf{E_0}(k_x, k_y, z_0, \omega) e^{ik_z(z-z_0)}, \tag{4.6}$$

where z_0 is the coordinate of the plane where the fields are known (i.e. the source disk). $\mathbf{E_0}$ is determined via the Fourier transform of the fields on the source disk

$$\mathbf{E_0}(k_x, k_y, z_0, \omega) = \int_{-\infty}^{\infty}\int_{-\infty}^{\infty}\int_{-\infty}^{\infty} \mathbf{E}(x, y, z_0, t) e^{i(k_x x + k_y y - \omega t)} dx dy dt . \tag{4.7}$$

Finally, the fields anywhere can be found from

$$\mathbf{E}(x, y, z, t) = \frac{1}{(2\pi)^3}\int_{-\infty}^{\infty}\int_{-\infty}^{\infty}\int_{-\infty}^{\infty} \mathbf{E_0}(k_x, k_y, z_0, \omega) e^{-ik_z(z-z_0)} e^{-i(k_x x + k_y y - \omega t)} dk_x dk_y d\omega . \tag{4.8}$$

Equation 4.8 is a phase shift in the k_z direction followed by an inverse FFT over k_x, k_y, and ω.

In some cases, the subsurface fields are not needed everywhere. Perhaps the fields are needed at a subsurface point, or in a vertical plane. In these cases, fast calculation of the fields is possible while still considering the full 3D nature of the source and the fields. Three general cases will be considered. The first is the vertical plane containing the survey line, the second is the vertical plane transverse to the survey line, and the last is an arbitrary vertical plane.

In all of the FDTD simulations of the RTDGPR antennas, the antenna polarization ($\hat{\mathbf{x}}$ direction) is perpendicular to the line of survey ($\hat{\mathbf{y}}$ direction). For the vertical plane containing the survey line, the $\hat{\mathbf{x}}$ polarized fields can be found from

$$E_x(x, y = 0, z, t) = \frac{1}{(2\pi)^3}\int_{-\infty}^{\infty}\int_{-\infty}^{\infty}\int_{-\infty}^{\infty} E_{x0}(k_x, k_y, z_0, \omega) e^{-ik_z(z-z_0)} e^{-i(k_x x - \omega t)} dk_y dk_x d\omega \tag{4.9}$$

where E_{x0} is the $\hat{\mathbf{x}}$ component of $\mathbf{E_0}$, and the inside integral over k_y is not an inverse FFT and is quickly evaluated. For uniformly convergent functions such as the integrand of Equation 4.9, the order of inverse transforms and integration can be arranged as desired

(Butkov, 1968). An analogous equation can be used to find the fields polarized in the $\hat{\mathbf{y}}$ or $\hat{\mathbf{z}}$ direction. For a vertical plane transverse to the survey line, the fields are found using

$$E_x(x=0,y,z,t)=\frac{1}{(2\pi)^3}\int_{-\infty}^{\infty}\int_{-\infty}^{\infty}\int_{-\infty}^{\infty}E_{x0}(k_x,k_y,z_0,\omega)e^{-ik_z(z-z_0)}e^{-i(k_y y-\omega t)}dk_x dk_y d\omega\,. \tag{4.10}$$

The preceding cases are specialized examples of the general case where the fields are desired on an arbitrary vertical plane. This vertical plane is called the plane of incidence and is depicted in Figure 4.2. Cylindrical coordinates will be used as appropriate. For a plane wave traveling in direction **k**, the electric and magnetic fields are transverse to the direction of propagation. Any wave traveling in direction **k** can be decomposed into a transverse magnetic and a transverse electric component. The transverse magnetic component is given by

$$E_\rho(\rho,\phi,z,t)=\frac{1}{(2\pi)^3}\int_{-\infty}^{\infty}\int_{-\infty}^{\infty}\int_{-\infty}^{\infty}E_{\rho 0}(k_\rho,\phi,\phi_k,\omega)e^{-ik_z(z-z_0)}e^{-i(k_\rho\rho-\omega t)}d\phi_k dk_\rho d\omega \tag{4.11}$$

where $E_{\rho 0}$ is found from

$$E_{\rho 0}(k_\rho,\phi,\phi_k,\omega)= \tag{4.12}$$
$$\cos(\phi)E_{x0}(k_\rho\cos(\phi_k),k_\rho\sin(\phi_k),\omega)+\sin(\phi)E_{y0}(k_\rho\cos(\phi_k),k_\rho\sin(\phi_k),\omega)\,,$$

and E_{x0} and E_{y0} are the $\hat{\mathbf{x}}$ and $\hat{\mathbf{y}}$ components of $\mathbf{E_0}$ respectively. The transverse electric component is given by

$$E_\phi(\rho,\phi,z,t)=\frac{1}{(2\pi)^3}\int_{-\infty}^{\infty}\int_{-\infty}^{\infty}\int_{-\infty}^{\infty}E_{\phi 0}(k_\rho,\phi,\phi_k,\omega)e^{-ik_z(z-z_0)}e^{-i(k_\rho\rho-\omega t)}d\phi_k dk_\rho d\omega\,, \tag{4.13}$$

where $E_{\phi 0}$ is found from

$$E_{\phi 0}(k_\rho,\phi,\phi_k,\omega)= \tag{4.14}$$
$$-\sin(\phi)E_{x0}(k_\rho\cos(\phi_k),k_\rho\sin(\phi_k),\omega)+\cos(\phi)E_{y0}(k_\rho\cos(\phi_k),k_\rho\sin(\phi_k),\omega)\,.$$

Note that Equations 4.11 and 4.13 reduce to Equations 4.9 and 4.10 for $\phi = 0$ and $\pi/2$ respectively.

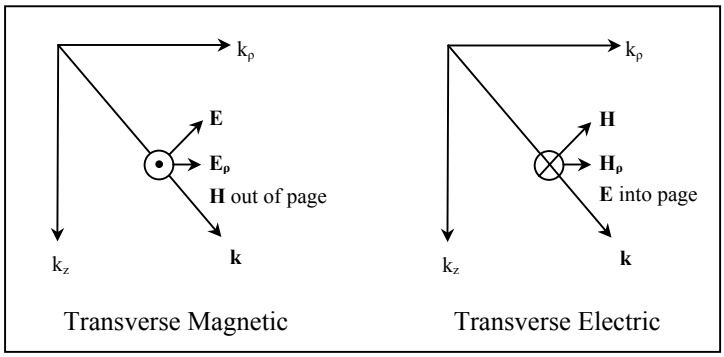

Figure 4.2. Transverse magnetic and transverse electric polarizations in the plane of incidence.

The preceding Equations (4.1-4.14) can be written in different coordinate systems or using other wave functions as the basis fields such as cylindrical waves or spherical waves. These approaches are preferred for scattering problems where the scatterer conforms to the shape of the basis fields (i.e. a pipe). Chew (1995) elaborates on these methods. There are methods other than FDTD that are feasible for determining the fields on the disk just below the ground surface such the as the plane wave scattering matrix and iterative mode matching techniques discussed in Section 2.5.1.

To implement a fast calculation of the subsurface fields, a catalog of FDTD simulations is made *a priori* for the antenna response over various soil types (see Chapter 2). Each cataloged simulation supplies the fields on the disk shown in Figure 4.1 for a combination of ground properties and antenna standoffs (i.e. the model parameters) such as those listed in Table 2.6 and shown as a grid in Figure 3.7. This catalog also contains the plane-wave spectrum of these fields as calculated by Equation 4.7. To calculate the subsurface fields, the first step is to estimate the soil properties and standoff using the IMSP algorithm (see Chapter 3). Next, find the catalog entry that most closely matches the IMSP model parameter estimates, and retrieve the frequency-domain fields on the disk $E_{x0}(k_x, k_y, z_0, \omega)$. Finally, calculate the subsurface fields using Equations 4.9-4.14

as appropriate. Note that it may be possible to calculate the subsurface waveform at a single point more accurately by interpolating between waveforms calculated for model parameters at each grid cell corner. The tri-linear interpolation method presented in Section 3.2 can be used. The interpolation should not be made in the time-domain. Rather, interpolating the amplitude and phase of the frequency-domain waveforms corresponding to each grid cell corner, $E_{l,m,n}(\omega)$ through $E_{l+1,m+1,n+1}(\omega)$, should provide better results (see Figure 3.8). With this method, it is possible to calculate an interpolated subsurface waveform as a continuous function of model parameters.

One problem with using the plane wave decomposition to quickly calculate the fields is that computing three-dimensional FFTs is time consuming. According to McGillem and Cooper (1984), an FFT involves $N\log_2 N$ complex additions and $(N/2)\log_2 N$ complex multiplications where N is the number of samples. A three-dimensional FFT requires $3N^3\log_2 N$ additions and $3N^2(N/2)\log_2 N$ multiplications (assuming the same number of samples in each direction). Fortunately, once $\mathbf{E_0}$ has been determined from Equation 4.7, the fields anywhere can be calculated by performing two two-dimensional FFTs (requiring $4N^2\log_2 N$ additions and $2N^2\log_2 N$ multiplications) using Equations 4.9-4.14. With N on the order of 1000, it is possible to compute two-dimensional FFTs in a few seconds on a standard PC (3 GHz Pentium4 with 1 GB or more of RAM). Significantly faster computing is possible by only integrating over the propagating portion of the spectrum where $k_x^2 + k_y^2 \le k^2$, but these results are only valid at a distance of several wavelengths or more from the antenna.

Another difficulty arises when using FDTD results to determine the fields on the infinite disk (see Figure 4.1). The FDTD grid is of limited spatial extent, and the fields on the disk cannot be specified outside the extents of the grid. Fortunately, the fields on the disk have limited support because the antenna can be treated as an aperture source. The scan plane can also be thought of as an aperture through which the fields are sampled. If the scan plane aperture is larger than the antenna aperture, then its effect on

the sampled fields is small when the apertures are close together. Refraction of waves traveling into the soil tends to cause the waves in the soil to travel in a more vertical direction. This in turn minimizes the difficulties associated with a non-infinite scan plane and with sampling of large wave numbers (see discussion below). Figure 4.3 shows the waves that are intercepted by the scan plane. Radzevicius (2001) describes spherical and lateral waves in the ground, and how these waves combine to increase the power radiated in certain directions. Obviously, the scan plane cannot intercept horizontally traveling waves, but these waves are usually of little interest.

The extent of the scan plane and the spatial sample interval are very important. The scan plane should be large enough to capture at least one complete cycle (spatially) of all waveforms transmitted into the subsurface, that is, its dimensions must be larger than the largest wavelength expected in the soil. If the scan plane is too small, then the downward propagated fields will be inaccurate. The spatial sampling interval must be at least twice the smallest wavelength expected. Guidelines for FDTD simulations require a sample interval of a tenth of a wavelength (Giannopoulos, 1997), which is 1 cm using a

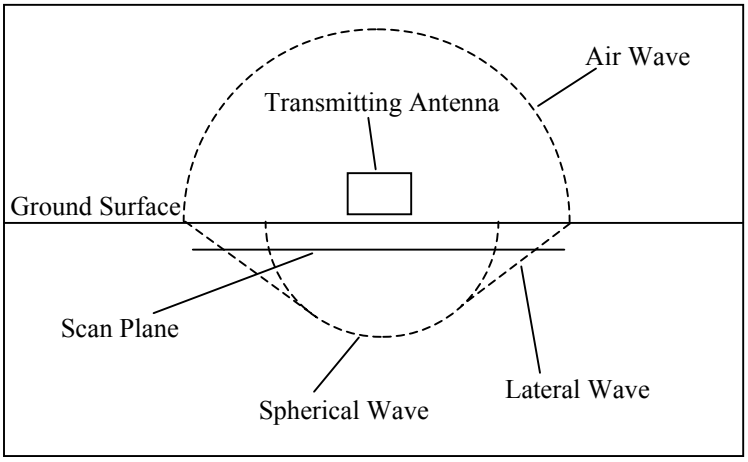

Figure 4.3. Section view illustrating subsurface wave fronts and scan plane.

maximum frequency of 300 MHz and a maximum RDP of 100. The FDTD time step interval is determined from the spatial sample interval and the Courant criterion for FDTD simulations (Taflove and Hagness, 2000). Based on this criterion, the fields on the scan plane are calculated and recorded by *GPRMax* every 19.25808 ps. The simulations made for the example presented in Section 4.3 provided fields on a scan plane 280 cm on a side, and at a 1 cm sample interval. Due to memory limitations with the FDTD simulations, only the transmitting antenna was simulated. However, comparisons to simulations with both antennas indicate that the presence of the receiving antenna causes a negligible change to the radiated fields except in the region very near the antennas (i.e. the top 10 cm of the ground). The 1 cm sample interval is more than adequate for the RTDGPR, however the limited horizontal extent of the scan plane (280 cm on a side) can only capture waves with a horizontal wavelength smaller than

$$2.80 > \lambda_h = \frac{2\pi \sin(\theta)}{\mathrm{Re}(k)}, \tag{4.15}$$

where λ_h is the horizontal wavelength, Re(k) is the real part of the wave number, and θ is the angle of wave propagation from vertical. Thus, for vertically traveling waves, the scan plane size is not an issue. Table 4.1 lists cutoff values of θ in terms of ε_r and σ at 50 MHz. A scan plane 2.8 meters on a side is adequate for most material properties expected in GPR surveys. However, if the scan plane is too far from the antenna, then energy traveling at a wide angle (large θ) may not be intercepted by the scan plane. Some researchers (i.e. Meinke and Hansen, 2004) have used filters to minimize the

Table 4.1. Minimum soil property values for scan plane to intercept waves traveling at angle θ from vertical at 50 MHz.

Min. RDP ε_r	Min. Conductivity σ (mS/m)	Angle 2θ (degrees)
4	0	138
4	9	180
4.6	0	180

effects of sharp truncation at the edges of the scan plane. However, Wang (1988) reports that filtering is unnecessary with proper sampling, and that filtering causes unwanted distortion in the spectrum.

The *GPR Wave Utilities* program has implemented a wave field propagator using Equations 4.7, 4.9-4.10. *GPR Wave Utilities* samples the fields on the scan plane according to the spatial extent and grid interval used in the FDTD simulations. *GPR Wave Utilities* pads the scan plane to 10 meters on a side (1000 x and y samples using a 1 cm interval) to improve the spectral resolution of the propagating spectrum, and assumes that that the fields beneath the antenna are symmetrical about the horizontal center of the antenna and scan plane. For the example presented in Section 4.3, the FDTD simulations record a 100 ns time series of the fields in 19.25808 ps intervals. This small time increment is not needed for the frequency domain propagation of the fields, therefore the *GPR Wave Utilities* propagator uses every 10^{th} time sample from the FDTD simulations (519 time samples). Evaluation of Equation 4.7 results in 1000 wave numbers in the $\hat{\mathbf{x}}$ and $\hat{\mathbf{y}}$ directions, and 250 temporal frequencies (approx. 0-2500 MHz). However, only 25 frequencies are stored in memory during calculations because there is no significant energy at higher frequencies (> 250 MHz). The higher order frequencies are included in the calculations so that the waveform returned from the inverse FFT has acceptable temporal resolution. The program starts by applying phase shifts over all k_x and k_y, and finishes with the integration and inverse FFTs. Evaluating Equation 4.7 requires a few hours because a standard 32-bit PC does not have enough RAM to make the calculation (with $N \approx 1000$) without using virtual memory on the hard drive. This is not a problem for fast calculation of the subsurface fields however, because the plane-wave decomposition for all the FDTD simulations for different soil types can be done *a priori*. The calculations in Equations 4.9 and 4.10 only require about 15 seconds to complete in a 3 GHz Pentium4 PC because a 3D FFT in not needed, and all of the relevant information can be contained in RAM. A real-time implementation of this method is possible using graphics processing units (GPUs). FFT implementations on

GPUs execute many times faster than on the CPU. For instance, Jansen et al. (2004) implemented a split-stream FFT on a GPU (ATI Radeon 9800) that executes 10 times faster than an enhanced butterfly FFT algorithm running on a 2.6 GHz Pentium4.

The catalog of FDTD simulations containing fields recorded on the scan plane has not been made at the time of this writing. However, the calibrated antenna models have been created and are described in Chapter 2. The input files for these models are included on the accompanying DVD-ROM. The frequency-domain propagator has been implemented in *GPR Wave Utilities*. Thus, all of the tools needed to build the catalog are provided in this dissertation. See Appendices B and C for more details.

4.3 Deconvolution for Reflector Properties

Deterministic deconvolution can be used to estimate the material properties of a scatterer if the incident and reflected waveforms are known, as well as the properties of the medium between the antenna and the scatterer. The problem is formulated as a deconvolution between the received waveforms and the system response, which estimates the reflection coefficient of the scatterer. The system response is defined as the GPR response that occurs when the antennas are positioned over an imaginary perfectly reflecting surface in the ground such as a plane, a cylinder, or a sphere. The system response is a function of the soil properties under the antennas, the known antenna response, the depth to the reflector, and its shape. The system response for the local soil properties can be determined by measuring the response over a known physical reflector, or it can be calculated from the known antenna response from simulations (see Chapter 2) and the IMSP estimates of the shallow soil properties (see Chapter 3). As a simple example, the properties of a planar surface (a lake bottom) are estimated. The system response used in the example is the GPR response of antennas over a perfect planar reflector in the subsurface. The properties of non-planar scatterers can also be estimated

by specifying the system response in terms of basis functions that have the same shape as the unknown scatterer. For a pipe, the formulas in the Section would be projected onto cylindrical basis functions so that the wave field is specified in terms of waves that are normally incident on the pipe.

Yilmaz (1987) discusses assumptions made in seismic deconvolution, but in the present work only a subset of these assumptions are made. Here, it is assumed that the source wavelet is known, that the waves are normally incident on the reflectors, and that scatterers are specular reflectors. The reflectors are in the far-field region of the antennas. The source wavelet and the recorded wavelet are not necessarily minimum phase, the wavelet need not be stationary. It is assumed that noise is white, and that signal to noise ratios are significantly greater than unity. Clutter and multiples are not accounted for. The assumptions in Section 4.1 also apply. The transmitting and receiving antennas must remain co-polarized. In the example below, it is assumed that the planar reflector is of infinite extent and no diffraction occurs. Finally, when measuring the system response, the perfectly reflecting surface that is used to define the system response must be deeper than the extent of the reactive near field of the antennas (discussed in more detail below). When the system response is determined from a completely characterized system such as the RTDGPR, the assumptions and limitations of Section 3.4 apply.

4.3.1 The Radar Equation and System Response Function

The Friis equation describes the general problem of transmission of an electromagnetic signal between two antennas by accounting for radiation, spreading, and reception of energy. The radar equation describes a more specific problem where a scatterer is placed between the antennas. Balanis (1997) and Orfanidi (2004) offer discussions on the Friis and radar equations and the standard parameters used here to

describe antennas. Consider the case of a generator transferring P_{tx} watts of power to a transmitting antenna with a gain G_{tx} in the direction of a scatter. If the scatter is a distance r from co-located, co-polarized transmitting and receiving antennas (i.e. monostatic), then the power received by the receiving antenna P_{rx} is

$$P_{rx} = P_{tx} G_{tx} \frac{1}{4\pi r^2} \sigma_s \frac{1}{4\pi r^2} A_{rx} . \tag{4.16}$$

where σ_s is the scatterer's radar cross section and A_r is the effective aperture or area of the receiving antenna. The effective aperture of the receiving antenna is related to it's gain G_{rx} by

$$A_{rx} = \frac{\lambda^2 G_{rx}}{4\pi} \tag{4.17}$$

where λ is the wavelength. If the medium between the antennas and scatterer is lossy, then the power at the recording device is

$$P_r = \frac{P_{tx} G_{tx} G_{rx} \sigma_s \lambda^2 e^{-2r\,\mathrm{Im}(k)} G_r}{(4\pi)^3 r^4} \tag{4.18}$$

where Im(k) is the imaginary part of the wave number (see Equation 1.1), and G_r is the gain of the receiver electronics. The dynamic range D_s needed by a radar system to image a scatterer with a cross section of σ_s in the absence of clutter is

$$D_s = \frac{P_r}{P_{tx}} = \frac{G_{tx} G_{rx} \sigma_s \lambda^2 e^{-2r\,\mathrm{Im}(k)} G_r}{(4\pi)^3 r^4} . \tag{4.19}$$

Equations 4.16-4.19 are far-field approximations where it is assumed that the dimensions of the antennas and scatterers are small compared to r, and that the wave field contains no near-field components. These equations also assume that the medium between the antennas and scatterers is homogeneous, linear, and isotropic, and an antenna standoff of zero is assumed. Even though these assumptions are not true for most cases in GPR, these Equations provide useful approximations. Since the normalized amplitude (see S-parameters in Section 2.2.1) is twice the square root of the power, the radar equation can

be used to relate the normalized wave amplitude at the transmitting antenna feed port a_{tx} to that of the receiving antenna b_{rx} according to

$$b_{rx} = a_{tx}\sqrt{\frac{G_{tx}G_{rx}\sigma_s\lambda^2 e^{-2r\,\mathrm{Im}(k)}}{(4\pi)^3 r^4}}\,. \tag{4.20}$$

Each component of the radar equation has an analogous expression using the plane-wave expansion in frequency-wave number space. Using this expansion, near-field components, arbitrary antenna standoff, and waves close to the antennas are properly treated. The plane-wave spectrum of the transmitted waves on the reference disk (see Figure 4.1) is given by

$$\mathbf{E_{0,t}}(k_x,k_y,\omega) = a_{tx}(\omega)\mathbf{T_0}(k_x,k_y,\omega)\,. \tag{4.21}$$

where a_{tx} is the excitation at the feed port, and $\mathbf{T_0}$ is the forward plane-wave scattering spectrum of the transmitting antenna, and $\mathbf{T_0}$ corresponds to the $\sqrt{G_{tx}}$ term in Equation 4.20. For identical transmitting and receiving antennas, reciprocity allows the receiving spectrum to be written in terms of the transmitting spectrum (Hansen and Yaghjian, 1999)

$$\mathbf{R_0}(k_x,k_y,\omega) = Z_0\sqrt{\frac{Y}{Z}}\frac{k_z}{k}\mathbf{T_0}(-k_x,-k_y,\omega)\,, \tag{4.22}$$

where Y and Z are the admittivity and impedivity of the medium (see Equations 1.2 and 1.3) and Z_0 is the characteristic impedance of the wave guide connected at the receiving antenna feed port. Note that $\mathbf{R_0}$ corresponds to the $\sqrt{G_{rx}}\lambda/4\pi$ terms in Equation 4.20. Combining Equations 4.21 and 4.22, the normalized wave amplitude at the receiving antenna port is

$$b_{rx}(x,y,t) = \int_{-\infty}^{\infty}\int_{-\infty}^{\infty}\int_{-\infty}^{\infty}\mathbf{b}_\Gamma(k_x,k_y,\omega)e^{-ik_z(z-z_0)}\cdot\mathbf{R_0}(k_x,k_y,\omega)e^{-i(k_x x+k_y y-\omega t)}dk_x dk_y d\omega\,, \tag{4.23a}$$

$$\mathbf{b}_\Gamma(k_x,k_y,\omega) = \int_{-\infty}^{\infty}\int_{-\infty}^{\infty}\mathbf{E_{0,t}}(k_x',k_y',\omega)e^{-ik_z(z-z_0)}\cdot\vec{\mathbf{\Gamma}}(k_x,k_x',k_y,k_y',\omega)dk_x'dk_y' \tag{4.23b}$$

where $\ddot{\boldsymbol{\Gamma}}$ is the dyadic reflection coefficient, $\mathbf{b}_\Gamma$ is the reflected spectrum, and (·) is the dot product. The dyadic reflection coefficient converts waves incident at a given polarity and direction into reflected (scattered) waves of (possibly) other polarities and directions. Note that both the sign of k_z and the sign of $(z\text{-}z_0)$ changes for upward propagating waves in Equation 4.23a resulting in the same phase shift term as for the downward propagating waves in Equation 4.23b. The dyadic reflection coefficient is the analog of the radar cross section. The exponential terms with $k_z(z\text{-}z_0)$ are the analog of the wave front spreading terms $1/4\pi r^2$ and the propagation loss term $e^{2r\,\mathrm{Im}(k)}$ in Equation 4.20.

A wave field decomposed into plane waves naturally lends itself to scattering problems involving planar scattering surfaces. For a horizontal specular reflector, the reflection coefficient does not change the electric field polarization of the incident waves that are parallel to the reflector. The vertical component of the reflected wave number has the opposite sign of that of the incident wave number. By using the equivalent mirror image problem shown in Figure 4.4, each incident wave 'reflects' into the incident direction. Assuming far-field normal incidence, the resulting reflection coefficient can be described as a frequency dependent scalar

$$\Gamma(\omega) = \frac{\sqrt{\varepsilon_1(\omega) + \dfrac{i\sigma_1}{\omega}} - \sqrt{\varepsilon_2(\omega) + \dfrac{i\sigma_2}{\omega}}}{\sqrt{\varepsilon_1(\omega) + \dfrac{i\sigma_1}{\omega}} + \sqrt{\varepsilon_2(\omega) + \dfrac{i\sigma_2}{\omega}}}. \tag{4.24}$$

Since the antennas are polarized in the $\hat{\mathbf{x}}$ direction, the waveform at the receiving antenna feed port is

$$b_{rx}(x=0, y=0, t) = \frac{1}{(2\pi)^3} \tag{4.25}$$
$$\int_{-\infty}^{\infty}\int_{-\infty}^{\infty}\int_{-\infty}^{\infty} E_{x0,t}(k_x, k_y, \omega) e^{-i2k_z(z-z_0)} \Gamma(\omega) R_{x0}(k_x, k_y, \omega) e^{i\omega t} dk_x dk_y d\omega$$

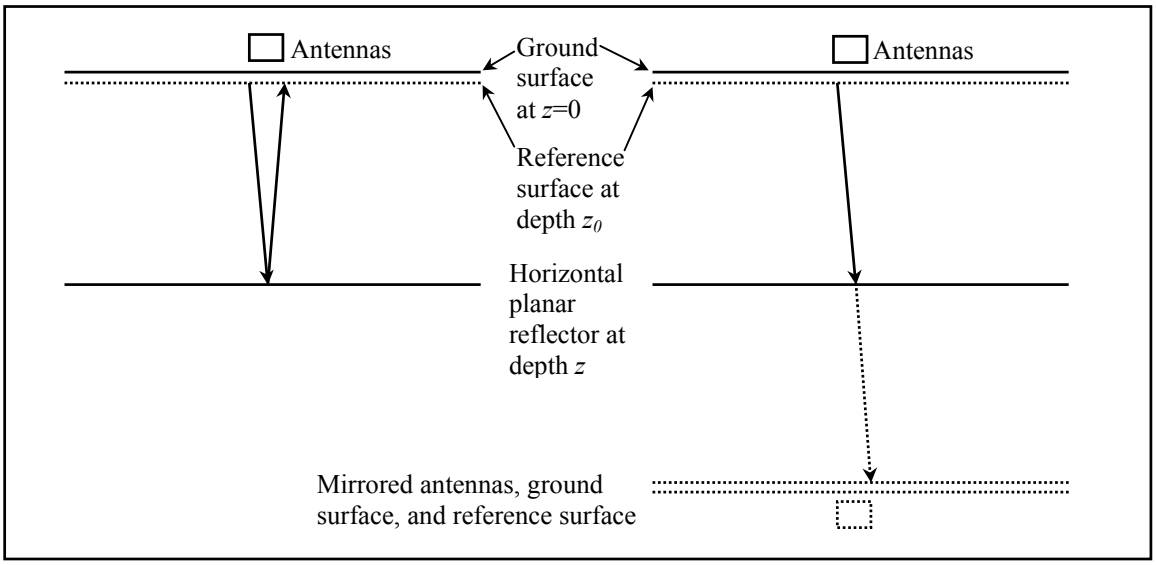

Figure 4.4. Equivalent reflection problems. On the left, rays indicate the path of waves reflecting from a sub-surface planar interface. On the right, the equivalent problem is shown where the mirror image of the reflected wave is shown.

where $E_{x0,t}$ is the $\hat{\mathbf{x}}$ component of $\mathbf{E_{0,t}}$ as in Equations 4.7, 4.21, and 4.23. Here, the dyadic reflection coefficient has been reduced to a scalar. Evaluating the integrals over wave number leaves

$$b_{rx}(t) = \frac{1}{2\pi}\int_{-\infty}^{\infty} H_{t,tx,rx}(z,\omega)\Gamma(\omega)e^{i\omega t}d\omega\,, \tag{4.26}$$

where $H_{t,tx,rx}$ is the response of the pulse generator (i.e. transmitting electronics) and antenna system over a perfect planar reflector (scatterer) at depth z. The system response $H_{t,tx,rx,r}$ is the response of the entire system (transmitting electronics, antennas, and receiving electronics), thus

$$b_r(t) = \frac{1}{2\pi}\int_{-\infty}^{\infty} H_{t,tx,rx}(z,\omega)s_{12r}(\omega)\Gamma(\omega)e^{i\omega t}d\omega = \frac{1}{2\pi}\int_{-\infty}^{\infty} H_{t,tx,rx,r}(z,\omega)\Gamma(\omega)e^{i\omega t}d\omega \tag{4.27}$$

where $b_r(t)$ is the recorded signal, and $s_{12r}(\omega)$ is the response of the receiver electronics (see Chapter 2). Subsequently, after recording the received time series $b_r(t)$, determining

Γ amounts to a deconvolution operation. The calculation of $H_{t,tx,rx,r}$ using results of the FDTD simulations has been implemented in *GPR Wave Utilities*. The *GPR Wave Utilities* deconvolution operator is discussed in Section 2.2.1. Note that it is possible to account for non-normal incidence on the scatterer and accommodate a scatterer in the near-field region (but out of the reactive near-field region) by using a specular reflection coefficient $\Gamma(k_x, k_y, \omega)$ in Equation 4.23. Determining $\Gamma(k_x, k_y, \omega)$ requires solving a three-dimensional integral equation (i.e. Equation 4.23).

The processing steps required to determine the perfect-reflector system-response function for the RTDGPR and determine depth to the planar reflector are shown in Figure 4.5. The soil properties can be estimated using the IMSP algorithm described in Chapter 3. The soil property estimates can be used to index the appropriate set of fields on the scan plane (see Figure 4.3) from a cataloged set of simulations. The perfect-reflector system-response function $H_{t,tx,rx,r}$ is found by evaluating Equation 4.27 using an estimated depth z to the reflector and a unity reflection coefficient. Dispersive media distorts the transmitted waveforms, and some difficulties may arise when measuring the exact travel time in the time-domain to determine the reflector depth. Since different frequency components travel at different velocities, a reference point on the transmitted waveform may not travel at the group velocity, or at the phase velocity at a certain frequency. In extremely dispersive media, the reference point on the waveform may not be identifiable after propagation through the dispersive medium. These difficulties are avoided by using a dispersive wave propagator to advance the waves, and then correlating these waves with the recorded data to determine reflector position. The system response function of Equation 4.27, accounts for dispersive propagation. To determine the depth to the reflector, the depth used to calculate $H_{t,tx,rx,r}$ is varied until a minimum phase correlation is obtained between the $H_{t,tx,rx,r}$ and the recorded reflection. Finally, the reflection coefficient can be estimated using deconvolution, and the material properties found using Equation 4.24. At a single frequency it is not possible to distinguish between

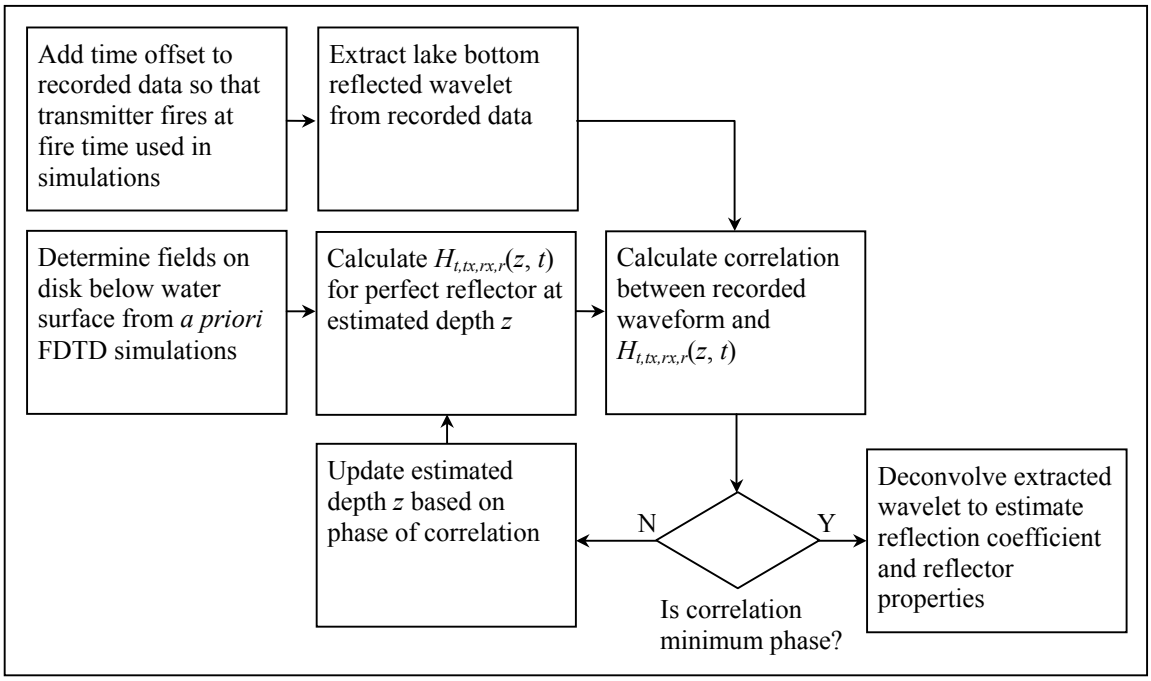

Figure 4.5. Flow chart for estimating electrical properties of lake bottom sediments.

conductivity and imaginary permittivity. This becomes less of a problem when using the entire spectrum to estimate material properties (Canan, 1999).

When working with radar systems whose response has not been characterized, it may be possible to directly measure the system response $H_{t,tx,rx,r}$ if a perfect subsurface reflector is available. Examples of nearly perfect reflectors are non-corroded or non-oxidized pipes, wires, or metal sheets. These reflectors should not be magnetic. Aluminum sheets and jacketed copper or aluminum wires are common in the subsurface. Note that the perfect reflector must have the same shape as other reflectors whose properties are of interest, and the formulae in this Section would need to be written in terms of the appropriate basis functions. When measuring the system response function, the physical reflector (i.e. reference surface in Figure 4.4) must be deeper than the extent of the reactive near-field region to insure that antenna loading by the ground and the

effects of the ground surface are included in the antenna response. This region includes soil at depths down to about $0.62\sqrt{l^3/\lambda}$ (where l is the length of the radiator and λ is the wavelength in the soil; Balanis, 1997). In effect, the shallow soil is part of the antennas, and must therefore be included in the system response. The drawback to this method is that the measured system response function is only valid for the soil properties where the measurement was taken. A fully characterized system such as the RTDGPR alleviates this problem.

4.3.2 Field Example: Determining Lake Bottom Properties

A simple field example illustrates how this technique can be used. A survey of the bottom of Big Soda Lake (Jefferson County, Colorado) was conducted by floating the RTDGPR antennas on the lake. The floating frame used to support the antennas is described in Section 2.5.4. The antennas were polarized such that their H field planes were co-linear (see Figure 2.30). Figure 4.6 shows the antenna locations during the survey. The pseudo-section showing reflections from the bottom of the lake is shown in Figure 4.7. No information on the position or orientation of the antennas was taken during the survey due to logistical constraints. The horizontal axis on the pseudo-section shows the time since recording was initiated. The survey began with the antennas in approximately 4 meters of water, and then the antennas were towed towards the shore (estimated distance of 40 meters). Towing began at about 20 seconds. Note the large amount of clutter in the pseudo-section. This clutter is likely due to reflections from objects above the water such as trees along the shoreline. In the subsequent analysis, it is assumed that the lake bottom is not sloping (i.e. horizontal) and is a specular reflector. Using an estimated towing distance of 40 meters and the location of the reflector in the pseudo-section, the actual slope is about 5 degrees. The criterion for a specular surface is that the average asperity height h is less than $\pi/(8k)$ and that the average slope is less than

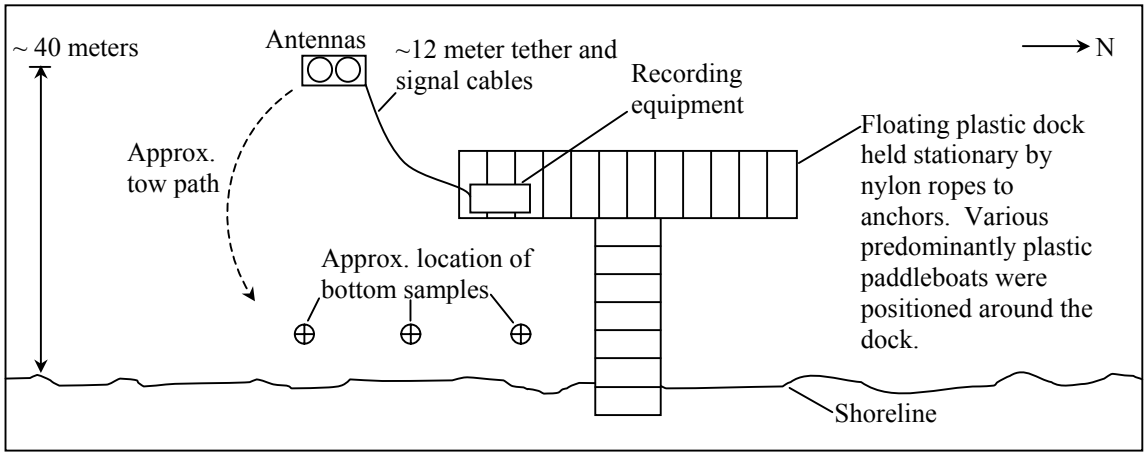

Figure 4.6. Illustration of lake bottom survey at Big Soda Lake, Jefferson County, Colorado. Drawing is not to scale.

10% (see Section 3.4). Thus, the asperity height must be less than about 4 cm at 50 MHz in water. It is assumed that the average slope is less than 10%. Examination of the lake bottom closer to the shore revealed numerous pebbles, which were generally less than 4 cm high. It is possible that some more broad undulations could have had heights greater than 4 cm. It is further assumed that there is no offset between the antennas. The original data and detailed processing records can be found on the accompanying DVD-ROM (see Appendix C).

Figure 4.8 shows the relevant portion of the raw trace taken from the raw data set at a traverse time of two seconds, and the extracted bottom reflection. Even though there is less clutter near the time of the bottom reflection before towing began (400 ns), the reflected signal contains visible noise and clutter. The fields on a scan plane below the water surface were determined by an FDTD simulation. The water properties used in the simulation were $\varepsilon_r = 81$ and $\sigma = 49$ mS/m. A water sample was measured to determine the conductivity. The perfect-reflector system-response function $H_{t,tx,rx,r}$ was found by evaluating Equation 4.27 using an estimated depth z to the lake bottom and a unity reflection coefficient. Note that $H_{t,tx,rx,r}$ was multiplied by two to compensate for the low

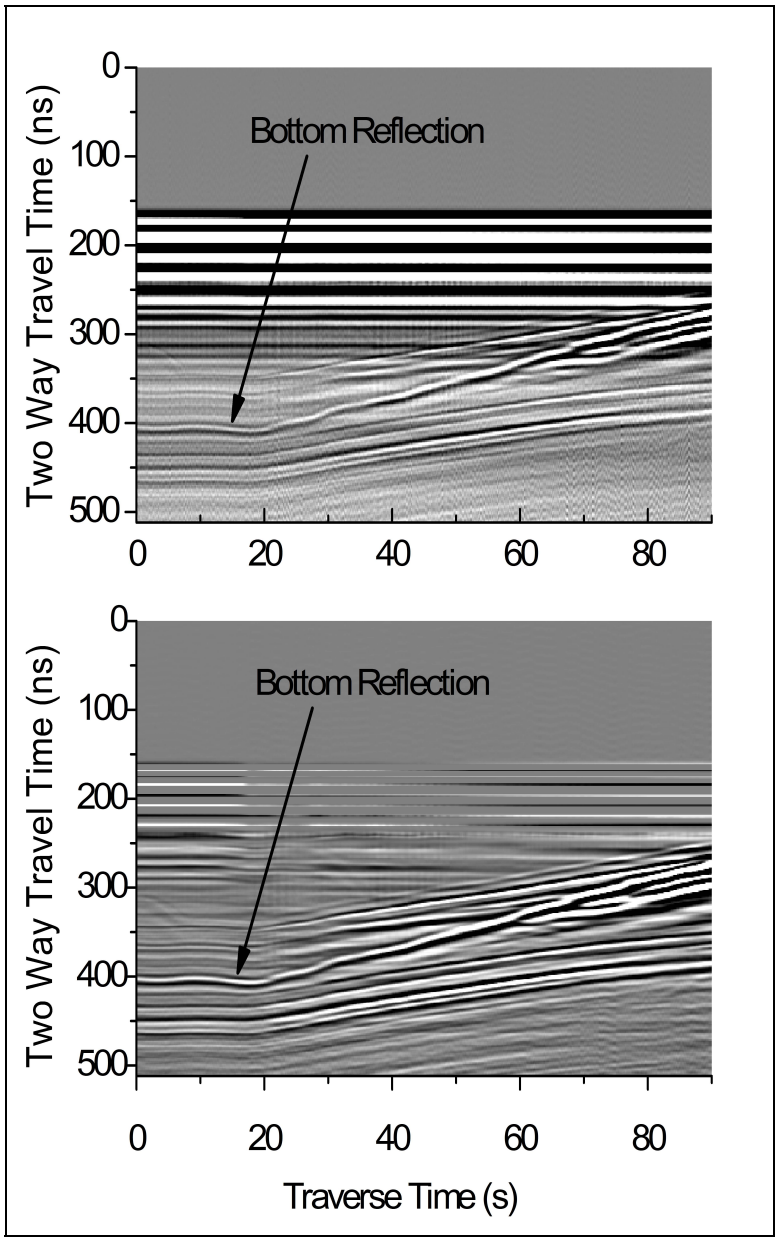

Figure 4.7. GPR pseudo-sections showing lake bottom reflection. The average background signal has been removed in lower section to clarify the bottom reflection. Towing begins at about 20 seconds.

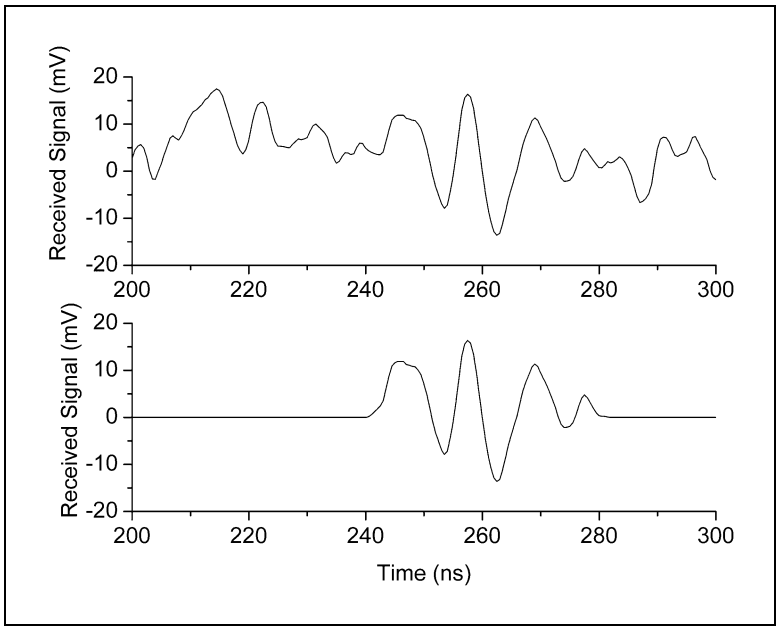

Figure 4.8. Raw and extracted reflection from lake bottom. A 125 MHz cosine squared taper was used to remove unwanted portions of the waveform. The time scales have been adjusted to synchronize waveforms with simulated data.

amplitude pulse generator output described in Section 3.5. By iteratively evaluating $H_{t,tx,rx,r}$ and correlating it with the extracted waveform, the bottom was estimated to be 3.9016 meters deep. The accompanying DVD-ROM contain the raw data from the lake, and detailed processing notes (see Appendix C).

Figure 4.9 shows the amplitude spectra of the system response function $H_{t,tx,rx,r}$ at the depth of the lake bottom, the lake bottom reflection, and the calculated lake bottom reflection coefficient. There are some low frequency components in the lake bottom reflection that are not present in the system response. These components are most likely due to noise and clutter. The resulting reflection coefficient has unreasonably large values below 50 MHz and above 220 MHz where there is no energy in the system response. The reflection coefficient between these frequencies is noisy but has

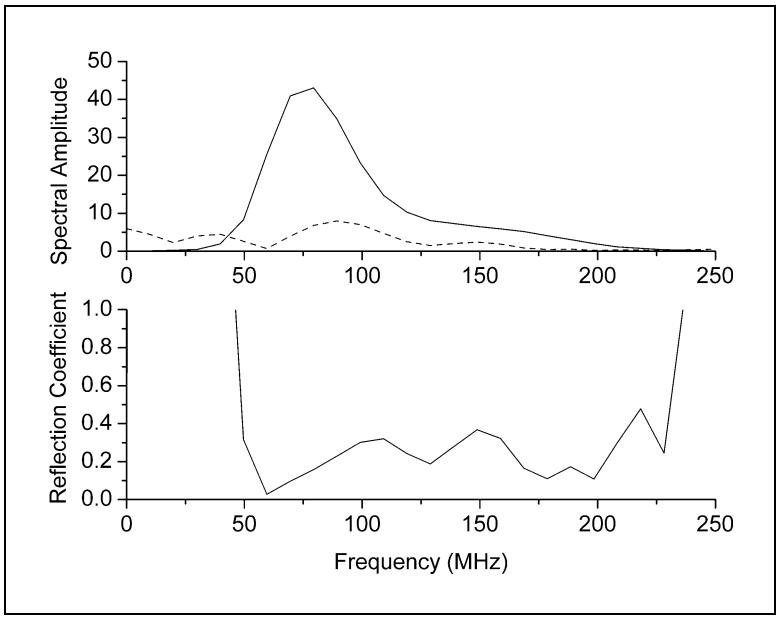

Figure 4.9. Amplitude spectra of $H_{t,tx,rx,r}$ (solid) and received reflection (dashed). The amplitude of the reflection coefficient is shown in the lower graph.

reasonable values based on laboratory analysis of samples taken from the lake bottom. Three samples of lake bottom sediments were taken at the locations shown in Figure 4.6. The electrical properties of these sediments were measured using transmission line tests (Kutrubes, 1986; Canan, 1999). The southern sample contained clay (size fraction) and sand, while the other two samples were predominantly sand with some clay. The Cole-Cole (Olhoeft, 1985) electrical properties of southern most sample are $\varepsilon_{r,dc} = 39$, $\varepsilon_{r,\infty} = 22$, $\tau = 410 \cdot^{-9}$, $\alpha = 0.8$, and $\sigma = 58$ mS/m, and the northern samples had essentially identical properties of $\varepsilon_{r,dc} = 22$, $\varepsilon_{r,\infty} = 18$, $\tau = 410 \cdot^{-9}$, $\alpha = 1.0$, and $\sigma = 16$ mS/m. The calculated reflection coefficients at normal incidence using Equation 4.24 and the Cole-Cole properties of the samples are shown in Figure 4.10. The deconvolved reflection coefficient is not of sufficient quality to provide spectral analysis of the reflection coefficient, or to positively distinguish between the two sediment types, but the reflection

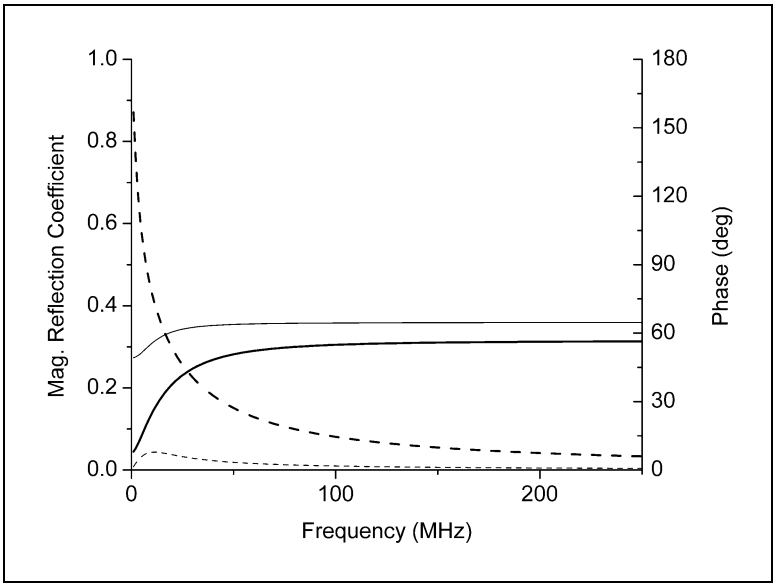

Figure 4.10. Reflection coefficients estimated from measurements of lake bottom sediments. Dashed lines are phase. The southern most sample is represented by thick lines, and the northern two samples are represented by thin lines.

coefficient of the more clay rich sample does match the deconvolved results better. These results are consistent with the geology of the area, because the lake is located in a shale outcrop (i.e. the Smokey Hill Shale Member of the Niobrara Formation; Scott, 1972). Localized sandy deposits from recent sedimentation (Quaternary) or anthropogenic activities are also likely. Even with the limited frequency band of the useful reflection coefficient estimate, materials with moderate or large contrast will likely be distinguishable. For example, spilled hydrocarbons on a lakebed may be distinguishable from the bottom sediments.

The ability to estimate the electrical properties of a reflector depends on the signal to noise ratio, signal to clutter ratio, the properties of the two media, and availability of prior knowledge. Even though most of the energy in the extracted waveform shown in

Figure 4.8 was likely reflected from the lake bottom, the pseudo-section in Figure 4.7 shows that there are other small amplitude reflections that are coincident with the bottom reflection (i.e. clutter). For example, when the upper medium is water, the reflection coefficient given by Equation 4.24 is a strong function of RDP and weak function of conductivity of the lower medium for frequencies above 50 MHz. Therefore the conductivity estimates will have more uncertainty. For this case, the phase of reflection coefficient is small (< 10 degrees) over the expected range of conductivities of the lower layer (0-100 mS/m), unless the lower layer has significant dielectric loss. When the phase of the reflection coefficient is significantly greater than zero, it can be difficult to resolve the difference between the phase of reflection coefficient and distance to reflector. When estimating material properties from reflection coefficients, the frequency dependence of the reflection coefficient is assumed to be due to material properties. Any frequency dependence due to volume scattering is ignored unless accounted for in the dispersive media properties. The uncertainty in the deconvolved results has not been estimated, but it is a function of the uncertainty in characterizing the system response, RF (radio frequency) noise, clutter, limited dynamic range, anisotropy, unfavorable survey conditions, magnetic materials, and non-linear material properties, etc. It is assumed that the effects of multipath and wave-guide propagation are insignificant.

4.4 Dispersive Frequency-Domain Migration

Surveys over conductive and/or lossy soils often result in poor image resolution. A method is presented in this Section that reduces the effects of dispersive wave propagation while migrating the data. With this method, diffracted waves are focused onto their scatterers, and the dispersive effects are partially reversed when back-propagating the waves to their scatterers. Combining these two operations improves images by reducing the effects of both diffraction and dispersion. This Section discusses

the details of the dispersive migration algorithm, and demonstrates its utility through a series of examples. All of the migration methods described below have been implemented in *GPR Workbench*. See Appendix B for more information on the software accompanying this dissertation. The algorithm is described in Section 4.4.1, and the necessary assumptions for applying this algorithm are discussed in Section 4.4.2.

The general problem of reverse propagation or inversion of wave fields in dispersive or even diffusive media has been widely considered. For example, the near-field part of an antenna's radiating plane-wave spectrum can theoretically be calculated from the far-field radiation pattern in any medium using analytic continuation (Hansen and Yaghjian, 1999). Unfortunately, noise, numerical errors, and limited dynamic range prevent finding a unique solution which makes this method impractical. Lewalle (2001) presents a class of solutions to the inverse diffusion problem based on Hermitian wavelets. These inverse solutions do not suffer from the instability problems that traditionally plague inverse diffusion problems, however these solutions are non-unique. Palamodov (2004) presents a method for finding a unique inverse solution to the Helmholtz equation for media with a limiting absorption condition. To construct a unique solution, the growth of the solution must be limited as time decreases. Unfortunately, noise was not considered in the analysis.

In previous work to reduce the effects of dispersion in geophysical surveys, Hargreaves and Calvert (1991) discuss an inverse Q filter for seismic data based on amplitude corrections for each component in the frequency-wave number domain. Wang (2002) stabilized the inverse Q filter by limiting the gain to an empirically determined ceiling, and by using a damped inverse filter. Irving and Knight (2003) show how to estimate a constant Q value from the downshift in the dominant frequency in the received signal with time. They applied a damped inverse Q filter to improve spatial resolution of GPR data from deep reflectors. All of these researchers assumed that Q was constant, which stipulates that attenuation is a linear function of frequency. Generally, Q is not approximately constant in the low frequency GPR band (10-500 MHz), where dispersion

occurs due to both conductivity and dielectric relaxation. The dispersive migration algorithm discussed below is not limited to a constant Q medium, and can handle any frequency dependent material properties.

4.4.1 The Dispersive Migration Algorithm

The dispersive migration algorithm combines Gazdag (1978) frequency-domain migration with a reverse dispersion operation. The algorithm is based on the Gazdag migration code found in Seismic Unix (Cohen and Stockwell, 2003). Early work on the dispersive migration algorithm presented here is discussed in Powers and Oden (2004). Dispersive migration requires the frequency dependent soil properties, and the system response spectrum for the GPR system (see Section 4.3.1). The system response spectrum is used to stabilize the reverse dispersion operation rather than damping. This spectrum combines the response of the electronics, the spectral content of the fields transmitted down through the reference plane (see Figure 4.4), and the response of the receiving antenna to waves traveling up through the reference plane. Methods for obtaining the required soil properties, systems response, and appropriate survey data are discussed in Section 4.4.2.

The operational principals behind the dispersive migration algorithm are straightforward. Using the Gazdag phase shift migration scheme, the migrated two-dimensional image of the electric field of an arbitrary polarization is given by

$$E(x,z,t=0)=\frac{1}{(2\pi)^2}\int_{-\infty}^{\infty}\int_{-\infty}^{\infty}E(k_x,\omega)e^{-ik_z z}e^{-i(k_x x)}dk_x d\omega\,, \tag{4.28a}$$

where $E(k_x,\omega)$ is given by

$$E(k_x,\omega)=\int_{-\infty}^{\infty}\int_{-\infty}^{\infty}E(x,z=0,t)e^{i(k_x x-\omega t)}dxdt\,,\ \text{and} \tag{4.28b}$$

$$k_z = \pm\sqrt{k^2 - k_x^2}\ , \tag{4.28c}$$

where the positive sign is used for downward propagating (or attenuating) waves. For zero offset surveys (or approximately zero offset), the exploding reflector model can be used. In this model, since the up-going and down-going waves traverse the same path, only one traverse of the up going path is needed if the wave number is doubled (and the velocity halved). The application of Equation 4.28 is often called downward continuation of the wave field. If data are collected on the surface ($z = 0$), Equation 4.28 expresses the wave field at some other depth z. During downward continuation, the effects of up-going wave propagation to the surface are being reversed. If a scatterer is present at depth z, then Equation 4.28a is evaluated at time $t = 0$ (the imaging condition) producing an image of the waves at the scatterer before they travel away from the it. The Gazdag method assumes that k is real. However, if the medium is conductive or exhibits dielectric relaxation, then k will be a complex number with the imaginary part determining how quickly the wave attenuates as it propagates (see Equation 1.1). For a dispersive medium, the waves recorded at the surface ($z = 0$) have been attenuated with respect to their original amplitude at the scatterer. This effect can be reversed by simply using the adjoint propagator $e^{-ik_z^* z}$ in the migration equation

$$E(x,z,t) = \frac{1}{(2\pi)^2}\int_{-\infty}^{\infty}\int_{-\infty}^{\infty} E(k_x,\omega)e^{-ik_z^* z}e^{-i(k_x x-\omega t)}dk_x d\omega\,. \tag{4.29}$$

Equation 4.29 is an analytic continuation of traditional phase-shift migration where k is real. Theoretically, the increasing exponential term will reverse any effects of wave attenuation during propagation between the scatterer and the surface. In practice however, noise in the recorded signal and in numeric processing will limit the degree to which attenuation can be reversed. A stabilized reversal of attenuation is the fundamental operation in dispersive migration, and is discussed in detail below. Note that this approach is similar to the method to migrate diffusive electromagnetic wave fields

presented by Zhdanov et al. (1996), except that the dispersive migration of Equation 4.29 includes an unstable reversal of attenuation.

In order to compare and contrast the results from various migration schemes, several scenarios have been simulated in two dimensions. The simulations were made using a dispersive two-dimensional modeling code called *2D Radar* (Powers, 1995), which has been incorporated into *GPR Workbench*. A typical diffraction pattern from a buried pipe is shown in Figure 4.11. This Figure shows simulated and migrated (using the Gazdag method) pseudo-sections of a perfectly conducting pipe in a lossless medium. The top of the pipe is seven meters deep, the pipe is two meters in diameter, and the medium velocity is 17.2 cm/ns. The antennas are co-located Hertzian dipoles, and the antenna feed waveform is a 50 MHz Ricker wavelet. Consult Powers (1995) for more details on the antennas and the excitation. In Figures 4.12-4.14, simulated and migrated pseudo-sections are shown for increasingly lossy media (tan δ_e = 0.2, 0.43, and 0.74 at 50

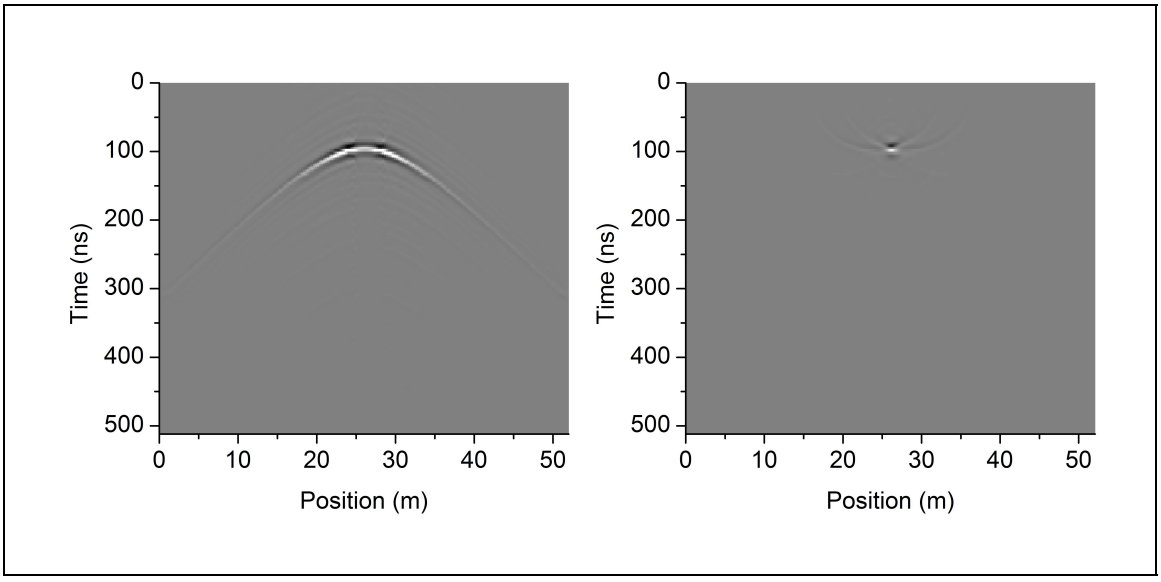

Figure 4.11. Simulated pseudo-section (left) of a conducting pipe in a lossless medium. Velocity is 17.2 cm/ns. Migrated pseudo-section (right) using the Gazdag method.

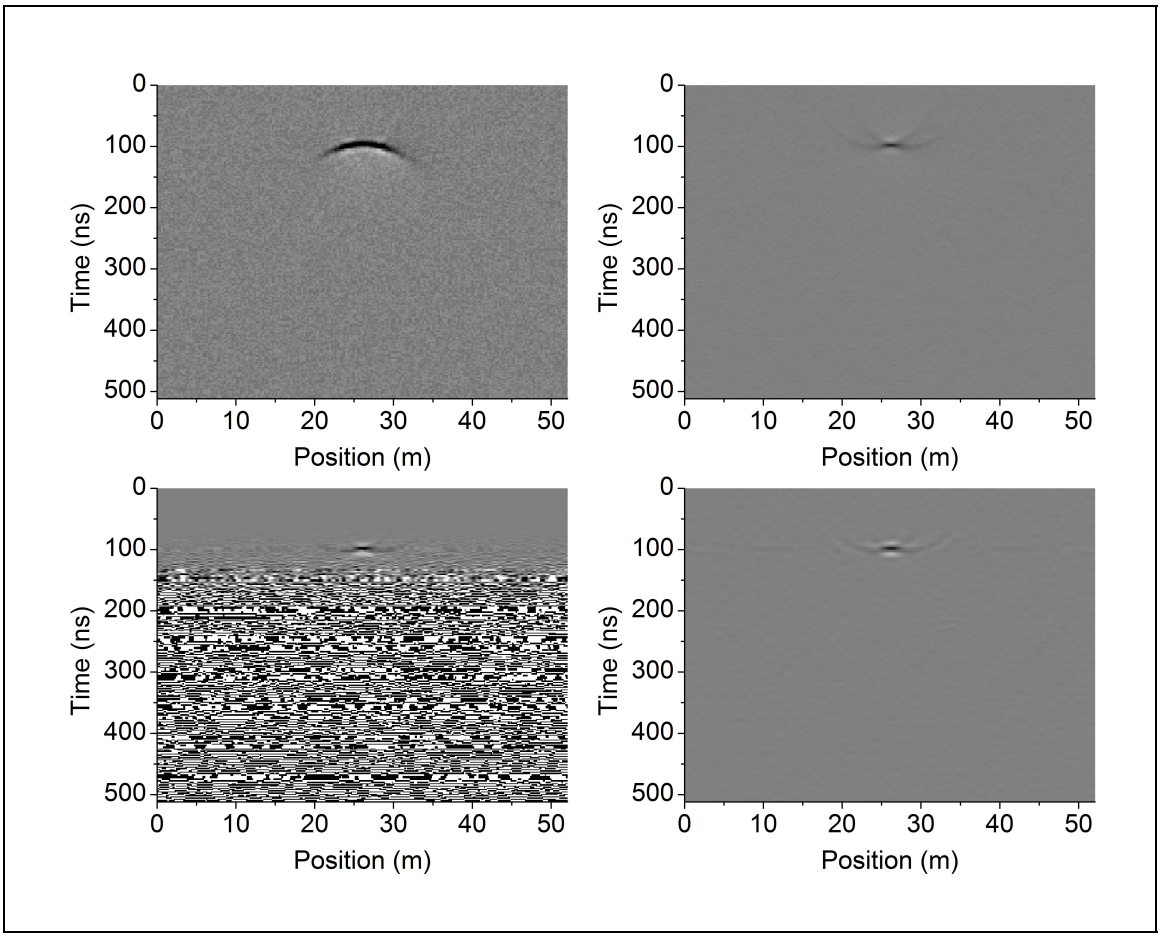

Figure 4.12. Simulated pseudo-section (top left) of a conducting pipe in a lossy medium. Conductivity is 10 mS/m, and the Cole-Cole dielectric parameters are $\varepsilon_{dc} = 16\varepsilon_0$, $\varepsilon_\infty = 13\varepsilon_0$, $\tau = 10^{-8}$, α=0.8, and tan $\delta_e = 0.2$ at 50 MHz. Gazdag migrated pseudo-section (top right), dispersive migration with constant gain cutoff (lower left), and dispersive migration using spectral content (bottom right). Late-time large-amplitude waveforms in the lower left panel have saturated the linear gray scale resulting in a black and white image.

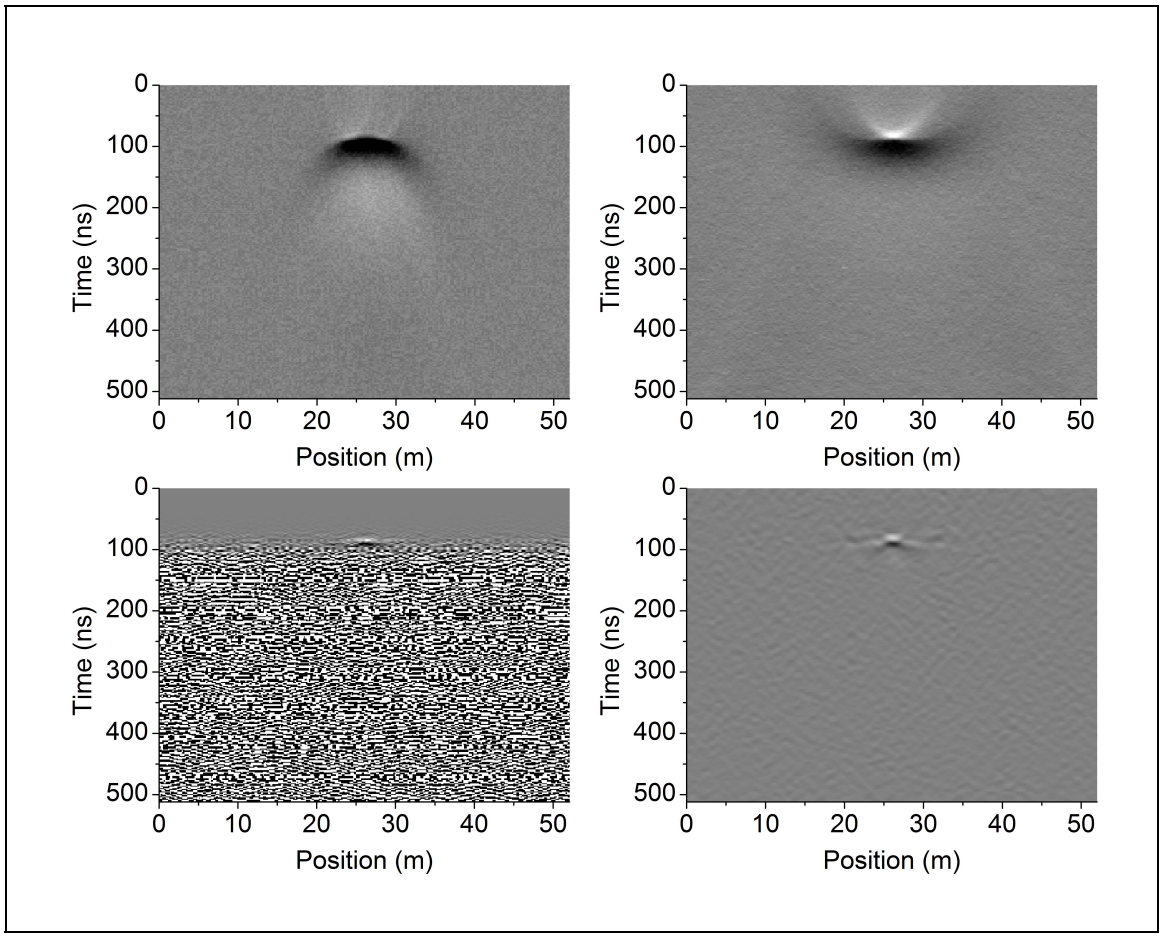

Figure 4.13. Simulated pseudo-section (top left) of a conducting pipe in a lossy medium. Conductivity is 15 mS/m, and the Cole-Cole dielectric parameters are $\varepsilon_{dc} = 13\varepsilon_0$, $\varepsilon_\infty = 10\varepsilon_0$, $\tau = 10^{-8}$, $\alpha = 0.8$, and tan $\delta_e = 0.43$ at 50 MHz. Gazdag migrated pseudo-section (top right), dispersive migration with constant gain cutoff (lower left), and dispersive migration using spectral content (bottom right). Late-time large-amplitude waveforms in the lower left panel have saturated the linear gray scale resulting in a black and white image.

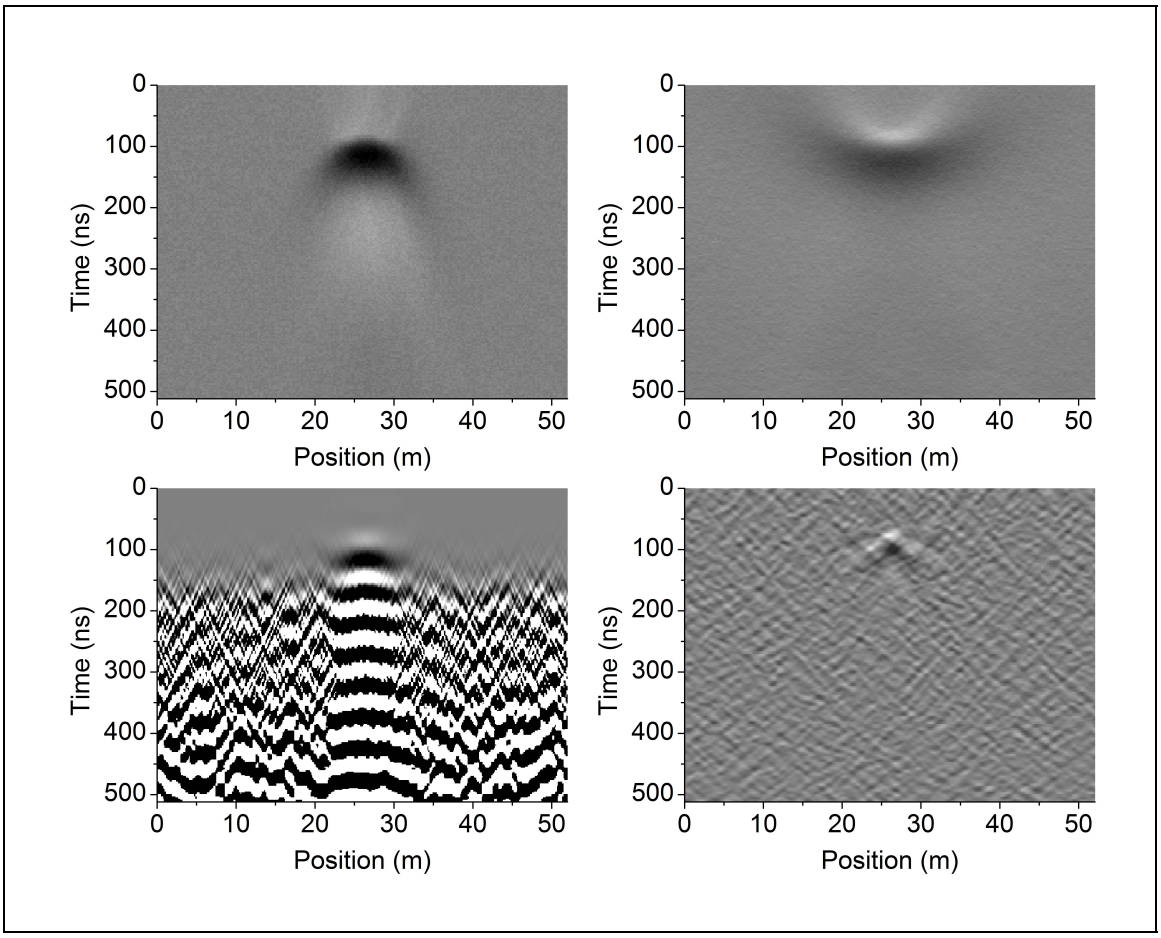

Figure 4.14. Simulated pseudo-section (top left) of a conducting pipe in a lossy medium. Conductivity is 20 mS/m, and the Cole-Cole dielectric parameters are $\varepsilon_{dc} = 11\varepsilon_0$, $\varepsilon_\infty = 8\varepsilon_0$, $\tau = 10^{-8}$, α=0.8, and tan $\delta_e = 0.74$ at 50 MHz. Gazdag migrated pseudo-section (top right), dispersive migration with constant gain cutoff (lower left), and dispersive migration using spectral content (bottom right). Late-time large-amplitude waveforms in the lower left panel have saturated the linear gray scale resulting in a black and white image.

MHz respectively) for the same pipe size and location used in Figure 4.11. The lossy media simulations include losses due to both conductivity and dielectric relaxation as indicated in the Figure captions (see Olhoeft, 1985 for a discussion of the Cole-Cole dielectric relaxation model). After simulating the data for each Figure, white noise was added at an RMS level corresponding to a radar system with 100, 120, and 140 dB of dynamic range respectively. The soil properties were chosen so that the peak signal from the pipe is 20 dB above the RMS noise level as determined using Equation 4.19. These Figures show the results from several migration algorithms, which are discussed below. No range gain is used in the simulations or the plots contained in these Figures, and a linear gray scale is used.

Applying the Gazdag algorithm to the pipe in the lossless medium gives the expected results; that is, the 'tails' of the diffraction hyperbola have been collapsed to a small region at the top of the pipe (see Figure 4.11). However, this is not always the case in lossy media. Figures 4.13 and 4.14 show that applying the Gazdag method to the lossy case results in a poor resolution image. Clearly, the dispersive effects must be mitigated to improve the image quality. The key to reversing the effects of dispersive propagation lies in limiting the gain applied during downward continuation. Some degree of success can be achieved by limiting the cumulative gain at each frequency during downward continuation to an empirically determined constant value. This method is referred to as the gain cutoff method, and is similar to a damped inverse Q filter (Irving and Knight, 2003; Wang, 2002). The lower left panels of Figures 4.12-4.14 show the migrated results using this gain cutoff method. The resolution of the pipe is better, but with noisy data, the effects of too much gain are evident below the pipe. For a given image, an empirically determined gain cutoff value can be found that attenuates the late time artifacts at the expense of resolution, but these artifacts cannot be entirely eliminated unless the gain is strongly reduced. Fortunately, using additional information to control the gain provides better results.

The dispersive migration algorithm utilizes the spectral content of the interrogating fields to stabilize gain during the reverse dispersion operation. The system response function $H_{t,tx,rx,r}$ at $z = z_0$ provides prior information to constrain the gain used to reverse the attenuating effects of propagation in a lossy medium. In dispersive migration, the factor $E(k_x,\omega)e^{-ik_z^* z}$ in Equation 4.29 is replaced by the following function

$$f(k_x,\omega,z)=\Big\{ E(k_x,\omega)e^{-ik_z^* z} \text{ if } \left|E(k_x,\omega)e^{-ik_z^* z}\right| \le \left|H_w(k_x,\omega)\right|, \\ E(k_x,\omega)e^{-i\,\mathrm{Re}(k_z)z}\left|H_w(k_x,\omega)/E(k_x,\omega)\right| \text{ otherwise}\Big\}, \tag{4.30}$$

where $H_w(k_x, \omega)$ is the weighted system response function described below. Additionally, the noise spectrum of the received waveform is used to help condition the problem. Rather than damping however, the received spectrum is filtered to remove components where the signal to noise ratio is less than unity. Much better results are achieved when noisy frequency components are eliminated. The lower right panels of Figures 4.12-4.14 show the migrated results using the dispersive migration method. A pseudo-code outline for the dispersive migration algorithm is shown in Figure 4.15.

To see how the gain limiting process is implemented, compare the received spectrum and the weighted system response spectrum in Figure 4.16. The system response spectrum $H_{t,tx,rx,r}(z_0, \omega)$ was estimated by simulating a buried aluminum sheet two meters below the ground ($z_0 = 2$) using *2D Radar*. Here, the system response includes the antenna excitation and the antenna response due to the ground properties (which is why the aluminum plate is two meters deep). See Section 4.3.1 for details on the system response. The system response can also be estimated from FDTD simulations used in the IMSP algorithm (see Section 4.3.1 and Chapter 3). The weighted system response $H_w(k_x, \omega)$ is the system response spectrum $H_{t,tx,rx,r}(z_0, \omega)$ multiplied by a weighting factor. The weighting factor accounts for the unknown reflection coefficient and wave front spreading, and is recalculated for each horizontal wave number k_x. The

```
//Input the following
//E(x,t): the wave field
//H_t,tx,rx,r(z_0,ω): the system response function at z=0^+
//SNR: the signal to noise ratio
//k_0(ω): frequency dependent material properties

E(k_x,ω)=FFT[E(x,t)]
for all k_x {
  //calc weighted system response spectrum
  H_p=H_t,tx,rx,r(z_0,ω) peak value
  E_p=E(k_x,ω) value at frequency where H_t,tx,rx,r(ω) peaks
  H_w(k_x,ω)=H_t,tx,rx,r(z_0,ω)*E_p/H_p

  //remove noisy frequency components
  for all ω, find max E(k_x,ω)
  for all ω
    if E(k_x,ω) < max E(k_x,ω)/SNR
      E(k_x,ω) = 0
  for (τ=0; τ <τ_max; τ= τ + Δτ ) {
    initialize: Image(k_x, τ) = 0
    for all ω {
      k_z= sqrt(k_0^2 - k_x^2)
      ck_z= conj(k_z)
      //don't add energy to image that was never there
      if (|E(k_x,ω)*exp(i*ck_z*τ*v)| < |H_w(k_x,ω)|)
           Image(k_x, τ) += E(k_x,ω)*exp(i*ck_z*τ*v)
      else
           Image(k_x, τ) += E(k_x,ω)*exp(i*Re(ck_z)*τ*v)*
                            |H_w(k_x,ω)/E(k_x,ω)|
    }
  }
Image(x, τ) = FFT[Image(k_x, τ)]
```

Figure 4.15. Outline of the dispersive migration routine.

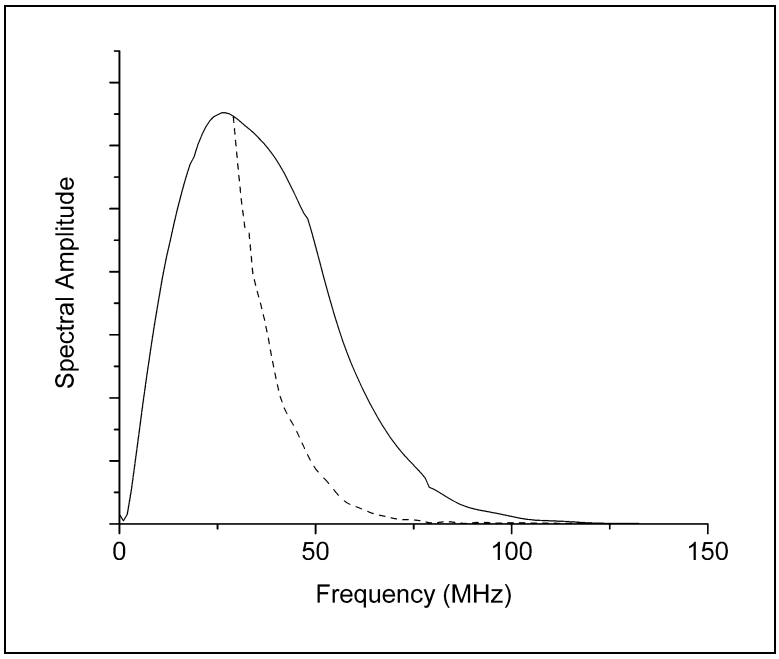

Figure 4.16. Weighted system response spectrum (solid) and received spectrum (dashed). The weighted system response spectrum overlies the received spectrum at low frequencies. The weighted system response spectrum is used to limit the gain of the received spectrum during migration.

weighting factor is the ratio of the amplitude of the received spectrum at the frequency of the peak system response to the peak amplitude of the system response spectrum. Weighting schemes based on equating the peak amplitudes of each spectrum or the RMS amplitudes of each spectrum gave inferior results. During downward continuation of the wave field, each spectral component in the received signal is amplified to compensate for the frequency dependent propagation loss. This loss is prescribed by the material properties. At each depth increment in downward continuation, this amplification is limited by the weighted system response spectrum. This limiting scheme works because it limits the gain of highly attenuated frequencies so that spectral content is not introduced if it was not present in the system response.

The example using a 100 dB dynamic range (see Figure 4.12) is significant because it shows that the effects of dispersion are less than with the 120 and 140 dB examples where the soils have more loss. Many commercial GPRs have about 100 dB of dynamic range. The examples presented in Figures 4.12-4.14 show that in some cases, the improvements to the images produced by commercial GPR systems using the dispersive migration algorithm can be small. For 100 dB systems, attenuation due to dispersion can reduce the field amplitudes below the noise level before notable degradation of resolution in the pseudo-sections is seen. The effectiveness of the dispersive migration algorithm is much greater for radars with a higher dynamic range such as the RTDGPR, which is greater than 140 dB. GPR systems with a lower dynamic range will not produce visible reflections in the high loss situations depicted in Figures 4.13 and 4.14. The dispersive migration algorithm will not improve penetration depth of a GPR system.

The Stolt (1978) frequency-domain migration method is more efficient than the Gazdag method, but it cannot account for vertically varying velocity. With the Gazdag method, an integral over frequency is evaluated at each discrete time value followed by a one-dimensional inverse FFT to obtain the migrated image; while the Stolt method returns the migrated image at all time values from a single two-dimensional inverse FFT. Unfortunately, the dispersive migration method cannot be efficiently implemented in the faster Stolt (1978) method. This is because the nonlinear gain limiting operation (see Equation 4.30) is a function of depth (or time) and cannot be moved outside the inverse FFT operation. The Stolt approach may be viable if the inverse dispersion filter is applied before migration, because the Stolt method can be modified to account for frequency dependent velocity. Applying the inverse dispersion filter before migration may not offer a computational advantage because the non-linear gain operation still must be evaluated at each time step. Applying the reverse dispersion operation during migration allows compensation for depth dependant attenuation, which is not possible when applying an inverse dispersion filter to each trace individually prior to migration.

The dispersive migration algorithm is widely applicable to many types of lossy media (within the constraints discussed in Section 4.4.2). In fact, the algorithm should prove useful for imaging in purely diffusive media. Dissipative loss and diffusion involve a loss of information (i.e. spectral content) and an increase in entropy. As a result, the bandwidth of the collected data is less than that of the original transmitted signal. Physically, this lost information cannot be retrieved, however the dispersive migration procedure stabilizes the inversion of the collected data, and restores a limited portion of the original spectrum. Since the fully diffusive case is a worse case scenario for dispersion, it is used as a generic example.

Consider a perfect impulse source containing spectral content at all frequencies in a diffusive media. The kernel or Green's function for diffusive energy transport is a Gaussian (Lewalle, 2001). The convolution of an impulse (i.e. the source function) with the kernel produces the received signal, which is another Gaussian (see Figure 4.17). Assuming that the noise level is the same for measurements at all frequencies, the resulting high frequency attenuation causes decreased signal to noise ratios and increased

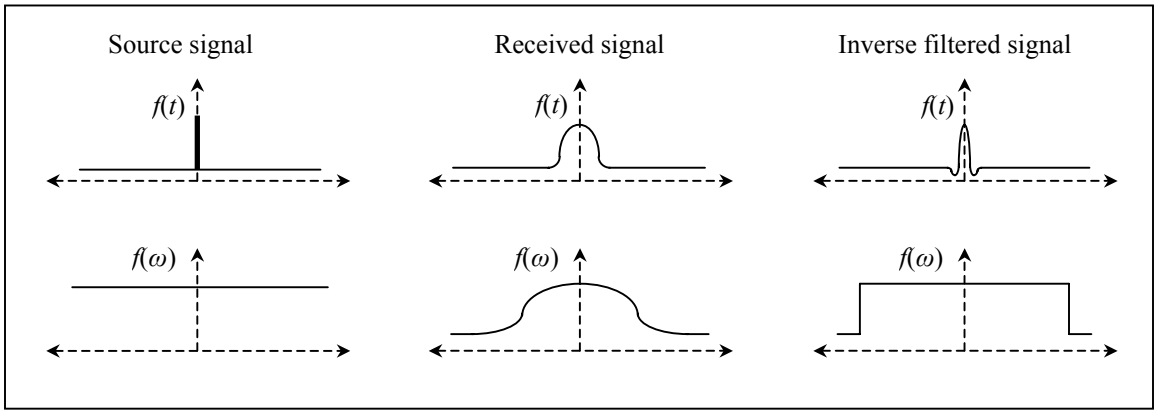

Figure 4.17. Schematic representation of an ideal impulse source signal in the time and frequency-domains (left), signal received after traveling through a diffusive medium (middle), and signal after inverse dispersive filtering (right).

uncertainty in the measurement of the high frequency components. The inverse dispersion filter used in the migration routine restores the portions of the spectrum where the signal to noise ratio is greater than unity, which results in improved resolution. Note that this technique does not improve the limited depth of investigation due to energy dissipation in dispersive and diffusive media. Also, since diffusive losses are quite large, noise, clutter, and limited dynamic range will greatly reduce the useful portion of the received spectrum.

4.4.2 Data Requirements, Assumptions, and Limitations

The data set collected for processing with the dispersive migration algorithm must meet the following criteria. The data must be sampled with sufficient density such that spatial and temporal aliasing is avoided (see Yilmaz, 1987). Any range gain used in data collection must be removed. The range gain can be restored after dispersive migration. This may require a converting the data to a format that can encode numbers varying over many orders of magnitude. The required electrical properties of the soil can be estimated using the methods described below. The system response is also required, and can be determined using the methods described in Sections 4.2 and 4.3.

There are several methods for estimating the required soil properties for dispersive migration. Most of these methods provide average material properties. Dispersive migration using average material properties often yields acceptable results when soil properties vary slowly and lateral variation is minimal. Average properties may be insufficient when the 'tails' of diffraction hyperbolae scattered from symmetrical objects have the different shapes and lengths. Perhaps the most common method to estimate velocity is to fit hyperbolas to the hyperbolic diffraction patterns of waves reflected from small scatterers (Annan, 2001). The average attenuation can be estimated from the penetration depth using the radar equation (Equation 4.19). The IMSP

algorithm (see Chapter 3) estimates shallow soil properties under the antennas. Soil properties can also be estimated using the deterministic deconvolution technique presented in the previous Section if the plane wave scattering matrix of the scatterer is known (equivalent to the dyadic reflection coefficient of Equation 4.24b; Kerns, 1981). The plane wave scattering matrices for perfectly conducting pipes and spheres are well known (Balanis, 1989). For cases where the shape, location, and material properties of an arbitrary reflector are known, the frequency dependent soil properties can also be estimated through inversion using an appropriate forward operator that simulates the wave field reflected by the target such as *2D Radar* (Powers, 1995). Alternatively, laboratory testing of soil samples can provide an estimate of these properties. Finally, the effective material properties can be estimated by iteratively migrating the data with various permittivity and conductivity values until artifacts from over and under migration are minimized. Artifacts from over and under migration are more sensitive to permeability values than to conductivity values. Initial soil property estimates can be determined from known values for typical soils and fluids. Independent measurements from TDR probes, neutron probes, cone penetrometer surveys, and other surface geophysical surveys should always be considered.

Many assumptions have been made and certain requirements must be met for proper application of the dispersive migration algorithm. It is required that the recorded data have spectral components with a signal to noise and signal to clutter ratios greater than unity. Systems with higher dynamic range can often provide better signal to noise ratios, unless a noise source such as a radio station is near the survey site. The signal to clutter ratio cannot be improved with increased dynamic range. The algorithm cannot improve imaging of deep objects beyond the depth of investigation for a particular system.

The spectral content of the subsurface waveforms can change due to propagation through dispersive materials, diffraction, material boundaries with different frequency dependent properties, multi-pathing, guided waves, and constructive and destructive

interference due to caustics and multiple scattering (Olhoeft and Capron, 1994). The only spectrum altering mechanism treated here is dispersive propagation. The effects of constructive and destructive interference are often localized, and altering the positioning of the survey equipment may circumvent the ill effects. Frequency dependant scattering can be caused by frequency dependant materials and by scatterers with a finite spatial extent (i.e. diffraction). Frequency independent reflection is a valid approximation for non-magnetic metallic objects when the wavelength is much shorter than the extent of the scatterer (i.e. optical scattering). This is because the contrast between the properties of metal and soil is large, and dispersive soil properties have little effect on the reflection coefficient. Modifications to the dispersive migration algorithm can be made to account for frequency dependant reflection coefficients due to frequency dependant material properties. It is assumed that no diffraction occurs (see further discussion below). Even though most scatterers depolarize the incident waves (Beckman, 1968), the depolarization of the incident wave field is also not considered here. Modifications to account for spectral distortion due to rough surface scattering of the target are also possible.

The dispersive migration algorithm and the *2D Radar* simulation program both assume optical scattering, and geometrical diffraction is not considered. However, the dispersive migration algorithm can be modified to account for the effects of diffraction when they are known. The radar cross section for scatterers of finite extent is frequency dependent, and the cross sections for simple scatterers such as plates, pipes, and spheres are well known (Balanis, 1989). In general, the variation of the reflection coefficient with frequency depends on the size, shape, and material properties of the target. Therefore, accounting for target specific variations in reflection coefficient requires a problem specific implementation of the dispersive migration routine. For example, Balanis (1989, p. 608) shows that the radar cross section of a perfectly conducting pipe is essentially a linear function of frequency for normally incident waves. This simple linear function could easily be incorporated into the dispersive migration algorithm.

The dispersive migration algorithm is designed for scatterer(s) embedded in a homogeneous host medium as described in Section 4.1. It is assumed that no lateral velocity or attenuation changes occur. Small variations can be tolerated, as long as the average velocity is such that hyperbolic diffraction patterns from small scatterers are nearly symmetric. It is assumed that velocity changes occur slowly so that no ray path bending occurs. Even though magnetic soils are not addressed in this dissertation, the dispersive migration algorithm can be easily modified to include linear magnetic relaxation effects.

A two-dimensional dispersive migration algorithm was presented, however it could be easily extended to three dimensions. For proper application of the two-dimensional algorithm, all reflectors must intersect the vertical plane containing the line of survey, and they must be symmetric about the plane (i.e. normal to the plane). It is assumed that the antenna offset is zero. Data collected with large offsets (greater than a wavelength) should be adjusted to zero offset using a normal move out correction (Yilmaz, 1987). It is assumed that all waves recorded at the surface are traveling upwards. No corrections for surface topography have been made.

It is assumed that the received energy has been reflected from objects at similar depths so that the received spectra from each reflector are similar. This is a reasonable assumption in a medium with enough loss to warrant dispersive migration because energy received from deeper objects will be weak and have little effect on the received spectral content from shallower objects. When incorporating frequency dependent reflection coefficients, difficulties may be encountered when multiple closely-spaced visible scatterers are present and the frequency dependent reflection coefficient differs significantly between scatterers. Forward scattering by shallow reflectors is not accounted for when imaging deep reflectors. Finally, targets must be deeper than the reference plane used for the system response (see Figure 4.4).

CHAPTER 5

SUMMARY AND CONCLUSIONS

5.1 Overview

The shallow subsurface is crucial to mankind's existence. The shallow subsurface provides nearly all of our needs through agriculture, quarrying, mining, and hydrology (Speidel, 1982). As a result, many industries are in need of better subsurface imaging. For example, accurate measurements of the electrical properties of soil can provide agricultural science with a better understanding of soil moisture distributions and salinity buildup. Better subsurface imaging can provide civil engineers with a better understanding of the strength and structure of subsurface bodies so that large structures such as tunnels or bridge foundations can be properly designed and built. Better subsurface imaging will also increase public health and safety at large. For example, serious accidents resulting from excavation damage to pipelines and communications cables can be avoided with better subsurface information (NTSB, 1977). This can be accomplished by providing the utility detection industry with tools that produce higher resolution images and better depth estimates to targets. Industrial contamination of groundwater and the vadose zone are also common problems. The ability to locate and monitor the cleanup of these contaminants is crucial.

The GPR method is unique in that it provides the highest resolution images of any standard geophysical technique. However, special challenges exist when conducting GPR surveys in lossy ground. Lossy ground limits the depth of penetration of GPR signals, and reduces the resolution of the subsurface images. Because lossy ground due to conductive fluids and dielectric relaxation in soils containing clay minerals are quite common (Doolittle et al., 2002), improvements to GPR systems and data processing techniques are greatly needed. The efforts described in this dissertation, together with the

hardware developed by the USGS (Wright et al., 2005) address this need. Three algorithms are discussed in this dissertation that improve subsurface information. They are the dispersive migration algorithm, the method to deconvolve for reflector properties, and the IMSP algorithm for estimating soil properties under the antenna. These algorithms illustrate that advancements can be made by focusing research and development efforts on GPR systems development and data processing techniques. The work in this thesis addresses industry needs, however more work in this area is needed because improvements will benefit a wide range of industries.

Most GPR surveys are interpreted in the field rather than extensively processed at the office. Therefore, providing more information in the field better serves the GPR community and public health and safety at large. All of the GPR data processing algorithms in this dissertation were designed to run in minutes rather than hours. The algorithms presented here do not run fast enough to run during data collection, but they are fast enough to run in the moments after collecting a data set. Little effort was made to minimize run time when implementing these routines. Optimizations may reduce run time of these algorithms by an order of magnitude. Suggestions and recommendations have been made in the preceding Chapters for decreasing the run time so that they might run during or directly after data collection. With today's technology, it is possible to provide the user with a two-dimensional migrated image where the blurring effects of dispersive soil have been reduced, and provide information about the properties of the soil and the reflectors within seconds of completing a survey line. Although the developmental efforts would be significant, the capability of such a system would be well received in today's market.

5.2 Results and Conclusions

This dissertation has been concerned with extracting more quantitative information from GPR surveys. The pivotal task is to calibrate and characterize a GPR system so that its response can be predicted in various field situations. A collection of techniques for calibrating an impulse GPR system were described in Chapter 2. The TDT experiments and the standard frequency-domain analysis techniques provide acceptable calibrations for the receiving electronics hardware. Several methods have been discussed for calibrating the impulse generators. The greatest difficulties in determining the overall GPR response stem from the characterization of the antenna response and ground coupling due to variable field conditions. The FDTD simulations have provided a marginally acceptable antenna characterization for the RTDGPR, but the remaining difference between experimental results and simulations are significant. These differences reduce the accuracy of subsequent processing algorithms designed to make use of the system response such as improved image resolution.

The IMSP algorithm (see Chapter 3) estimates the electrical properties of the soil beneath the antennas (relative permittivity and conductivity), as well as the antenna standoff (height of the antennas above the ground). The basis for the method is the changing wave shape of the early arriving waveforms due to changing soil properties and antenna-ground coupling. The algorithm is built on a catalog of FDTD simulations that assume frequency independent dielectric properties. Despite this, it can be successfully applied to frequency dependent dielectric soils. Applying the algorithm to the simulated response of a soil with frequency dependent dielectric properties produced conductivity estimates that included the imaginary permittivity component. Tests show that the algorithm's resolution of each parameter (relative permittivity, conductivity, and standoff) is different, with standoff having the best resolution and conductivity having the least. Results also show that an independent means of measuring the antenna standoff such as an acoustic ranging device would improve the run-time performance of the IMSP

algorithm, and better constrain the soil property estimates. The algorithm's ability to converge to a solution, and the accuracy of the results are degraded when the survey conditions are not ideal. Examples of non-ideal survey conditions include a rough surface and vertically gradational soil properties. A vertical gradient in soil properties can occur after a rainfall event. The IMSP algorithm was successfully applied to survey data taken in an environment with relatively homogeneous soil, although some of the conductivity estimates were poorly resolved.

As an example of the utility of a fully calibrated GPR system, a method to estimate the frequency dependent reflection coefficient of a horizontal planar reflector was discussed (see Chapter 4). This method assumes that the wave fields in the upper layer are known, as are the electrical properties of the upper layer. These fields can be determined from the antenna calibrations (Chapter 2) and the IMSP soil property estimates (Chapter 3). In some situations, the electrical properties of the upper layer can be provided by the IMSP soil property estimates. There is an inherent ambiguity between depth to the reflector and phase of the unknown reflection coefficient. Because of this, there may not be enough information to uniquely determine the electrical properties of the scatterer. The inability to determine unique electrical properties is exacerbated by uncertainties in the upper layer wave field, heterogeneity, clutter, RF (radio frequency) noise, and the dynamic range of the radar system. The method was used to estimate the reflection coefficient of a lake bottom. Noise and clutter in the data prohibited determining the reflection coefficient over a broad range in frequencies, however the narrow band information was of sufficient quality that moderate and high contrast materials could likely be distinguished. For example, dense contaminants on a lakebed may be distinguishable from the bottom sediments.

Another example of the utility of a calibrated system is the dispersive migration algorithm presented in Chapter 4. When the spectral content of the transmitted subsurface waves is known, then the dispersive migration routine can significantly improve GPR imaging in lossy soil conditions. Wave propagation in dispersive ground

can be highly lossy and causes the transmitted energy pulse to broaden in time as it propagates. The algorithm improves resolution by restoring much of the frequency content that was lost during propagation. Lost spectral content can only be restored for received spectral components that have a sufficient signal to noise ratio. In some cases, the resolution of the migrated image can be nearly as high as imaging in lossless media. The algorithm provides the best results with data that have been collected with a GPR system with a large dynamic range (120 dB or more). Older commercial GPR systems with limited dynamic range are not able to record the low amplitude signals that exhibit dispersive wave propagation. Surveys conducted with these instruments will benefit less from dispersive migration than will surveys conducted with the newer high dynamic range instruments. In essence, the dispersive effects must be recorded before they can be corrected. This algorithm may also produce improved images from data collected with systems that have not been fully calibrated and where the transmitted wave spectrum is only approximately known.

5.3 Data Processing with a Calibrated GPR System

Several new techniques have been introduced in this dissertation, and they can be applied in concert when processing GPR data. The fundamental basis for these techniques is the ability to calibrate a GPR system. This Section presents an overview of the suggested data processing methodology to use with a calibrated GPR system. The process is outlined in 10 steps, which are described below. This process is certainly more involved than processing typical GPR data, but the extra effort is rewarded with clearer images and more information about subsurface objects. Surveys should be planned so that the steps below can be performed without violating the assumptions and limitations for each step. Appropriate warning signs indicating a violation of the assumptions are

also found below. Note that the order of steps 6-9 may vary, and that some iteration over these steps may be needed.

There are some common assumptions that are made when applying all of the techniques described below. In all cases, it is assumed that the subsurface media are linear, homogeneous, isotropic, and non-magnetic. To testing for anisotropic media, rotate the antennas about a vertical axis at a fixed position on the ground surface. It is expected that the response due to anisotropic scatterers such as a pipe will change during rotation. However, if the response to a horizontal planar reflector such as the ground surface changes during rotation, then the soil is likely anisotropic. It is possible to modify most of the data processing algorithms in this dissertation to account for magnetic media. The difficulty lies in detecting and quantifying the magnetic properties. It is not possible to separate magnetic and dielectric effects with conventional GPR systems using electric field antennas. Independent indicators of magnetic soils include independent measurements, laboratory tests of soil samples, mineralogy, and environment (see Section 1.4). Finally, topographic variations have not been accounted for. Topographic corrections may be needed for example, when known planar subsurfaces appear as undulating reflections in pseudo-sections.

1. Calibrate the GPR System. Apply the techniques of Chapter 2 to obtain the system response as a function of the shallow soil properties. The calibration involves laboratory measurements to determine the response of the GPR receiving and transmitting electronics, and numerical simulations to estimate the antenna response over various soil types. In addition to the electronics response, the system response is comprised of the plane-wave response matrices for each antenna-soil type combination. It may be difficult to obtain enough information about physical construction of the antennas to make accurate numerical simulations. Alternatively, the antenna response can be measured in an antenna range, and the combined response of the antenna and soil can be calculated from these measurements. Another alternative involves measuring the antenna response while the antennas are held over a tank of fluid, where the fluid

properties can be changed to reflect various soil properties. In any case, field experiments should be conducted to assess the uncertainties of the calibrations, which should be less than about 10%. The calibrations should account for the range of soil properties expected in most GPR surveys. Calibrations should be made at various signal levels to verify that the response is linear, and should be repeated periodically to verify that the response does not change over time.

2. Collect Survey Data. The survey should be planned to accommodate the processing steps below. If two-dimensional migration is planned, then the survey lines should be oriented perpendicular to the major axis trend of subsurface objects. Consider using a line spacing that is dense enough to preclude the need for interpolation to avoid spatial aliasing (see Step 3). Perhaps the ground surface can be made smoother by raking and/or removing shrubs. Irrigating the ground before the survey may help provide a more homogeneous sensitive region for the IMSP algorithm (see Step 4), although this may also increase loss.

3. Pre-Processing. After collecting survey data, additional traces or samples may need to be added by interpolation to prevent spatial and temporal aliasing (Yilmaz, 1987). Interpolation and extrapolation of the data may be required to obtain data in a regular grid in time and space. Spatial aliasing can cause noise to appear between reflectors in the migrated image that is not present in the un-migrated image. The deconvolution and migration processes of Steps 7 and 8 require true amplitudes. Therefore, any range gain used during data acquisition should be removed. This may require changing the data to a format that can store the true amplitude range of the data. The range gain can be re-applied after deconvolution and migration.

4. Determine the Shallow Ground Properties. The shallow ground properties affecting the antenna response can be estimated using the IMSP algorithm described in Chapter 3. The IMSP algorithm is based on the simulated early arriving waveforms that were made for the range of soil properties expected in most GPR surveys. It is assumed that the shallow soil is effectively homogeneous and isotropic under the effective

combined apertures of the transmitting and receiving antennas (about 3.5 by 1.5 m for the RTDGPR). No visible subsurface reflections are allowed in the first 30 ns (for 50 MHz RTDGPR antennas) of the received waveform. Note that the combined apertures and the time window for no subsurface reflections both decrease for higher frequency antennas (e.g. ~40 cm and 3 ns at 500 MHz). The soil surface must be smooth enough that reflections from the surface are effectively specular. A rough surface and shallow lateral inhomogeneities are indicated by waveforms that vary over the horizontal span of the antenna apertures (3.5 m) and/or in the first 30 ns of data. Since shallow structures with layered or gradationally varying properties may occur that do not result in early-time waveform variations, a method to indicate a heterogeneous sensitive region is given in Section 3.4. The soil properties should be estimated for as many antenna positions in the survey as possible without violating the assumptions. Augment the soil property information with independent information and measurements when available. Unfavorable conditions for applying the IMSP algorithm are indicated when the algorithm produces a solution set with a small population (see Chapter 3).

5. Determine Antenna Coupling and System Response. Combine the shallow soil property estimates with the system calibrations to determine the system response function for each antenna position. This process is described in Sections 4.1-4.3. The system response is comprised of the plane-wave response matrices, and is a function of the soil properties and antenna standoff at each antenna position. At antenna locations where the assumptions of the previous steps are invalid, it may not be possible to determine the system response function.

6. Estimate Subsurface Velocities. The primary purpose of the step is to provide information for the dispersive migration algorithm. There are a number of methods for estimating subsurface velocities. An overview is given here, and more details can be found in Section 4.4.2. The average velocity between the surface and a scatterer can be determined from travel times when the location of a subsurface object is known. The average velocity between the surface and a scatterer can also be estimated by fitting

hyperbolas to the scatterer's hyperbolic diffraction pattern. In this dissertation, it is assumed that there are no lateral velocity variations. Lateral velocity variations are probable when the 'tails' of diffraction hyperbolae scattered from symmetrical objects have the different shapes and lengths. When lateral velocity variations are small, the use of average properties in subsequent processing steps usually provides acceptable results. Deterministic deconvolution (see Section 4.3) can be used to estimate the properties of a layer or object if the properties of the overlying or embedding media are known. Alternatively, deterministic deconvolution can be used to estimate the properties of a medium overlying a layer or containing an object if the properties of the layer or object are known. Iterative migration can be used to find the velocity structure that produced the most compact images of scatterers. Shallow properties can be estimated from the IMSP algorithm (see Chapter 3). Laboratory tests, independent information, and independent field measurements can also be used. Some of these methods inherently estimate frequency dependant velocities, and various band-pass filters can be used with the other techniques to estimate velocities in various frequency bands.

7. Estimate Subsurface Attenuation. The primary purpose of the step is to provide information for the dispersive migration algorithm. The average attenuation can be estimated from the penetration depth using the radar equation (Equation 4.19). Some of the methods for estimating velocity can also be used to estimate attenuation, including deterministic deconvolution (see Section 4.3) and the IMSP algorithm (see Chapter 3). Laboratory tests, independent information, and independent field measurements can also be used. The Kramers-Kronig relations (Jackson, 1999) relate the real and imaginary part of the permittivity, which further constrains velocity and attenuation estimates.

8. Deterministic Deconvolution. This step has been separated from steps 6 and 7 because the purpose of this step is to provide information about a subsurface object such as a layer or a pipe rather than the medium between the object and the surface. This step helps to identify materials and/or assess the condition of an object. This step is unnecessary when the objective is only to provide a clear image of the subsurface.

Deterministic deconvolution for a horizontal planar reflector is described in Section 4.3. For this operation, the data quality must be such that a high quality reflected wavelet can be extracted that has a good signal to noise ratio, a good signal to clutter ratio, and low interference from multi-path. One or more of these adverse effects may be occurring when the magnitude of the slope of the material properties estimates versus frequency is greater than unity on a log-log plot.

9. Dispersive Migration. The purpose of this step is to improve object delineation by providing higher image resolution. A two-dimensional dispersive migration routine is included with this dissertation. The assumptions associated with this algorithm are discussed in Section 4.4.2, and the salient details are repeated here. It is assumed that all subsurface reflectors are normal to the vertical line-of-survey plane. The antenna offset is assumed to be zero. Zero offset conditions can be approximated from large offset data by using the normal move out correction (Yilmaz, 1987). Frequency dependant scattering has not been accounted for. However, the algorithm can be modified to account for the frequency dependent scattering of known targets when the size and material properties of a target are known. Migration collapses diffracted wave fields onto their scatterers, and dispersive migration partially reverses some of the effects of dispersive media. Reversing the dispersive effects provides marked improvement in image resolution only when the subsurface has significant loss (e.g. conductivities greater than 20 mS/m). With significant loss, and a high dynamic range radar system is needed to provide adequate penetration. The dispersive migration routine included with this dissertation assumes that scatterers are embedded in a homogeneous medium. The algorithm can easily be modified to account for vertical material property variations. It is assumed that there are no lateral changes in material properties. Average velocities can be used for migration when the lateral variations are small. Lateral velocity variations are acceptably small when hyperbolic diffraction patterns from small scatterers are nearly symmetric. One or more or the assumptions may be violated when the algorithm fails to produce an image with improved resolution over the un-migrated image.

10. Image Filtering and Final Image Production. Filters can be used to improve image quality. Removal of the average background signal often improves image contrast. Range gain can be re-applied. The wavelet nature of reflections can be removed by using an RMS or Hilbert envelope filter. Horizontal features can be attenuated/accentuated and dipping features accentuated/attenuated by using a moving average spatial cut/pass filter. Final images can be produced from the processed data. These images may a collection of time slice images, movies, or three-dimensional renderings with cutaway sections. Rendered models of subsurface objects can be produced.

5.4 Recommendations for Future Work

The data processing methods discussed in this dissertation require a calibrated radar system. The calibration processes for a radar system should be streamlined so that they can be applied periodically to a given system. The response of a system may change due to use because connectors become dirty, worn, or damaged, cables become distressed, moisture becomes trapped in the antennas, or when the system is operated at a much different temperature than the calibration temperature. Quality assurance programs specify periodic calibrations of the survey equipment. This is especially important when extracting quantitative information from survey data. In fact, special circuitry should be included in radar systems that would allow calibration of both the electronics response and the antenna response without the need for additional equipment. Ideally, a radar system would monitor and perhaps compensate for its changing response. For example, an ideal system would account for antenna loading by the soil, and adjust the reference time of the recorded waveforms to account for the varying transfer delays between the antenna feed ports and the outer bounds of the reactive near field zones of the antennas. It may be possible to adjust the excitation so that the signals transmitted into the

subsurface do not change due to ground loading. It is also necessary to continue improvements to the dynamic range of GPR systems to increase investigation depths.

A large amount of time and effort was put into characterizing the antenna response due to varying soil properties. Despite this, a better match between the simulated and measured response is desired. Although costly for large low frequency antennas, better results are expected if the actual antenna response is measured rather than calculated. Furthermore, the antenna response characterization has only been made for ideal field situations. The response due to rough surfaces under the antennas, heterogeneous soil, imperfect antenna attitudes, and antennas that are not perfectly co-polarized should be investigated. The time delay between the transmitter fire time, the time the pulse leaves the antenna's reactive near field zone, and the reception time of early energy changes due to antenna loading and needs further study. This is important because more accurate system timing produces more accurate depth estimates to targets. Finally, this work has only focused on dipole antennas, and the effects of varying soil properties on other antenna types should be investigated as well.

Further testing of the IMSP algorithm is needed in heterogeneous ground conditions. Creating a denser catalog of antenna response simulations will reduce uncertainty in some parts of the model space for the RTDGPR. The IMSP algorithm should be extended to GPRs other than the RTDGPR. Perhaps the IMSP algorithm will work better with high frequency systems or different antenna configurations. Antenna configurations with different polarizations, orientations, or even magnetic field sensors should be investigated. It may be possible to estimate magnetic soil properties and/or estimate soil properties in vertical profile.

Many possibilities exist for extracting more information about the subsurface and producing higher resolution images when the GPR response is known for various field conditions. In marine seismic surveys, the waveform transmitted at the sea surface is measured at depth in the sea, and is then used in image processing. Perhaps some seismic processing routines could be adapted to GPR surveys. For example, spectral content

provides more information for use in inversion for velocity models. Further testing and development of the dispersive migration algorithm and reflector deconvolution are needed. For instance, modifying the dispersive migration routine to account for the diffractive effects of a known scatterer such as a pipe may provide better depth estimates to pipes.

REFERENCES CITED

Annan, A. P., 1973, Radio Interferometry Depth Sounding: Part I – Theoretical Discussion, Geophysics, v. 38, p. 557-580.

Annan, A. P. 2001, Ground Penetrating Radar Workshop Notes, Sensors and Software, Mississauga, Ontario, Canada, 192 p.

Arcone, S. A., 1995, Numerical Studies of the Radiation Patterns of Resistiviely Loaded Dipoles, J. of Applied Geophysics, v. 33, p. 39-52.

Arcone, S. A., Paige, R. P., and Liu, L., 2003, Propagation of a Ground-Penetrating Radar (GPR) Pulse in a Thin-Surface Waveguide, Geophysics, v. 68, n. 6, p. 1922-1933.

Balanis, C. A., 1997, Antenna Theory, Wiley and Sons, New York, 941 p.

Balanis, C. A., 1989, Advanced Engineering Electromagnetics, Wiley and Sons, New York, 981 p.

Beckmann, P., 1968, The Depolarization of Electromagnetic Waves, Golem Press, Boulder, Colorado, 214 p.

Bergmann, T., Robertsson, J. O. A., and Holliger, K., 1998, Finite-Difference Modeling of Electromagnetic Wave Propagation in Dispersive and Attenuating Media, Geophysics, v. 63, n., 3, p. 856-867.

Bogorodsky, V. V., Bentley, C. R., and Gudmandsen, P. E., 1985, Radioglaciology, Reidel Publishing Co., Boston, 254 p.

Bourgeois, J. M., and Smith, G. S., 1996, A Fully Three-Dimensional Simulations of a Ground Penetrating Radar: FDTD Theory Compared with Experiment, IEEE Trans. Geoscience and Remote Sensing, v. 34, n. 1, p. 36-44.

Buechler, D. N., Roper, D. H., Durney, C. H., and Christensen, D. A., 1995, Modeling Sources in the FDTD Formulation and Their Use in Quantifying Source and Boundary Condition Errors, IEEE Trans. Microwave Theory and Techniques, v. 43, n. 4, p. 810-814.

Butkov, E., 1968, Mathematical Physics, Addison-Westley Publishing Co., Reading, MA, 735 p.

Canan, B., 1999, Dielectric Properties of Clay-Water-Organic Compounds, PhD Thesis, Department of Geophysics, Colorado School of Mines, Golden, Colorado, 332 p. with CD-ROM.

Chew, W. C., 1995, Waves and Fields in Inhomogeneous Media, IEEE Press, Piscataway, NJ, 608 p.

Cohen, J. K., and Stockwell, J. W., Jr., 2003, CWP/SU: Seismic Unix Release 37: a Free Package for Seismic Research and Processing, Center for Wave Phenomena, Colorado School of Mines, Golden, Colorado, 141 p.

Dahan, O., McDonald, E. V., and Young, M. H., 2003, Flexible Time-domain Reflectometry Probe for Deep Vadose Zone Monitoring, Vadose Zone Journal, n. 2, p. 20-275.

Daniels, D. J., 1996, Surface-Penetrating Radar, IEE Radar, Sonar, Navigation and Avionics Series, 6, UK, 320 p.

de Jongh, R. V., 2000, Ultra-wideband Sensor for Electromagnetic Field Measurements in Time-domain, Electronics Letters, Sept., p. 1679-1680.

Deng, H. L., 1997, A Complexity Analysis of Generic Optimization Problems: Characterizing the Topography of High-Dimensional Functions, Ph.D. Thesis, Dept. of Geophysics, Colorado School of Mines, Golden, Colorado, USA, 114 p.

Dhaene, T., Martens, L., and Zutter, D., 1994, Extended Bennia-Riad Criterion for Iterative Frequency-Domain Deconvolution, IEEE Trans. Instrumentation and Measurement, v. 42, n. 2, p. 176-180.

Doolittle, J. A., Minzenmayer, F. E., Waltman, S. W., and Benham, E. C., 2002, Ground-Penetrating Radar Soil Suitability Map of the Conterminous United States, *in* Proceedings of the Ninth International Conference on Ground Penetrating Radar, Santa Barbara, CA, paper 4758-163.

Duke, S., 1990, Calibration of Ground Penetrating Radar and Calculation of Attenuation and Dielectric Permittivity versus Depth, Masters Thesis, T-3920, Colorado School of Mines, Golden, CO, 236 p.

Durig, U., Pohl, D. W., and Rohner, F., 1986, Near-Field Optical-Scanning Microscopy, J. Applied Physics, v. 59, n. 10, p. 3318-3327.

Engheta, N., and Papas, C. H., 1982, Radiation Patterns of Interfacial Dipole Antennas, Rdio Science, v. 17, n. 6, p. 1557-1566.

Feldman, M., 1994, Non-Linear System Vibration Analysis Using Hilbert Transform—I. Free Vibration Analysis Method 'Freevib', Mechanical Systems and Signal Processing, v. 8, n. 2, p. 119-127.

Fetter, C. W., 2001. Applied Hydrogeology, Prentice-Hall, Upper Saddle River, New Jersey, 598 p.

Fisher, E., McMechan, G. A., Annan, A. P., 1992, Acquisition and Processing of Wide-Aperture Ground Penetrating Radar Data, Geophysics, v. 57, n. 3, p. 495-504.

Gazdag, J., 1978, Wave Equation Migration with the Phase Shift Method, Geophysics, v. 43, p. 1342-1351.

Giannopoulos, A., 1997, The Investigation of Transmission-Line Matrix and Finite-Difference Time-Domain Methods for the Forward Problem of Ground Probing Radar, Ph.D. Thesis, University of York, York, UK.

Gill, P. E., Murry, W., and Wright, M. H., 1986, Practical Optimization, Elsevier, Amsterdam, 401 p.

Gish, T. J., Dulaney W. P., Kung, K. J. S., Daughtry C. S. T., Doolittle, J. A., and Miller, P. T., 2002, Evaluating Use of Ground Penetrating Radar for Identifying Subsurface Flow Pathways, Soil Sci. Soc. Am. J., v. 66, p. 1620-1629.

GPRMax, 2004, publicly available at http://www.gprmax.org, v. 1.5, Giannopoulos, A.

Hargreaves, N. D., and Calvert, A. J., 1991, Inverse Q Filtering by Fourier Transform, Geophysics, v. 56, n. 4, p. 519-527.

Hansen, T. B., and Yaghjian, A. D., 1999, Plane-Wave Theory of Time-Domain Fields: Near-field Scanning Applications, IEEE Press Series on Electromagnetic Wave Theory, Wiley-IEEE Press, 400 p.

Hendrickx, J. M. H., Borchers, B., and Woolslayer, J., 2001, Spatial Variability of Dielectric Properties in Field Soils, *in* Detection and Remediation Technologies for Mines and Minelike Targets VI, SPIE Proceedings Volume 4394, p. 398-408.

Hunt, A. G., and Gee, G. W., 2002, Water-Retention of Fractal Soil Models Using Continuum Percolation Theory: Tests of Hanford Site Soils, Vadose Zone Journal, n., 1, p. 252-260.

Irving, J. D., and Knight, R. M., 2003, Removal of Wavelet Dispersion from Ground Penetrating Radar Data, Geophysics, v. 68, n. 3, p. 960-970.

Ishida, T., Makino, T., and Wang, C., 2000, Dielectric-Relaxation Spectroscopy of Kaolinite, Montmorillonite, Allophane, and Imogolite Under Moist Conditions, Clays and Clay Minerals, v. 48, n. 1, p. 75-84.

Jackson, J. D., 1999, Classical Electrodynamics, 3rd Ed., Wiley ad Sons, Hoboken , NJ, 808 p.

Jansen, T., von Rymon-Lipinski, B., Hanssen, N., Keeve, E., 2004, Fourier Volume Rendering on the GPU Using Split-Stream-FFT, *in* Proceedings of the 9th International Fall Workshop, Vision, Modeling, Visualization 2004, Stanford, CA, USA, p. 395-403.

Jordan, T.E., and Baker, G.S., 2002, A Conceptual Model for the Detection of NAPL Using Amplitude and Phase Variation with Offset (APVO) Analysis of Ground Penetrating Radar Data, *in* Proceedings of the Symposium on the Application of Geophysics to Engineering and Environmental Problems, Las Vegas, NV.

Kaatze, U., Menzel, K., and Pottel, R., 1991, Broad-Band Dielectric Spectroscopy on Carboxylic Acid/Water Mixtures. Dependence upon Composition., J. Phys. Chem., v. 95, p. 324-331.

Kaya, A., and Fang, H. Y., 1997, Identification of Contaminated Soils by Dielectric Constant and Electrical Conductivity, J. Environmental Engineering, ASCE, v. 123, n. 2, p. 169-177.

Kelso, C. M., Flammer, P. D., DeSanto, J. A., and Collins, R. T., 2001, Integral Equations Applied to Wave Propagation in Two Dimensions: Modeling the Tip of a Near-Field Scanning Optical Microscope, J. Opt. Soc. Am. A, p. 1993-2001.

Kerns, D. M., 1981, Plane-Wave Scattering-Matrix Theory of Antennas and Antenna-Antenna Interactions, NBS Monograph 162, Washington, D.C.: U.S. Government Printing Office, 162 p.

Klysz, G., Balayssac, J. P., Laurens, S., and Ferrieres, X., 2004, Numerical FDTD simulation of the Direct Wave Propagation of a GPR Coupled Antenna, *in* Proceedings of the Tenth International Conference on Ground Penetrating Radar (GPR 2004), Delft, The Netherlands, p. 45-48.

Kunz, K., and Luebbers, R., 1993, The Finite Difference Time-domain for Electromagnetics, CRC Press, Catalog Number 8657, 496 p.

Kutrubes, D. L., 1986, Dielectric Permittivity Measurements of Soils Saturated with Hazardous Fluids, Masters Thesis, Department of Geophysics, Colorado School of Mines, Golden, Colorado, 300 p.

Langman, A., 2002, The Design of Hardware and Signal Processing for a Stepped Frequency Continuous Wave Ground Penetrating Radar, PhD Thesis, Department of Electrical Engineering, University of Cape Town, South Africa, 195 p.

Lambot, S., Slob, E. C., van den Bosch, I., Antoine, M., Gregoire, M., and Vanclooster, M., 2004a, Modeling of GPR Signal and Inversion for Identifying the Subsurface Dielectric Properties, *in* Proceedings of the Tenth International Conference on Ground Penetrating Radar (GPR 2004), Delft, The Netherlands, p. 79-82.

Lambot, S., Slob, E. C., van den Bosch, I., Stockbroeckx, B., Scheers, B., and Vanclooster, M., 2004b, Estimating Soil Electric Properties from Monostatic Ground-Penetrating Radar Signal Inversion in the Frequency-domain, Water Resources Research, v. 40, W04205, 12 p.

Lambot, S., Rhebergen, J., van den Bosch, I., Slob, E. C., and Vanclooster, M., 2004c, Measuring the Soil Water Content Profile of a Sandy Soil with an Off-Ground Monostatic Ground Penetrating Radar, Vadose Zone Journal, v. 3, p. 1063-1071.

Lampe, B., Hollinger, K., and Green, A. G., 2003, A Finite-Difference Time-Domain Simulation Tool for Ground-Penetrating Radar Antennas, Geophysics, v. 68, n. 3, p. 971-987.

Lampe, B., and Hollinger, K., 2003, Effects of Fractal Fluctuations in Topographic Relief, Permittivity and Conductivity on Ground-penetrating Radar Antenna Radiation, Geophysics, v. 68, n. 6, p. 1934-1944.

Lee, K. H., Chen, C. C., Teixeira, F. L., and Lee, R., 2004, Modeling and Investigation of a Geometrically Complex UWB GPR Antenna Using FDTD, IEEE Trans. Antennas and Propagation, v. 52, n. 8, p. 1983-1991.
Lewalle, J., 2001, A Class of Solutions for the Inverse Diffusion Problem, App. Math. Let., v. 14, p. 617-624.

Lestari, A. A., Yarovoy, A. G., and Ligthart, L. P., 2001, Numerical Analysis of Transient Antennas, *in* Proc. International Conference on Electromagnetics and Advanced Applications, Turin, Italy, pp. 435-438.

Liao, S. Y., 1990, Microwave Devices and Circuits, Third Edition, Prentice-Hall, Englewood Cliffs, NJ, 592 p.

McGillem, C. D., and Cooper, G. R., 1984, Continuous and Discrete Signal and System Analysis, HRW Series in Electrical and Computer Engineering, Holt, Rinehart, and Winston, New York, NY, 418 p.

Meincke P., and Hansen, T. B., 2004, Plane-Wave Characterization of Antennas Close to a Planar Interface, IEEE Trans. Geoscience and Remote Sensing, v. 42, n. 6, p. 1222-1232.

Mishchenko, M. I., Travis, L. D., Lacis, A. A., 2002, Scattering, Absorption, and Emission of Light by Small Particles, Cambridge University Press, Cambridge, MA, 448 p.

NTSB (National Transportation Safety Board), 1997, Protecting public safety through excavation damage prevention: Safety Study NTSB/SS-97/01, Washington DC, 106p.

Oden, C. P., Wright, D. L., Powers, M. H., and Olhoeft, G. R., 2005, Ground Penetrating Radar Antenna System Analysis for Prediction of Earth Material Properties, *in* Proc. IEEE Antennas and Propagation Society Meeting, Washington, DC, submitted.

Olhoeft, G. R., 1985, Electrical Properties of Rocks and Minerals, Short Course Notes, http://mars.mines.edu/pub/85ShortCourseNotes.pdf, 218 p.

Olhoeft, G. R., 1987, Electrical Properties from 10-3 to 10+9 Hz – Physics and Chemistry, *in* Proc. of the 2nd International Symp. on the Physics and Chemistry of Porous Media, Schlumberger-Doll Research, Ridgefield, CT, October, 1986, Am. Inst. Phys. Conf. Proc. 154, J. R. Banavar, J. Koplik, and W. W. Winkler, eds., NY, AIP, p. 281-298.

Olhoeft, G. R., 1991, Spatial Variablity: *in* Proceedings of NSF/EPRI Workshop on Dynamic Soil Properties and Site Characterization, EPRI NP-7337, v. 1, p. 5-1 – 5-20.

Olhoeft, G. R., and Capron, D. E., 1994, Petrophysical Causes of Electromagnetic Dispersion, *in* Proceedings of the Fifth International Conference on Ground Penetrating Radar (GPR 1994), Kitchener, Ontario, Canada, p. 145-152.

Olhoeft, G. R., Powers, M. H., and Capron, D. E., 1994, Buried Object Detection with Ground Penetrating Radar, *in* Proceedings of Unexploded Ordinance (UXO) Detection and Range Remediation Conference, Golden, CO, May 17-19, 1994, p. 207-233.

Olhoeft, G. R., 1994, Applications and Limitations of Ground Penetrating Radar, *in* Society of Exploration Geophysics Expanded Abstracts, 54th Annual International Meeting and Expo., Dec. 2-6, 1984, Atlanta, GA, p. 147-148.

Olhoeft, G. R., 1994, Geophysical Observations of Geological, Hydrological, and Geochemical Heterogeneity, *in* Proceedings of the Symposium on the Application of Geophysics to Engineering and Environmental Problems, Boston, MA, p. 129-141.

Olhoeft, G. R., 1996, Application of Ground Penetrating Radar, *in* Proceedings of the 6th Int'l. Conf. on Ground Penetrating Radar, GPR'96, Sendai, Japan, p. 1-4 (keynote address).

Olhoeft, G. R., and Smith, S. S., 2000, Automatic Processing and Modeling of GPR Data for Pavement Thickness and Properties, *in* Proceedings of the 8th Int'l. Conf. on Ground Penetrating Radar, GPR 2000, Gold Coast, Australia, Concrete/Pavement Evaluation I.

Orfanidis, S. J., 2004, Electromagnetic Waves and Antennas, www.ece.rutgers.edu/orfanidi/ewa, 819 p.

Palamodov, V. P., 2004, Fundamental Solutions of the Acoustic and Diffusion Equations in Nonhomogeneous Medium, Arkiv för Matematik, v. 42, p. 119-152.

Powers, M. H., and Oden, C. P., 2004, Migration of Dispersive GPR Data, *in* Proceedings of the 10th Int'l. Conf. on Ground Penetrating Radar, Delft, The Netherlands, p. 333-336.

Powers, M. H., 1995, Dispersive Ground Penetrating Radar Modeling in 2D, PhD Thesis, Department of Geophysics, Colorado School of Mines, Golden, Colorado, 198 p.

Press, W. H., Teukolsky, S. A., Vetterling, W. T., and Flannery, B. P., 1992, Numerical Recipes in C, The Art of Scientific Computing, 2nd ed., Cambridge University Press, New York, 994 p.

Radzevicius, S. J., 2001, Dipole Antenna Properties and Their Effects on Ground Penetrating Radar Data, PhD Dissertation, Ohio State University, 158 p.

Ralston, D. R., and Chapan, S. L., 1969, Water Level Changes in the Mud Lake Area, Idaho, 1958-1968, Water Information Bulletin No. 7, Idaho Department of Reclamation, Boise, ID, 29 p.

Rossiter, J. R., 1977, Interpretation of Radio Interferometry Depth Sounding, with Emphasis on Random Scattering from Temperate Glaciers and the Lunar Surface: Ph.D. Thesis, Dept. of Physics, University of Toronto, 223 p.

Rea, J. and Knight, R. J., 1998, Geostatistical Analysis of Ground-Penetrating Radar Data: A Means of Describing Spatial Variation in the Subsurface, Water Resources Research, v. 34, n. 3, p. 329-339.

Riad, S. M., 1986, The Deconvolution Problem: An Overview, Proceedings of the IEEE, v. 74, n. 1, p. 82-85.

Roberts, R. L., and Daniels, J. J., 1997, Modeling Near-field GPR in Three Dimensions Using the FDTD Method, Geophysics, v. 62, n. 4., p. 1114-1126.

Robinson, D. A., 2004, Measurement of the Solid Dielectric Permittivity of Clay Minerals and Granular Samples Using a Time-domain Reflectometry Immersion Method, Vadose Zone Journal, v. 3, p. 705-713.

Rowe, R. K., Shang, J. Q., and Zie, Y., 2001, Complex Permittivity Measurement System for Detecting Soil Contamination, Canadian Geotechnical Journal, v. 38, n. 3, p. 498-506.

Scales, J. A., Docherty, P., and Gersztenkorn, A., 1990, Regularization of Nonlinear Inverse Problems: Imaging the Near Surface Weathering Layer, Inverse Problems, v. 6, n. 1, p. 115-131.

Scales, J. A., Smith, M. L., and Treitel, S., 1997, Introductory Geophysical Inverse Theory, Samizdat Press, Golden, Colorado, 193 p.

Schneeberger, K., Schwank, M., Stamm, C., de Rosnay, P., Matzler, C., and Fluhler, H., 2004, Topsoil Structure Influencing Soil Water Retrieval by Microwave Radiometry, Vadose Zone Journal, n. 3, p. 1169-1179.

Scott, G. R., 1972, Geologic Map of the Morrison Quadrangle, Jefferson County, Colorado, Folio of the Morrison Quadrangle, Colorado, Map I-790-A, U. S. Geological Survey, Washington, D.C.

Sihvola, A., 1999, Electromagnetic Mixing Formulas and Applications, IEE, London, 284 p.

Smith, B. M. E., Evans, S., 1972, Radio Echo Sounding Absorption and Scattering by Water Inclusion and Ice Lenses, J. of Glaciology, v. 11, n. 61, p. 133-146.

Smith, G. S., 1997, An Introduction to Classical Electromagnetic Radiation, Cambridge University Press, New York, 653 p.

Smith, G. S., and Nordgard, J. D., On the Design and Optimization of the Shielded-Pair Transmission Line, IEEE Trans. Microwave Theory and Techniques, v. MTT-28, n. 8, p. 887-893.

Smith, P. H., 1995, Electronic Application of the Smith Chart in Waveguide, Circuit, and Component Analysis, Noble Publishing Classic Series, Tucker, GA, 237 p.

Speidel, D. H., 1982, Earth Resources, *in* Physical Geology, Ludman, A., and Coch, N. K., 587 p., McGraw-Hill Book Co., New York, p. 492-515.

Stanley, W. D., Dougherty, G. R., and Dougherty, R., Digital Signal Processing, Prentice-Hall, Englewood Cliffs, NJ, 514 p.

Stolt, R. H., 1978, Migration by Fourier Transform, Geophysics, n. 43, p. 23-48.

Suleiman, A. A., and Ritchie, J. T., 2003, Modeling Soil Water Redistribution during Second-Stage Evaporation, Soil Sci. Soc. Am. J., 67, p. 377-386.

Taflove, A., and Hagness, S. C., 2000, Computational Electrodynamics: The Finite-Difference Time-Domain Method, 2nd Ed., Artech House, Boston, 852 p.

Tai, C. T., 1971, Dyadic Green's Functions in Electromagnetic Theory, Intext Educational Publishers, Scranton, OH, 246 p.

Tarantola, A., 2005, Inverse Problem Theory and Methods for Model Parameter Estimation, Society for Industrial and Applied Mathematics, Philadelphia, PA, 342 p.

Teixeira, F. L., Chew, W. C., Straka, M., Oristaglio, M. L., and Wang, T., 1998, Finite-Difference Time-Domain Simulation of Ground Penetrating Radar on Dispersive, Inhomogeneous, and Conductive Soils, IEEE Trans. Geoscience and Remote Sensing, v. 36, n. 6, p. 1928-1937.

Tindall, J. A., and Kunkel, J. R., 1999, Unsaturated Zone Hydrogeology for Scientists and Engineers, Prentice-Hall, Upper Saddle River, NJ, 624 p.

Turcotte, D. L., 1997, Fractals and Chaos in Geology and Geophysics, 2nd ed., Cambridge University Press, New York, 398 p.

Ulaby, F. T., Moore R. K., and Fung, A. K., 1982, Microwave Remote Sensing, Active and Passive, Volume II, Radar Remote Sensing and Surface Scattering and Emission Theory, Addison-Wesley Publishing, London, p. 456-1064.

Valle, S., Zanzi, L., Sgheiz, M., Lenzi, G., and Friborg, J., 2001, Ground Penetrating Radar Antennas: Theoretical and Experimental Directivity Functions, IEEE Trans. Geoscience and Remote Sensing, v. 39, n. 4, p. 749-758.

van Dam, J. M., Hendrickx, J. M. H., Harrison, B., Borchers, B., Norman, D. I., Ndur, S., Jasper, C., Niemeyer, P., Nartey, R., Vega, D., Calvo, L., Simms, J. E., 2004, Spatial Variability of Magnetic Soil Properties, *in* Detection and Remediation Technologies for Mines and Minelike Targets IX, SPIE Proceedings Volume 5415, p. 665-676.

Wakita, Y., and Yamaguchi, Y., 1996, Estimation of the Soil Permittivity and Conductivity by a GPR Antenna, *in* Proceedings of the 6th International Conference on Ground Penetrating Radar (GPR'96), Sendai, Japan, p. 123-127.

Wang, Y., 2002, A Stable and Efficient Approach of Inverse Q Filtering, Geophysics, v. 67, n. 2, p. 657-663.

Wang, Z., Jury, W. A., Tuli, A. and Kim, D. J., 2004, Unstable Flow during Redistribution: Controlling Factors and Practical Implications, Vadose Zone Journal, n. 3, p. 549-559.

Ward, S. H., and Hohmann, G. W., 1987, Electromagnetic Theory for Geophysical Applications, *in* Electromagnetic Methods in Applied Geophysics, M. N. Nabighian, ed., Investigations in Geophysics, n. 3., Soc. Exploration Geophysics, Tulsa, OK, p. 131-311.

Watts, R. D., and England, A. W., 1976, Radio-echo Sounding of the Temperate Glaciers: Ice Properties and Sounder Design Criteria, J. of Glaciology, v. 17, n. 75, p. 39-48.

Widess, M. B., 1973, How Thin is a Thin Bed?, Geophysics, v. 38, n. 6, p. 1176-1180.

Wtorek, J., 2003, Electrical and Magnetic Properties of Soil, EUDEM2 Technology Survey, IST-2000-29220, http://www.eudem.info/.

Wright, D. L., Oden, C. P., Powers, M. H., Moulton, C. W., Hutton, S. R., Kibler, J. D., Olhoeft, G. R., and Woodruff, W. F., 2005, A Ground Penetrating Radar System for High Loss Environments, *in* Proc. Symposium on the Application of Geophysics to Engineering and Environmental Problems, Atlanta, GA, p. 1-10.

Wu, T. T., and King, W. P., 1965, The Cylindrical Antenna with Nonreflecting Resisitive Loading, IEEE Trans. Antennas and Propagation, v. 13, pp. 369-373.

Wu, Y., Munson, D.C. Jr., and Lanterman, A.D., 2002, Multistatic Passive Radar Imaging of Aircraft: A Feasibility Study Using FISC, Proc. URSI National Radio Science Meeting, Boulder, CO, Jan. 9-12.

Yee, K. S., 1966, Numerical Solution of Initial Boundary Value Problems Involving Maxwell's Equations in Isotropic Media, IEEE Trans. Antennas and Propagation, v. AP-14, n. 8, p. 302-307.

Yilmaz, O., 1987, Seismic Data Processing, Doherty, S. M., Ed., Series: Investigations in Geophysics v. 2, Neitzel, E. B., Series Ed., Soc. Exploration Geophysicists, Tulsa, OK, 526 p.

Zeng, X., McMechan, G.A., and Xu, T., 2000, Synthesis of Amplitude-Versus-Offset Variations in Ground Penetrating Radar, Geophysics, v. 65, n. 1, p. 113-125.

Zhdanov, M. S., Traynin, P., and Booker, J. R., 1996, Underground Imaging by Frequency-Domain Electromagnetic Migration, Geophysics, v. 61, n. 3, p. 666-682.

Zhdanov, M. S., 2002, Geophysical Inverse Theory and Regularization Problems, Elsevier, Amsterdam, 628 p.

APPENDICES

APPENDIX A: RAMP GENERATOR

This appendix describes the ramp generator that can be used to calibrate GPRs that have a non-linear amplitude response and a flat frequency response over the operating frequency band. The schematic is shown in Figure A.1, and the parts list is contained in Table A.1. The generator can be built using inexpensive and readily available electronics components. The unit can be powered from two 9 volt batteries connected at J3, or with a standard laboratory DC power supply. The generator produces a ramp when an optical pulse is received at U4. The length of the negative slope is controlled by SW1, and the magnitude of both the negative and positive slopes are controlled by SW2. The ramp signal can be coupled to external circuits on a 50 ohm port (J1), or a 200 ohm port (J2).

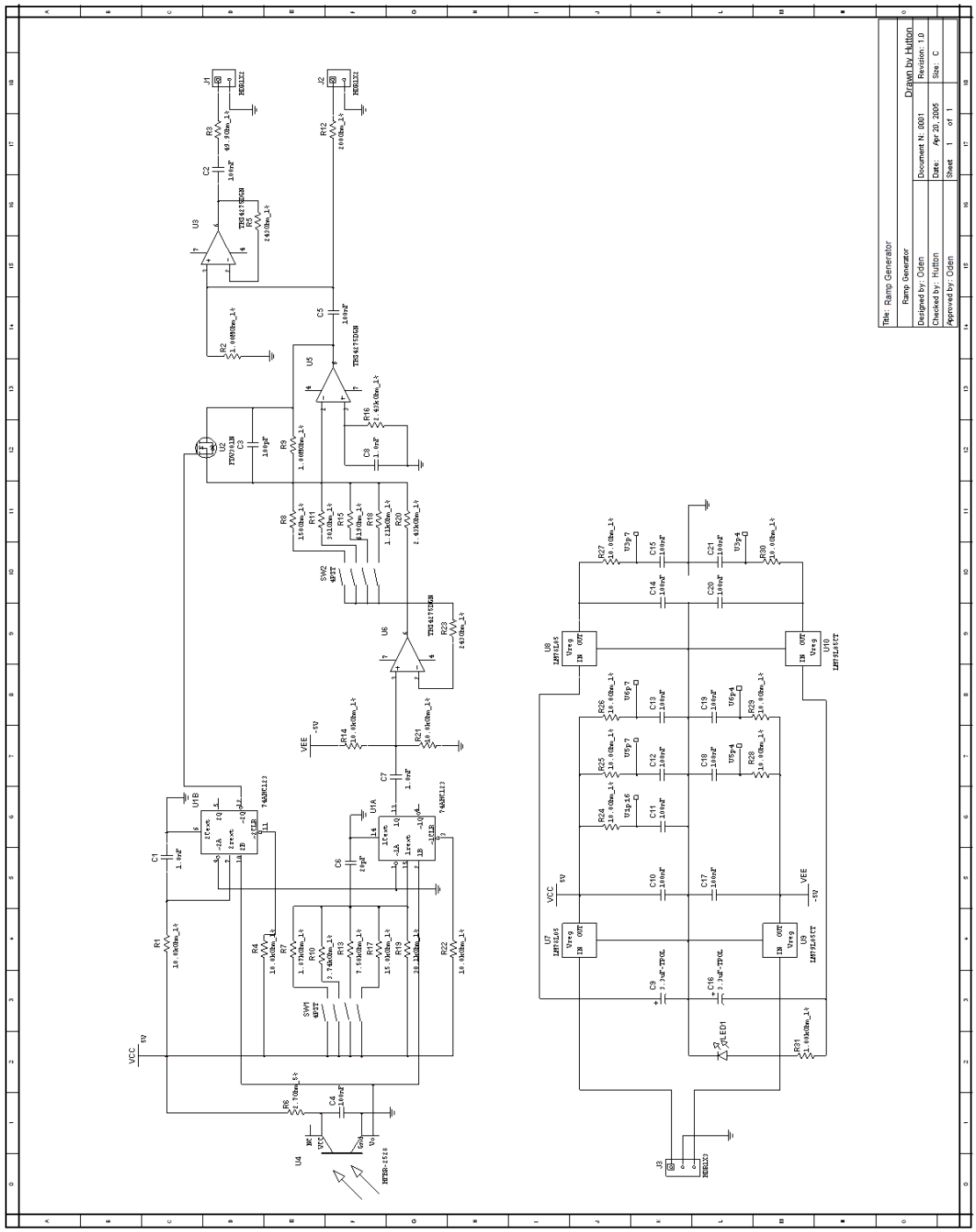

Figure A.1. Schematic of ramp generator.

Table A.1. Ramp generator parts list.

Quantity	Part Number	Description
1	HFBR-2528	optical receiver
1	FDV301N	transistor
2	THS4275DGN	high speed op amp
1	74AHC123	dual one shot
2	LM74L05	voltage reg.
2	LM2905CT	voltage reg.
1	LED	power indicator
12	100 nF	capacitor
4	1 nF 10V	capacitor
2	3.3 uF 16 V tant.	capacitor
1	20 pF 10V	capacitor
1	100 pF 10V	capacitor
1	1 k ohm 1%	resistor
7	10 ohm 1%	resistor
1	2.7 ohm 5%	resistor
4	10 k ohm 1%	resistor
2	1 M ohm 1%	resistor
1	243 ohm 1%	resistor
1	200 ohm 1%	resistor
1	50 ohm 1%	resistor
1	150 ohm 1%	resistor
1	301 ohm 1%	resistor
1	619 ohm 1%	resistor
1	1.21 k ohm 1%	resistor
1	2.43 k ohm 1%	resistor
1	1.87 k ohm 1%	resistor
1	3.74 k ohm 1%	resistor
1	7.50 k ohm 1%	resistor
1	15.0 k ohm 1%	resistor
1	30.1 k ohm 1%	resistor
2	4PST DIP SW	switch

APPENDIX B: PROCESSING SOFTWARE

This appendix describes the software that was written for this dissertation. The software provides many general purpose routines for processing GPR data from many manufacturers, and calibrating the equipment. Two programs are included: *GPR Workbench* and *GPR Wave Utilities*. *GPR Workbench* provides the standard 2D and 3D processing for GPR data, as well as some research features. High quality images of processed data can be generated for reports. Data from all of the main commercial radar manufacturers can be imported as well as data from several USGS prototype systems. The native file format is SU (Seismic Unix, Cohen and Stockwell, 2003). Files generated by *GPR Workbench* can be read by SU as well as many other data processing packages. *GPR Wave Utilities* provides a wide range of processing algorithms for single waveforms. *GPR Wave Utilities* is used primarily for calibrating radar systems and processing individual traces. Both programs are written to run on the Windows ™ operating system. The intent of releasing this software is not to duplicate the commercial GPR processing packages, but to provide a framework for researchers to test and implement new processing algorithms.

These programs provide a toolbox that is applicable to a wide range of equipment and problems. By adding to the source code provided here, scientists can investigate new processing algorithms. In should be noted that because to feature list of these programs grew rapidly, the structural organization of the software is not optimal. Individual routines have not been optimized for speed. Little thought was given to the end result primarily so that something could be developed quickly. The goal is to clean up and better organize the programs for release at a later date. Although the software is object oriented, strict adherence to object oriented programming methodologies has not been followed. The only conventions followed are to write in an active voice and to use

'Hungarian notation' in naming variables. Unless otherwise noted, frequencies are in MHz and time is in ns.

Both *GPR Workbench* and *GPR Wave Utilities* were written with Microsoft Visual C++ 6.0. All files are contained in two main project directories (one for each program) and are organized in the standard manner for Visual C++ projects. An easily distributable installation program is generated using the freely available Inno Setup Compiler (2004). A few functions rely on programs that were written by others. A GPR forward modeling program (Powers, 1995) was modified and included, as well as a program to summarize information in GPR file headers (Lucius and Powers, 2002). *GPR Workbench* uses a Windows automation interface to Golden Software's Surfer 8 package (not included) to generate high quality plan views of time slice GPR data. The MatClass library (Birchenhall, 1993) is used for matrix calculations. A more detailed list of features and functions for each program are listed below.

The file names containing *GPRMax* FDTD simulation results that will be used to create an IMSP interpolated forward operator describing the antenna response must follow a prescribed naming convention. *GPR Wave Utilities* requires the soil properties and antenna standoff used in the simulation to be encoded in the file name. The beginning of the file name can be anything, but the end must be written as follows

`RTDGPR_IMSP_W_SS1_p9_c0_02_s7.out`,

Where the number following the `p` is the RDP, the number following the `c` is the conductivity, and the number following the `s` is standoff. An underscore is used in place of the decimal point in the conductivity value, and to separate fields. The file extension must be `out`. Other than the file extension, no naming convention is needed for simulations that will not be used in the IMSP algorithm.

- Main *GPR Workbench* functions.

- Import (*.aq1; RTDGPR), (*.dzt; GSSI GPR), (*.dt1; Sensors and Software GPR), (*.rd3; Mala GPR), (*.su; Seismic Unix files), and other USGS formats. Exports (*.su; Seismic Unix files) and (*.csv; comma separated text files).
- Complete control over gridding and rubber sheeting using marks or position stamps on each trace. Marks can be visually added and removed.
- Section view provides hyperbola fitting for velocity analysis, zooming in time or position, and panning. Waveforms are displayed at mouse click position as well as depth to reflector. User specified color palates.
- An entire survey can be loaded and examined in plan view. Several gridding and filtering options available. Several plan view imaging methods with a trade-off between quality and speed. Automatically generate a high quality Surfer plan view image (*.jpg) for each slice. These images can be used to make a time slice movie.
- Many temporal, spatial, and frequency filters can be applied to the data.
- Migration of data that compensates for dispersive wave propagation.
- Generation of horizontal variograms.

- Main *GPR Wave Utilities* functions.
  - Imports (*.aq1; RTDGPR), many types of *GPRMax* files, many types of XFDTD files, and text files.
  - Time and frequency-domain graphs of waveforms.
  - Rich set of wave processing tools: frequency filters, re-sampling, linear operators, time shifting, taper functions, moving average filters, and more.
  - Convolution and deconvolution operations. Waveform differencing, Hilbert transform. Envelope calculations. Various waveform parameterizations.

- Calculates non-linearity function of test data and applies linearity correction.
- Interactive tabulation of waveform parameters and waveform graphing to compare experimental and simulated waveforms.
- Propagate FDTD wave fields beyond FDTD grid produced by the transmitting antenna.
- Calculate received waveforms from fields incident on receiving antenna using a reciprocity relationship with the transmitting antenna response.
- Inversion routine to estimate material properties under antennas. Constructs forward operator from FDTD simulations.

To demonstrate the utility of the software and how to use it, instructions for making the calculations to generate various figures in this thesis are reference in Table B.1. This Table cross-references various figures with files containing instructions for making the figures. The instructions describe the processing steps applied to the measured data to calculate the values graphed in the figures. These files are located on the accompanying DVD-ROM. See Appendix C for more information. *GPR Wave Utilities* was used in all processing except dispersive migration. *GPR Workbench* was used for dispersive migration.

Table B.1. Cross-reference between figures and files containing instructions for calculating the data shown in the figures.

Figure	File Name	DVD-ROM Archive File
2.13	Processing History TDR Cal 6-24-05.txt	Lab.exe
2.22	Processing History Pulser Test 5-9-05.txt	Lab.exe
2.32	Processing History RTDGPR Calibration.txt	RTDGPR_C.exe
3.10	Processing History Mud Lake.txt	Mud_Lake.exe
3.24	Processing History Mud Lake.txt	Mud_Lake.exe
4.9	Processing History Lake Air 6-27-05.txt	Lab.exe
4.13	Processing History Dispersive Migration.txt	Migrate.exe

REFERENCES

Birchenhall, C. R., 1993, A Draft Guide to MatClass, A Matrix Class for C++, Version 1.0d, Dept. Econometrics and Social Statistics, U. Manchester, UK, ftp://ftp.mcc.ac.uk/pub/matclass/pc.

Cohen, J. K., and Stockwell, J. W., Jr., 2003, CWP/SU: Seismic Unix Release 37: a Free Package for Seismic Research and Processing, Center for Wave Phenomena, Colorado School of Mines, Golden, Colorado, 141 p.

Inno Setup Compiler, 2004, http://www.jrsoftware.org.

Lucius, J. E., and Powers, M. H., 2002, GPR Data Processing Computer Software for the PC, U.S. Geological Survey, Open-File Report 02-166, 98 p.

Powers, M. H., 1995, Dispersive Ground Penetrating Radar Modeling in 2D, PhD Thesis Department of Geophysics, Colorado School of Mines, Golden, Colorado, 198 p.

APPENDIX C: CONTENTS OF THE DVD-ROM

The DVD-ROM accompanying this dissertation contains the software, raw data from laboratory and field measurements, and processed data. Digital versions of this dissertation and the *GPR Workbench* and *GPR Wave Utilities* software programs are included. A utility (*GPRMaxView*) for viewing *GPRMax* geometry files is included. Data and notes from all relevant experiments and survey sites have been included. Many FDTD simulation setup files and results for calibrating the RTDGPR are also included. The setup files and results of the FDTD simulations made for calculating the wave field at the Big Soda Lake site are also included. More detailed information is contained in the file *Contents.txt*, which describes the directory contents and special instructions for decompressing files if necessary. Many of the compressed files listed below contain simulated and experimental data in various subdirectories. There are processing history files located in each subdirectory that describe the step by step processing that was made with the data in that directory. All compressed files on the DVD-ROM are self-extracting executables.

- DVD-ROM Contents
  - *Contents.txt* Describes the contents of each file listed below.
  - *CPO_Dsrt.doc* Contains a Microsoft Word document file containing the accompanying dissertation
  - *CPO_Dsrt.pdf* Contains an Adobe Acrobat portable document file containing the accompanying dissertation
  - *WrkBnch.exe* Contains compressed source code and project files for the *GPR Workbench* program.
  - *GPRUtil.exe* Contains compressed source code and project files for the *GPR Wave Utilities* program.
  - *MaxView.exe* Contains compressed source code and project files for the *GPRMaxView* program.
  - *Misc.exe* Contains a self extracting zip file containing various excitation files used in simulations and processing, and example *GPRMax* geometry files.

- *SodaLake.exe* Contains *GPRMax* FDTD simulation setup and results for simulations made to determine fields on scan plane for Soda Lake experiment. Snapshot files are not included, but they can be regenerated using GPRMax3W.exe (included).
- *Migrate.exe* Contains *2D Radar* files input files for generating synthetic GPR sections for testing migration algorithms. Also contains a text file describing how to generate migrated images found in this dissertation.
- *Lab.exe* Contains various directories containing recorded data and notes during various experiments. Each subdirectory has a processing history file which describes the processing steps made on the data in that directory in detail. Contains data and field notes from the Big Soda Lake experiments. See *Contents.txt* for more information.
- *RTDGPR_C.exe* Contains *GPRMax* FDTD simulation setup and results for simulations made to calibrate and characterize the RTDGPR antenna system. See *Contents.txt* for more information.
- *RTDGPR.exe* Contains *GPRMax* FDTD simulation setup and results for simulations made for the IMSP algorithm using the 113 cm antenna offset.
- *RTDGPR_W.exe* Contains *GPRMax* FDTD simulation setup and results for simulations made for the IMSP algorithm using the 173 cm antenna offset.
- *Mud_Lake.exe* Contains data and field notes collected at the Mud Lake, ID site.
- *GPRMax3W.exe* A custom version of GPRMax used for the work in this dissertation.

In order to reduce the volume of data in the DVD-ROM, many of the *GPRMax* output files (geometry files and snapshot files) have not been included due to their large size. They can be generated with the included program *GPRMax3W.exe*. This is a custom version of the publicly available *GPRMax* program created for the work in this dissertation. *GPRMax3W* is based on the publicly available *GPRMax* version 1.5. Modifications were made to record current and allow a user specified voltage source excitation. *GPRMax* version 2.0 has recently become publicly available (www.gprmax.org), and this version has all of the capability of *GPRMax3W* (and more). It is highly suggested that *GPRMax* version 2.0 is used for all future work. Note however, that the output file formats with *GPRMax* version 2.0 have changed, and the

version of *GPR Wave Utilities* program on the DVD-ROM cannot read files generated by *GPRMax* version 2.0.

APPENDIX D: PLOTS OF SIMULATED ANTENNA RESPONSE WAVEFORMS AND THE IMSP FORWARD RESPONSE

The following pages contain plots of the FDTD simulated response of the antennas over a homogeneous half-space. The waveforms at the receiving antenna port at various values of RDP, conductivity, and standoff are shown in three sets of Figures. The standoff and offset of the antennas is shown in Figure D.1. Figures D.2-D.4 and D.12-D.14 illustrate the effects of changing RDP, Figures D.5-D.7 and D.15-D.17 illustrate the effects of changing conductivity, and Figures D.8-D.11 and D.18-D.21 show the effects of changing standoff. The accompanying DVD-ROM contains all of the *GPRMax* configuration files required to make the FDTD simulations as well as the results. Figures D.2-D.11 are for an offset of 113 cm center-to-center, and Figures D.12-D.21 are for a 173 cm offset.

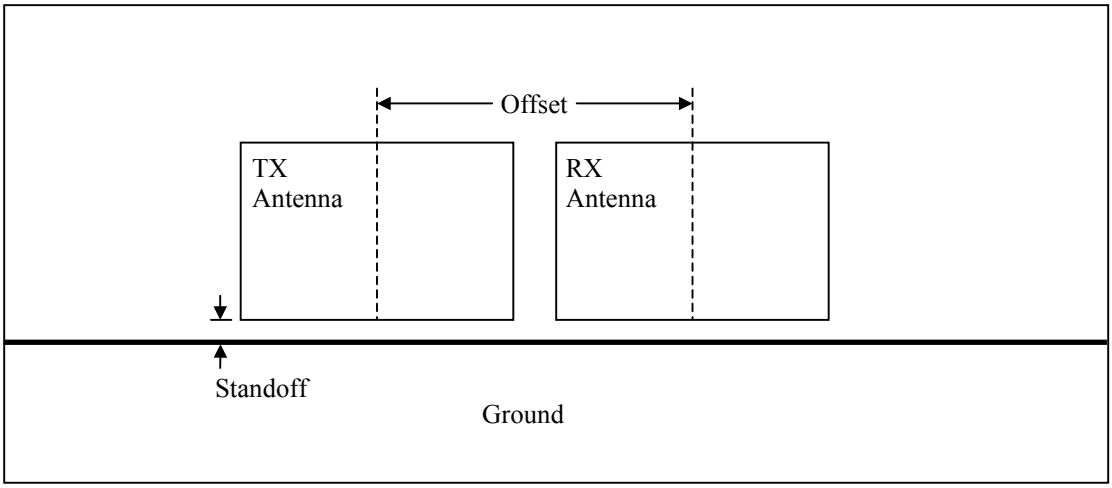

Figure D.1. Position of antennas for simulations. The offset is measured center to center. Drawing is not to scale.

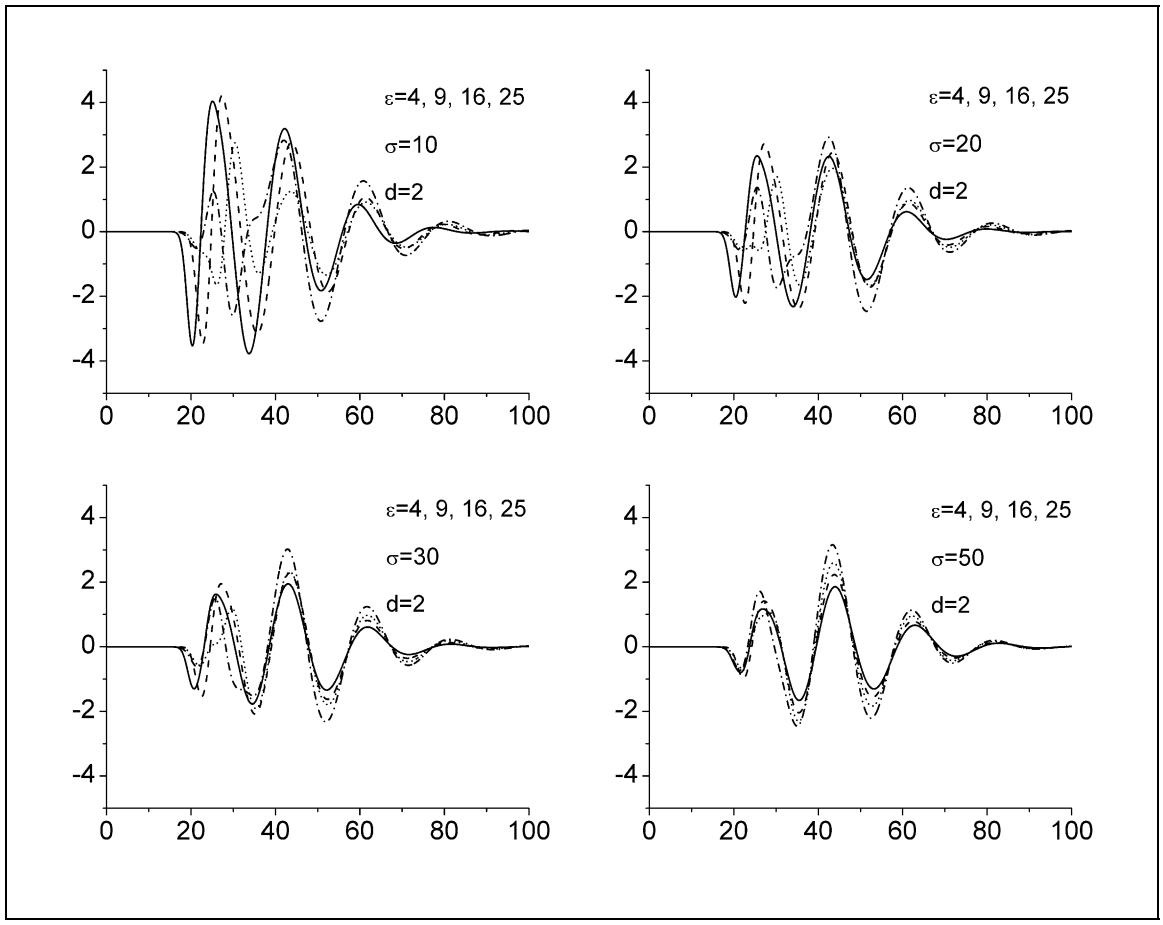

Figure D.2. Results of FDTD simulations at receiving antenna port as a function of RDP and conductivity. Antenna offset is 113 cm. Standoff is 2 cm. Vertical axis is amplitude in volts, and horizontal axis is time in ns. Four RDP values are plotted on each graph (ε_r = 4: solid, ε_r = 9: dashed, ε_r = 16: dotted, and ε_r = 25: dash-dot).

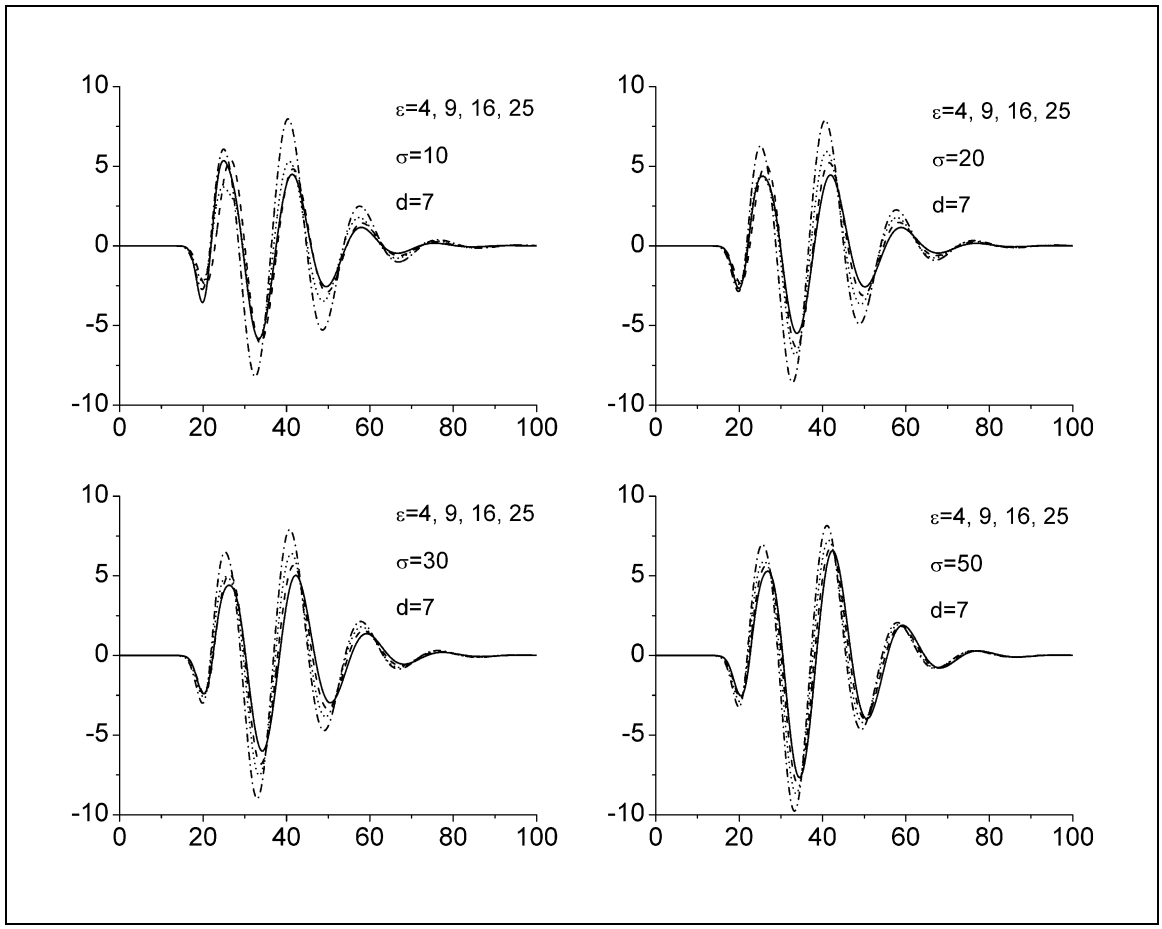

Figure D.3. Results of FDTD simulations at receiving antenna port as a function of RDP and conductivity. Antenna offset is 113 cm. Standoff is 7 cm. Vertical axis is amplitude in volts, and horizontal axis is time in ns. Four RDP values are plotted on each graph (ε_r = 4: solid, ε_r = 9: dashed, ε_r = 16: dotted, and ε_r = 25: dash-dot).

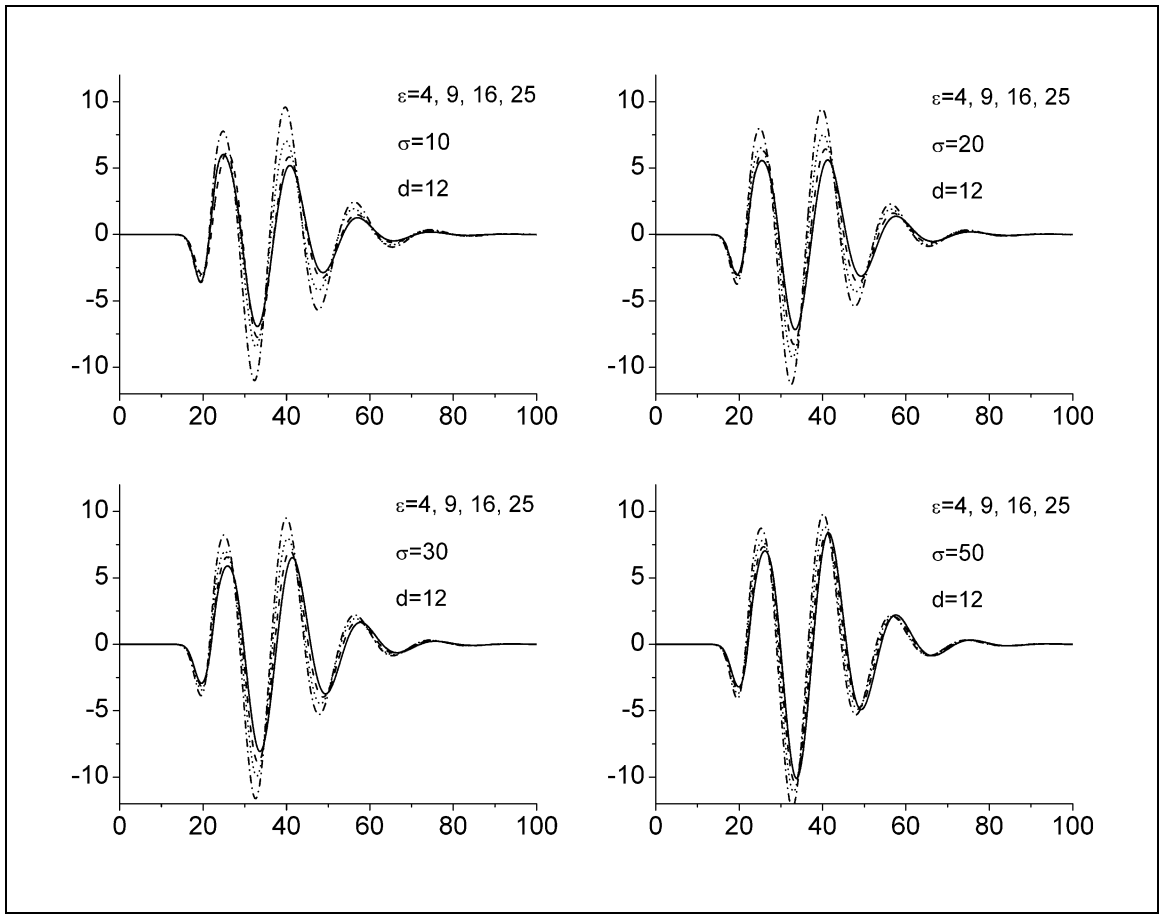

Figure D.4. Results of FDTD simulations at receiving antenna port as a function of RDP and conductivity. Antenna offset is 113 cm. Standoff is 12 cm. Vertical axis is amplitude in volts, and horizontal axis is time in ns. Four RDP values are plotted on each graph ($\varepsilon_r = 4$: solid, $\varepsilon_r = 9$: dashed, $\varepsilon_r = 16$: dotted, and $\varepsilon_r = 25$: dash-dot).

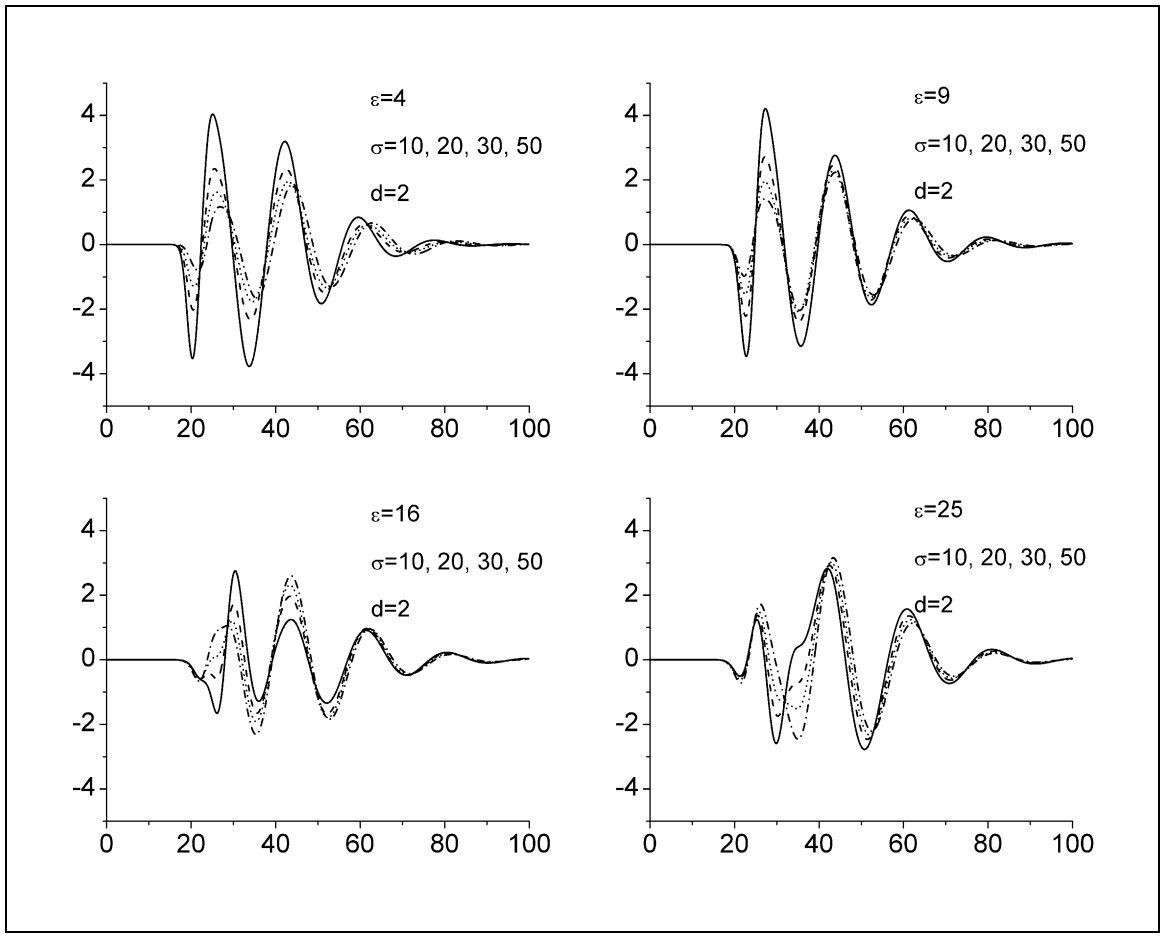

Figure D.5. Results of FDTD simulations at receiving antenna port as a function of conductivity and RDP. Antenna offset is 113 cm. Standoff is 2 cm. Vertical axis is amplitude in volts, and horizontal axis is time in ns. Four conductivity values are plotted on each graph (σ = 10: solid, σ = 20: dashed, σ = 30: dotted, and σ = 50: dash-dot).

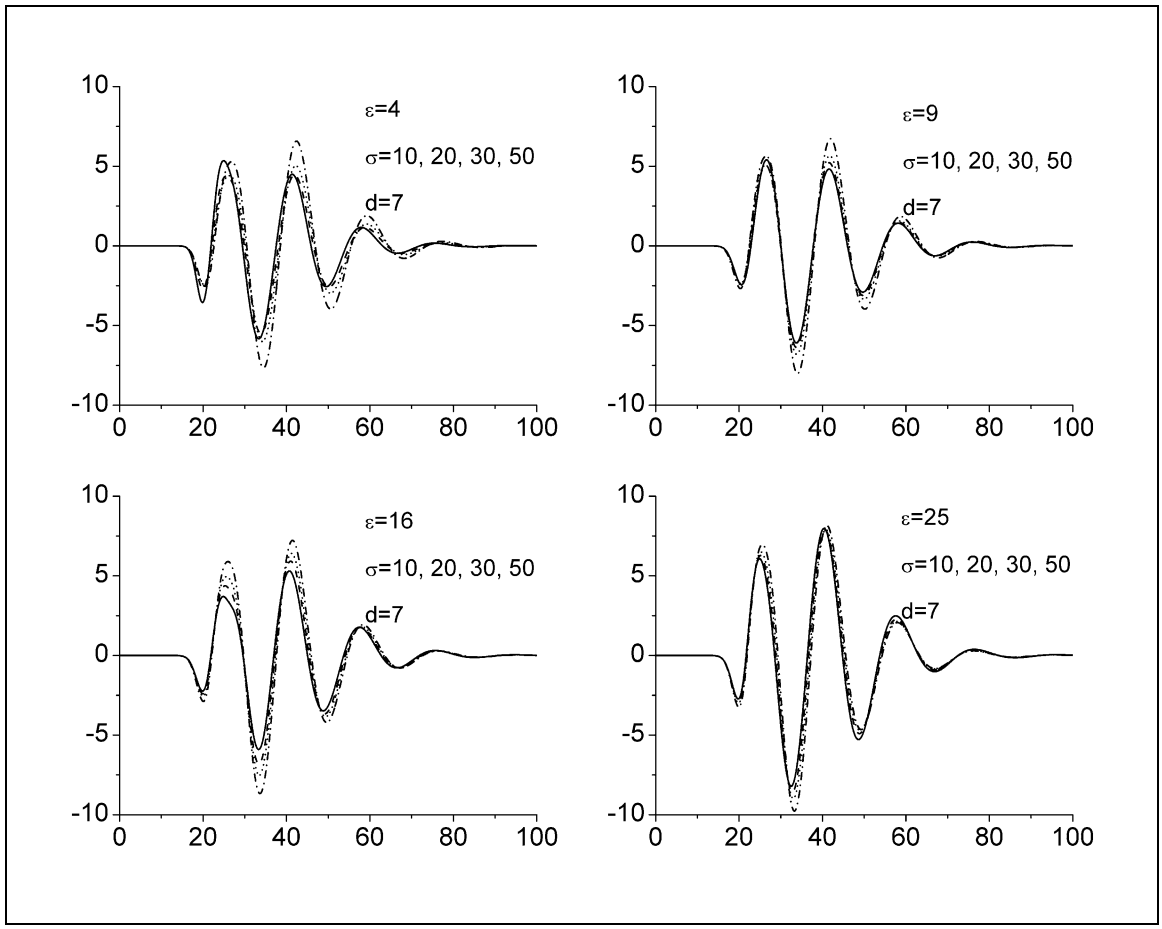

Figure D.6. Results of FDTD simulations at receiving antenna port as a function of conductivity and RDP. Antenna offset is 113 cm. Standoff is 7 cm. Vertical axis is amplitude in volts, and horizontal axis is time in ns. Four conductivity values are plotted on each graph (σ = 10: solid, σ = 20: dashed, σ = 30: dotted, and σ = 50: dash-dot).

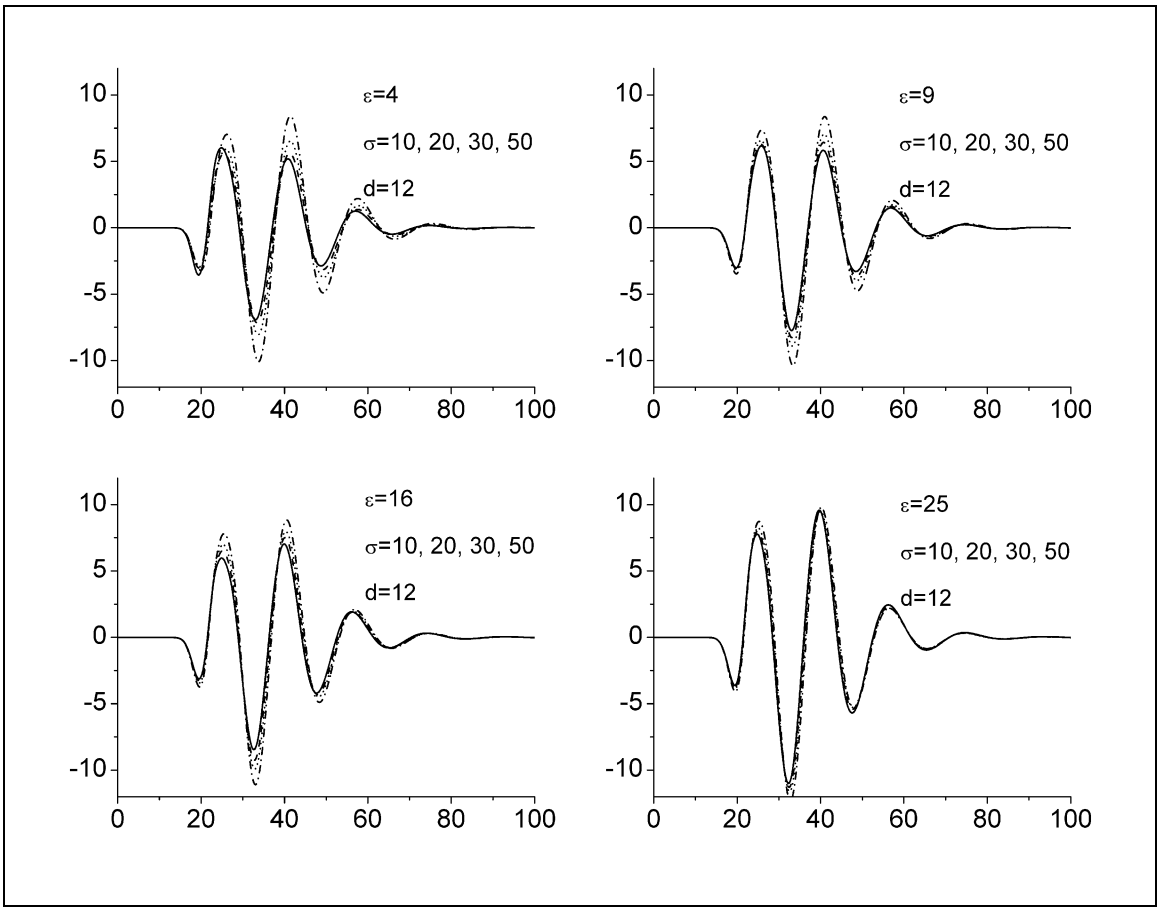

Figure D.7. Results of FDTD simulations at receiving antenna port as a function of conductivity and RDP. Antenna offset is 113 cm. Standoff is 12 cm. Vertical axis is amplitude in volts, and horizontal axis is time in ns. Four conductivity values are plotted on each graph (σ = 10: solid, σ = 20: dashed, σ = 30: dotted, and σ = 50: dash-dot).

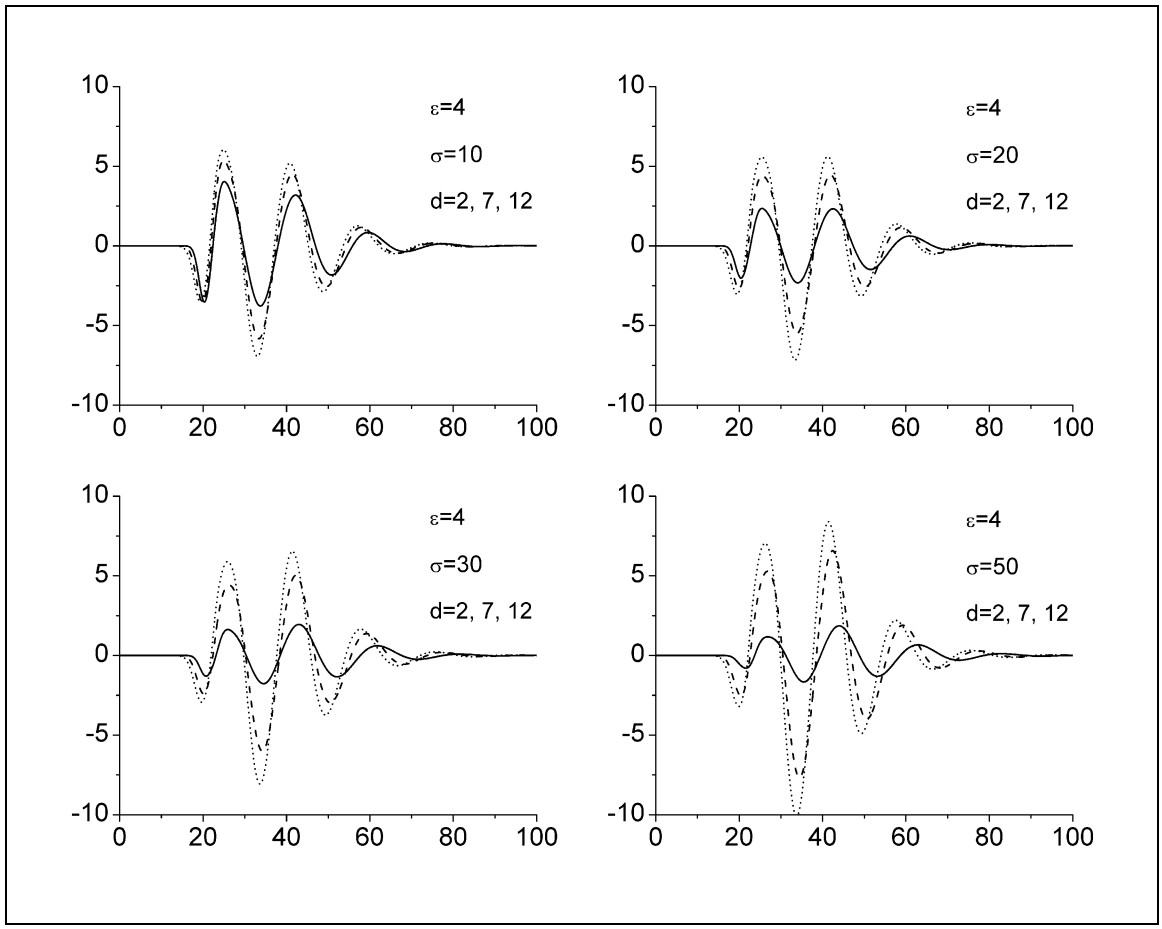

Figure D.8. Results of FDTD simulations at receiving antenna port as a function of standoff and conductivity. Antenna offset is 113 cm. RDP is 4. Vertical axis is amplitude in volts, and horizontal axis is time in ns. Three standoff values are plotted on each graph (d = 2: solid, d = 7: dashed, and d = 12: dotted).

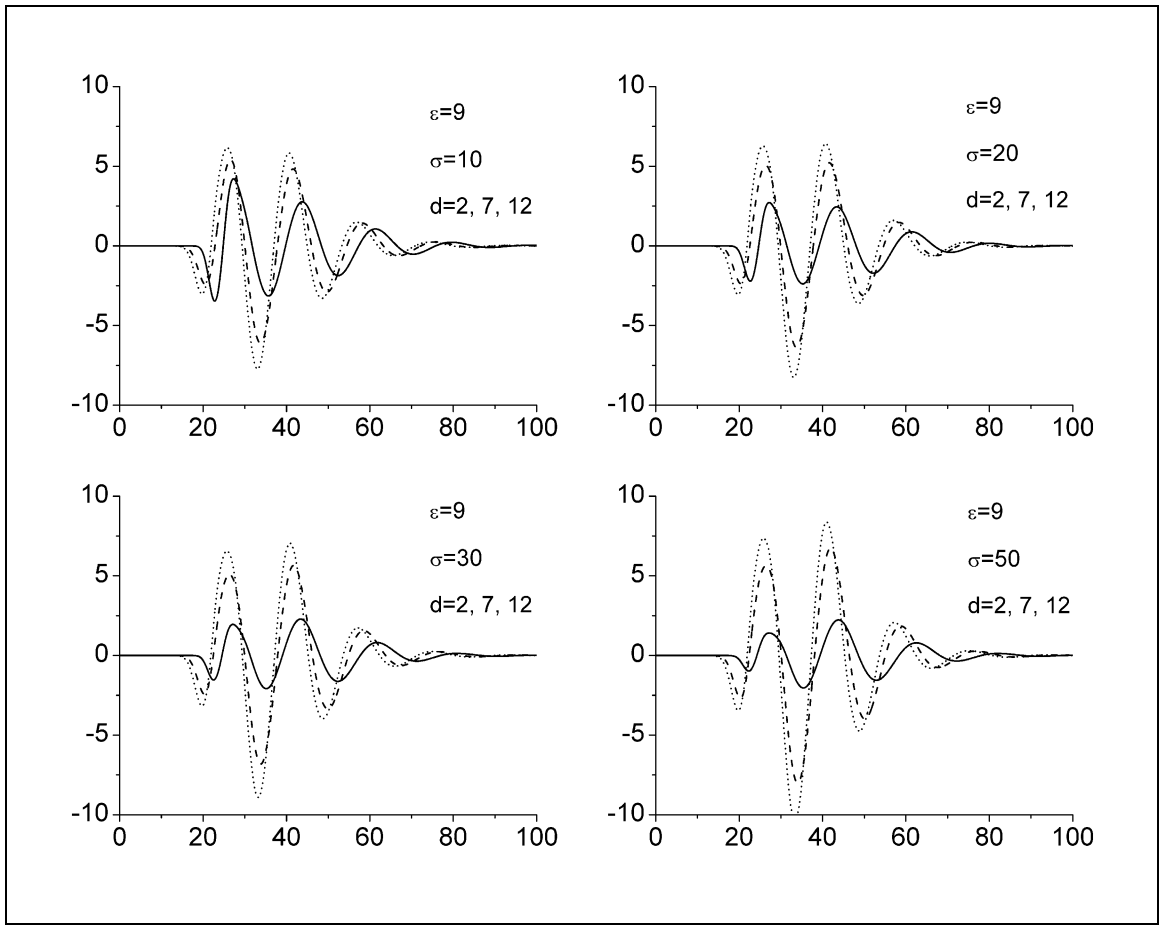

Figure D.9. Results of FDTD simulations at receiving antenna port as a function of standoff and conductivity. Antenna offset is 113 cm. RDP is 9. Vertical axis is amplitude in volts, and horizontal axis is time in ns. Three standoff values are plotted on each graph (d = 2: solid, d = 7: dashed, and d = 12: dotted).

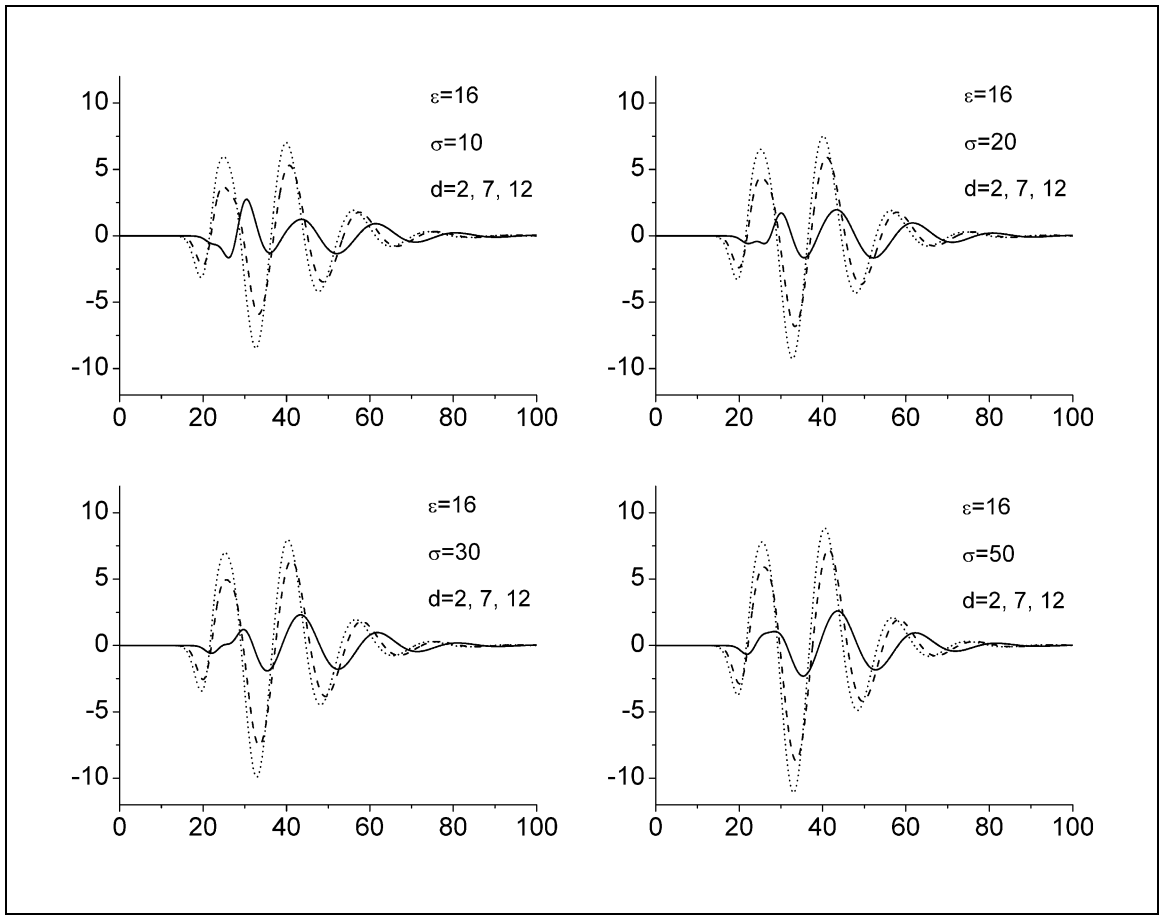

Figure D.10. Results of FDTD simulations at receiving antenna port as a function of standoff and conductivity. Antenna offset is 113 cm. RDP is 16. Vertical axis is amplitude in volts, and horizontal axis is time in ns. Three standoff values are plotted on each graph (d = 2: solid, d = 7: dashed, and d = 12: dotted).

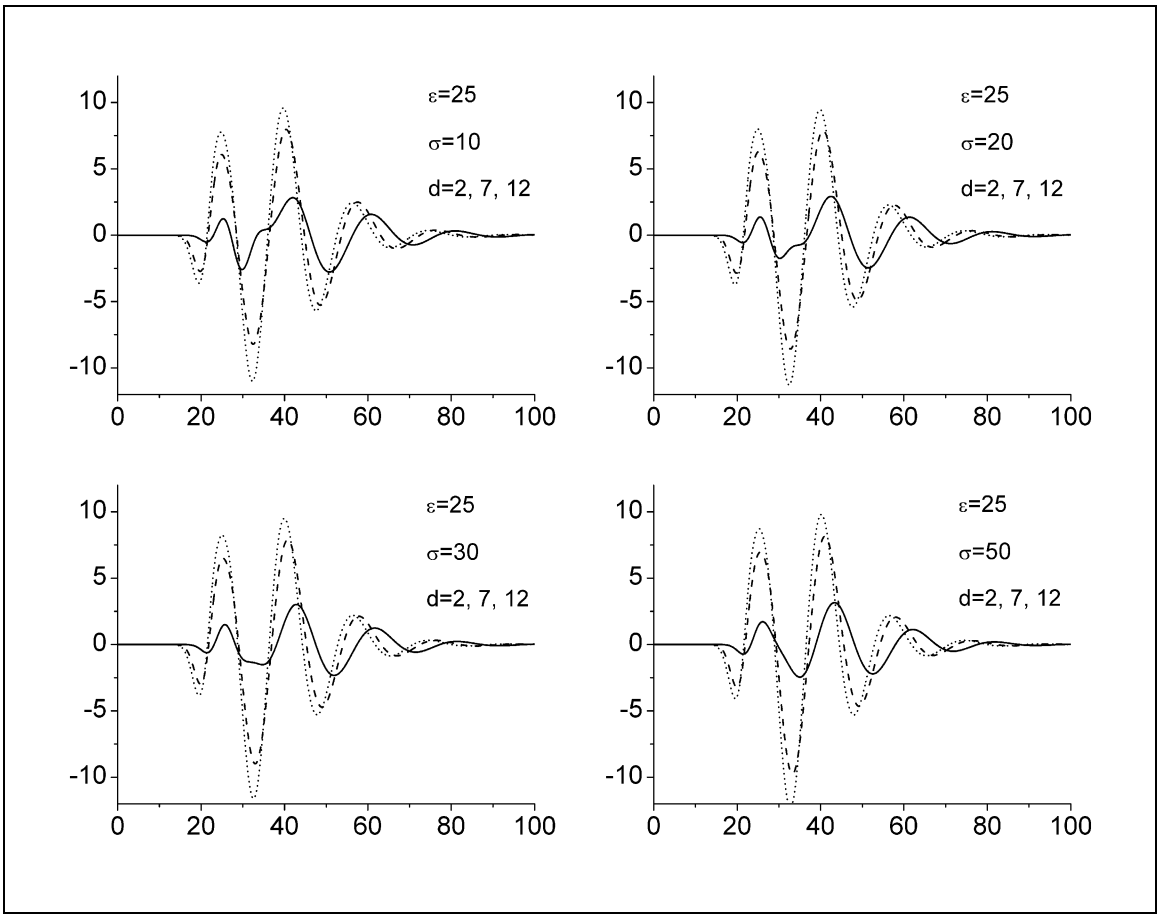

Figure D.11. Results of FDTD simulations at receiving antenna port as a function of standoff and conductivity. Antenna offset is 113 cm. RDP is 25. Vertical axis is amplitude in volts, and horizontal axis is time in ns. Three standoff values are plotted on each graph (d = 2: solid, d = 7: dashed, and d = 12: dotted).

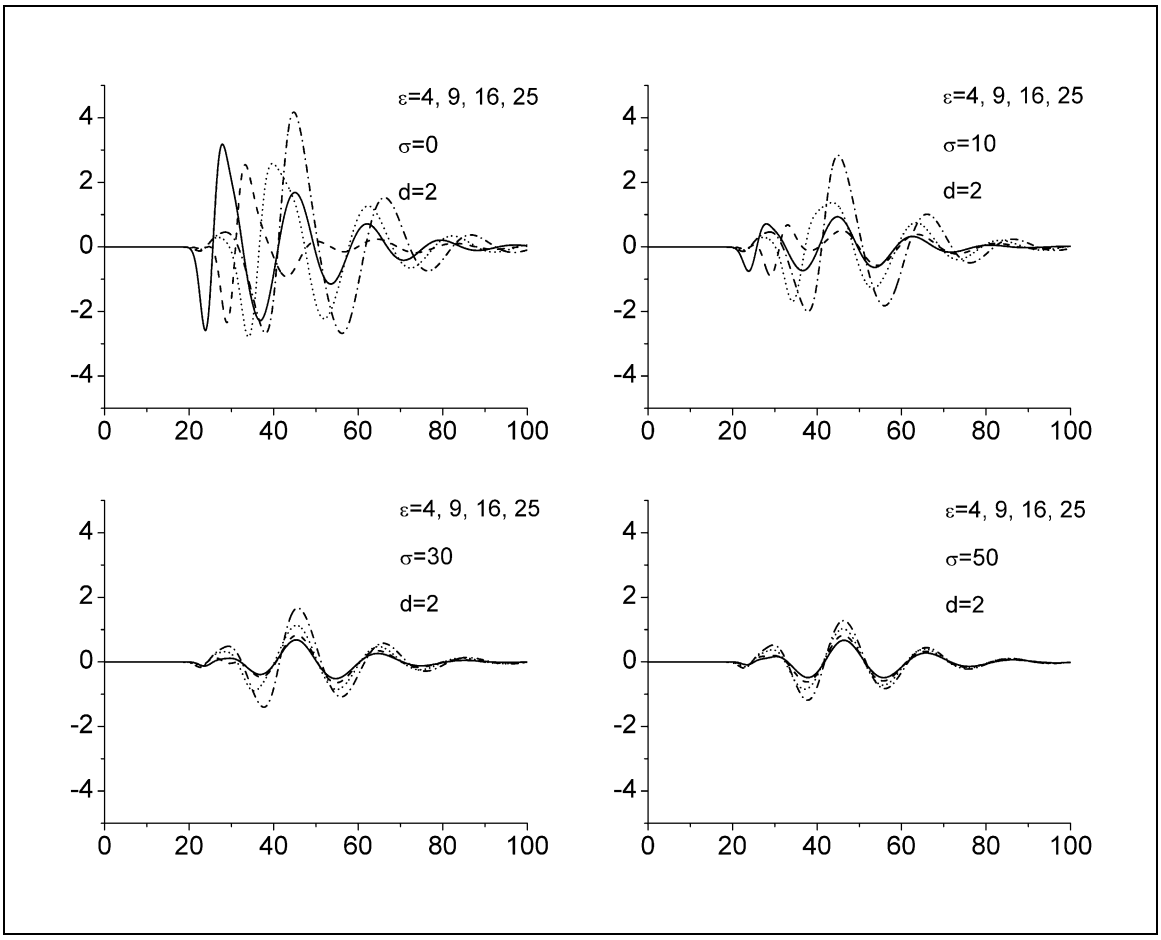

Figure D.12. Results of FDTD simulations at receiving antenna port as a function of RDP and conductivity. Antenna offset is 173 cm. Standoff is 2 cm. Vertical axis is amplitude in volts, and horizontal axis is time in ns. Four RDP values are plotted on each graph ($\varepsilon_r = 4$: solid, $\varepsilon_r = 9$: dashed, $\varepsilon_r = 16$: dotted, and $\varepsilon_r = 25$: dash-dot).

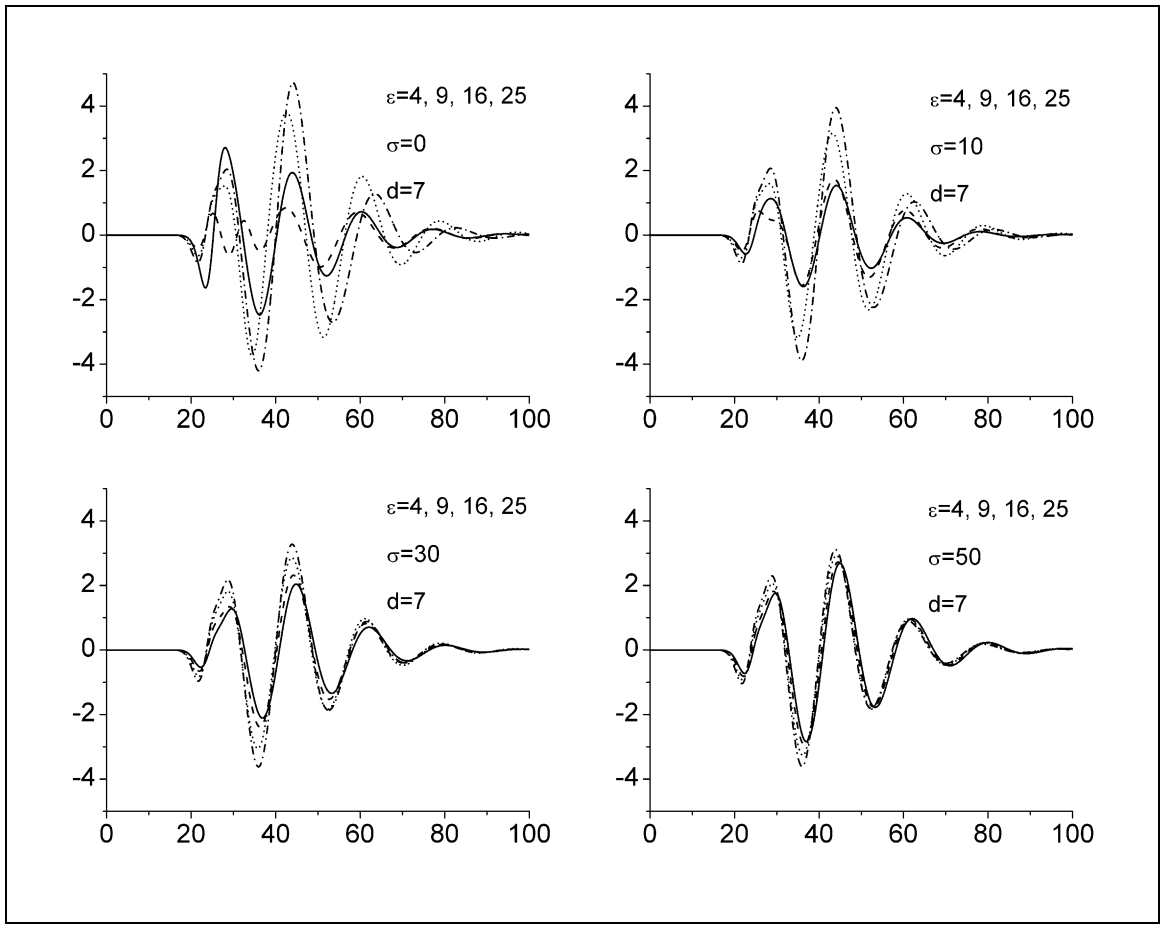

Figure D.13. Results of FDTD simulations at receiving antenna port as a function of RDP and conductivity. Antenna offset is 173 cm. Standoff is 7 cm. Vertical axis is amplitude in volts, and horizontal axis is time in ns. Four RDP values are plotted on each graph ($\varepsilon_r = 4$: solid, $\varepsilon_r = 9$: dashed, $\varepsilon_r = 16$: dotted, and $\varepsilon_r = 25$: dash-dot).

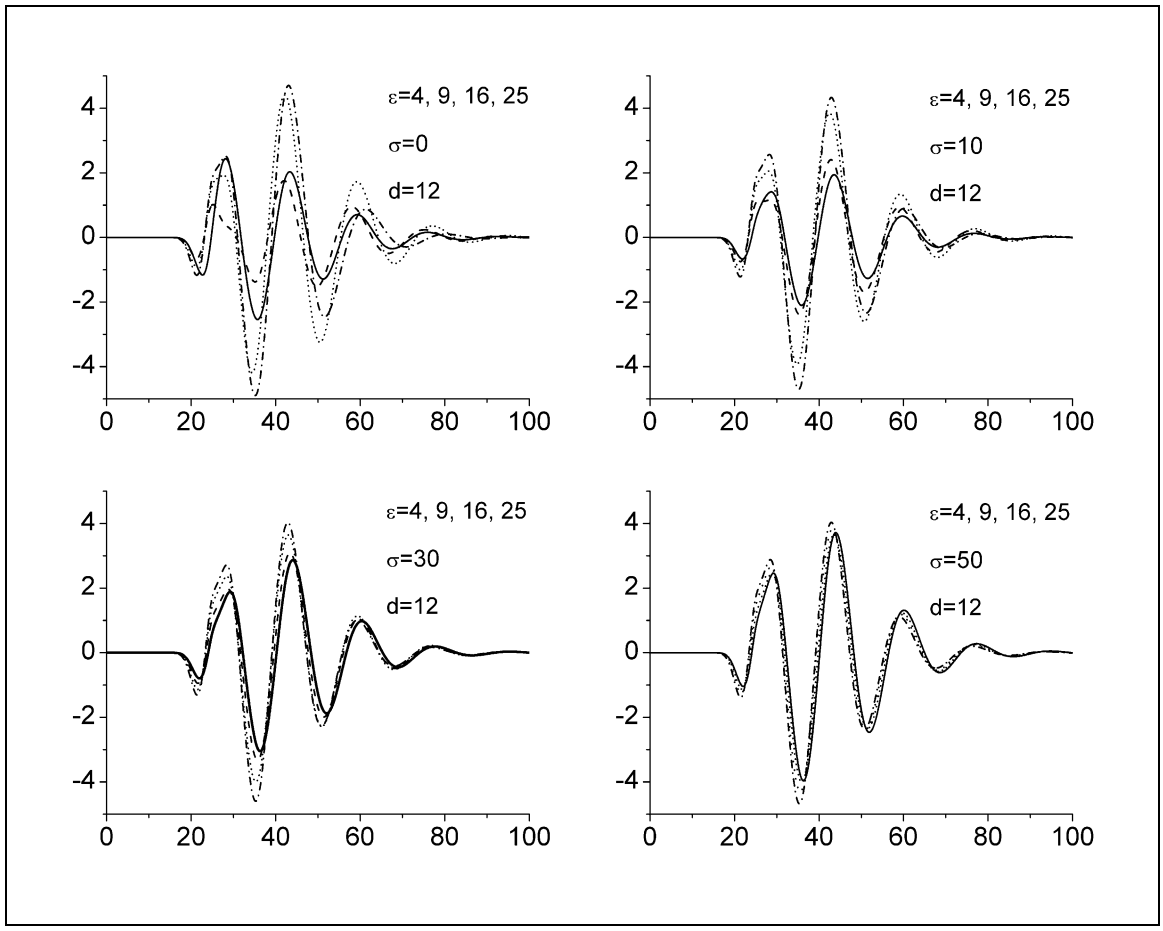

Figure D.14. Results of FDTD simulations at receiving antenna port as a function of RDP and conductivity. Antenna offset is 173 cm. Standoff is 12 cm. Vertical axis is amplitude in volts, and horizontal axis is time in ns. Four RDP values are plotted on each graph ($\varepsilon_r = 4$: solid, $\varepsilon_r = 9$: dashed, $\varepsilon_r = 16$: dotted, and $\varepsilon_r = 25$: dash-dot).

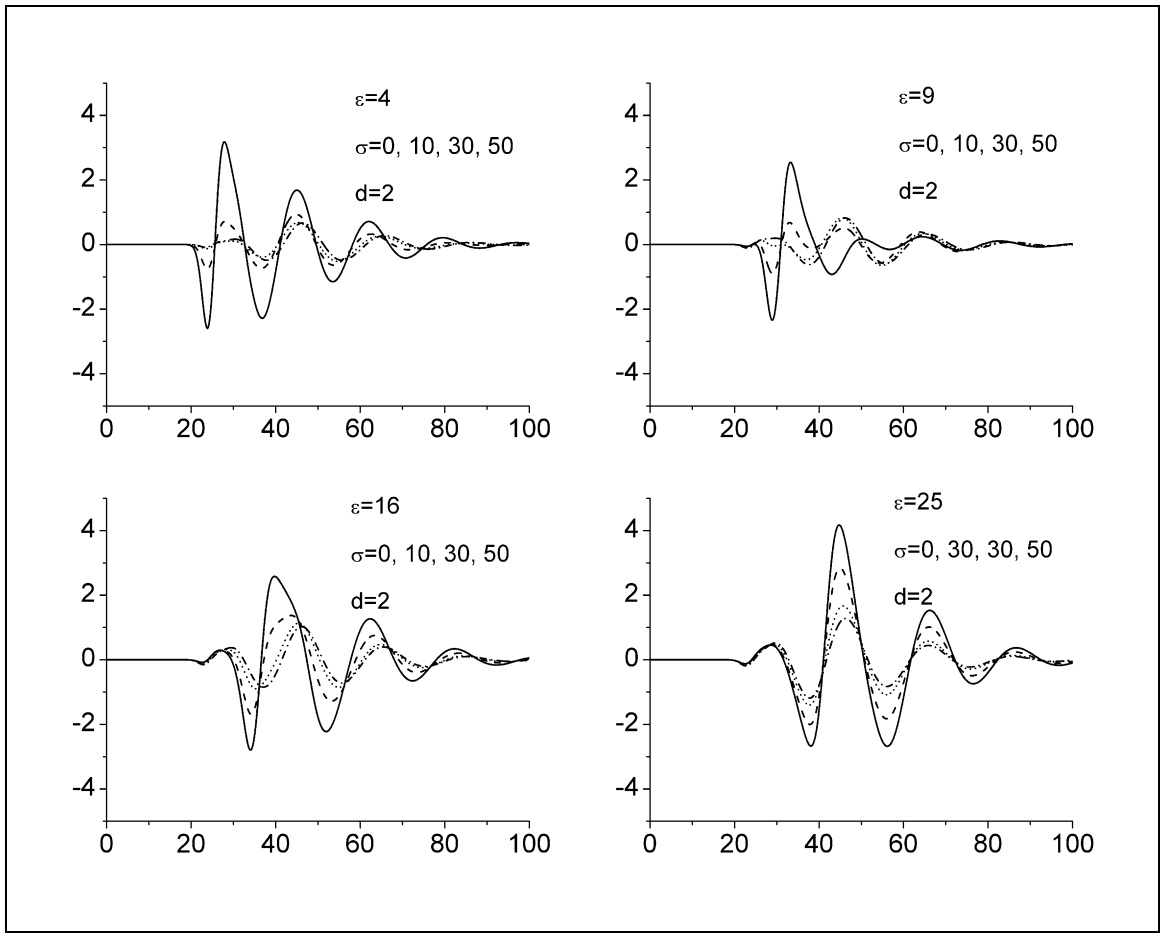

Figure D.15. Results of FDTD simulations at receiving antenna port as a function of conductivity and RDP. Antenna offset is 173 cm. Standoff is 2 cm. Vertical axis is amplitude in volts, and horizontal axis is time in ns. Four conductivity values are plotted on each graph ($\sigma = 0$: solid, $\sigma = 10$: dashed, $\sigma = 30$: dotted, and $\sigma = 50$: dash-dot).

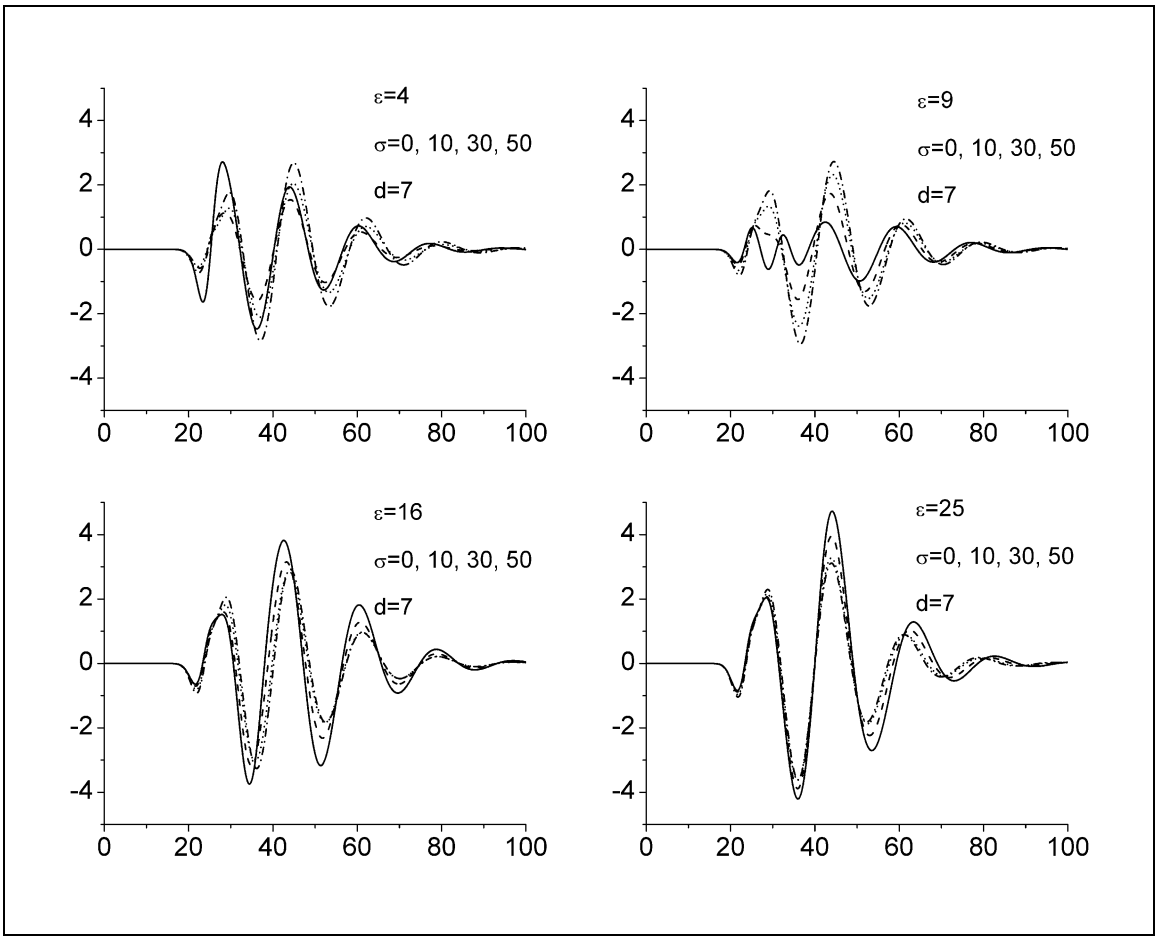

Figure D.16. Results of FDTD simulations at receiving antenna port as a function of conductivity and RDP. Antenna offset is 173 cm. Standoff is 7 cm. Vertical axis is amplitude in volts, and horizontal axis is time in ns. Four conductivity values are plotted on each graph ($\sigma = 0$: solid, $\sigma = 10$: dashed, $\sigma = 30$: dotted, and $\sigma = 50$: dash-dot).

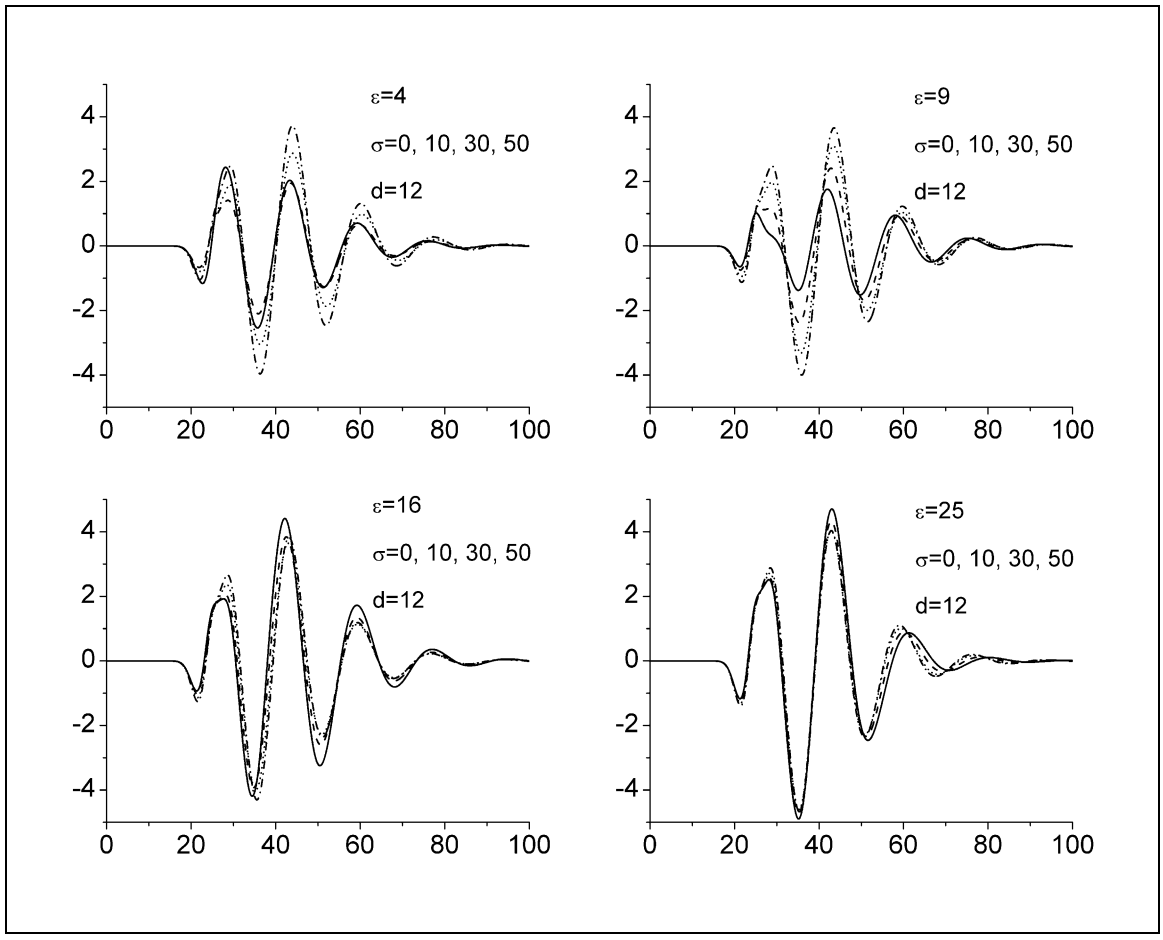

Figure D.17. Results of FDTD simulations at receiving antenna port as a function of conductivity and RDP. Antenna offset is 173 cm. Standoff is 12 cm. Vertical axis is amplitude in volts, and horizontal axis is time in ns. Four conductivity values are plotted on each graph ($\sigma = 0$: solid, $\sigma = 10$: dashed, $\sigma = 30$: dotted, and $\sigma = 50$: dash-dot).

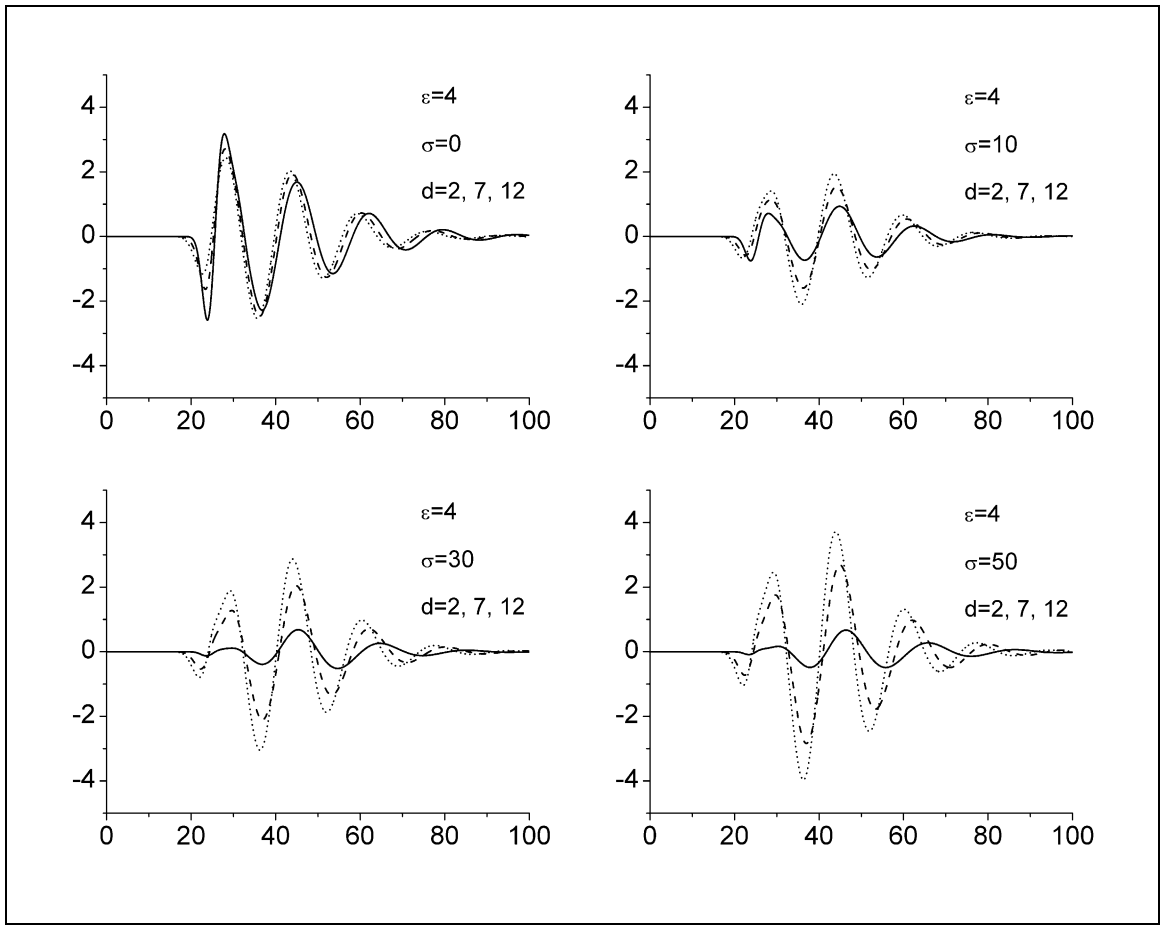

Figure D.18. Results of FDTD simulations at receiving antenna port as a function of standoff and conductivity. Antenna offset is 173 cm. RDP is 4. Vertical axis is amplitude in volts, and horizontal axis is time in ns. Three standoff values are plotted on each graph (d = 2: solid, d = 7: dashed, and d = 12: dotted).

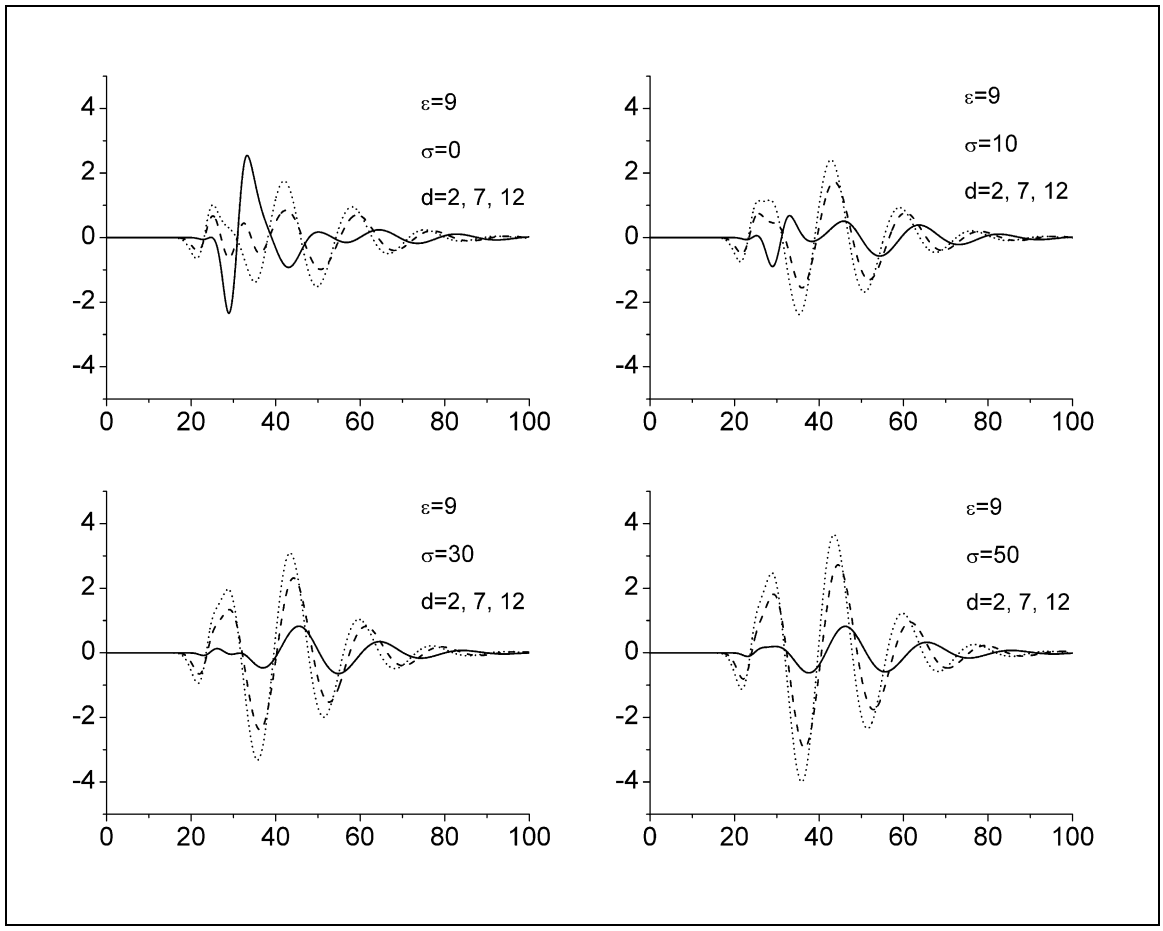

Figure D.19. Results of FDTD simulations at receiving antenna port as a function of standoff and conductivity. Antenna offset is 173 cm. RDP is 9. Vertical axis is amplitude in volts, and horizontal axis is time in ns. Three standoff values are plotted on each graph (d = 2: solid, d = 7: dashed, and d = 12: dotted).

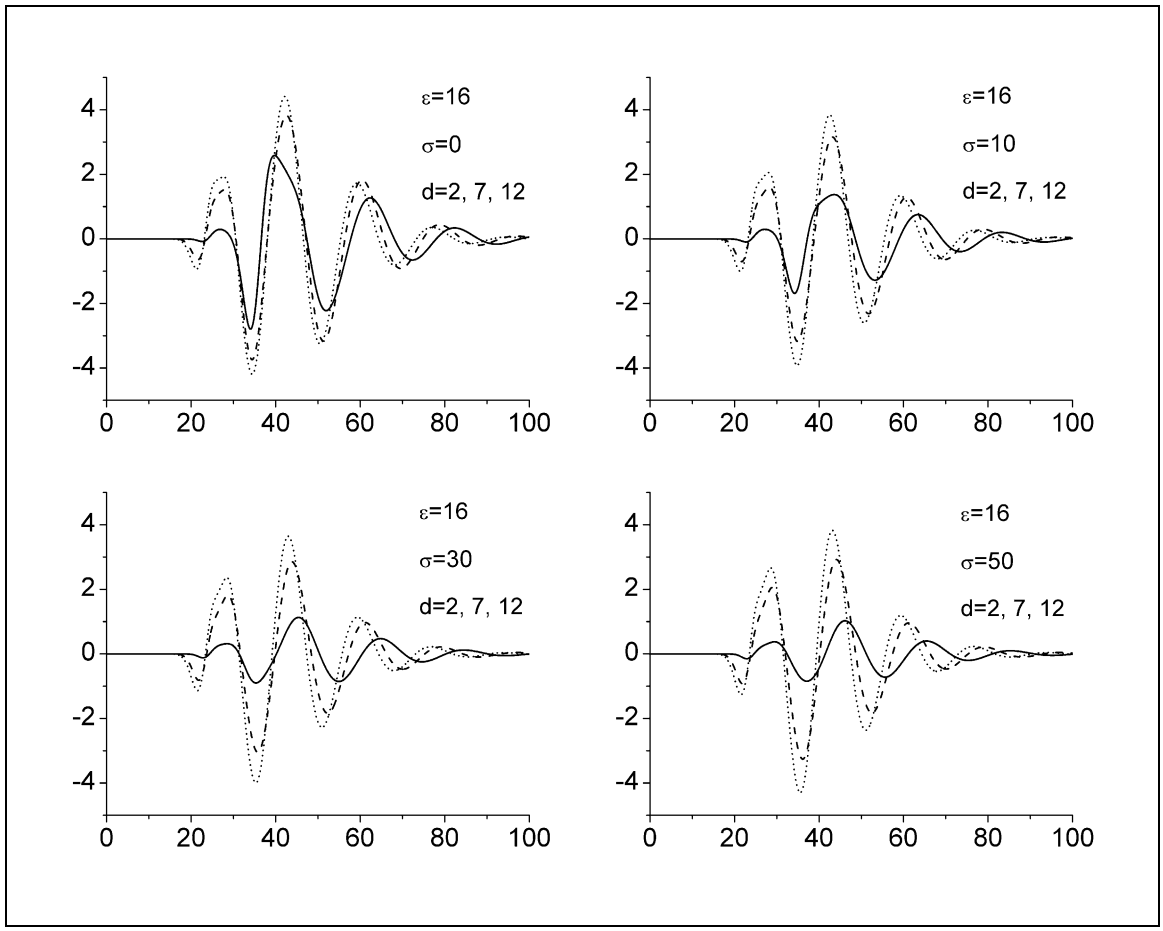

Figure D.20. Results of FDTD simulations at receiving antenna port as a function of standoff and conductivity. Antenna offset is 173 cm. RDP is 16. Vertical axis is amplitude in volts, and horizontal axis is time in ns. Three standoff values are plotted on each graph (d = 2: solid, d = 7: dashed, and d = 12: dotted).

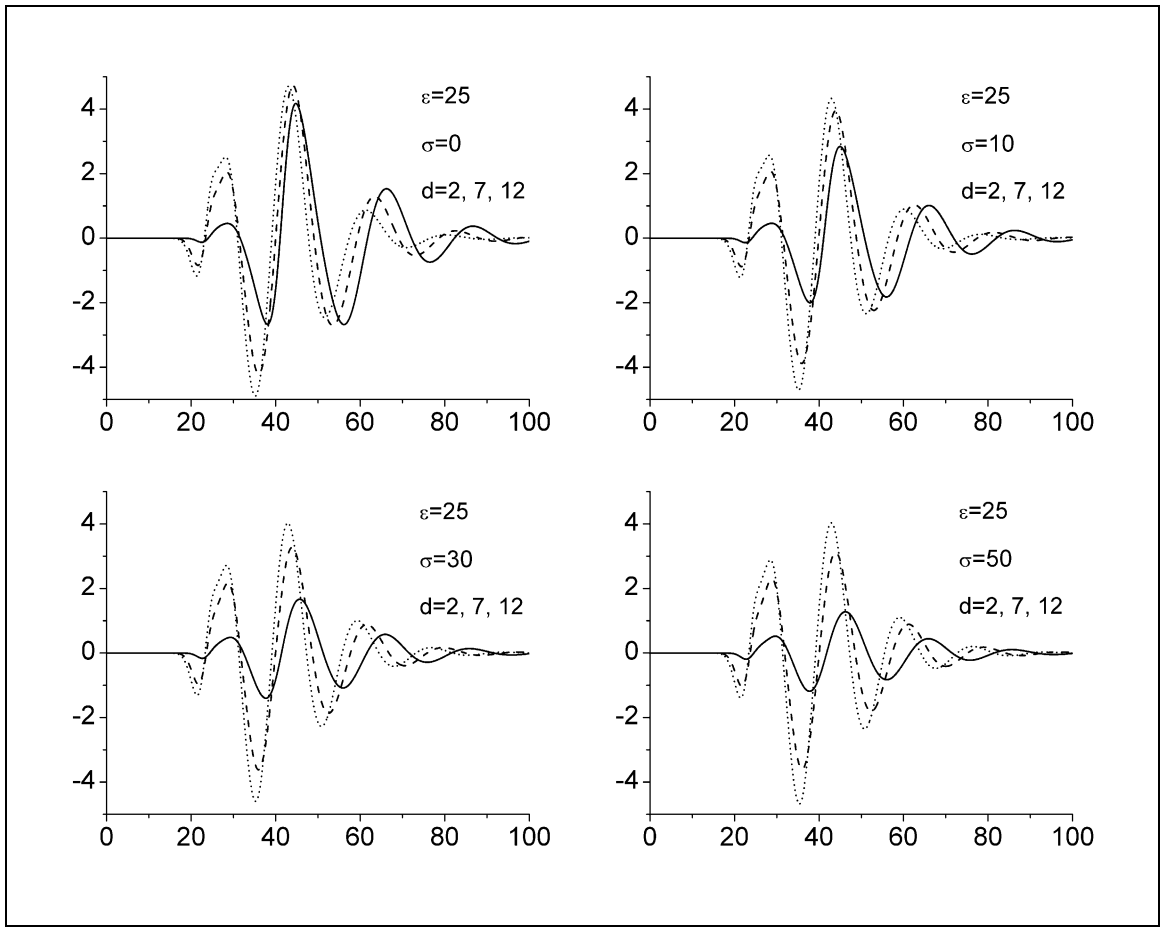

Figure D.21. Results of FDTD simulations at receiving antenna port as a function of standoff and conductivity. Antenna offset is 173 cm. RDP is 25. Vertical axis is amplitude in volts, and horizontal axis is time in ns. Three standoff values are plotted on each graph (d = 2: solid, d = 7: dashed, and d = 12: dotted).

An IMSP forward operator **A** was constructed for two antenna offsets, 113 and 173 cm. Two dimensional plots of the interpolated forward response **A**(**x**) for the 113 cm offset using waveform the *Spectral* attribute set are shown in Figures D.22-D.24, and plots for the *Hilbert* attribute set are shown in Figure D.25-D.27. The analogous plots for the 173 cm offset are shown in Figures D.28-D.33. The FFT spectral amplitudes of the simulated received waveform make up the *Spectral* attribute set. The Hilbert envelope is the modulus of the waveform and its Hilbert transform (or quadrature component). The *Hilbert* attribute set is contains time-domain samples at 2 ns intervals of the Hilbert envelope. Only a few waveform attributes are shown to avoid an inordinate number of plots. These contour maps are slices through the 3D model parameter space. Although abbreviated, these plots convey the nature of the interpolated forward response. See Sections 3.2 and 3.3 for discussions on extracting waveform attribute sets and constructing the forward operator.

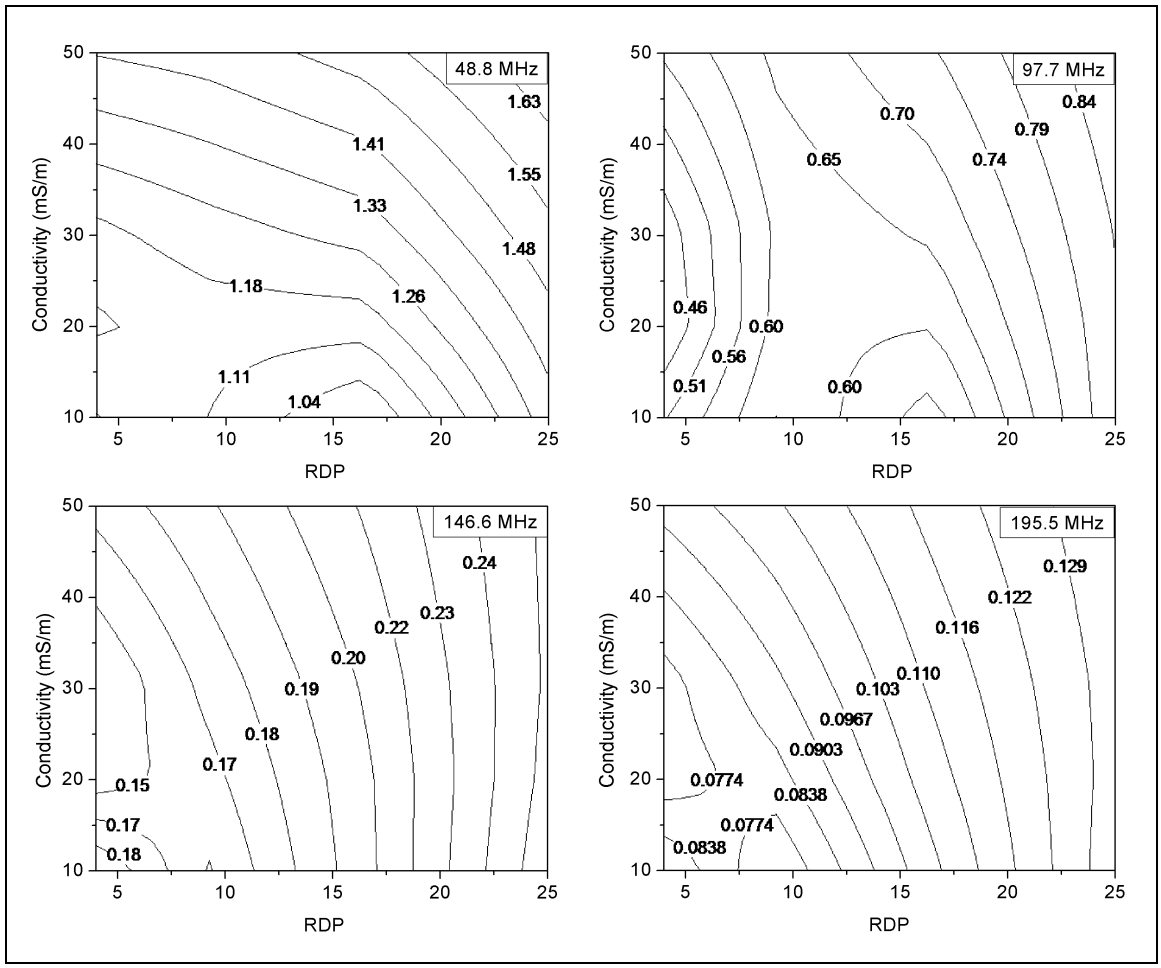

Figure D.22. Interpolated forward response of selected waveform attributes using the *Spectral* attribute set for a 7 cm standoff and a 113 cm offset.

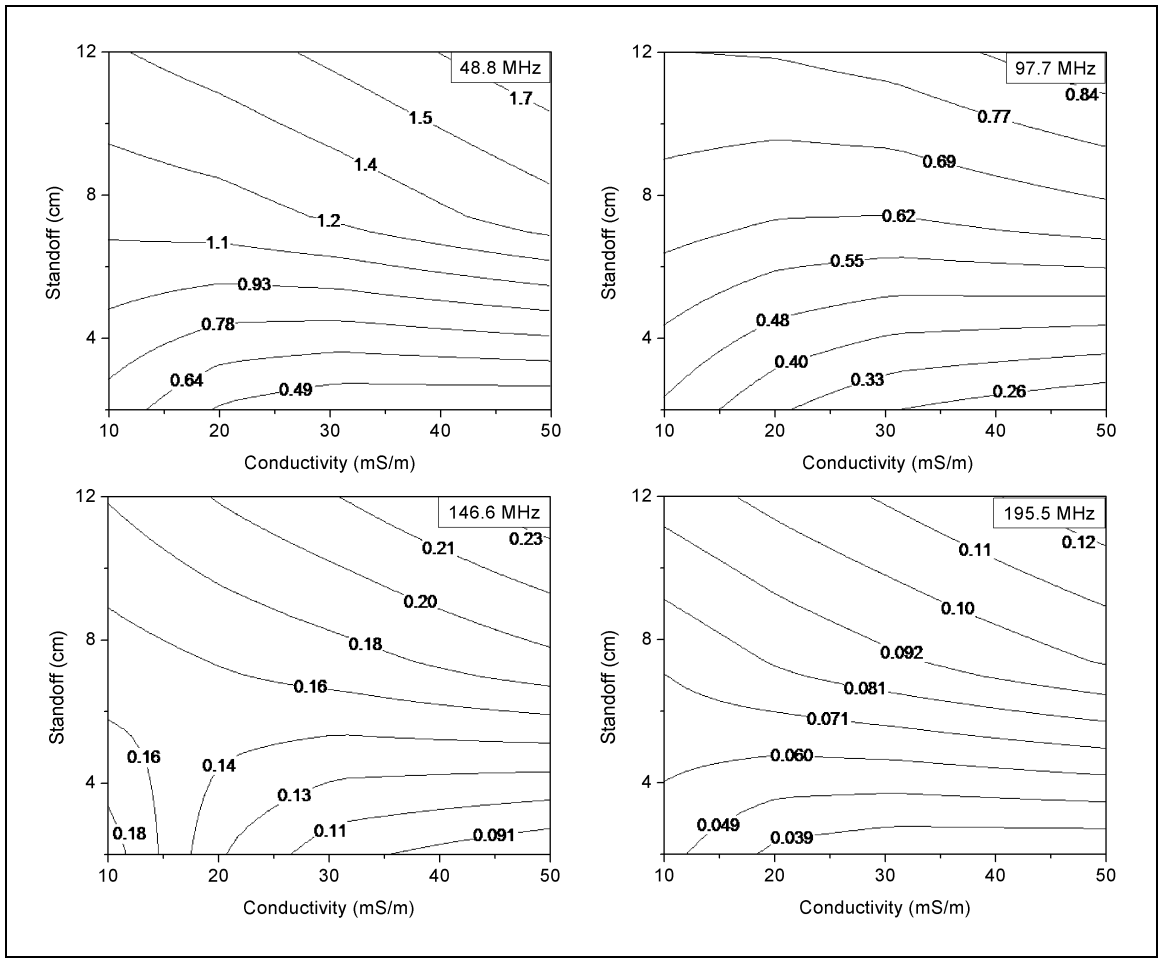

Figure D.23. Interpolated forward response of selected waveform attributes using the *Spectral* attribute set for an RDP of 9 and a 113 cm offset.

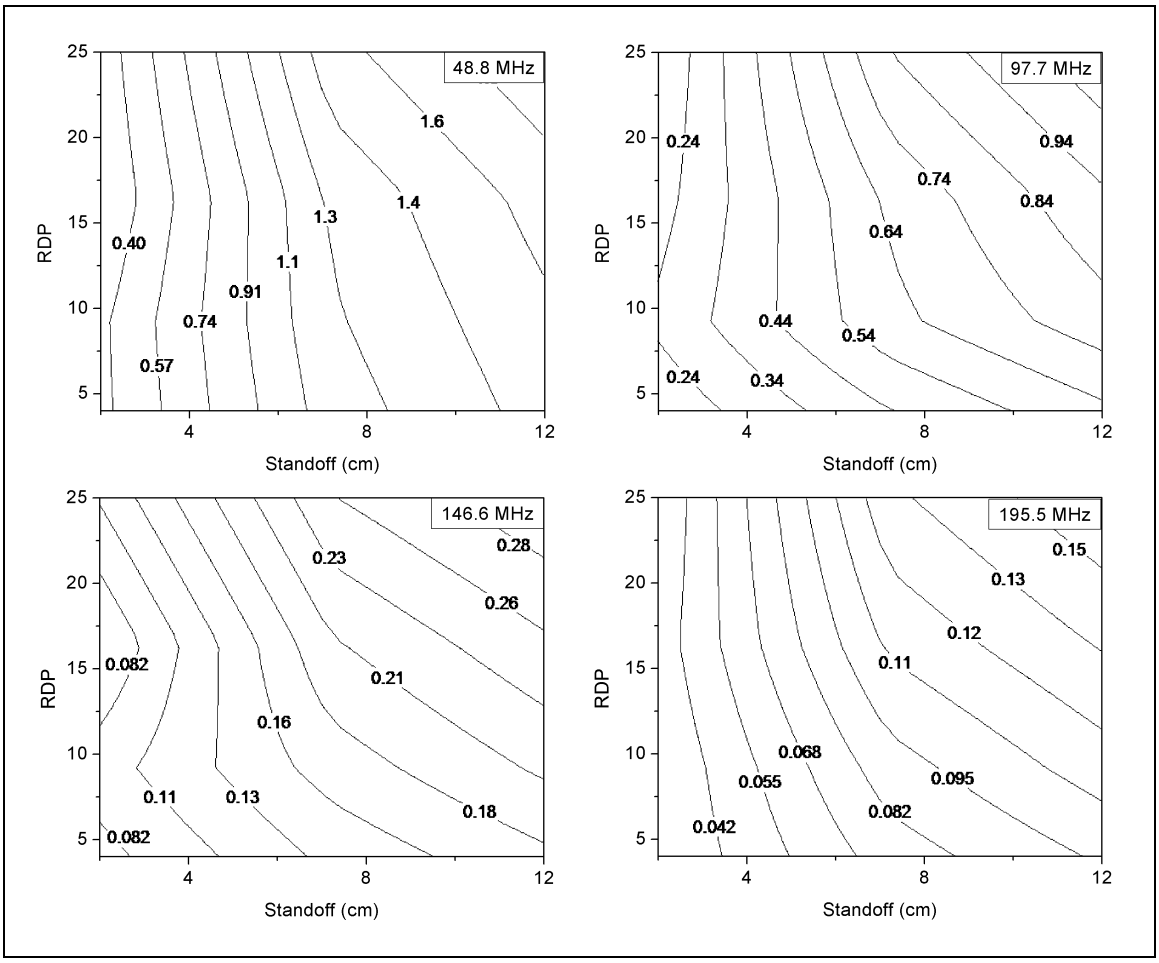

Figure D.24. Interpolated forward response of selected waveform attributes using the *Spectral* attribute set for a conductivity of 30 mS/m and a 113 cm offset.

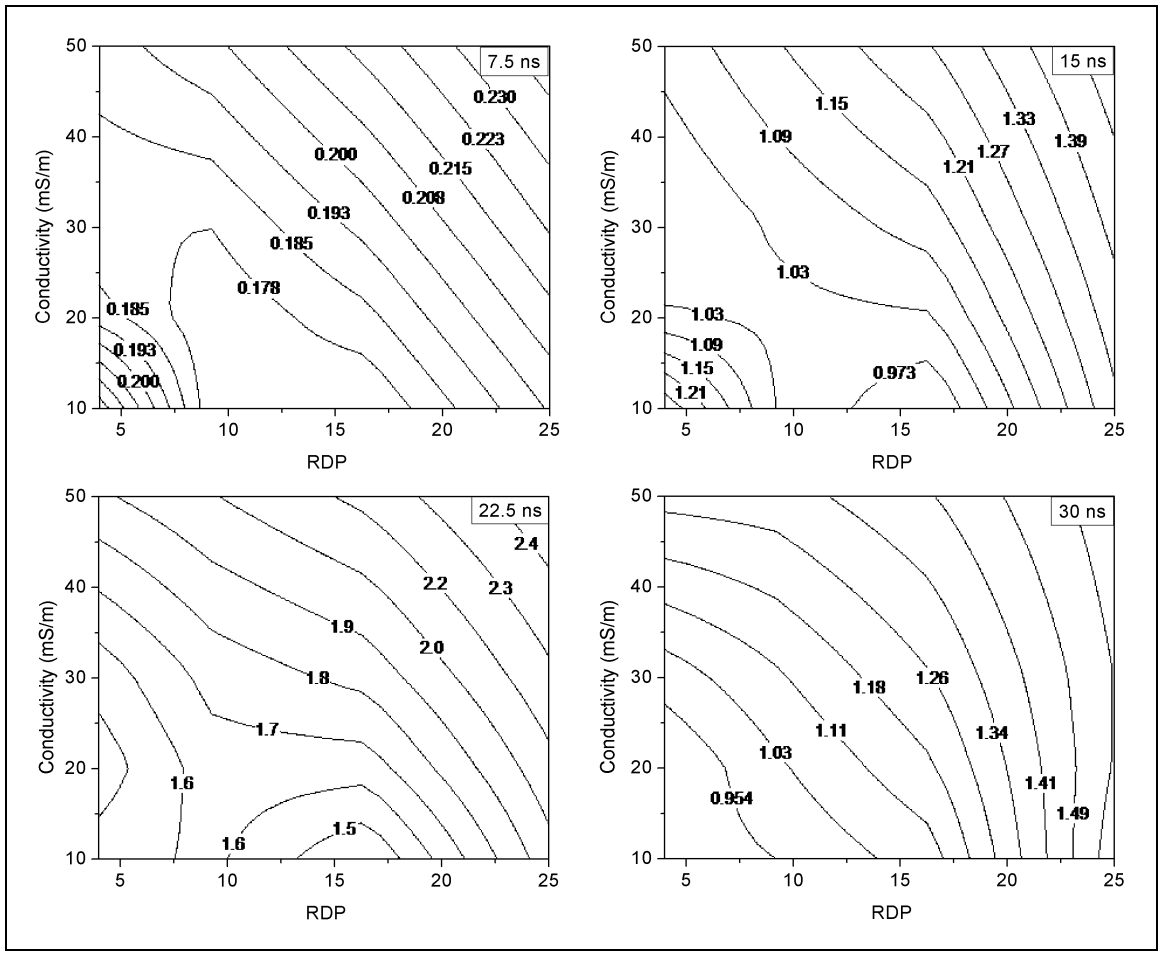

Figure D.25. Interpolated forward response of selected waveform attributes using the *Hilbert* attribute set for a 7 cm standoff and a 113 cm offset.

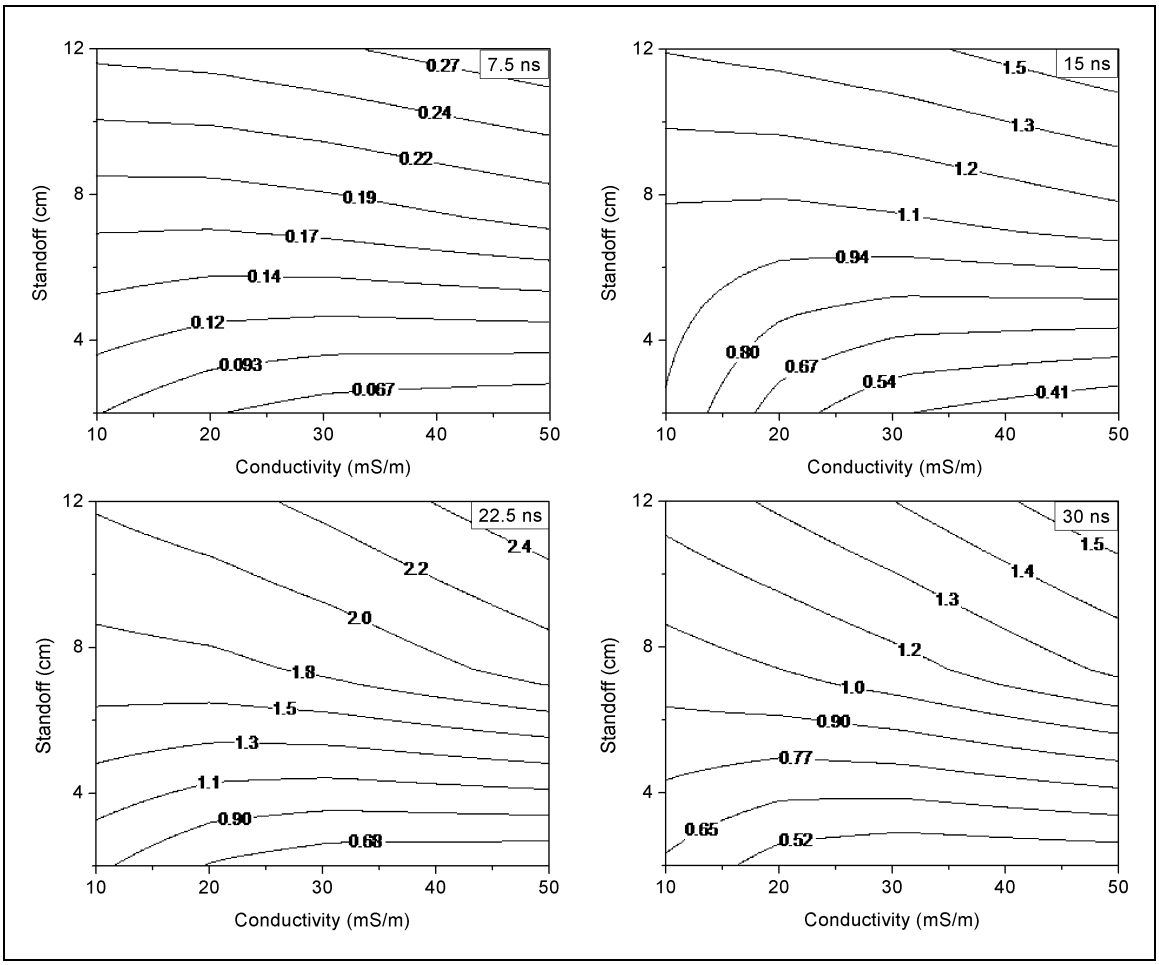

Figure D.26. Interpolated forward response of selected waveform attributes using the *Hilbert* attribute set for an RDP of 9 and a 113 cm offset.

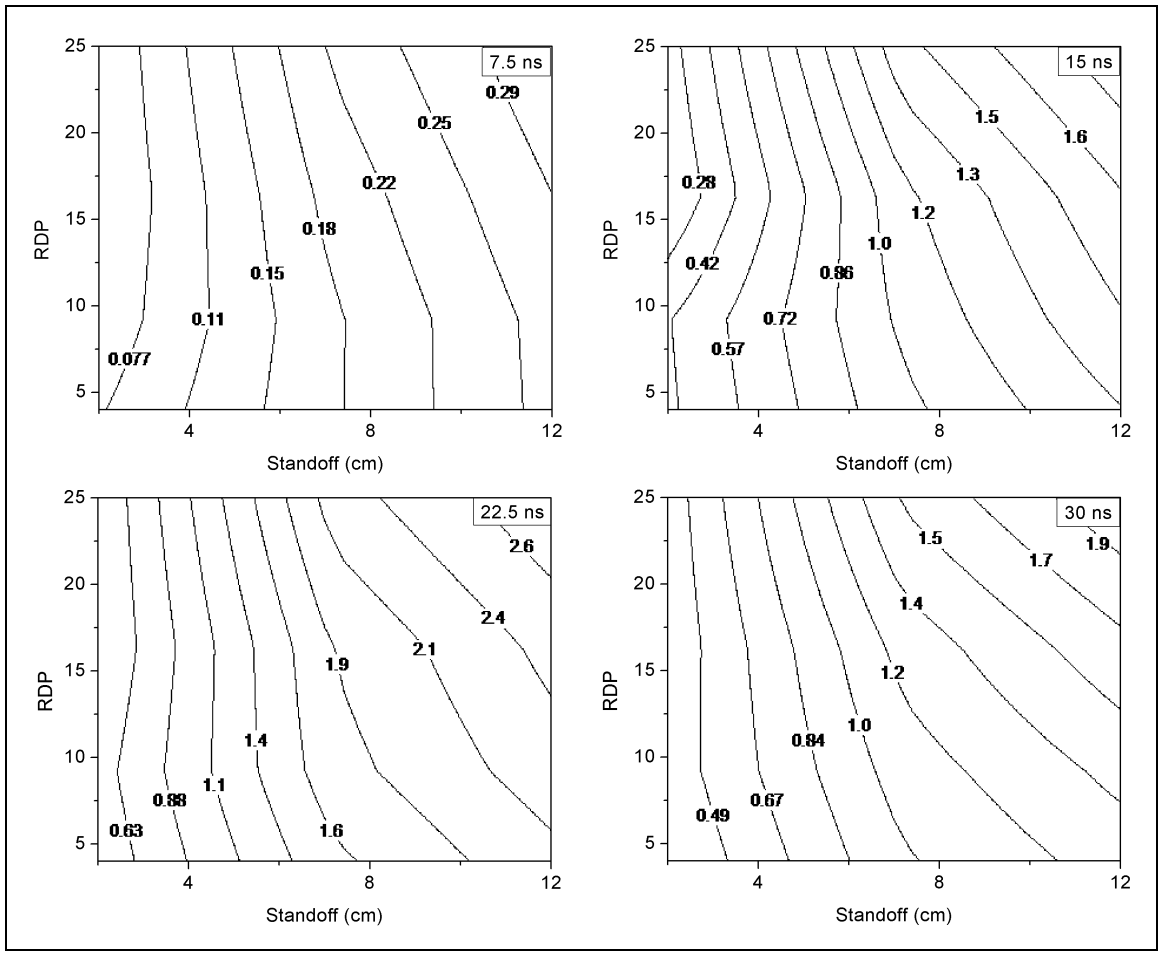

Figure D.27. Interpolated forward response of selected waveform attributes using the *Hilbert* attribute set for a conductivity of 30 mS/m and a 113 cm offset.

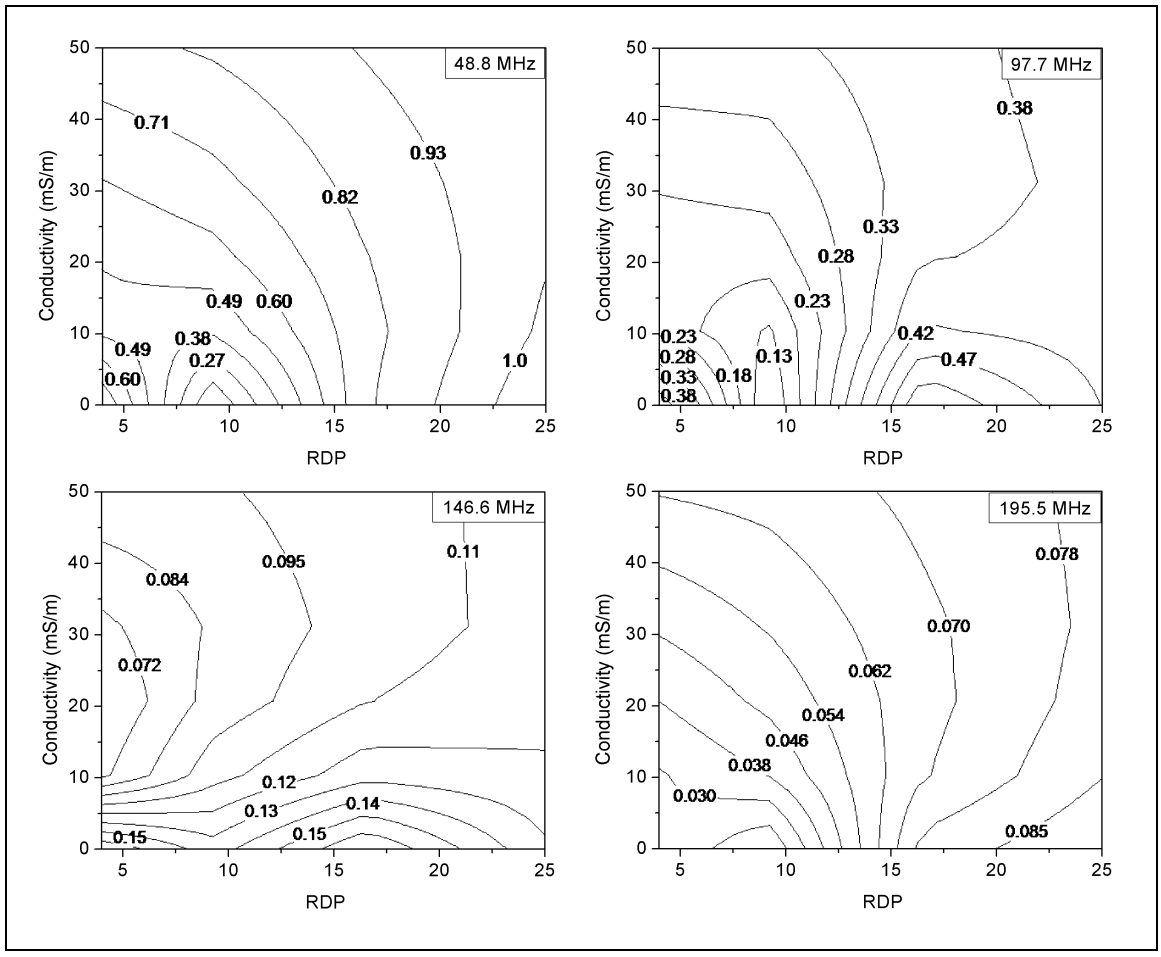

Figure D.28. Interpolated forward response of selected waveform attributes using the *Spectral* attribute set for a 7 cm standoff and a 173 cm offset.

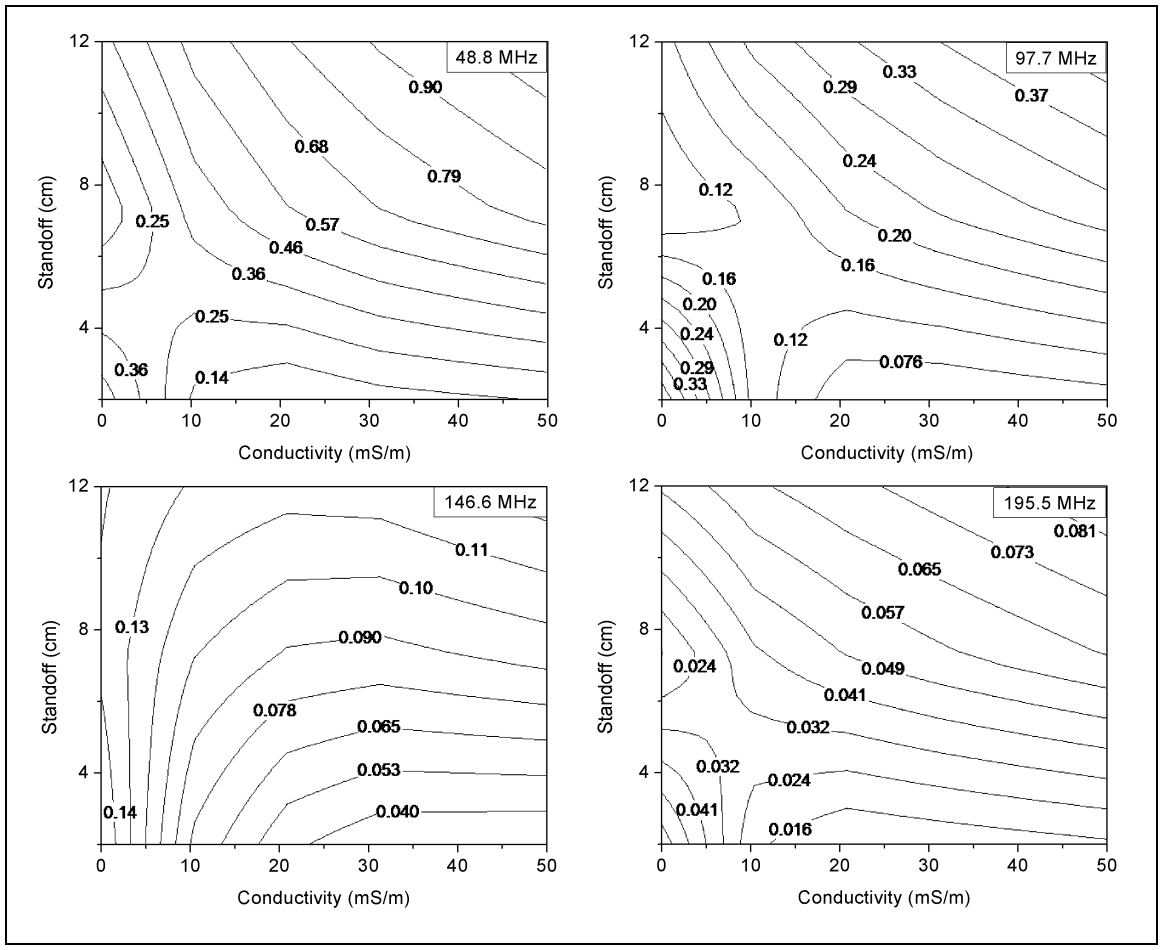

Figure D.29. Interpolated forward response of selected waveform attributes using the *Spectral* attribute set for an RDP of 9 and a 173 cm offset.

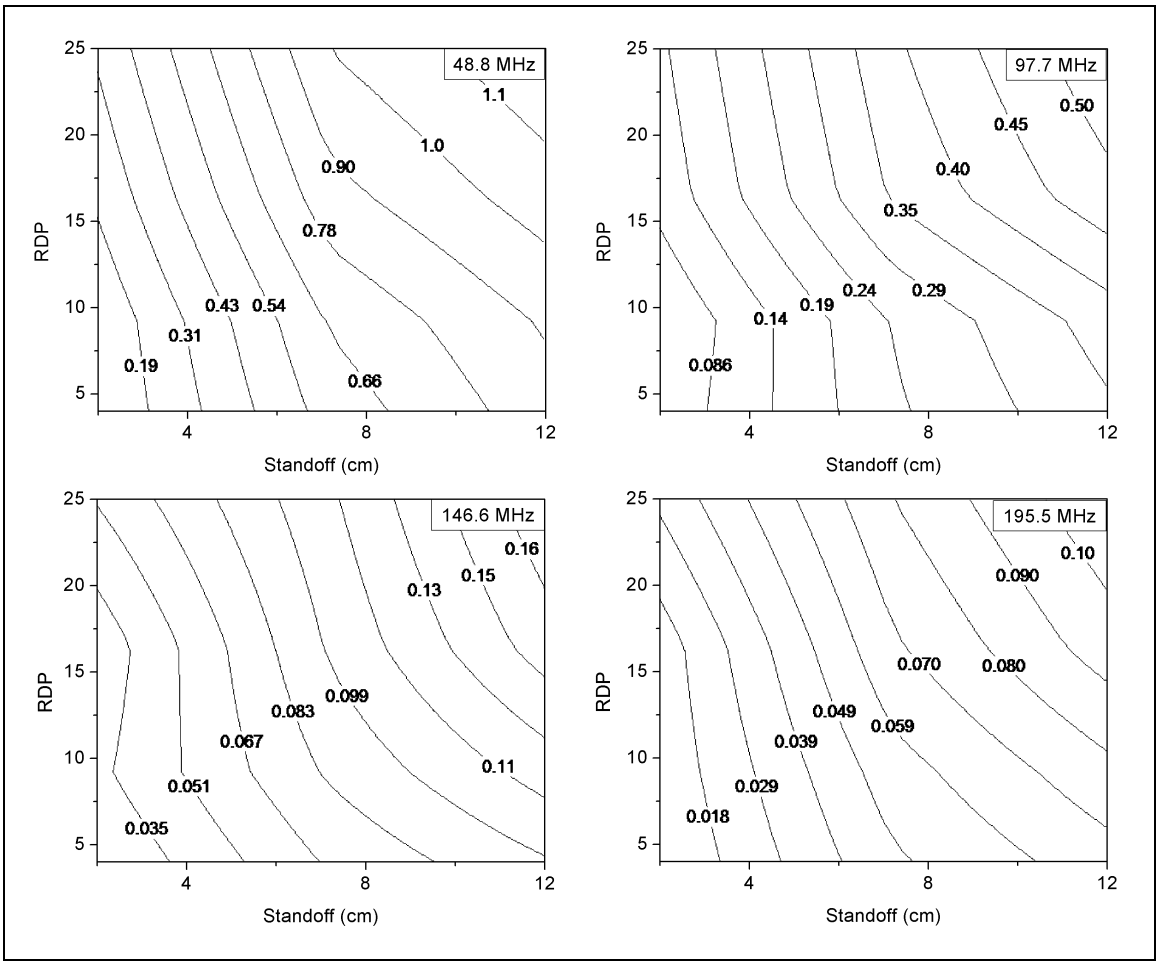

Figure D.30. Interpolated forward response of selected waveform attributes using the *Spectral* attribute set for a conductivity of 30 mS/m and a 173 cm offset.

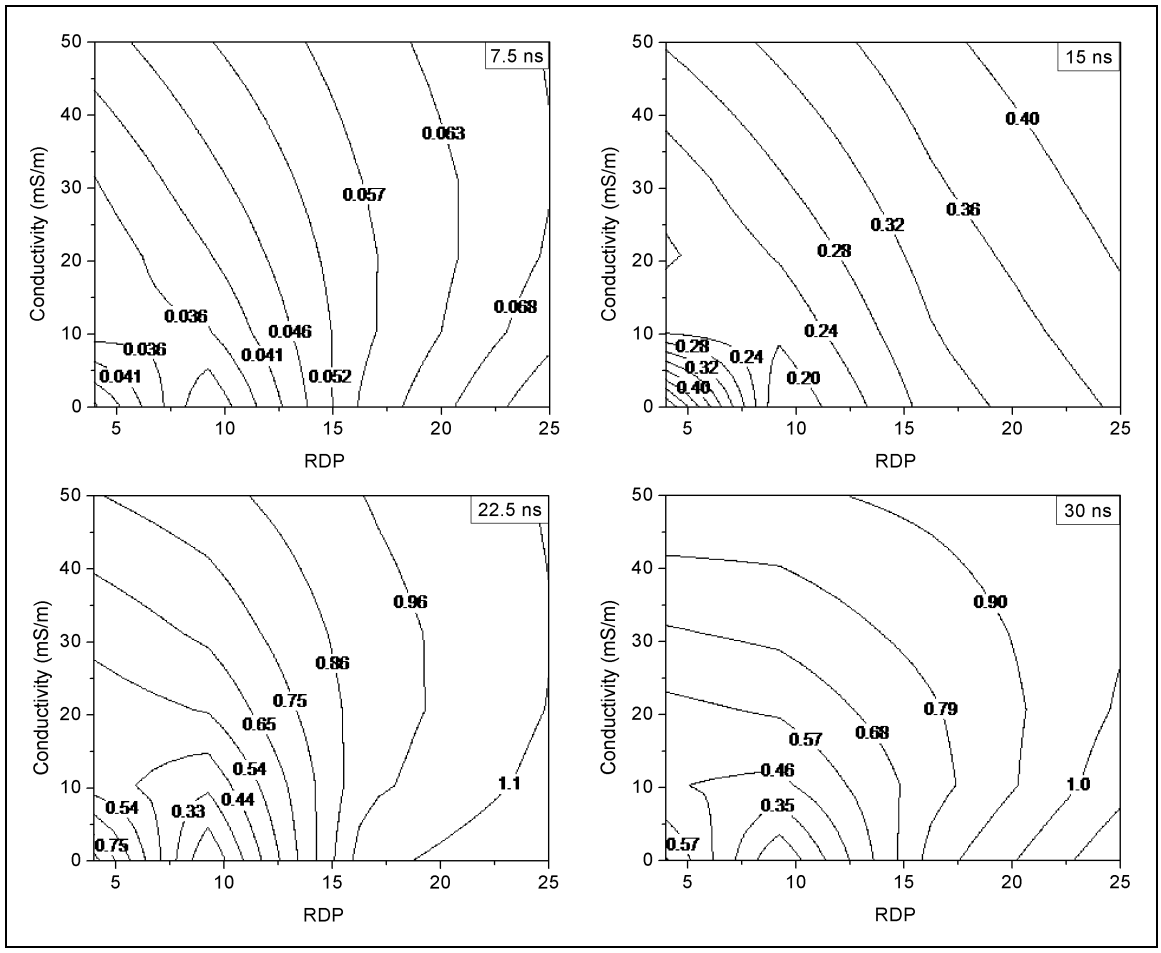

Figure D.31. Interpolated forward response of selected waveform attributes using the *Hilbert* attribute set for a 7 cm standoff and a 173 cm offset.

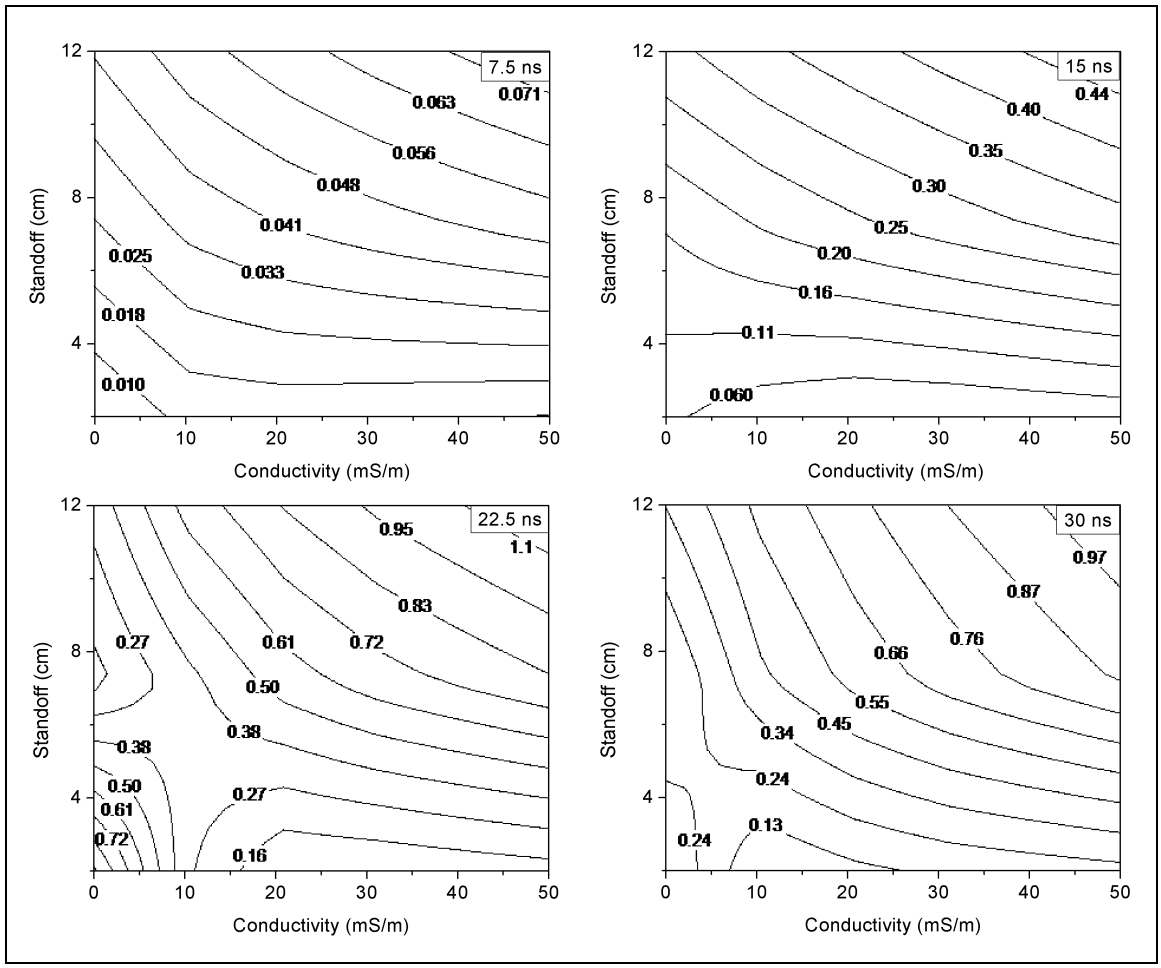

Figure D.32. Interpolated forward response of selected waveform attributes using the *Hilbert* attribute set for an RDP of 9 and a 173 cm offset.

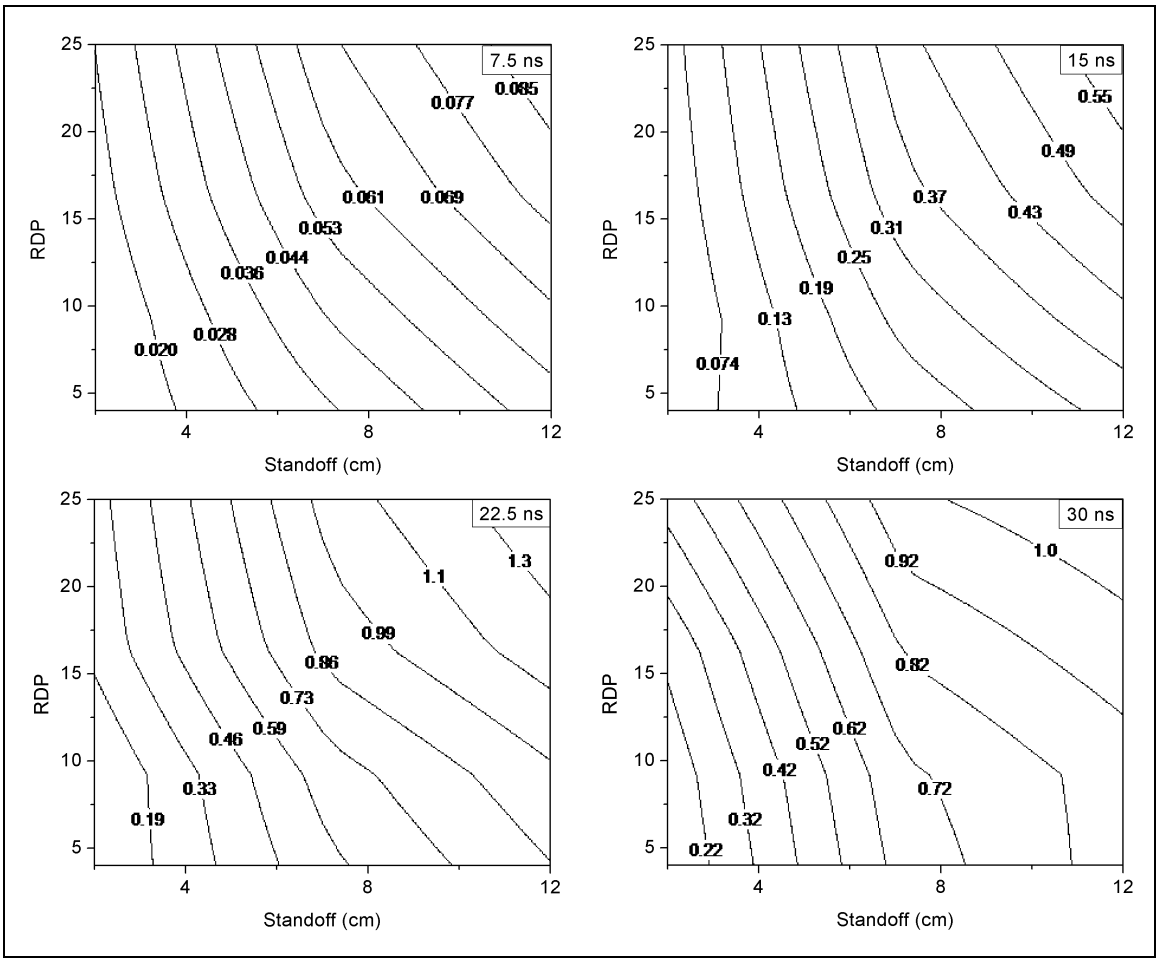

Figure D.33. Interpolated forward response of selected waveform attributes using the *Hilbert* attribute set for a conductivity of 30 mS/m and a 173 cm offset.